Università degli Studi di Napoli Federico II
Ph.D. Program in Seismic Risk
XXIV Cycle

Study of seismic hazard mitigation at different time scales: applications and technological development

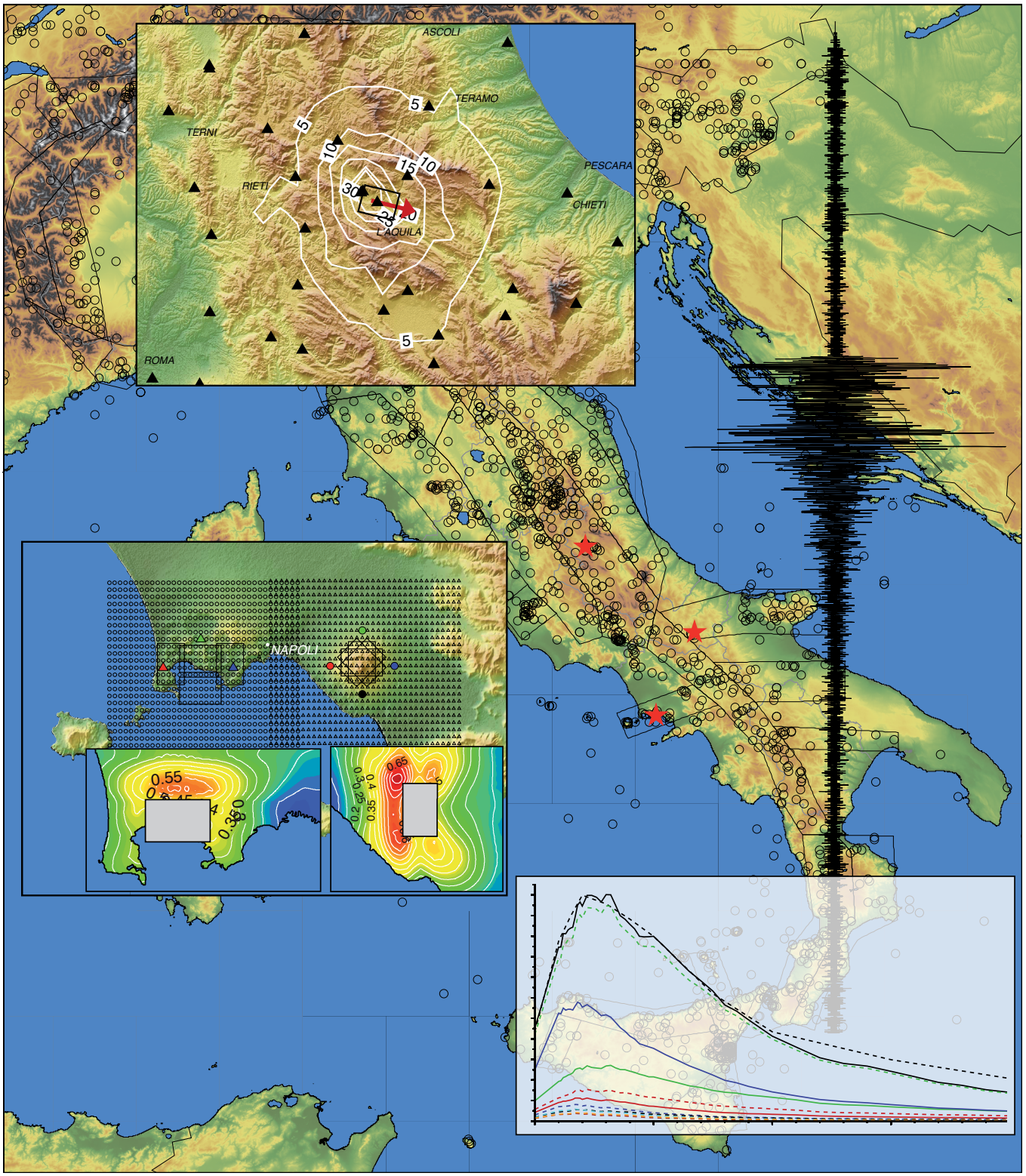

Mauro Caccavale

Università degli Studi di Napoli Federico II
Facoltà di Scienze Matematiche Fisiche e Naturali

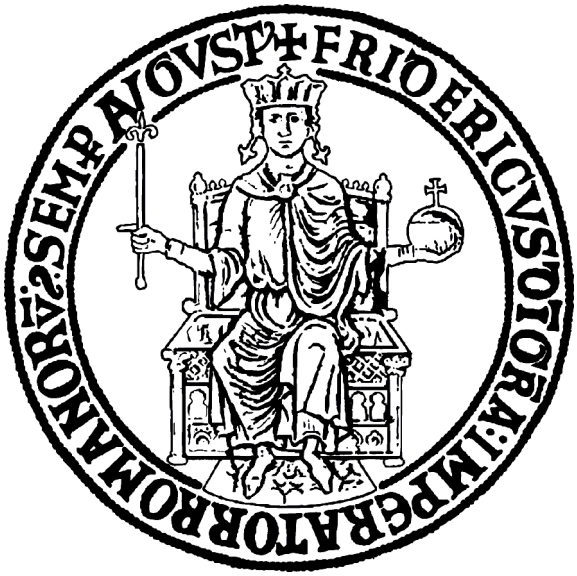

Dottorato di Ricerca in Rischio Sismico
XXIV Ciclo

Study of seismic hazard mitigation at different time scales: applications and technological development

Dott. Mauro Caccavale

Relatori:
Dr. Emolo Antonio
Dr. Iannaccone Giovanni

Napoli – 2011

To Michela Alfè,
Wife, friend, muse
Missing half of my life

Acknowledgements

Napoli, November 2011

Sicuramente è questo il momento più difficile da affrontare degli ultimi anni. Non è semplice riuscire correttamente a esprimere I propri sentimenti di gratitudine.
Senza voler offendere nessuno ritengo che liste di nomi e motivazioni siano un po' inappropriate e dispersive. Tuttavia sarebbe un rammarico non ricordare mia moglie, il Prof. Fancesco Silvestri e l'emerito Prof. Paolo Emilio Strolin. Certo del fatto che sapranno da soli giustificare I loro nomi su questo lavoro. Qualora non ci riuscissero avrei la certezza di aver fatto la cosa giusta a ricordarli.
Grazie,

Certainly this is the hardest challenge in the past few years; it's not always simple to be able to express one's gratitude.
Without meaning any offense towards anyone, I believe that lists of names and reasons are inappropriate and pointless. On the other hand, I would be at fault by not mentioning my wife, Professor Francesco Silvestri and last but not least by far, Professor Emeritus Paolo Emilio Strolin. I am confident they are aware of the significance they have had to me. If this were not the case, then I would be sure it was fair to acknowledge them on this page.
Thanks,

Mauro

Contents

Abstract

Earthquakes, weak or strong, represent always a psychological and emotional stress for people, but also a strong socio-economic impact for the affected area. The earthquake generation, the propagation of seismic waves, the seismic waves modification due to the propagation media and the interaction between seismic wave and human structures, are the main topics of different research disciplines. In the last years a wide interdisciplinary research program (physics, seismology, mathematics, geology, engineering, etc.) was world wide experienced aiming at improving the earthquake knowledge and mitigating the ground-shaking effects.

The seismic risk, namely the probability of occurrence of losses[1], can be described as the convolution of three variables:

Seismic Risk = Seismic Hazard * Vulnerability * Exposition

The *Seismic Hazard* represents the probability for a selected strong motion parameter (Peak Ground Acceleration, Velocity, Spectral Acceleration…) to be exceeded in a given time interval at a target site. The *Seismic Hazard* term mainly depends on the earthquake characteristics, target site-epicenter distance and geomorphologic conditions. More generally the *Seismic Hazard* describes the potential for a dangerous, earthquake-related natural phenomena such as ground shaking, fault rupture, or soil liquefaction. These phenomena could result in adverse consequences to society such as the destruction of buildings or the loss of life. From the seismological point of view all new information about the incoming ground shaking or the possible future ground motion amplitude represent a contribution to the "seismic hazard mitigation". In fact the knowledge of the expected ground acceleration is the first step for a better build design, while the knowledge of the incoming acceleration amplitude, during an earthquake occurrence, can define an alert action rather than others.

[1] Instructional Material Complementing FEMA 451, Design Examples; http://www.nibs.org/client/assets/files/bssc/Topic01-CourseIntroduction.pdf

The *Vulnerability* represents the probability that people, infrastructure and activity suffer the consequence of an earthquake. The damages can be direct as the collapse of structures or collateral as the fall of productivity due to power station injuries.

The *Exposition* represents a qualitative and quantitative evaluation of the elements exposed to seismic hazard also in terms of their geographical distribution.
Seismic risk increases as earthquake-prone regions become more densely populated and urbanized. Although local planning and zoning activities can help to shape regional growth over time, additional development is generally (and understandably) promoted as a means of strengthening of local economies.

The seismic hazard mitigation can be subdivided in two main time intervals:

- *Pre-event*
- *Real-time*

The "pre-event" period is characterized by different methodology and actions to prevent the casualties and damages produced by an earthquake. The main goal of the pre-event action is the estimation of casualties, structural collapse or damages as consequence of an earthquake occurrence that can affect the area of interest. As it will be reported in the following chapters the seismological results of the pre-event actions like seismic hazard analysis strongly depend on the knowledge about the seismicity characteristics of the target area, seismic wave generation and propagation.
The main pre-event approaches to the seismic hazard mitigation are the Probabilistic Seismic Hazard Analysis (PSHA) (**Chapter 1**) and the Hybrid Seismic Hazard Analysis (**Chapter 2**).

A PSHA study for Molise region, Italy, was conducted to refining the seismic hazard characterization for identifying a set of relevant earthquakes for the engineering analysis of structures. The results of this study, in combination with an experimental structural health monitoring system, represent a real innovation for the pre-event action to minimize the casualties and the structural damages. In fact the possibility to tracking at different time scales the structural response and the evolution of damage can provide important information to support rescue operations. The methodology and the results for the PSHA analysis at Molise region are reported in the **Chapter 1**.

The hybrid approach to seismic hazard analysis represents a combination of the main characteristic of the Deterministic Seismic Hazard Analysis (DSHA) and the probabilistic methodology. The probabilistic/deterministic approach is able to overcome the limitations of PSHA when a single causative fault and an associated maximum (credible) earthquake is considered as the threat for the site of interest and to considered the earthquake return period using the DSHA. This methodology was applied to high densely populated volcanic areas in Campania region, Italy, where the occurrence of a moderate seismic event represents a threat for the inhabitants and for the civil and/or industrial infrastructures. The hybrid approach in these high dangerous zones is considered as the first step for the hazard mitigation. The results of the analysis are reported in **Chapter 2**.

The "real-time" phase represents the modern seismological challenge. In fact only at the present the technology allows to perform analysis on seismic signal during the earthquake occurrence. However the technological development is not enough advanced to assure to undertake always the right alert actions. The shake maps play a relevant role to reduce the earthquake damages. It was reported by Wald et al. that: "For rapid response, ShakeMap ground motion values are used for emergency response and loss estimation, assessment of damage to the lifeline and utility networks, and for providing information to the general public"[2]. Shake maps are representations of the space distribution of the more representative parameters useful for description of the possible injuries to the infrastructures, which are the Peak Ground Acceleration (PGA) and the Peak Ground Velocity (PGV) and Spectral accelerations at different periods (Sa). The shake maps are a possible reference instrument for the civil protection operating units, for the army, for the Red Cross, etc. in order to assure timely and effective service on the territory. However at the present the shake maps calculated in real-time represent an approximation of the real ground motion parameters space distribution. The lack of reliability of the maps is strictly related to the lack of knowledge about the fault extension and the not well-defined source to target site distance. As discussed in the **Chapter 3,** a new methodology has been developed to define the dimension of the surface projection of fault plane during the earthquake to calculate a better spatial distribution of acceleration and velocity using the appropriate source to target site distance.

[2] ShakeMap: Its Role in Pre-Earthquake Planning and Post-Earthquake Response and Information; David Wald, C. Bruce Worden, Vincent Quitoriano and James Goltz; Proceedings of SMIP02 Seminar on Utilization of Strong-Motion Data (2002)

Instruments able to recognize an earthquake, to estimate the incoming ground motion and subsequently produce an early warning signal represent a valid real-time approach to mitigate the seismic hazard. This instruments combines seismological know-out with technological aspect about for instance seismic sensors, data-loggers, computer elaboration, and so on, and usually are defined as Earthquake Early Warning System (EEWS). The EEWS represent a challenge from different point of view because different knowledge is need to perform a signal analysis in real time to assure the large and reliable possible warning time interval. At the present the time interval necessary to perform very fast-automated action such as to stop the elevators, to shut-off gas, to stop the trains, to start-up the generators, is of order of few seconds. In high densely populated or industrialized areas few seconds could be sufficient to minimized the casualties and damages, to maximize the efficiency of rescue operation and the faster return to a normal and safe condition. **Chapter 4** reports a preliminary study for "EEWS-BOX" that represents a new approach for a stand-alone earthquake early warning system.

Capitolo 1

Probabilistic Seismic Hazard Analysis and Disaggregation in the Molise region, Italy: the case study of Campobasso

1.1 Introduction

Large-scale experimentations play a relevant role in the earthquake engineering research; similarly Structural Health Monitoring is able to give information of real structures. A few geotechnical structures are documented, because only data on seismic permanent deformations are available. The present chapter deals with seismic hazard analysis of the site of the Hospital of Campobasso and Student House at University of Molise, where a geotechnical monitoring system has been designed and is currently under implementation. The monitoring system is aimed at refining the seismic hazard characterization for identifying a set of relevant earthquakes for the theoretical analysis of the structure. Reference earthquakes expressed in terms of magnitude (M), distance (R) and ε[1], were therefore investigated. The Uniform Hazard Spectra (UHS) at different structural periods for different return period were disaggregated.

Structural Health Monitoring (SHM) for civil structures represents an interesting option for structural engineers to gain knowledge about real response of the structural to service gravity and wind loads during time. SHM offers opportunities in the fields of construction management and maintenance. If structures in seismic areas are concerned, an additional advantage of such techniques exists. In fact, a real or near real-time tracking of the structural response and of evolution of damage can support methods and techniques to develop post-earthquake scenarios and support rescue operations.

SHM is based on in-situ, non-destructive measurements and analysis of structural characteristics and aims at defining location and severity of damage, and at the evaluation of its consequences on the residual life of the structure (Silkorski, 1999; Mufti, 2001). SHM is a very multidisciplinary field, where a number of different skills (seismology, electronic and civil engineering, computer science) and institutions can work together in order to increase performance and reliability of such systems, whose promising perspectives seem to be almost clearly stated. Information obtained from such systems could be useful for maintenance or structural safety evaluation of both existing and historical structures by using rapid evaluation of conditions of damaged structures after

[1] The residual variability of the *PGA* with respect to the selected Ground Motion Prediction Equation

an earthquake, estimation of residual life of structures, repair and structures retrofitting (Rainieri et al., 2008).

An example of integrated structural and geotechnical-monitoring system (Fig.1.1.1) has been designed and is currently under implementation by the Structural and Geotechnical Dynamic Laboratory at University of Molise (Fabbrocino et al., 2009). Experimental activities are associated to numerical investigations both in the static and dynamic field (Rainieri et al., 2010). In this framework, the problem of the site-specific hazard in the area of the University of Molise in Campobasso, Italy, is tackled. In particular, the refinement of seismic hazard characterization is carried out in order to reference parameters for selecting dynamic input for theoretical analyses.

In the present study, attention is focussed on disaggregation of seismic hazard at the Vazzieri (Student house at University of Molise) and Tappino (Campobasso Hospital) sites (Fig.1.1.1) and on the selection of reference earthquakes expressed in terms of M-R-ε triplet. In particular, as proposed in Convertito et al. (2009) the UHS at different structural and return periods were disaggregated. For each of the disaggregated variable the shapes of both the joint and marginal probability density functions were studied and the first two modes of M, R and ε were extracted and discussed. Results are provided and are intended as an interesting support for design of monitoring systems and retrofitting of existing constructions (Iervolino et al., 2010).

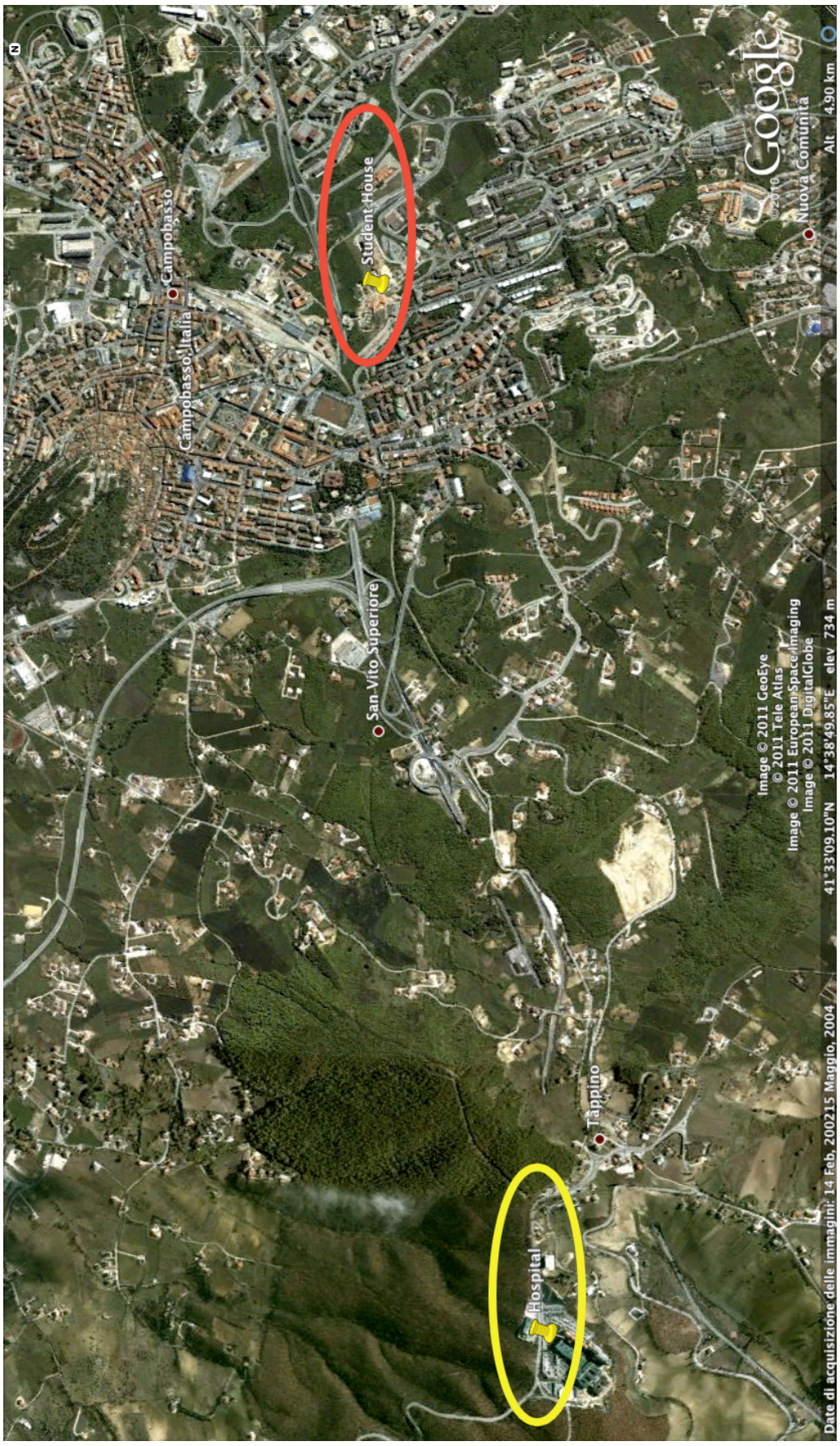

Figure 1.1.1. Google map of Campobasso area with the hospital (yellow) and the student house (red).

1.2 Methodology

In this section the Probabilistic Seismic Hazard Analysis (PSHA) to investigate the design earthquakes, expressed in terms of representative magnitude (M), distance (R) and ε, is presented and applied for a wide region of the Apennines region, Italy (Fig.1.2.1) (Caccavale et al, 2010).

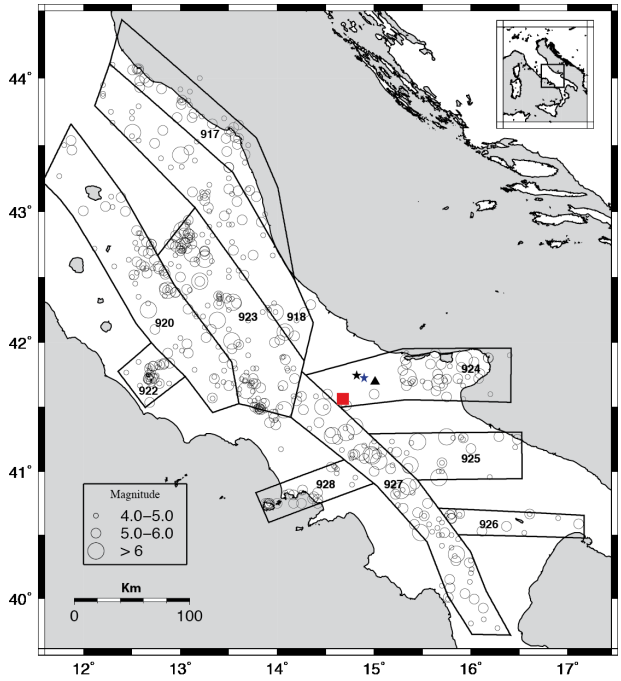

Figure 1.2.1. Seismic source zones configuration used to compute the hazard. Location of the target area used in the analysis is identified by red square. Circles, whose width is proportional to magnitude, represent the location of the earthquakes (M>4.0) retrieved from the CPTI04 catalog (Gruppo di lavoro, 2004). Stars represent Molise earthquakes sequence: 2002-10-31 Mw 5.7 (Blue) and 2002-11-01 Mw 5.7 (Black). Black triangle represents San Giuliano di Puglia village.

The PSHA, introduced by Cornell (1968), combines the contributions to the hazard from all potential sources of earthquakes and the average activity rates associated to each seismogenic zone considered. The PSHA can be synthetized in four steps (Fig.1.2.2) as reported by Kramer (1996):

1. Identification and characterization of the probability distribution of the potential rupture location capable of producing significant ground motion at the site. In

most case, uniform probability distributions are assigned to each zone, implying that earthquakes are equally liked to occur at any point within the source zone. These distributions are then combined with the source geometry to obtain the corresponding probability distribution of source-to-site distance.

2. The temporal distribution of earthquakes recurrence must be characterized. A recurrence relationship, which specifies the average rate at which an earthquake of some size will be exceeded, is used to characterize the seismicity of each source zone.
3. The ground motion produced at the site by earthquakes of any possible size occurring at any possible point in each source zone must be determined with the use of predictive relationship. The uncertainty inherent in the predictive relationship is also considered in a PSHA.
4. The uncertainties in earthquake location, earthquake size, and ground motion parameter prediction are combined to obtain the probability that the ground motion parameter will be exceeded during a particular time period.

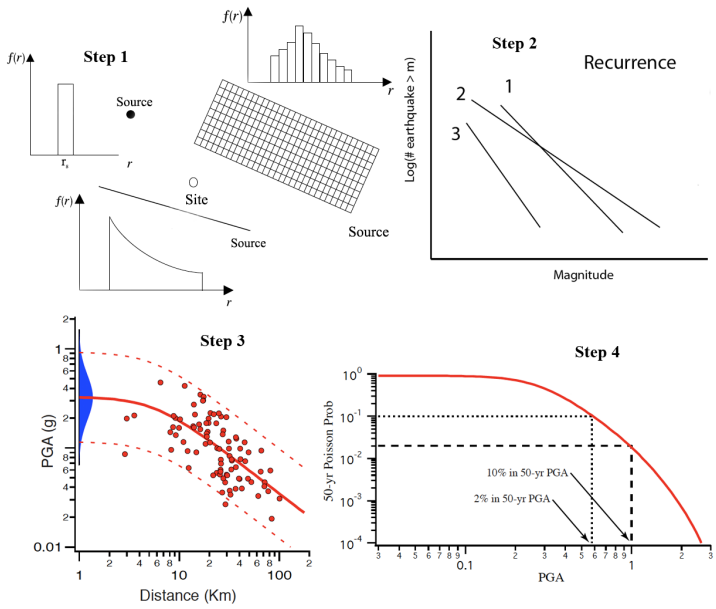

Figure 1.2.2. The four steps of the PSHA Kramer (1996).

The result of the PSHA, for a specified site, is a hazard curve that represents the probability of exceed of a ground-motion parameter *A,* such as Peak Ground Acceleration (PGA) or Response Spectral Acceleration (SA), in a time interval of interest.

The hazard curve is obtained assuming a Poissonian model for the temporal occurrence of the earthquake. This model is based on the hypothesis that earthquakes are random independent variables with tree main properties (Kramer, 1996):

1. The number of occurrences in one time interval is independent of the number that occur in any other time interval.
2. The probability of occurrence during a very short time interval is proportional to the length of the time interval.
3. The probability of more than one occurrence during a very short time interval is negligible.

These proprieties indicate that a Poissonian process is stationary and without memory of time, size or location respect to the preceding event. The Poissonian probability can be represented by the following equation:

$$P(N,t) = \frac{(\lambda t)^N e^{(-\lambda t)}}{N!} \tag{1.2.1}$$

Where λ represents the mean rate of occurrence of the event and t is the time period of interest. It can be demonstrated that the probability of at least one event is:

$$P(N \geq 1, t) = 1 - e^{(-\lambda t)} \tag{1.2.2}$$

and the return period (T_R) is:

$$T_R = -\frac{1}{\ln\left(1 - P(N \geq 1, t)\right)} \tag{1.2.3}$$

The construction of the hazard curve requires the computation of the hazard integral (Cornell, 1968; Bazzurro and Cornell, 1999) that provides the mean annual rate of exceeding of a given threshold value A_0 as in Eq. 1.2.4,

$$\sum_{i=1}^{N} E_i(A > A_0) = \sum_{i=1}^{N} \alpha_i \left\{ \int_M \int_R \int_\varepsilon P[A > A_0 | m, r, \varepsilon] f(m) f(r) f(\varepsilon) dm dr d\varepsilon \right\}_i \tag{1.2.4}$$

Where P represent the conditional probability of exceeding a threshold value (A_0) of a ground-motion parameter (A) for a given magnitude (*m*) distance (*r*), and *ε*.
The ε parameter represents the residual variability of the *A* with respect to the selected ground motion prediction equation (GMPE) (see cap.1.2.1 for more details). This P function represents the probability of exceed the A_0 level of the considered parameter for a given triplet m-r-ε. The probability density functions (PDFs) of magnitude *M*, *f(m)*, distance *R*, *f(r)* and *ε*, *f(ε)* depend, respectively, upon the adopted earthquake recurrence model (e.g., Gutenberg and Richter, 1944), and upon source geometry and the selected GMPE. Finally, α_i for each zone is the mean annual rate of occurrence of earthquakes with magnitude greater than some specified lower bound.
Combined the equation (1.2.2) and (1.2.4) is possible to compute the probability of exceeding P of the selected ground motion parameter during a fixed time period:

$$P(A \geq A_0, t) = 1 - e^{-\sum_{i=1}^{N} E_i(A>A_0)\cdot t} \quad (1.2.5)$$

The resolution of the integral (1.2.4) needs the knowledge of each PDF.
The Gutenberg-Richter (1944) linear relation, who expresses the cumulative number of earthquake with a magnitude greater than a fixed threshold is:

$$log\lambda_m = a - bm \quad (1.2.6)$$

Where λ_m is the mean annual rate of exceeding of an earthquake with magnitude m, *a* is the annual rate of earthquake and *b* represent the slop of the regression line or the relative number of small and large earthquakes. The determinations of *a* and *b* values is based on statistical analysis of events catalogue. The completeness of the catalogue is fundamental to obtain reliable estimations of the equation (1.2.6) coefficients. The Gutenberg-Richter recurrence law is valid for all magnitude intervals, but for engineering propose only earthquakes with magnitude greater than a threshold value (M_{min}) are relevant. On the other hand a seismic source zone is unable to generate event of magnitude greater than fixed value (M_{max}). Introducing this threshold in (1.2.6) a truncated version of Gutenberg-Richter relation is obtained (McGuire and Arabasaz, 1990):

$$\lambda_m = e^{(\alpha-\beta m_{min})} \frac{e^{(-\beta(m-m_{min})} - e^{(-\beta(m_{max}-m)}}{1 - e^{(-\beta(m_{max}-m_{min})}} \quad (1.2.7)$$

and the associated probability density function f_M(m):

$$f_M(m) = \frac{\beta e^{(-\beta(m-m_{min})}}{1 - e^{(-\beta(m_{max}-m_{min})}} \quad (1.2.8)$$

Where $\beta=b(ln10)$ and $\alpha=a(ln10)$.

The P function (eq.1.2.4) can be expressed by error function (eq.1.2.9) under the hypothesis that the considered ground motion parameter is log-normal distributed:

$$P[A > A_0|m,r,\varepsilon] = \frac{1}{\sqrt{2\pi}\sigma} \int_{A_0}^{+\infty} e^{-\frac{(A-\bar{A})}{2\sigma^2}} dA \quad (1.2.9)$$

Where $\bar{A}$ is the value of the selected ground motion parameter obtained by GMPE for the triplet (m-r-ε) and A_0 is a threshold value for the same parameter.

The mathematical expression for $f_R(r)$ is complex for geometry source different than point or line and need to be computed numerically.

The PDF of ε represents the standard Gaussian distribution under the hypothesis that estimated ground motion parameter is log-normal distributed.

For engineering analyses purposes, it may be important to identify the most threatening earthquakes for the site of interest, while PSHA, for its integral nature, combines the contribution to the hazard from all *N* considered sources. However, the disaggregation procedure allows the decomposition of each point on the hazard curve, in terms of M, R and ε, from each selected source. Disaggregation in terms of ε may be useful to choose records for nonlinear dynamic analysis having the correct spectral shape at a period relevant for the dynamic behaviour of the structure (Convertito et al., 2009). From an analytical point of view, the disaggregation's result is the joint PDF in Eq. 1.2.10,

$$f(m,r,\varepsilon|A > A_o) = \frac{\sum_{i=1}^{N} \alpha_i \{P[A > A_0|m,r,\varepsilon] f(m) f(r) f(\varepsilon)\}_i}{\sum_{i=1}^{N} E_i(A > A_0)} \quad (1.2.10)$$

Which is the distribution of magnitude, distance, and ε conditional on the exceedance of the hazard level being disaggregated. In other words, given the exceedance of the A_0 ground-motion value, disaggregation provides how likely it is caused by each specific M, R, ε set (McGuire, 1995).

From the PDF in Eq. 1.2.10 marginal PDFs may be obtained. They are univariate distributions of the disaggregation variables. The marginal PDF of a variable is obtained from the joint PDF saturating the other variables, that is, adding up all their contributions (Benjamin and Cornell, 1970). This gives the contribution to hazard of each variable alone. Marginal PDFs for M, R, and ε may be computed with Eq. 1.2.11, 1.2.12 and 1.2.13,

$$f(m|A > A_o) = \int_R \int_\varepsilon f(m, r, \varepsilon|A > A_o)\, dr d\varepsilon \tag{1.2.11}$$

$$f(r|A > A_o) = \int_M \int_\varepsilon f(m, r, \varepsilon|A > A_o)\, dm d\varepsilon \tag{1.2.12}$$

$$f(\varepsilon|A > A_o) = \int_R \int_M f(m, r, \varepsilon|A > A_o)\, dr dm \tag{1.2.13}$$

In the case one wants or is allowed by the seismic code to use disaggregation of seismic hazard to identify the design earthquakes for the site of interest, semi arbitrary approaches based on these PDFs are usually adopted. For example, representative values of the distributions (e.g., median, modal, or the mean values of M, R, and ε) may be considered if a single design earthquake is sought.

The first step in the analyses of the present study consisted of the computation of the hazard curve (see Cap.1.3 for more details) and the Uniform Hazard Spectra (UHS) (see Cap.1.4 for more details) for two target site shown in Figure 1.2.1 (red square), in terms of peak ground acceleration (PGA) and spectral acceleration Sa(T), for the 47 different structural of ASB96 (Ambraseys et al., 1996) at four different return period for each site. The use of a so large number of spectral ordinates in this study allows to retrieve detailed information for the fundamental periods of bulkhead of the student house and the fundamental periods of the student house and hospital for which the seismic design is carried out.

1.2.1 Ground Motions Prediction Equations

The Ground Motion Prediction Equations (GMPEs) are mathematical equations that predict ground motion parameter of engineering interest.

To define the form of a GMPE the starting point is a large number of recorded earthquakes that can adequately cover the value range of interest in terms of magnitude, distance, site condition, …

Different statistical regression analysis technique can be performed to define the value of GMPE's coefficient only if a complete and homogeneous database is available. The reliability of ground motion parameter estimate and the range of validity of the GMPE, in terms of magnitude and distance, is function of data distribution in the selected dataset (Fig. 1.2.1.1).

The modern database rarely match the complete and homogeneous condition required to produce reliable ground motion parameter estimation. This may be an important limitation because the number of data at short distance or for high magnitude is not always sufficient for statistical propose. To avoid this problem, related with the bias and scatter of data, Campbell and EERI (1985) proposed few rules:

1. Tectonic provinces of similar attenuation and source characteristics
2. Recording instruments of similar response characteristics
3. Consistent and accurate record-processing techniques
4. Consistent definitions of strong-motion, earthquake, path, site and structure parameters

The general form of a GMPE is (Campbell, 1985):

$$Y = b_1 ln f_1(M) f_2(R) f_3(M,R) f_4(P_i) \varepsilon \qquad (1.2.1.1)$$

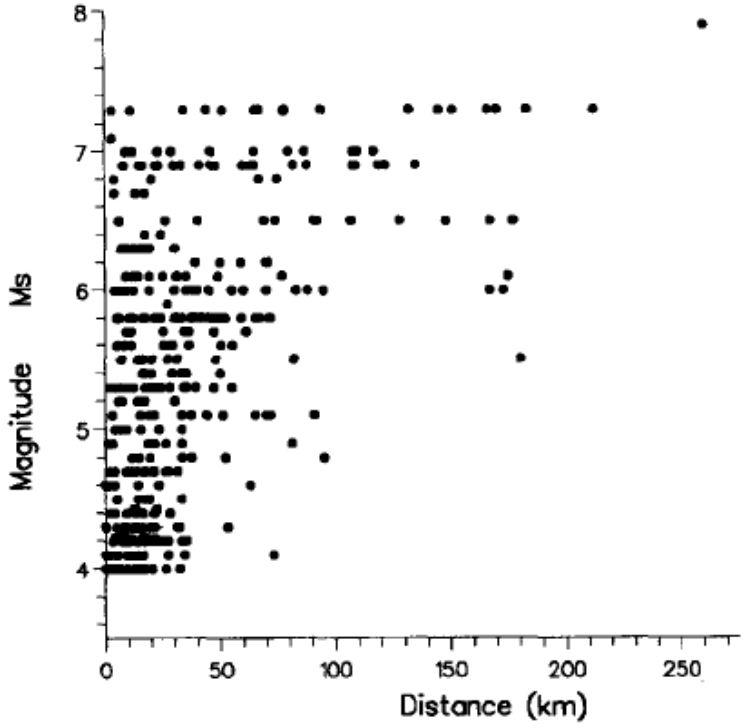

Fig. 1.2.1.1: Distribution of data in ASB96 dataset in terms of magnitude and distance.

Where Y is the ground motion parameter to predict, b_1 represent a constant to determinate by regression analysis, f_1(M) is a function of earthquake magnitude, f_2(R) is a function of source to site distance, f_3(M,R) is a joint function of magnitude and distance and represent the interdependence of two variables. The term $f_4(P_i)$ represents possible site effects, source mechanisms, … The ε term represents the uncertainty of Y.
Under the hypothesis that Y have a log-normal distribution (Campbell, 1985) it is possible to replace (1.2.1.1) with an easier to handle form:

$$lnY = lnb_1 + lnf_1(M) + lnf_2(R) + lnf_3(M,R) + lnf_4(P_i) + ln\varepsilon \qquad (1.2.1.2)$$

The independent variables of (1.2.1.1) and (1.2.1.2) consist of a set of parameters describing the seismic source, the waves path from source to site (*geometric spreading*) and the propagation media effect that can affect the ground motion parameter amplitude.
The most common ground motion parameters esteemed by GMPE are the peak ground acceleration (PGA), velocity (PGV) and spectral acceleration (SA), that are well correlated with the energy and force acting on a build during an earthquake.

The main variable in GMPE is the magnitude that takes into account the earthquake size. Usually each GMPE uses a different magnitude scale: moment magnitude M_W is used for large earthquake to avoid saturation problem or local magnitude while M_L is used for small events (less than 5.5).

The attenuation of the seismic signal is taking into account by R (source to site distance). There are a lot of different definitions for R (Fig. 1.2.1.2), the selection of one of them is usually a function of the specific database used. The principal definitions for R are hypocental (M1) or epicentral (M2) that represents the distance between the fractures starting point and the receiver or its surface projection, respectively. M1 and M2 are right definition if a point source approximation is used. When a finite fault is considered and enough information about it are available, R can be defined as the distance between the receiver and the energetic zone (M3) or the closest distance from rupture zone (M4). The M5 represent the closest distance from the surface projection of fault plane and it is the widely used definition in the GMPE.

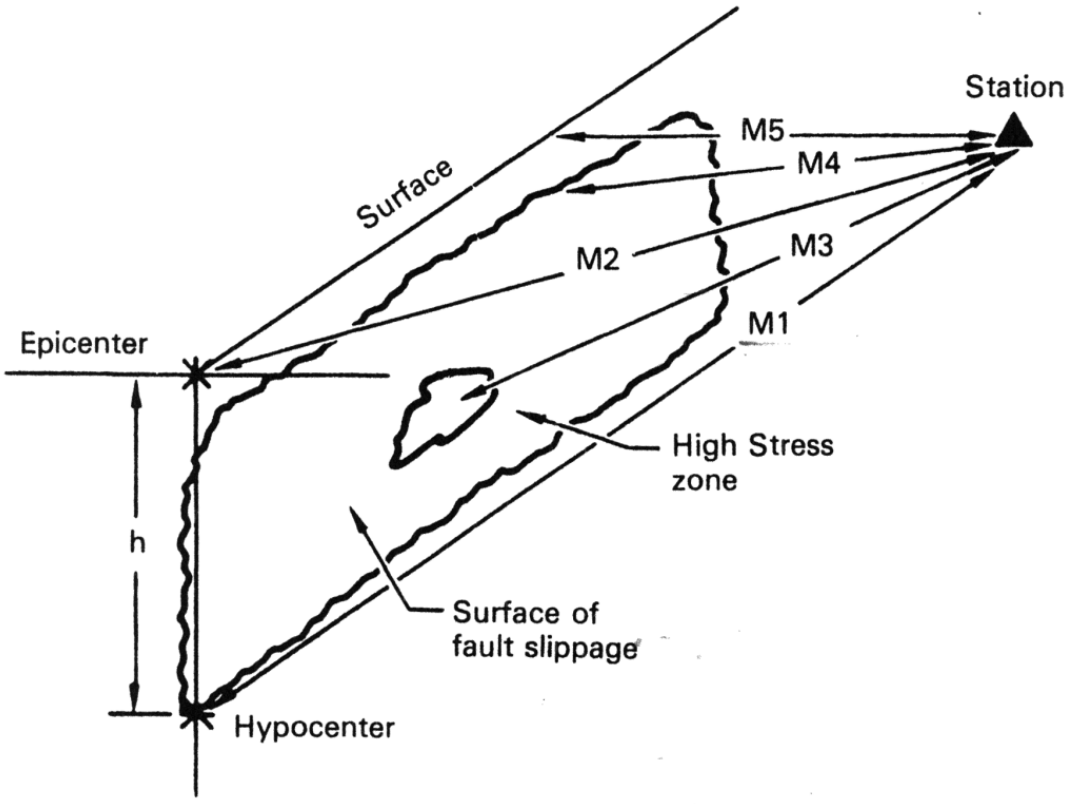

Fig. 1.2.1.2: Graphic representation of different source to site distance definition (see text for more details).

Some GMPE consider the interdependence of magnitude (M) and distance (R) as variables using a joint function f_3(M,R). This term explain the variation of R value (defined as the shortest distance from surface projection of fault plane) as a function of M (measure of rupture areas) when extended fault is considered. The function or the set of functions $f_4(P_i)$ represent the effect related source characteristic not accounted in magnitude variable, possible variation in frequency and amplitude of seismic signal due to local effect of propagation media (site effect) or to the presence of structures in the neighbourhood of the receiver. The random variable ε represents the error associated to the Y estimate by GMPE (Campbell and EERI, 1985) and it is a function of the regression algorithm and data distribution used. For more GMPE this term is not a good estimate of confidence limits, but can be interpreted as an estimate of these limits (Reiter, 1995). Figure 1.2.1.3 reports the values of the peak ground accelerations as a function of the epicentral distance for Sabetta and Pugliese (1984) and Ambraseys et al. (1996) GMPE. It can be observed that the shape of the curves vary as functions of the magnitude for both GMPEs.

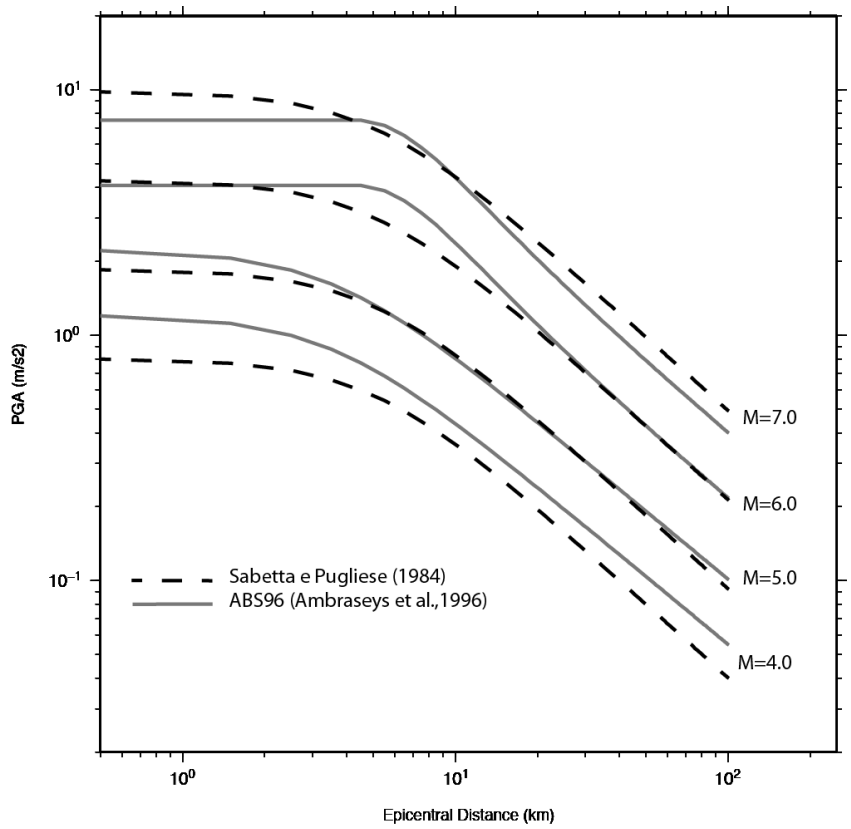

Fig. 1.2.1.3: Shape of different GMPE at different magnitude.

To perform the PSHA and disaggregation in the Molise region the ASB96 (Ambraseys et al., 1996) GMPE was selected.

Based on more the 400 triaxial records at free-field stations with a surface wave magnitude (Ms) range between 4.0 and 7.0 the ASB96 can be used to construction of hazard design spectra up to 200Km. The limit on magnitude is consistent with the minimum and maximum magnitude for the sismogenetic zone considered in this study (Barani et al., 2009). Earthquakes with Ms value less than 4.0 was not considered in ASB96 because not of engineering significance. The general form of Ambraseys GMPE for rock site condition is:

$$\log(y) = C_1 + C_2 M + C_3 log\left(\sqrt{D^2 + h^2}\right) + \sigma \qquad (1.2.1.3)$$

Where y represents the peak horizontal ground acceleration predicted, M the surface magnitude of the earthquake, h and $C_{1\text{-}3}$ are constant (Tab.1.2.1.1) and D is the closest distance to surface projection of rupture zone. The epicentral distance definition (R_{epi}) is more appropriate in order to properly use the hypothesis that the seismicity is uniformly distributed inside each seismogenetic zone. A linear relationship (Gruppo di lavoro, 2004) was used to convert D (Eq. 1.2.1.3) in R_{epi} (Fig. 1.2.1.2) for earthquake of $M_s \geq 6.0$:

$$D = -3.5525 + 0.8845 R_{epi} \qquad (1.2.1.4)$$

The term h in equation (1.2.1.3) was introduced because the closest point on the surface projection of the fault generally does not generate the predicted acceleration.

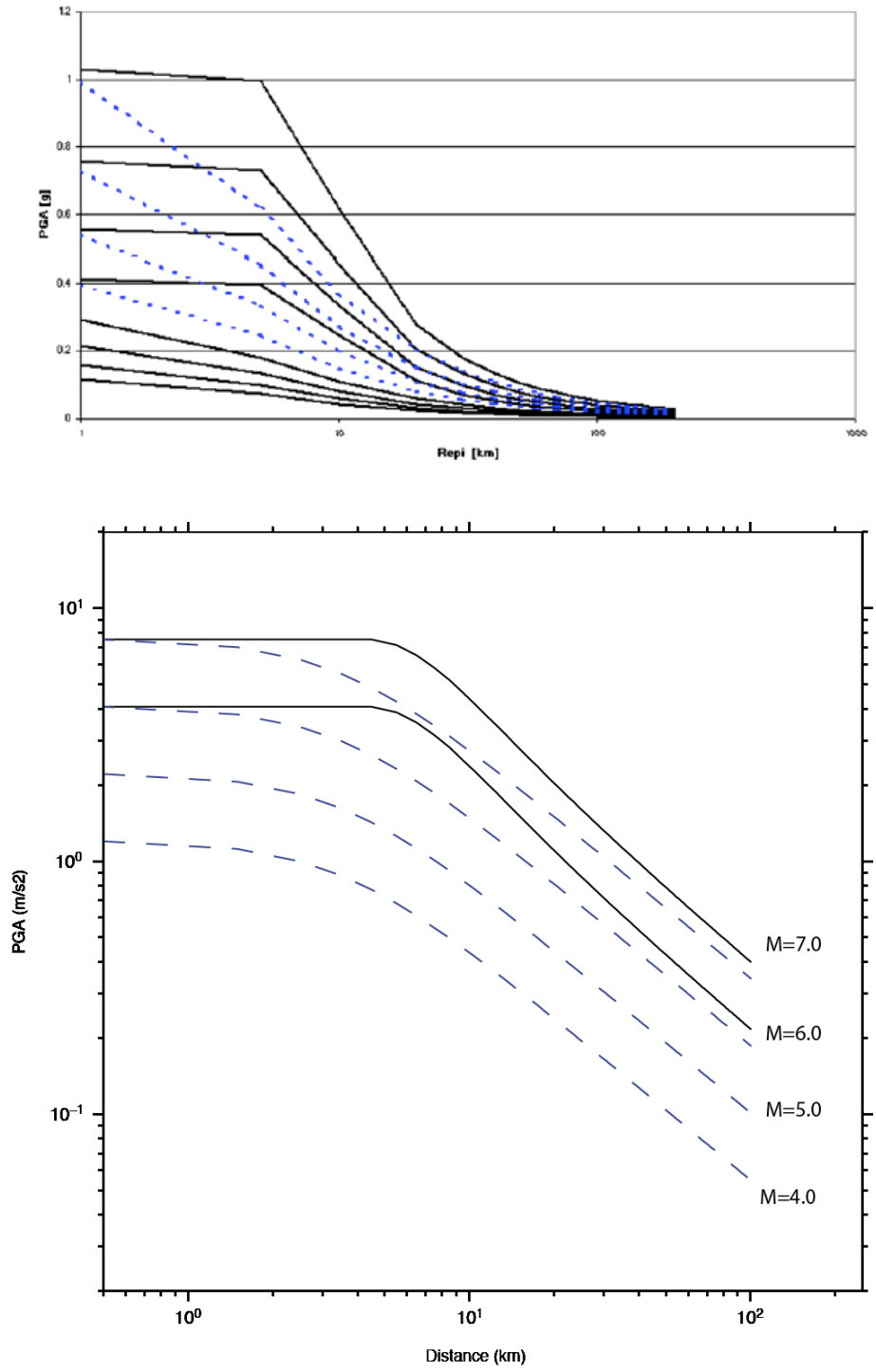

Fig. 1.2.1.4: Attenuations curves for ASB96 at different magnitude. The blue dished lines represent the curves corrected by eq. 1.2.1.4 ($4.0 \leq M_s \leq 7.0$), the black lines, plotted only for $M_s \geq 6.0$, represent the ASB96 curves not modified. (Gruppo di lavoro, 2004).

Table 1.2.1.1: Coefficients of equation (1.2.1.3) adapted from Ambraseys et al. (1986).

T	C_1	C_2	h	C_3	σ
PGA	-1.48	0.266	3.5	-0.922	0.25
0.10	-0.84	0.219	4.5	-0.954	0.27
0.11	-0.86	0.221	4.5	-0.945	0.27
0.12	-0.87	0.231	4.7	-0.960	0.27
0.13	-0.87	0.238	5.3	-0.981	0.27
0.14	-0.94	0.244	4.9	-0.955	0.27
0.15	-0.98	0.247	4.7	-0.938	0.27
0.16	-1.05	0.252	4.4	-0.907	0.27
0.17	-1.08	0.258	4.3	-0.896	0.27
0.18	-1.13	0.268	4.0	-0.901	0.27
0.19	-1.19	0.278	3.9	-0.907	0.28
0.20	-1.21	0.284	4.2	-0.922	0.27
0.22	-1.28	0.295	4.1	-0.911	0.28
0.24	-1.37	0.308	3.9	-0.916	0.28
0.26	-1.40	0.318	4.3	-0.942	0.28
0.28	-1.46	0.326	4.4	-0.946	0.29
0.30	-1.55	0.338	4.2	-0.933	0.30
0.32	-1.63	0.349	4.2	-0.932	0.31
0.34	-1.65	0.351	4.4	-0.939	0.31
0.36	-1.69	0.354	4.5	-0.936	0.31
0.38	-1.82	0.364	3.9	-0.900	0.31
0-40	-1.94	0.377	3.6	-0.888	0.31
0.42	-1.99	0.384	3.7	-0.897	0.32
0.44	-2.05	0.393	3.9	-0.908	0.32
0.46	-2.11	0.401	3.7	-0.911	0.32
0.48	-2.17	0.410	3.5	-0.920	0.32
0.50	-2.25	0.420	3.3	-0.913	0.32
0.55	-2.38	0.434	3.1	-0.911	0.32

0.60	-2.49	0.438	2.5	-0.881	0.32
0.65	-2.58	0.451	2.8	-0.901	0.32
0.70	-2.67	0.463	3.1	-0.914	0.33
0.75	-2.75	0.477	3.5	-0.942	0.32
0.80	-2.86	0.485	3.7	-0.925	0.32
0.85	-2.93	0.492	3.9	-0.920	0.32
0.90	-3.03	0.502	4.0	-0.920	0.32
0.95	-3.10	0.503	4.0	-0.892	0.32
1.00	-3.17	0.508	4.3	-0.885	0.32
1.10	-3.30	0.513	4.0	-0.857	0.32
1.20	-3.38	0.513	3.6	-0.851	0.31
1-30	-3.43	0.514	3.6	-0.848	0.31
1.40	-3.52	0.522	3.4	-0.839	0.31
1.50	-3.61	0.524	3.0	-0.817	0.31
1-60	-3.68	0.520	2.5	-0.781	0.31
1.70	-3.74	0.517	2.5	-0.759	0.31
1-80	-3.79	0.514	2.4	-0.730	0.32
1.90	-3.80	0.508	2.8	-0.724	0.32
2.00	-3.79	0.503	3.2	-0.728	0.32

1.3 Probabilistic Seismic Hazard for Campobasso

The seismicity of central and southern Apennines (Italy), is often characterized by multiple sequences, with at least two main earthquakes of similar magnitude (Vallèe and Di Luccio, 2005). This behaviour was observed for Irpinia (1980/11/23), Abruzzo (1984), Potenza (Basilicata, 1990–1991) and Umbria-Marche (1997) earthquakes with a time interval between events varying from a few tenths of seconds to several months. Similarly, the 2002 Molise sequence was characterized by compound earthquakes (2002/10/31 and 2002/01/11). The first shock (blue star in Figure 2, Mw 5.7, latitude: 41.72°N, longitude: 14.89°E) occurred in the vicinity of the village of San Giuliano di Puglia (green triangle in Figure 2), which caused the death of 29 people, most of them in the collapse of a primary school. The second shock (black star in Figure 2, Mw 5.7, latitude: 41.74°N, longitude: 14.84°E) occurred a few kilometres westward from the first one, without making strong damages. Taking in account the position of the target sites, that is close to the border between the zone 924 and 927 (Fig.1.3.1), and the structure investigated in the present study, a site specific hazard analysis and disaggregation study may be of main concern.

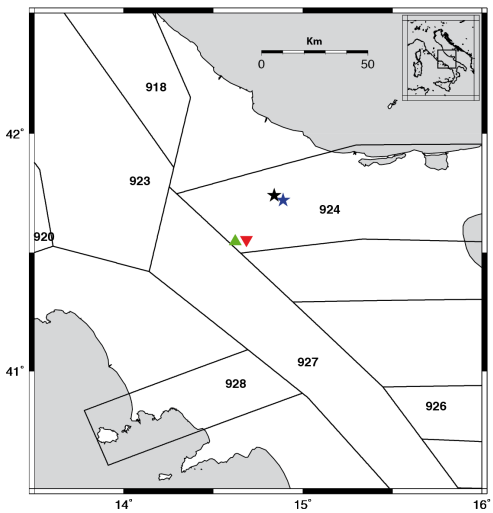

Figure 1.3.1. Zoomed version of figure (1.2.1). Location of the target sites used in the analysis is identified by red and green triangle, for the Hospital and the Student House respective. Stars represent Molise earthquakes sequence: 2002-10-31 Mw 5.7 (Blue) and 2002-11-01 Mw 5.7 (Black). Black triangle represents San Giuliano di Puglia village.

The selected seismogenic zones have been retrieved from the Italian zonation (ZS9) also adopted by the Istituto Nazionale di Geofisica e Vulcanologia (INGV) (Meletti et al., 2008). The activity rates, *b*-values, and minimum and maximum magnitudes for each zone are listed in Table 1.3.1. Figure 1.3.1 shows the location of the main earthquakes, both historical and recent, having magnitude larger than M 4.0, contained in the CPTI04 catalogue (see the Data and Resources section). The activity rates and the values selected for the analyses performed in this work are based on the study proposed by Barani et al. (2009).

Table 1.3.1. Seismic source zone parameters adapted from Barani et al. (2009). For each selected zone are reported the seismc zone ID (Zone), the minimum (M_{min}) and maximum (M_{max}) surface magnitude, the annul rate of earthquake occurrence (α) above M_{min} threshold and slope of the Gutenberg-Richter relationship (b).

Zone	M_{min}	M_{max}	α(event/yr)	b
917	4.3	6.1	0.121	-0.794
918	4.3	6.4	0.217	-0.840
920	4.3	5.5	0.317	-1.676
922	4.3	5.2	0.090	-1.436
923	4.3	7.3	0.645	-0.802
924	4.3	7.0	0.192	-0.945
925	4.3	7.0	0.071	-0.508
926	4.3	5.8	0.061	-1.017
927	4.3	7.3	0.362	-0.557
928	4.3	5.8	0.054	-1.056

The selected GMPE comes from Ambraseys et al. (1996)(see cap.1.2.1), which was derived from more than 100 earthquakes in Europe and adjacent regions. This GMPE has a validity range in magnitude between 4.0 and 7.9 and up to 200Km in distance.

The hazard curves have been computed for 100 log-spaced values from 0.001m/s^2 to 15.0m/s^2. The use of a log-spaced interval allows to better defining the shape of the curves increasing the number of point for low acceleration values. From the hazard curves the Uniform Hazard Spectra (UHS) was retrieved for eight different the return period (between 45 and 2475 years), four for each target site as functions of engineering

building class and the disaggregation analysis was performed (see Cap.1.4 for more details).

The numerical computation of equation (1.2.4), which is continuous in principle, was carried out using relatively small increments: 1.0 km for distance, 0.05 for magnitude, and 0.25 for ε. These steps was selected as good compromise for computation time and results precision and, from a disaggregation point of view, allow to limit the issues related to the appropriate selection of the bins used to collect the contributions of the hazard variables (see cap. 1.4). In fact, the identification of the modes of the PDFs may depend on the size of the M, R, and ε bins used for disaggregation (Bazzurro and Cornell, 1999).

To better understand the results for the target site, the hazard was computed considering the contribution of all seismogenic zone (SZ) and each one separately.

The selected sites are both located in Campobasso area (Molise region, Italy). The first one is represented by the Student House at University of Molise (latitude: 40.5532° N, longitude: 14.6649° E), the second one is the Hospital (latitude: 40.5478° N, longitude: 14.6225° E. The two sites, shown in Figure 1.3.1 (red and green triangle respectively), have been selected because both site are site of large scale experimentation for Structural Health Monitoring.

1.3.1 Student House at University of Molise

The first result of a Probabilistic Seismic Hazard Analysis (PSHA) is represented by the hazard curves. These curves can by plotted in terms of probability or annual frequency of exceedence.

For the student house was calculated the hazard curves for a 75 yr exposure period and for 47 different periods. Moreover the influence of all Seismogenic Zone (SZ) and of each SZ individually was considered to calculate the hazard curves. In Figure (1.3.1.1-3) it is possible to observe a different contribute from each ZS to the hazard curves. The differences in the shapes of the hazard curves depend on the specific seismic characteristics of each zone like seismic-activity rates.

This analysis represents a first step in the individuation of more dangerous SZ for the target site. Figure (1.3.1.1-3) show that for reported period the main contribute to hazard is represented by SZ 923 and SZ 927, but it can be noted that the SZ 924 at high acceleration contributes to the hazard as SZ 927. The participation to hazard of different SZs is related to the particular position of target site, near the border between the different SZs.

In this thesis only the results for Peak Ground Acceleration (PGA), SA(T=0.75) and SA(T=0.30sec) have been reported because they are strictly related to some fundamental periods of the structure (Fig.1.3.1.1-3).

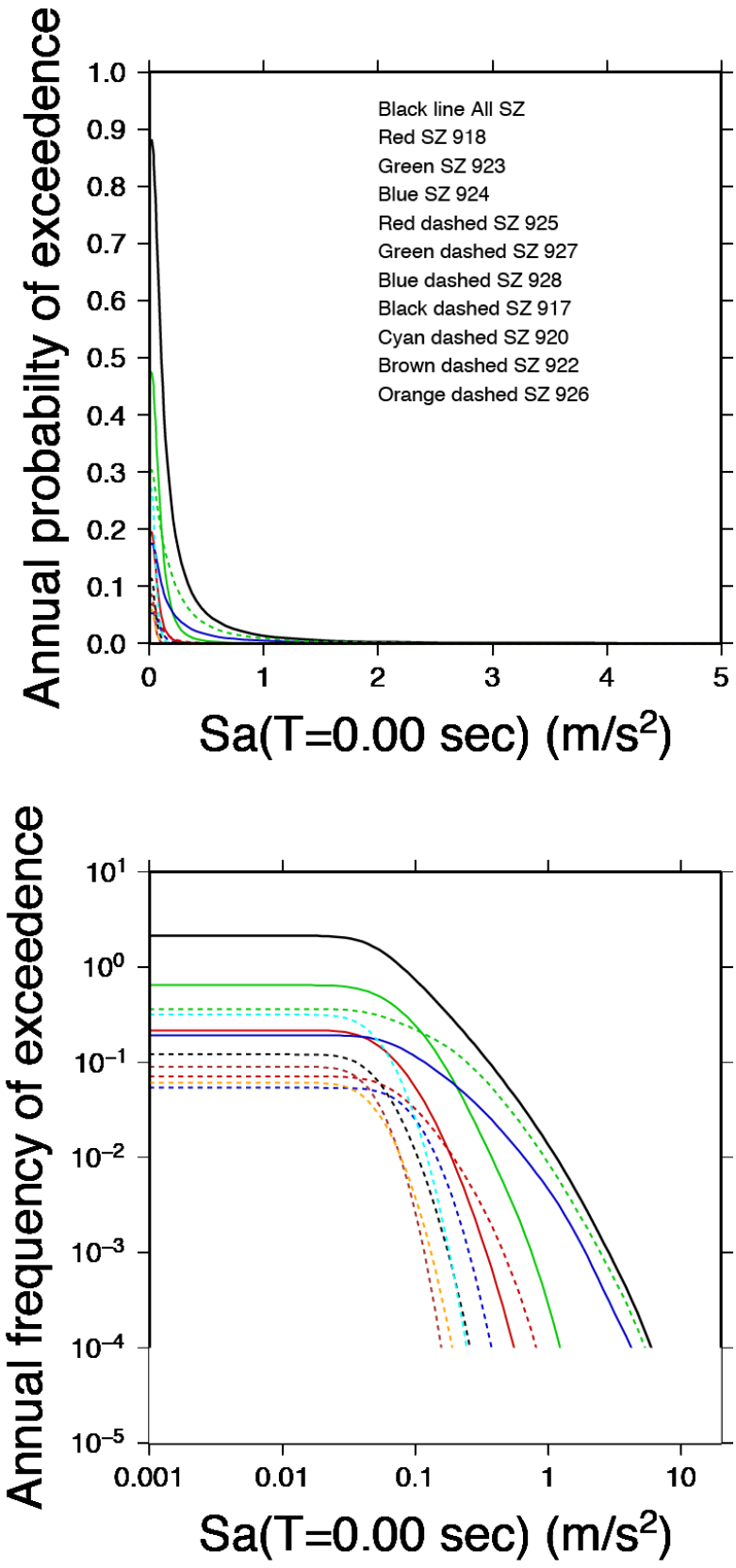

Figure 1.3.1.1 Hazard curve in terms of probability (top) and annual frequency of exceedence (Bottom) for target site for PGA. Lines represent the hazard curve computed considering the contribution of all seismogenic zones (black), SZ 918 (red), SZ 923 (green), SZ 924 (blue), SZ 925 (red dashed), SZ 927 (green dashed), SZ 928 (blue dashed),SZ 917 (black dashed), SZ 920 (cyan dashed), SZ922 (brown dashed), SZ 926 (orange dashed).

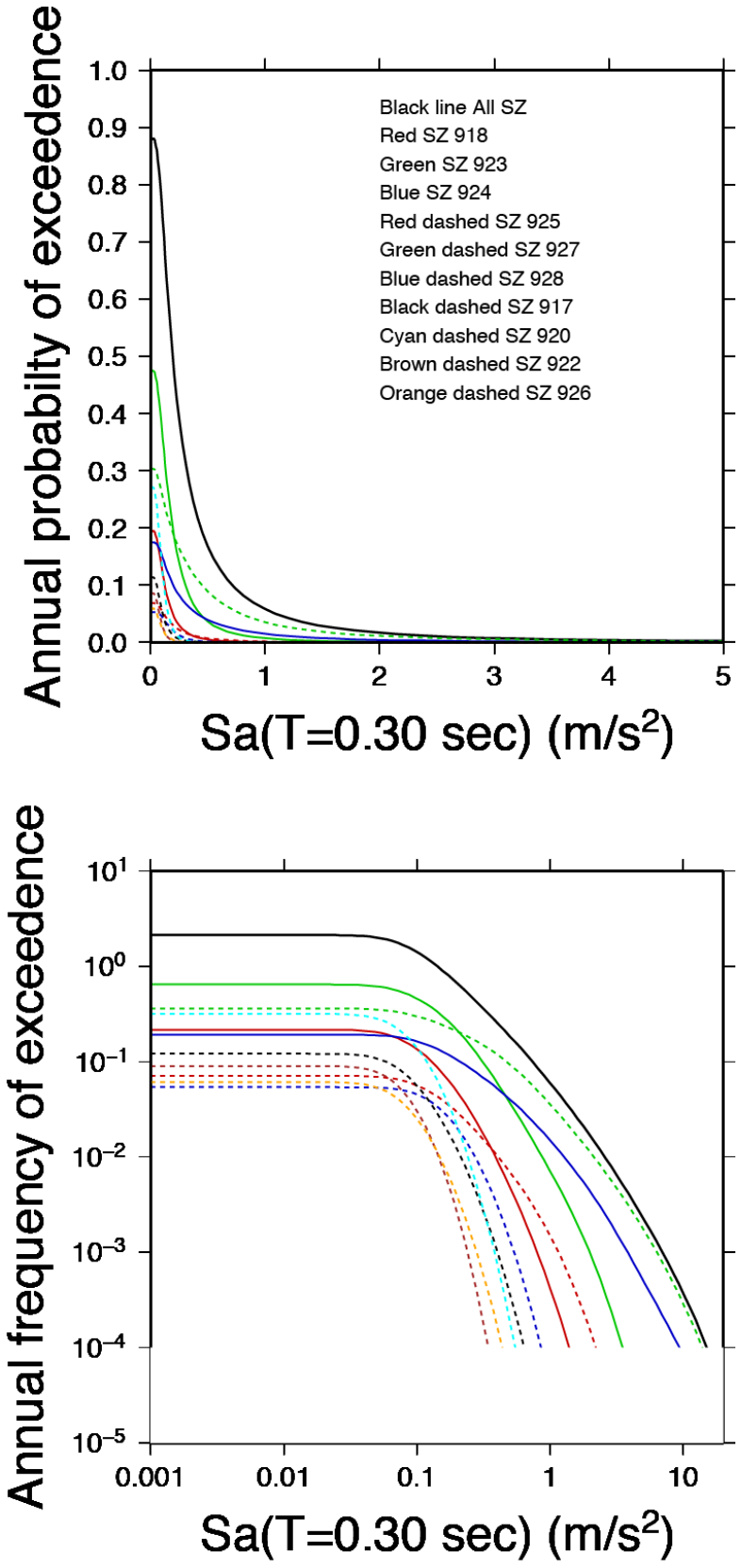

Figure 1.3.1.2 Hazard curve in terms of probability (top) and annual frequency of exceedence (Bottom) for target site for SA(T=0.30sec). Lines represent the hazard curve computed considering the contribution of all seismogenic zones (black), SZ 918 (red), SZ 923 (green), SZ 924 (blue), SZ 925 (red dashed), SZ 927 (green dashed), SZ 928 (blue dashed),SZ 917 (black dashed), SZ 920 (cyan dashed), SZ922 (brown dashed), SZ 926 (orange dashed).

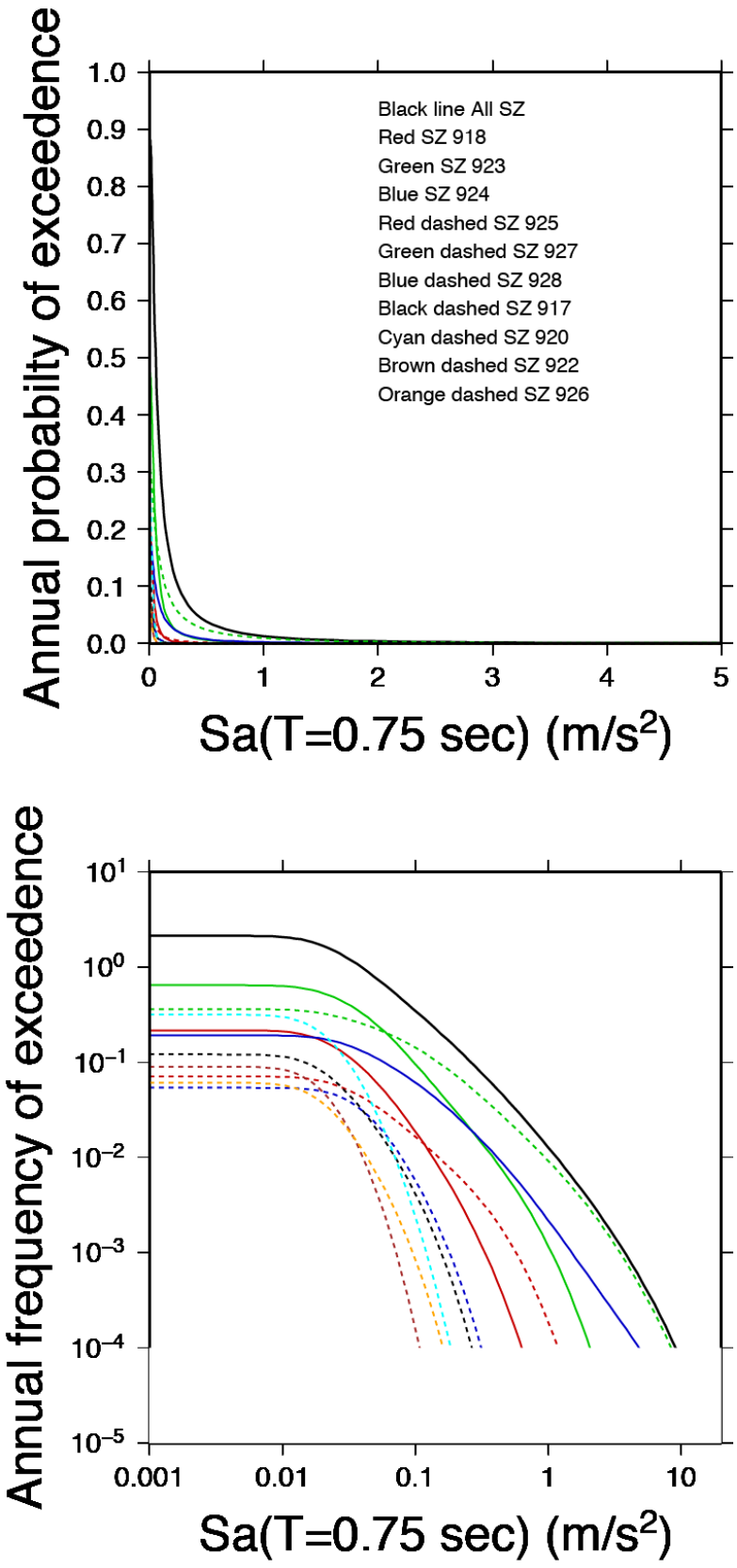

Figure 1.3.1.3 Hazard curve in terms of probability (top) and annual frequency of exceedence (Bottom) for target site for SA(T=0.75sec). Lines represent the hazard curve computed considering the contribution of all seismogenic zones (black), SZ 918 (red), SZ 923 (green), SZ 924 (blue), SZ 925 (red dashed), SZ 927 (green dashed), SZ 928 (blue dashed),SZ 917 (black dashed), SZ 920 (cyan dashed), SZ922 (brown dashed), SZ 926 (orange dashed).

1.3.2 Campobasso Hospital

As reported in Cap.1.3.1 the first result of a Probabilistic Seismic Hazard Analysis (PSHA) is represented by the hazard curves. These curves can by plotted in terms of probability or annual frequency of exceedence.

For the Campobasso hospital was calculated the hazard curves for a 200 yr exposure period and for 47 different periods. Moreover to calculate the hazard curves the influence of all Seismogenic Zone (SZ) and of each SZ individually was taken into account. In Figure (1.3.2.1-3) it is possible to observe a different contribute from each ZS to the hazard curves. The differences in the shapes of the hazard curves depend on the specific seismic characteristics of each zone like seismic-activity rates.

This analysis can be represent a first step in the individuation of more dangerous SZ for the target site. Can be note that for PGA and SA(T=0.30sec) the main contribute to hazard is represented by SZ 923 and SZ 927 at low and high acceleration, but for SA(T=1.50sec) and from about 1 m/s^2 the SZ 924 contributes to the hazard more than SZ 927. The participation to the hazard of different SZs is related to the particular position of target site, near the border between different SZs.

For this target site only the results for Peak Ground Acceleration (PGA), SA(T=0.50) and SA(T=1.50sec) have been reported because they are strictly related to some fundamental periods of the structure (Fig.1.3.2.1-3).

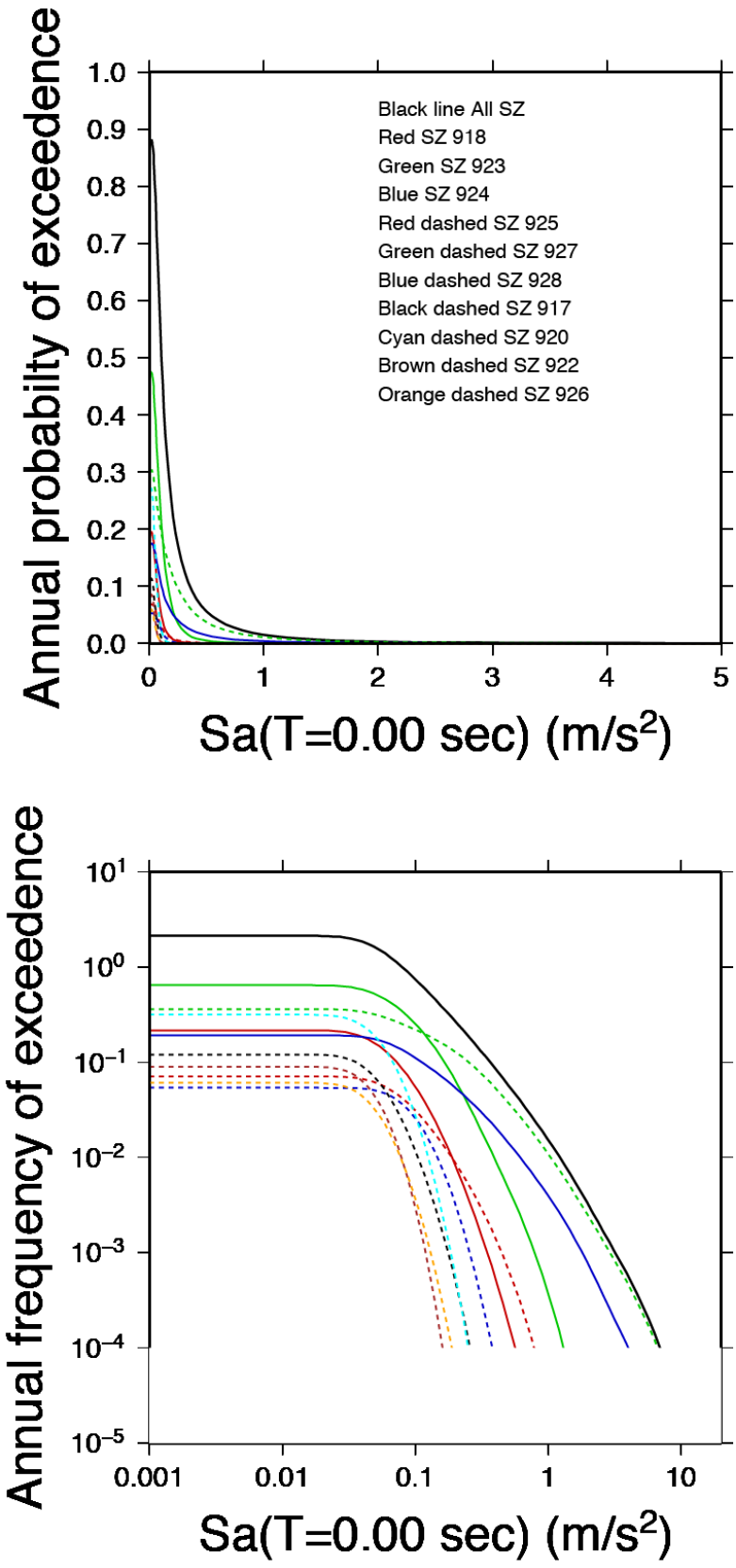

Figure 1.3.2.1 Hazard curve in terms of probability (top) and annual frequency of exceedence (Bottom) for target site for PGA. Lines represent the hazard curve computed considering the contribution of all seismogenic zones (black), SZ 918 (red), SZ 923 (green), SZ 924 (blue), SZ 925 (red dashed), SZ 927 (green dashed), SZ 928 (blue dashed),SZ 917 (black dashed), SZ 920 (cyan dashed), SZ922 (brown dashed), SZ 926 (orange dashed).

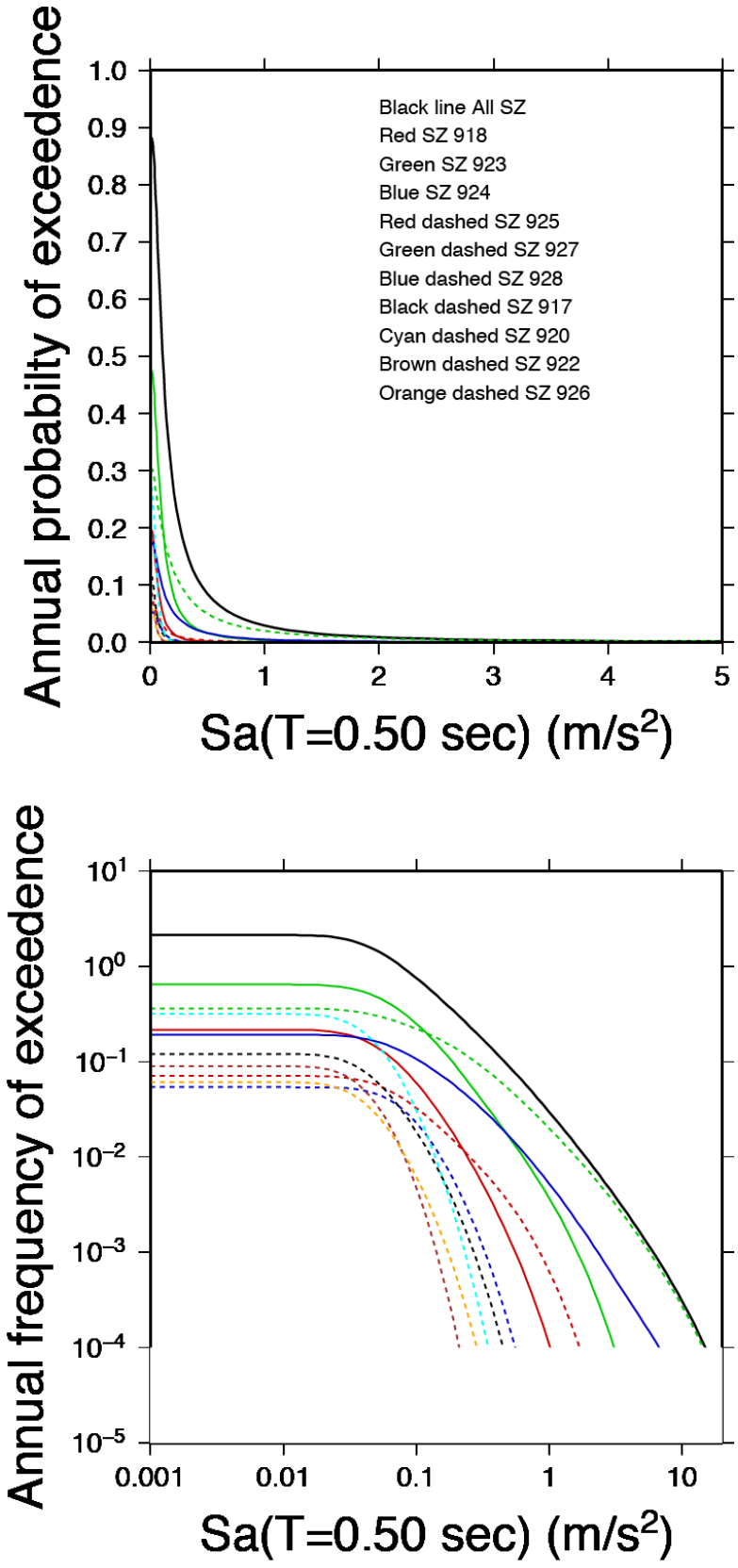

Figure 1.3.2.2 Hazard curve in terms of probability (top) and annual frequency of exceedence (Bottom) for target site for SA(T=0.50sec). Lines represent the hazard curve computed considering the contribution of all seismogenic zones (black), SZ 918 (red), SZ 923 (green), SZ 924 (blue), SZ 925 (red dashed), SZ 927 (green dashed), SZ 928 (blue dashed),SZ 917 (black dashed), SZ 920 (cyan dashed), SZ922 (brown dashed), SZ 926 (orange dashed).

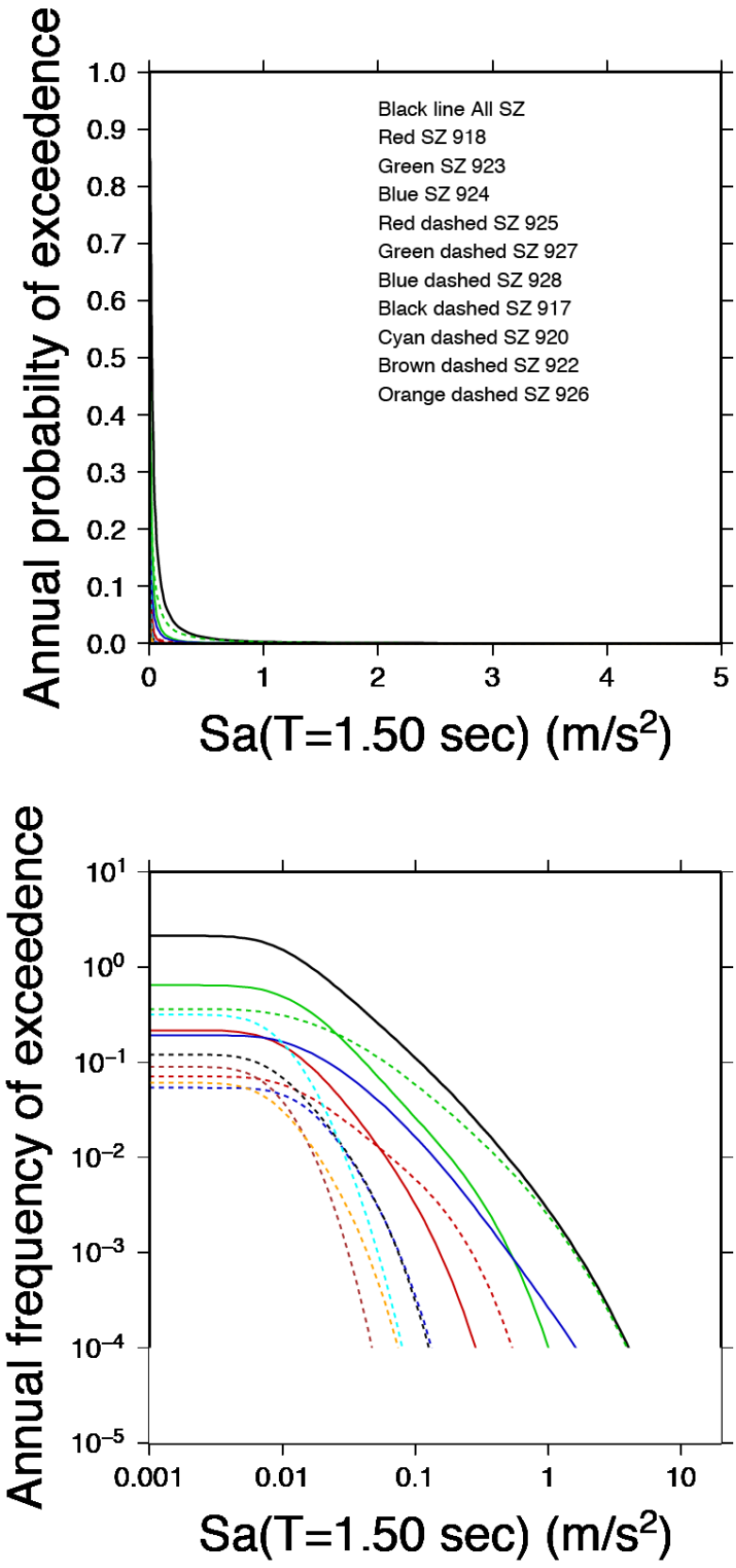

Figure 1.3.2.3 Hazard curve in terms of probability (top) and annual frequency of exceedence (Bottom) for target site for SA(T=1.50sec). Lines represent the hazard curve computed considering the contribution of all seismogenic zones (black), SZ 918 (red), SZ 923 (green), SZ 924 (blue), SZ 925 (red dashed), SZ 927 (green dashed), SZ 928 (blue dashed),SZ 917 (black dashed), SZ 920 (cyan dashed), SZ922 (brown dashed), SZ 926 (orange dashed).

1.4 Disaggregation: identification of design earthquake

The result of PSHA is represented by a hazard curve (Cap.1.3) that can be represented by the annual frequency or the probability of exceed of a ground motion parameter for the period of interest. However for engineering proposes is more friendly and usable representing together all ground motion parameters with the same probability of exceeding in the period of interest. This representation, note as Uniform Hazard Spectra (UHS), is a function of the reference period (V_R) structure and the prescriptions of EC8 (Eurocode, 2003) for seismic actions.
The reference period (V_R) is represented by the following equation:

$$V_R = V_N \cdot CU \tag{1.4.1}$$

Where V_N represents the nominal life of a structure and CU represent its coefficient of use. The V_N parameter can be interpreted as the number of years that a structure can be used, for the design destination, if subjected to regular maintenance. A reasonable value for ordinary building and structures is 50 yrs that became 100 yrs for large o strategic constructions.
On the other hand the CU coefficient is related to the class of use of the constructions. Its value can vary from 0.7 up to 2.0 for agriculture construction or public and strategic building, respectively.
The EC8 represents a guidelines for the seismic actions analysis and define four different values of probability of exceed a ground motion parameter (PGA or SA(T)). These values representing the damage limit state (SLO, SLD) and the ultimate limit state (SLU, SLC) are reported in Tab. 1.4.1. According to de Magistris Santucci (2011) SLO, SLD, SLU, SLC are defined as in the following:

1. Operability limit state (SLO): after an earthquake, the entire structure, including its structural elements, non structural elements, and apparatuses relevant to its functionality, is neither damaged nor subject to significant interruptions in functioning.

2. Limit state of prompt use or Damage (SLD): after an earthquake, the entire structure, including structural elements, non structural elements, and apparatuses relevant to its functionality, has damage that does not compromise its stiffness and resistance against vertical and horizontal actions. The structure is ready to be used but the apparatuses might be subject to malfunctioning.
3. Limit state for the safeguard of human life or Ultimate state (SLU): after an earthquake, the construction is affected by failures and collapses of no-structural components and apparatuses and significant damage to structural components that result in a significant reduction of stiffness and resistance against horizontal actions. The construction retains significant stiffness and resistance against vertical actions and retains, as a whole, a significant safety margin against collapse from horizontal seismic actions.
4. Limit state for collapse prevention (SLC): after an earthquake, the construction has suffered serious failures and collapses of non structural components and apparatuses and very serious damage to structural components that result in a substantial loss of stiffness and a contained loss of resistance against horizontal actions. The construction retains a significant stiffness and resistance against vertical actions but has a small safety margin against collapse from horizontal actions.

Table 1.4.1. Variation of the probability of exceedance of the seismic motion for different limit states de Magistris Santucci (2011).

Limit state		Probability P of exceedance in the
Serviceability limit	SLO	81%
	SLD	63%
Ultimate limit state	SLU	10%
	SLC	5%

The knowledge of the V_R value (the time period of interest) and the probability of occurrences of a particular event in the time interval of interest (P) allow the determination of the returning period (T_R) of the design earthquake. Under the hypothesis of a Poissonian model (cap.1.2) T_R is obtained by:

$$T_R = \frac{V_R}{\ln(1-P)} \tag{1.4.2}$$

Fixing P as in Table (1.4.1), the return period is function of the particular kind of structure considered and of its use (Eq.1.4.2).

An example of PSHA for PGA and SA(T), provided by INGV[1] is in given in Figure 1.4.1, for the city of Campobasso.

It is worth noting that the PGA for a returning period of 475 yrs (10% of probability to be exceed in 50yrs) is equal to 0.2237 g.

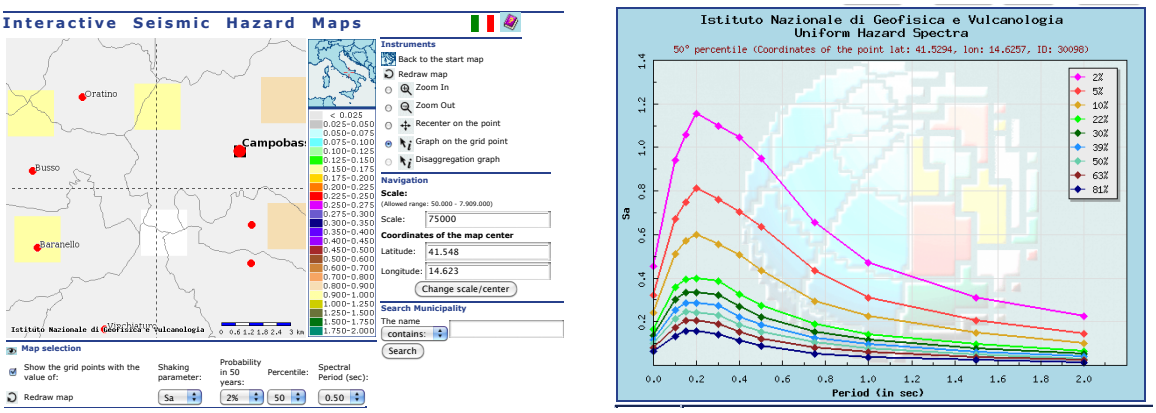

Figure 1.4.1. Seismic hazard analysis for the city of Termoli (CB) in terms of PGA (Left) and uniform hazard spectra (Right) on outcropping bedrock (data from http://esse1-gis.mi.ingv.it/s1_en.php?restart=0)).

The result of PSHA is a hazard curve or UHS that represents the probability of exceed of a ground motion parameter (see Cap. 1.2 and 1.3) that combine all possible contribution from all seismic source due to its integral nature. The nature of the PSHA result not allow obtaining information about which magnitude-distance-ε (m-r-ε) triplet is responsible for the ground motion exceedance. The disaggregation procedure (McGuire, 1995) allows the decomposition of each point on the hazard curve or UHS, in terms of M, R and ε, from each selected source. The m-r-ε triplet defines the reference earthquake that controls the site hazard. The knowledge of the earthquake scenarios is strategic for engineering proposes such as to select appropriate ground motions time history for nonlinear dynamic analyses of structures. The results of the disaggregation procedure can be easily explained in terms of both joint and marginal PDFs (Eq.1.2.10-13).

For the selected sites, the UHS was calculated and the disaggregation analysis was performed. The results were compared to that provided by INGV, considered as a benchmark, for the site of interest (Caccavale et al., 2010). It has to be underlined that the comparison is only qualitative because INGV used a more sophisticated approach, based on logic tree accounting for several GMPEs, a larger number of seismic zones and parameters that refer to two earthquake catalogue and different seismic rate models.

[1] http://esse1-gis.mi.ingv.it/help_s1_en.html

Moreover the INGV considered only 9 probabilities of exceedance within 50 years (from 2% to 81%) that not always coincides with the selected returned period of the structures. For each evaluation the return period interpolation low (NTC, 2008) was used to represent the INGV UHS in terms of the selected return period:

$$Log(P) = Log(P_1) + Log\left(\frac{P_2}{P_1}\right) Log\left(\frac{T_R}{T_{R1}}\right) \left[Log\left(\frac{T_{R2}}{T_{R1}}\right)\right]^{-1} \quad (1.4.3)$$

Where P represents the value of the selected parameter for the desired return period T_R, $P_{1,2}$ is the value of the same parameter corresponding to return period $T_{R1,2}$.

The INGV through the same Web site[2] provides disaggregation of seismic hazard in terms of contribution of M and R bins, but only for PGA. In particular, Table 1.4.1 lists the range of variability of M and R for the four closest grid points to the target site. Concerning the ε variable, only the mean value obtained from disaggregation is provided by INGV. The comparisons of disaggregated values in terms of modal and mean values for the target sites, obtained from the joint PDFs are shown in next sections. In particular, $(\bar{M}, \bar{R}, \bar{\varepsilon})$ refers to the mean values, and (R*, M*, ε*) refers to the modal values. A graphical representation of disaggregation results obtained in this study, for both target sites, in terms of joint and marginal PDFs is presented (Cap.1.4.1 and 1.4.2). To plot the integral in eq. (1.2.4), which can be hardly represented in a figure, the three bivariate PDFs shown have been obtained by marginalizing on the third hazard variable not given in the plot. As an example, Eq.1.4.4,

$$f(m, r|A > A_o) = \int_{\varepsilon} f(m, r, \varepsilon|A > A_o)\, d\varepsilon \quad (1.4.4)$$

Indicates how to obtain the joint PDF of M and R only from that of M, R and ε.

[2]http://esse1-gis.mi.ingv.it/help_s1_en.html

Table 1.4.1. Modal and mean values for the hazard variables for the target site and for PGA, Sa(T= 0.3 sec) and Sa (T= 0.75 sec)*

		R* (Km)	M*	ε*	$\bar{R}$ (km)	$\bar{M}$	$\bar{\varepsilon}$
Target site							
PGA	This study	9,25	6,2	0,400	13,92	6,5	0,533
	INGV	0-10	4.5-5.5	NA	9.87-11.50	5.7-5.9	0.861-1.040
T= 0.30 sec		10,75	6,4	0,400	14,82	6,4	0,720
T= 0.75 sec		21,75	7,0	0,400	20,61	6,8	0,602

The values have been retrieved from the joint PDFs. $\bar{M}, \bar{R}$ and $\bar{\varepsilon}$ refer to the mean values, and M, R*and ε*to the modal values.

1.4.1 Student House at University of Molise

The result of the probabilistic hazard analysis performed for the student house at University of Molise is reported in terms of Uniform Hazard Spectra (UHS) because, as discussed in Cap.1.4, from an engineering point of view it represents the better way to summarize the result of a seismic hazard analysis.

The UHS was computed in terms of PGA and Sa(T) for 47 different values of T (0.1-2.0 sec.) for a 75 years exposure period and for four different return periods (45, 75, 713, 1463 years). The choice of return period (as described in Cap.1.4) is driven basically by the regulation actually in force in the Italian territory about anti-seismic planning corresponding to the EC8 (Eurocode, 2003).

For example Figure 1.4.1.1 shows the UHSs corresponding to TR = 45yr calculated at 47 vibration periods for the target site. In the same figure, the UHS retrieved from the INGV (black solid dashed line) is also shown. The latter UHS corresponds to the weighted mean of the UHSs at the four closest grid points to the target site, at which INGV computed PSHA (See cap.1.4 for more details).

For the selected sites, the disaggregation analysis was also performed. The figures 1.4.1.5-16 show the results of disaggregation for the student house obtained in the present study in terms of both joint and marginal PDFs, as described in Cap.1.4.

From disaggregation analysis was retrieved the mean and the first and second mode (where it exists) value of the triplet magnitude-distance-ε (M-R-ε) which is responsible for the ground motion exceedance. A second mode in not always present (Fig.1.4.1.13 or Fig.1.4.1.15), but when it exists it can provide useful information from the engineering point of view to perform the better non-linear dynamic analysis of a future build.

The results, in terms of mean and modal values, have been compared to the results obtained by INGV. The comparison of disaggregated values in terms of modal and mean values for the student house, obtained from the joint PDFs, is given in Table1.4.1.1. In particular, $(\bar{M}, \bar{R}, \bar{\varepsilon})$ refers to the mean values, and (R*, M*, ε*) refers to the modal values. As expected, disaggregation shows different results at different periods and return period (unimodal and bimodal shape) due to different contribution to hazard of each SZ. As a

consequence, for the selected spectral ordinate and return period, at least two design earthquakes do exist and must be considered during the engineering structures design.

Table 1.4.1.1: Modal and mean values for the hazard variables for the target site; for PGA, Sa(T= 0.30 sec) and Sa (T= 0.75 sec)*

	R* (Km)	M*	ε*	$\overline{R}$ (km)	$\overline{M}$	$\overline{\varepsilon}$
	Tr=45yr					
PGA	6/23	4.33/6.03	0.4/0.2	20.7	5.77	0.5
T= 0.30 sec	5/25	4.33/6.03	0.6/0.4	26.7	5.97	0.6
T= 0.75 sec	26/6	6.03/4.93	0.4/0.6	37.2	6.27	0.5
	Tr=75yr					
PGA	4/18	4.33/6.03	0.4/0.2	18.1	5.87	0.5
T= 0.30 sec	4/18	4.38/6.03	0.8/0.2	23.5	6.1	0.6
T= 0.75 sec	18/12	6.03/5.88	0.2/0.4	32.1	6.39	0.5
	Tr=713yr					
PGA	9/3	6.03/5.13	0.4/0.8	11.3	6.34	0.6
T= 0.30 sec	9/4	6.03/5.68	0.6/0.8	14.6	6.56	0.7
T= 0.75 sec	10/10	6.38/6.38	0.4/0.4	17.1	6.72	0.7
	Tr=1463yr					
PGA	8/3	6.03/5.58	0.2/0.8	9.9	6.48	0.7
T= 0.30 sec	9/9	6.33/6.33	0.6/0.6	12.5	6.64	0.8
T= 0.75 sec	10/10	6.63/6.63	0.4/0.4	14.1	6.77	0.7

The values have been retrieved from the joint PDFs. $\overline{M}, \overline{R}, \overline{\varepsilon}$ refer to the mean values, and M, R*and ε*to the modal values.

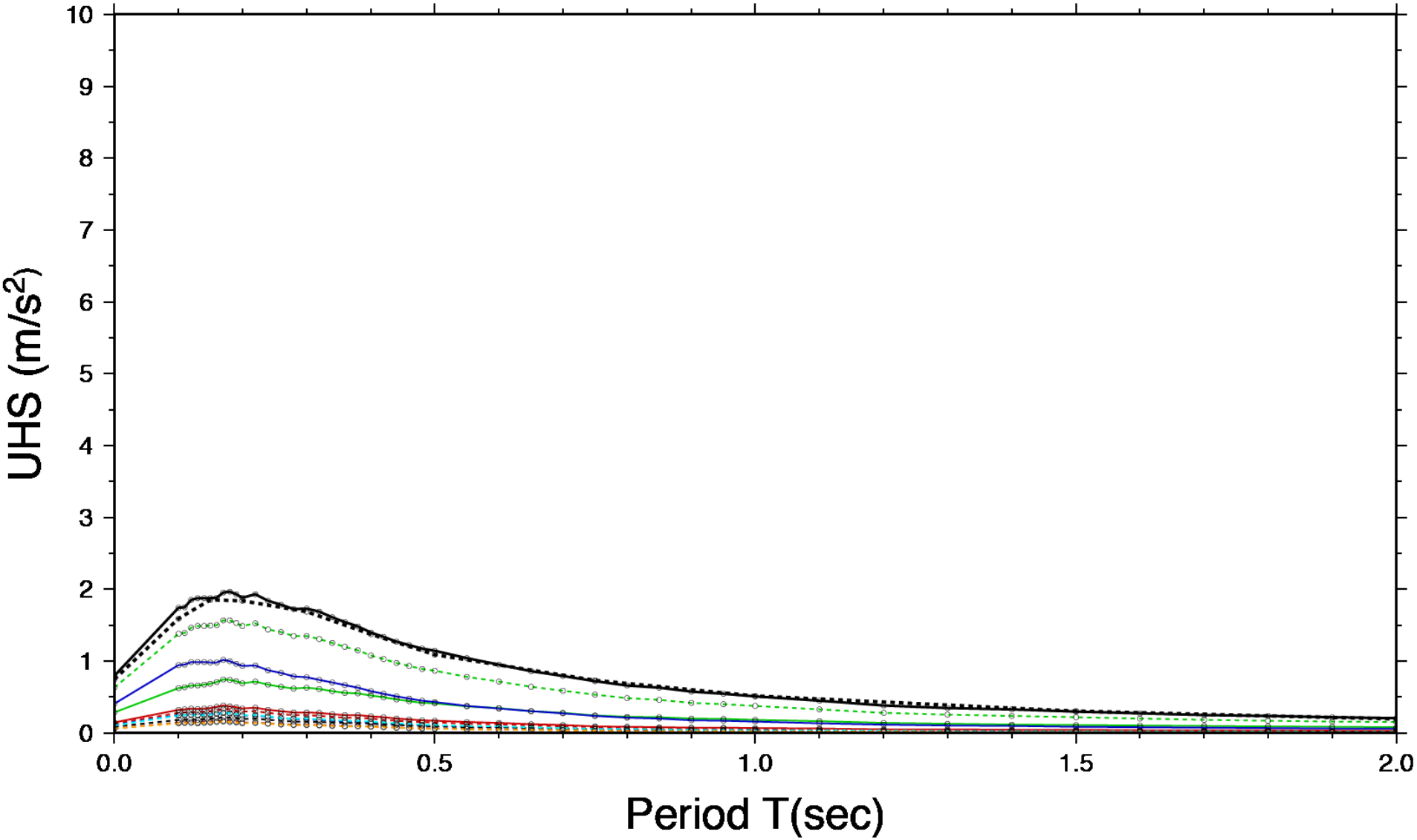

Figure 1.4.1.1. Uniform hazard spectra in m/s² for the target site and 45 yr return period. Lines represent the uniform hazard spectra computed considering the contribution of all seismogenic zones (black), SZ 918 (red), SZ 923 (green), SZ 924 (blue), SZ 925 (red dashed), SZ 927 (green dashed), SZ 928 (blue dashed),SZ 917 (black dashed), SZ 920 (cyan dashed), SZ922 (brown dashed), SZ 926 (orange dashed). The black dashed line represents the INGV uniform hazard spectrum.

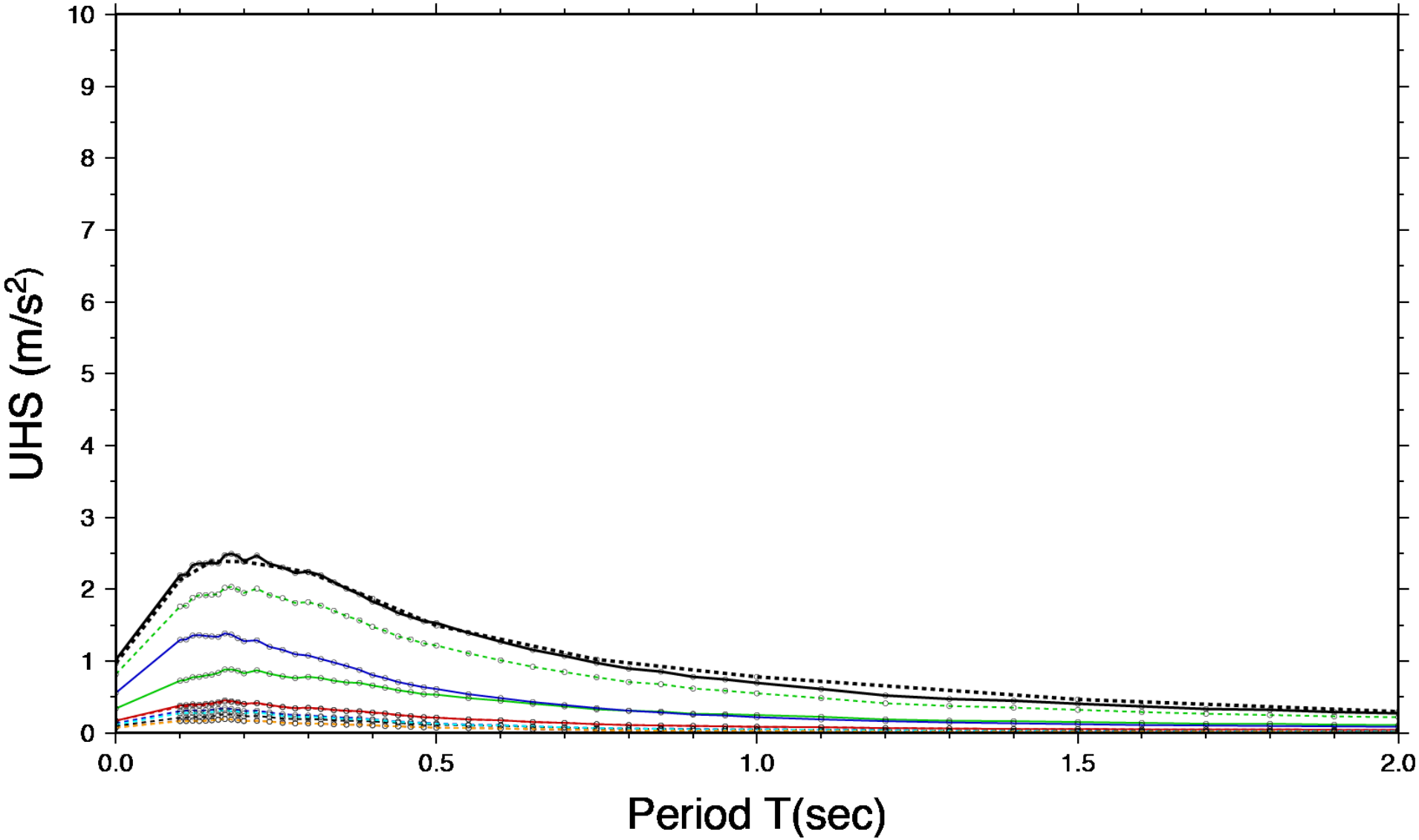

Figure 1.4.1.2. Uniform hazard spectra in m/s² for the target site and 75 yr return period. Lines represent the uniform hazard spectra computed considering the contribution of all seismogenic zones (black), SZ 918 (red), SZ 923 (green), SZ 924 (blue), SZ 925 (red dashed), SZ 927 (green dashed), SZ 928 (blue dashed),SZ 917 (black dashed), SZ 920 (cyan dashed), SZ922 (brown dashed), SZ 926 (orange dashed). The black dashed line represents the INGV uniform hazard spectrum.

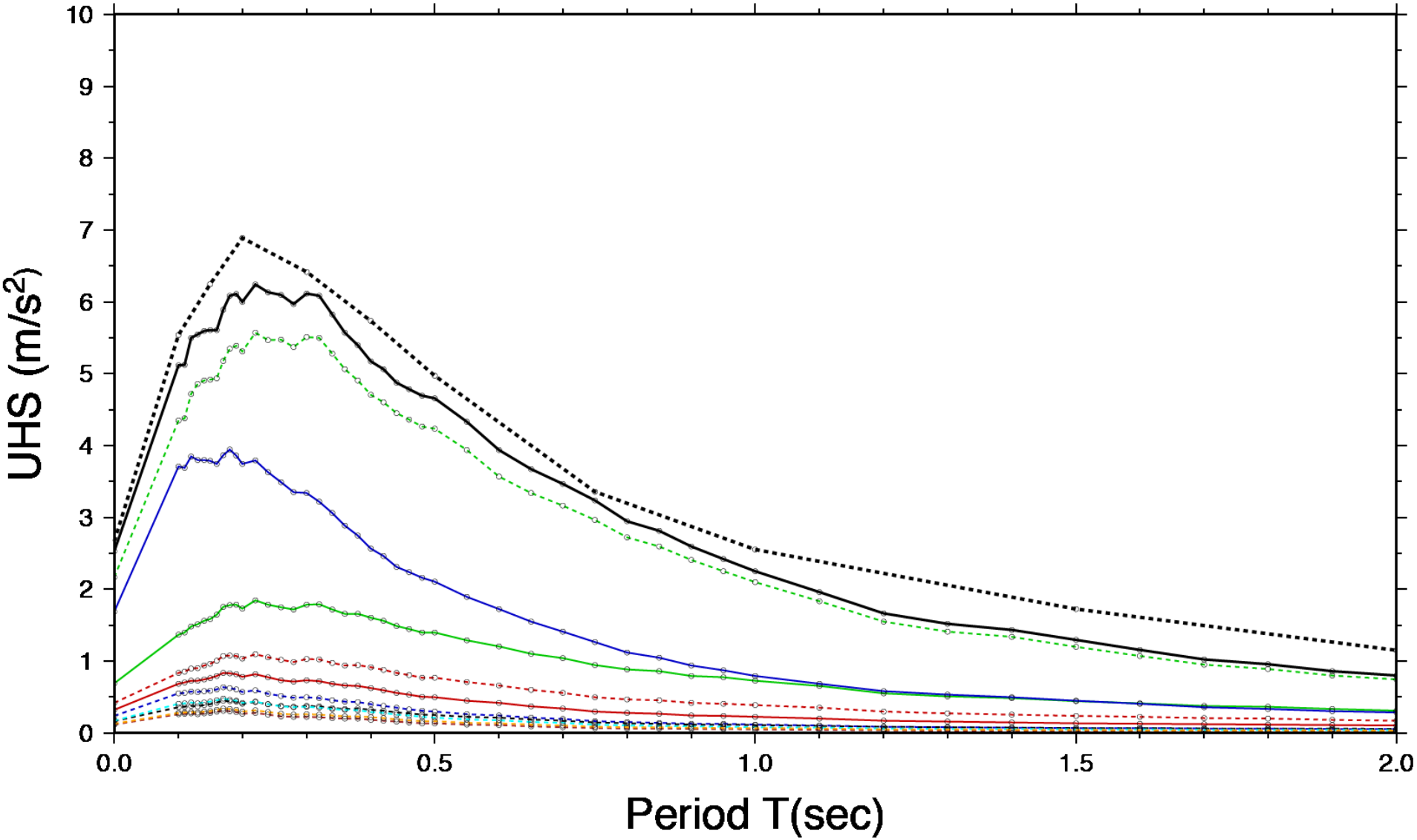

Figure 1.4.1.3. Uniform hazard spectra in m/s² for the target site and 713 yr return period. Lines represent the uniform hazard spectra computed considering the contribution of all seismogenic zones (black), SZ 918 (red), SZ 923 (green), SZ 924 (blue), SZ 925 (red dashed), SZ 927 (green dashed), SZ 928 (blue dashed),SZ 917 (black dashed), SZ 920 (cyan dashed), SZ922 (brown dashed), SZ 926 (orange dashed). The black dashed line represents the INGV uniform hazard spectrum.

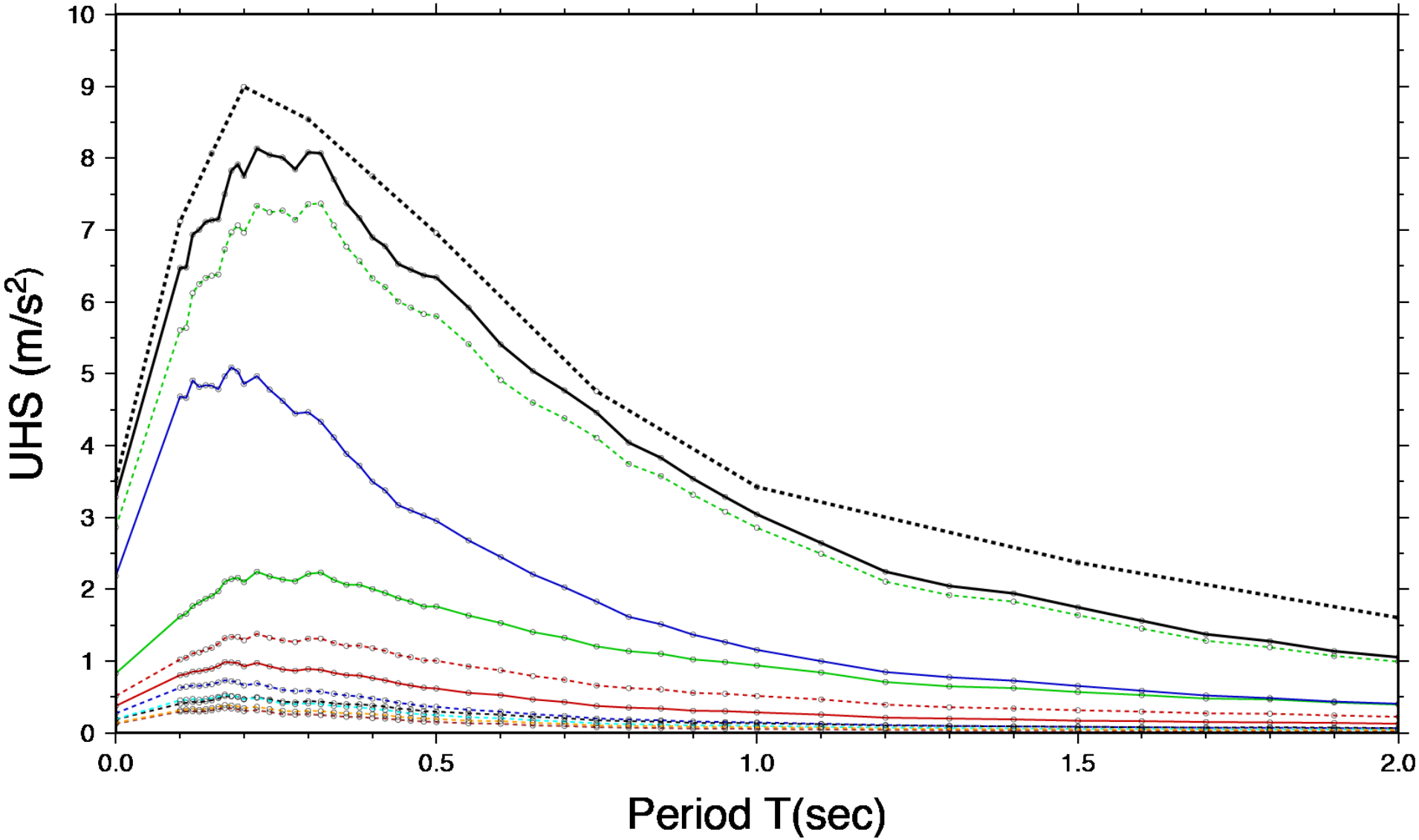

Figure 1.4.1.4. Uniform hazard spectra in m/s² for the target site and 1463 yr return period. Lines represent the uniform hazard spectra computed considering the contribution of all seismogenic zones (black), SZ 918 (red), SZ 923 (green), SZ 924 (blue), SZ 925 (red dashed), SZ 927 (green dashed), SZ 928 (blue dashed),SZ 917 (black dashed), SZ 920 (cyan dashed), SZ922 (brown dashed), SZ 926 (orange dashed). The black dashed line represents the INGV uniform hazard spectrum.

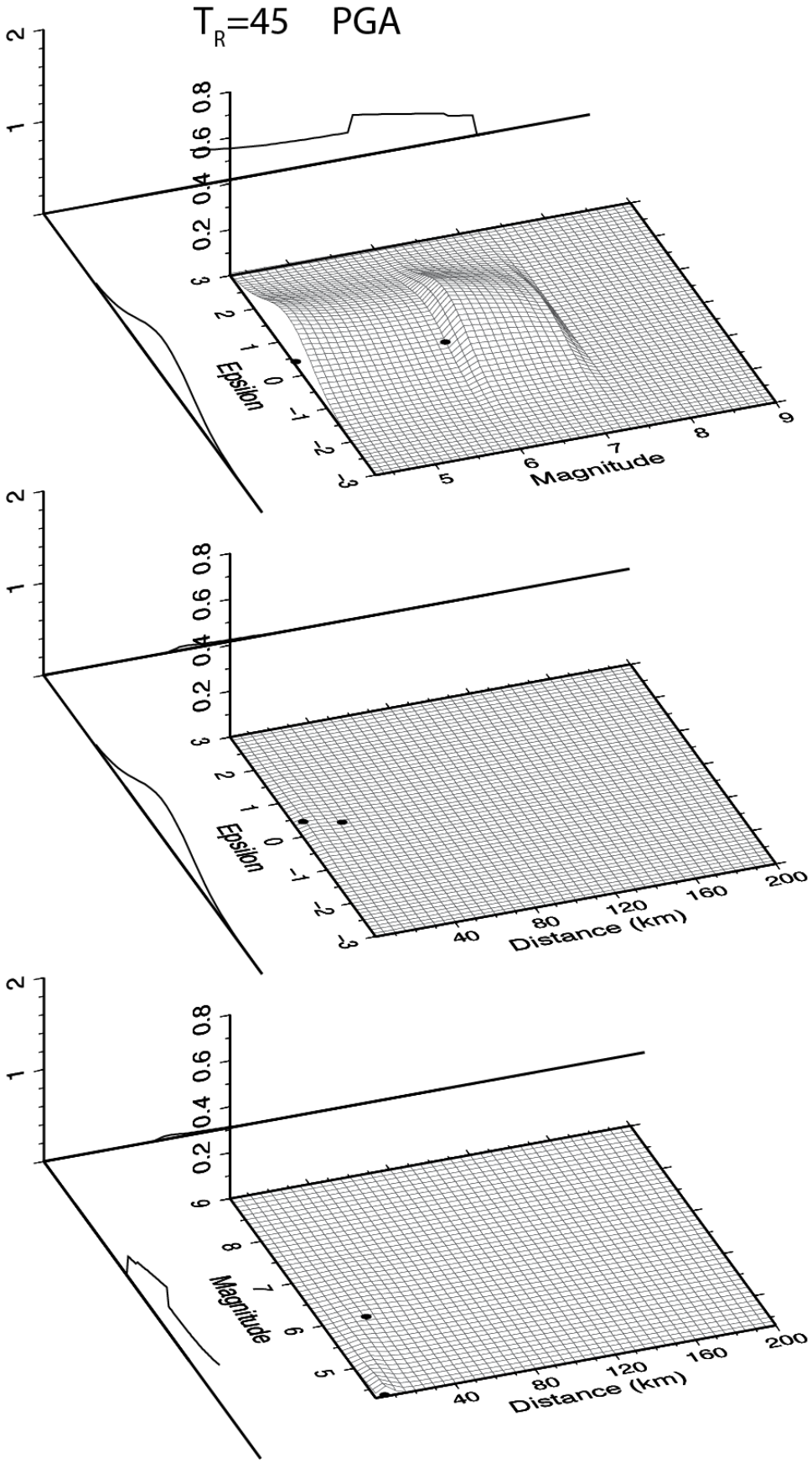

Figure 1.4.1.5. Disaggregation results expressed as contribution to 45 yr return period hazard for the target site. The central part of each panel shows the joint PDFs for the specific hazard variable pair for PGA. On the external axes the marginal PDFs obtained from the joint PDFs area also shown.

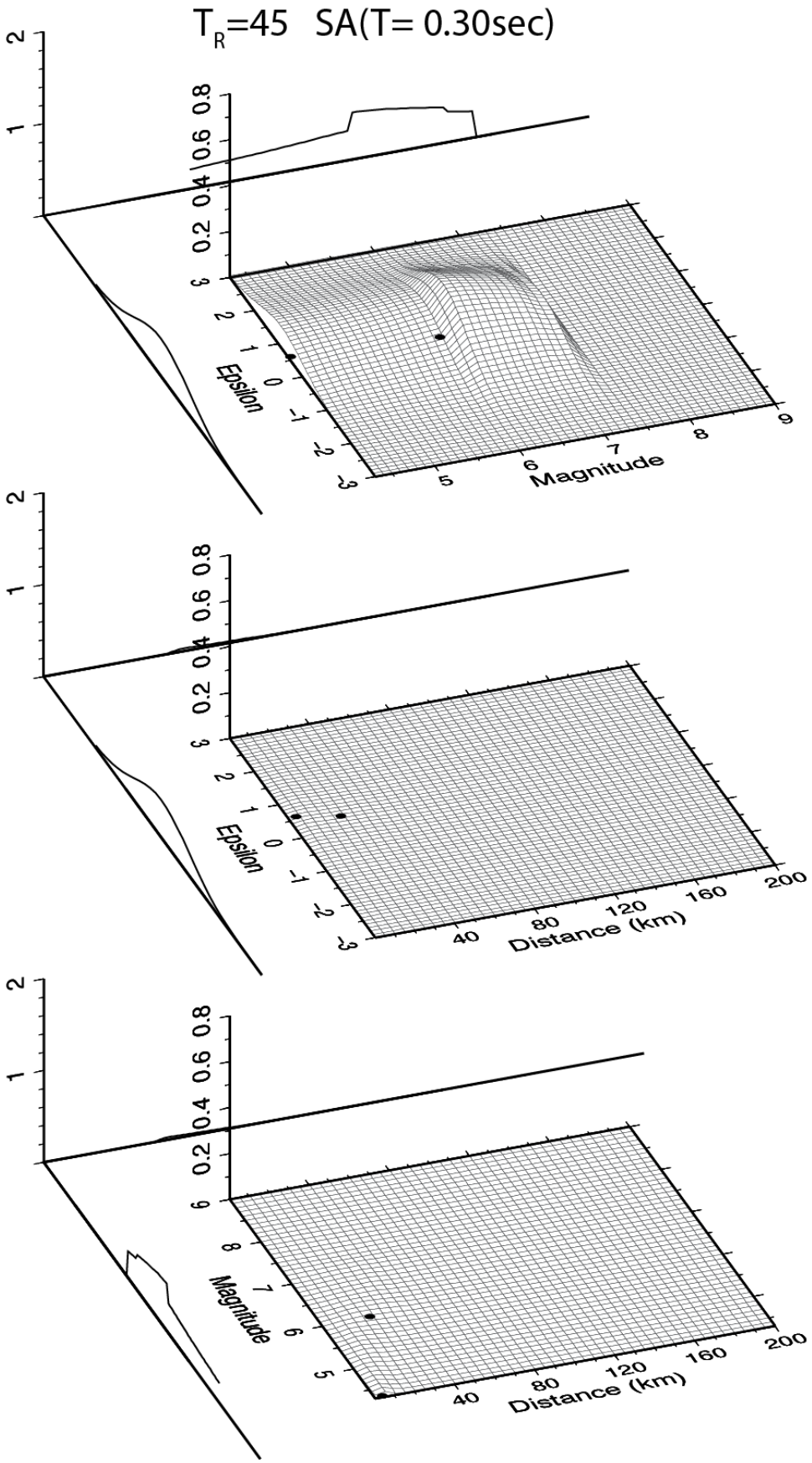

Figure 1.4.1.6. Disaggregation results expressed as contribution to 45 yr return period hazard for the target site. The central part of each panel shows the joint PDFs for the specific hazard variable pair for SA(T=0.30 sec). On the external axes the marginal PDFs obtained from the joint PDFs area also shown.

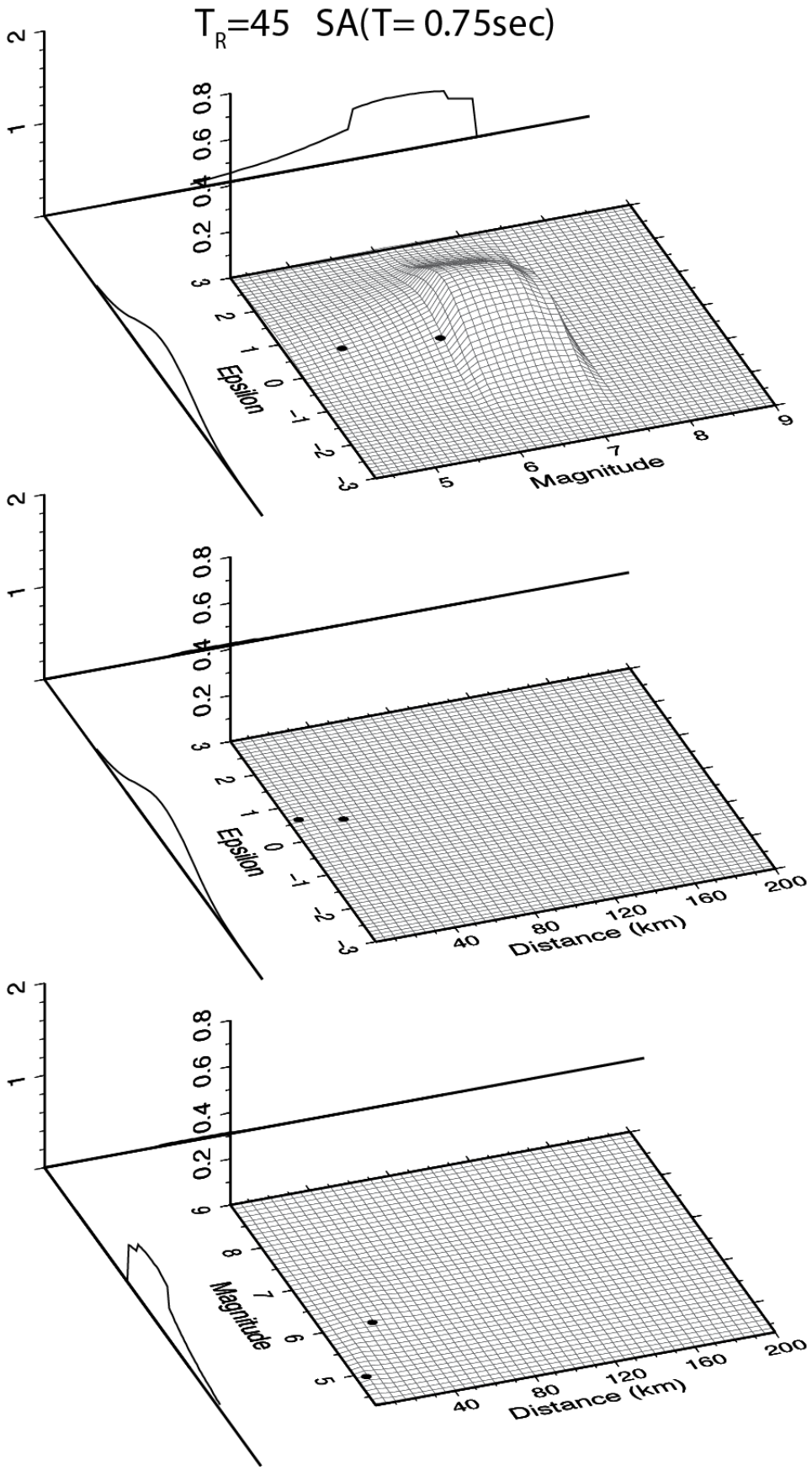

Figure 1.4.1.7. Disaggregation results expressed as contribution to 45 yr return period hazard for the target site. The central part of each panel shows the joint PDFs for the specific hazard variable pair for SA(T=0.75 sec). On the external axes the marginal PDFs obtained from the joint PDFs area also shown.

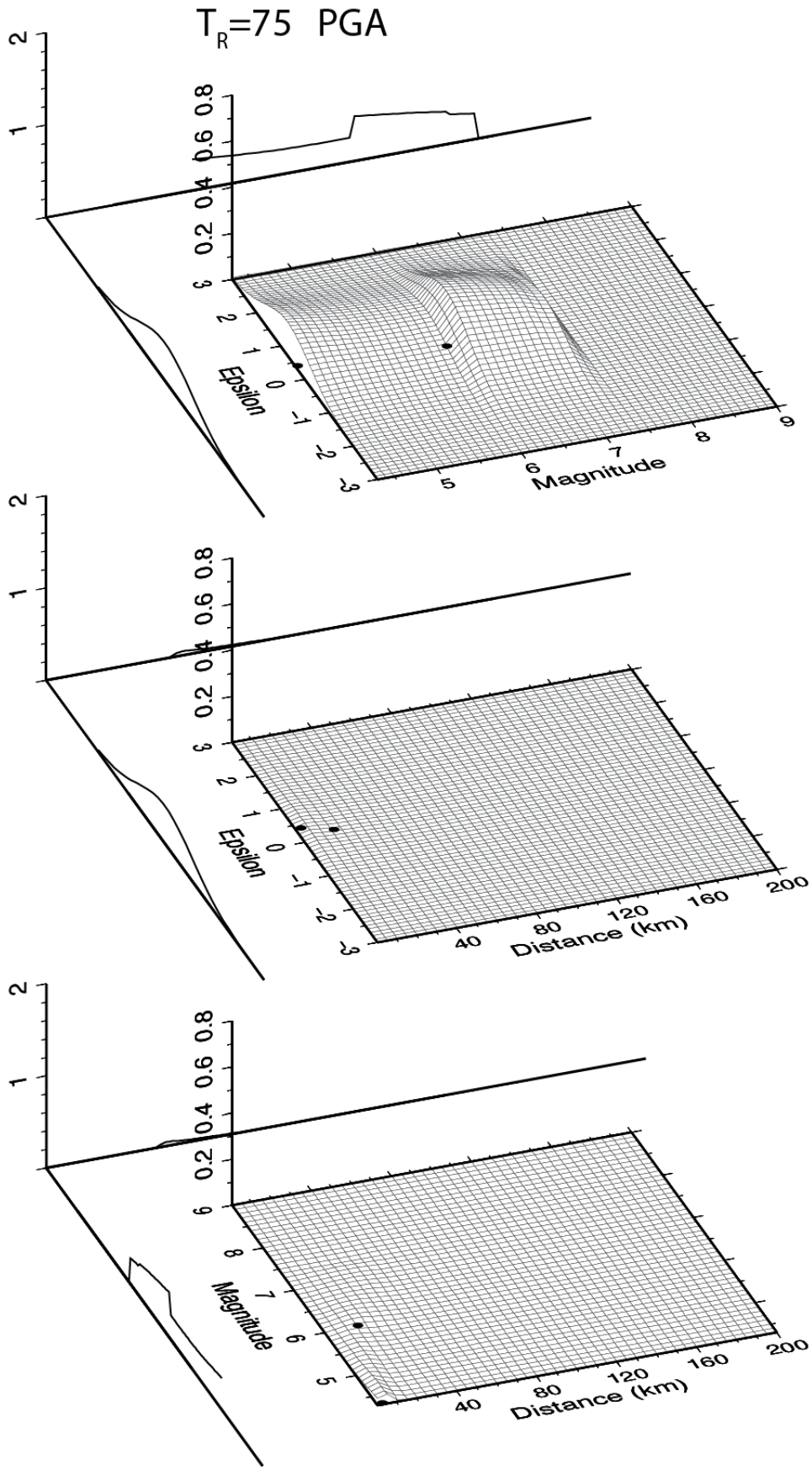

Figure 1.4.1.8. Disaggregation results expressed as contribution to 75 yr return period hazard for the target site. The central part of each panel shows the joint PDFs for the specific hazard variable pair for PGA. On the external axes the marginal PDFs obtained from the joint PDFs area also shown.

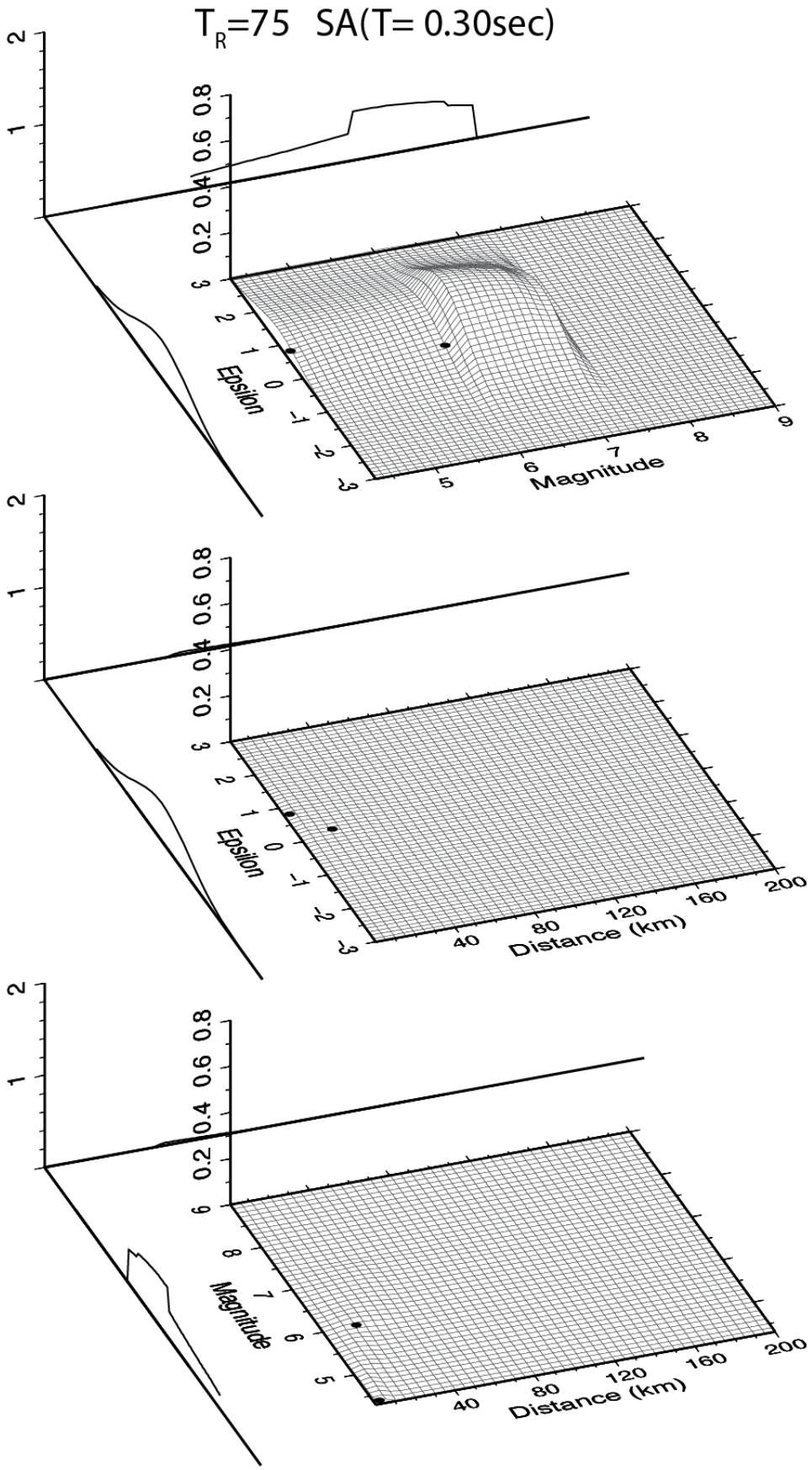

Figure 1.4.1.9. Disaggregation results expressed as contribution to 75 yr return period hazard for the target site. The central part of each panel shows the joint PDFs for the specific hazard variable pair for SA(T=0.30 sec). On the external axes the marginal PDFs obtained from the joint PDFs area also shown.

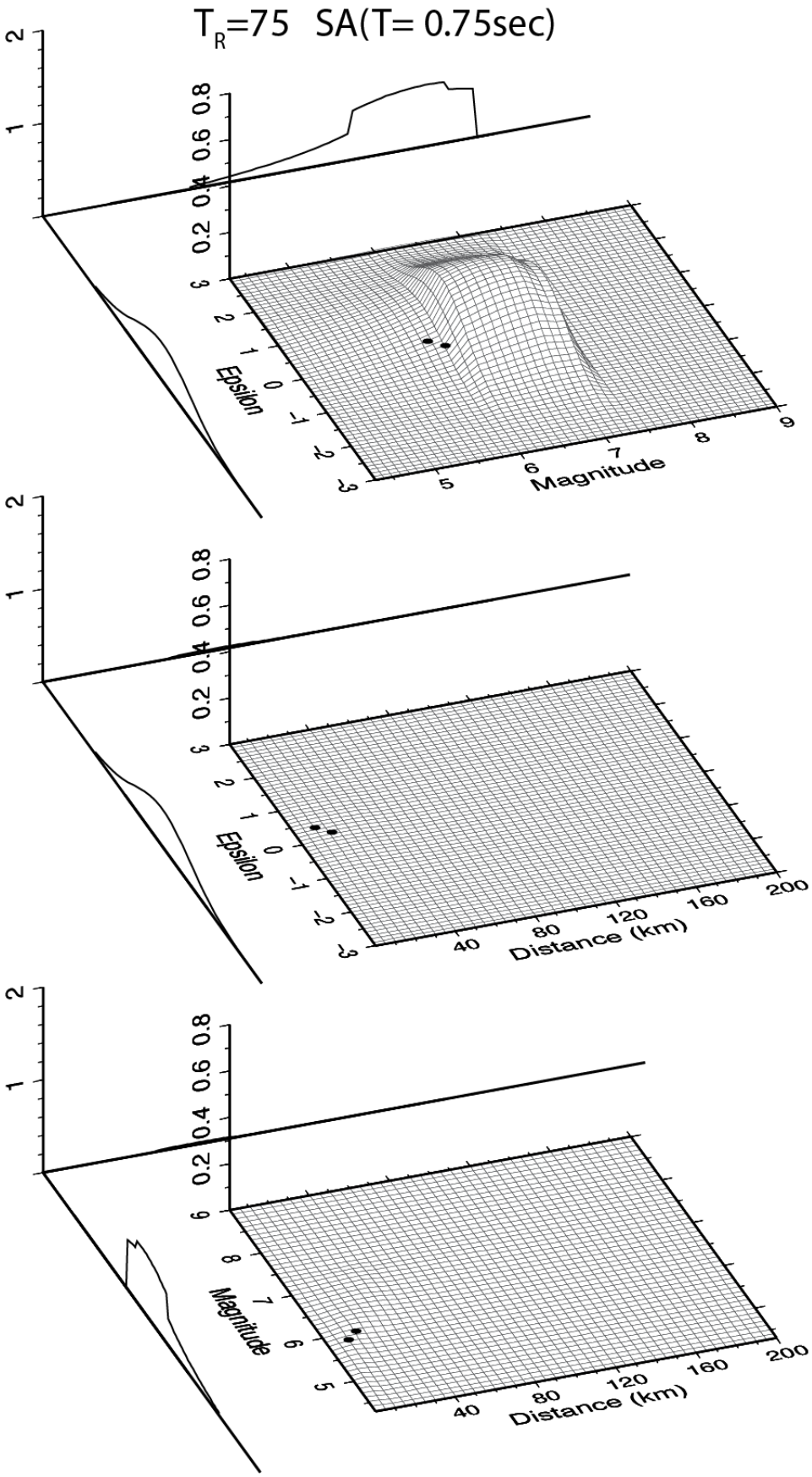

Figure 1.4.1.10. Disaggregation results expressed as contribution to 75 yr return period hazard for the target site. The central part of each panel shows the joint PDFs for the specific hazard variable pair for SA(T=0.75 sec). On the external axes the marginal PDFs obtained from the joint PDFs area also shown.

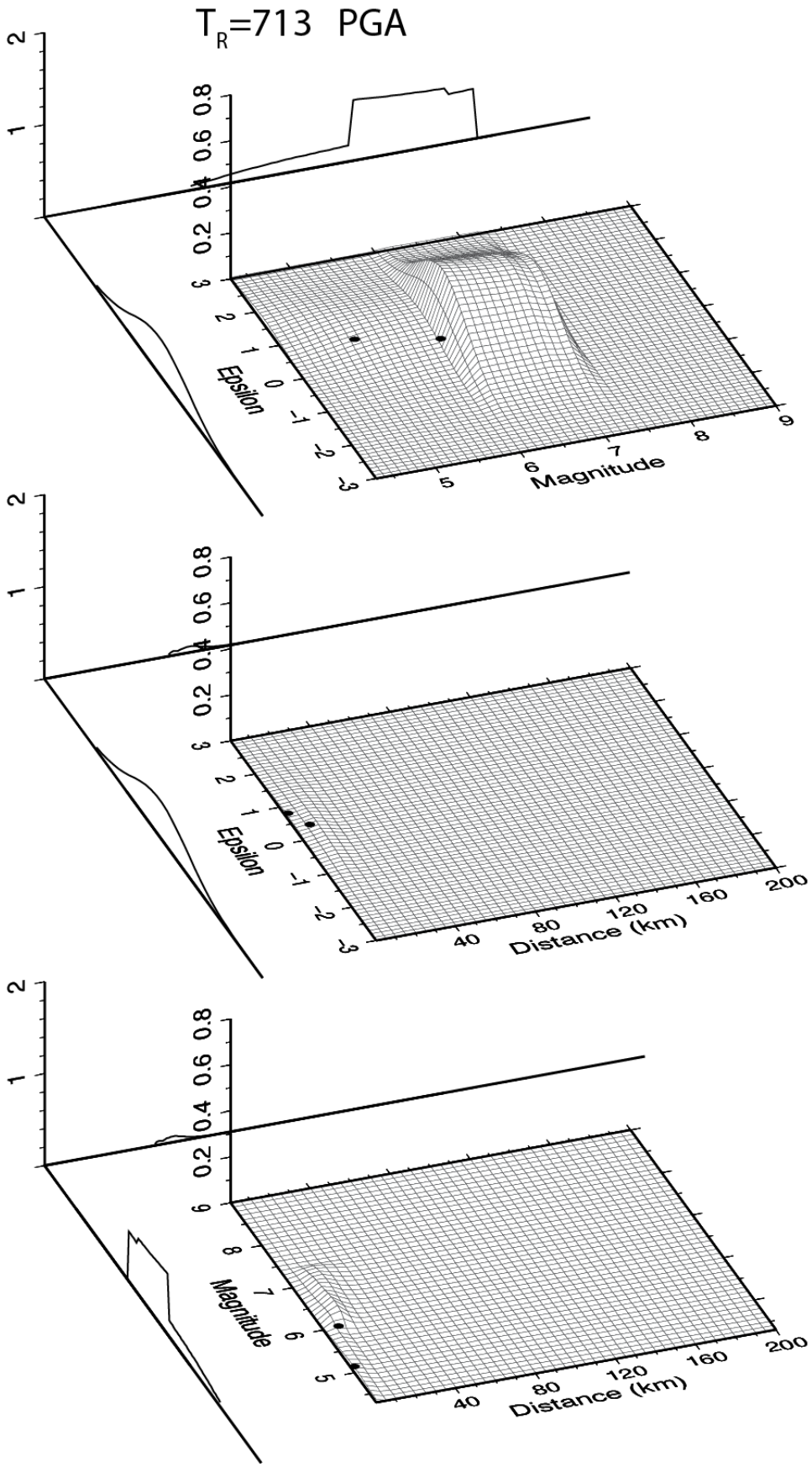

Figure 1.4.1.11. Disaggregation results expressed as contribution to 713 yr return period hazard for the target site. The central part of each panel shows the joint PDFs for the specific hazard variable pair for PGA. On the external axes the marginal PDFs obtained from the joint PDFs area also shown.

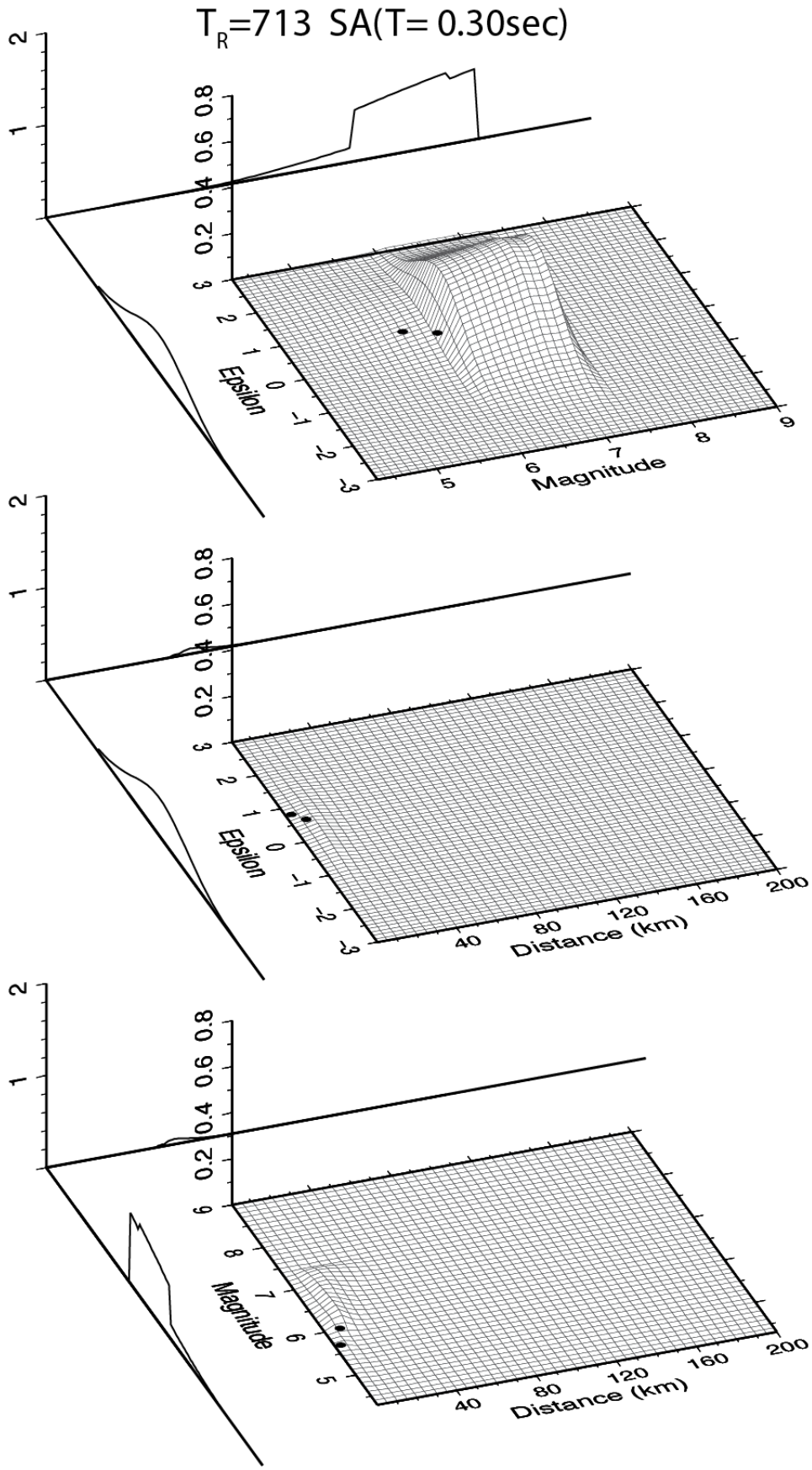

Figure 1.4.1.12. Disaggregation results expressed as contribution to 713 yr return period hazard for the target site. The central part of each panel shows the joint PDFs for the specific hazard variable pair for SA(T=0.30 sec). On the external axes the marginal PDFs obtained from the joint PDFs area also shown.

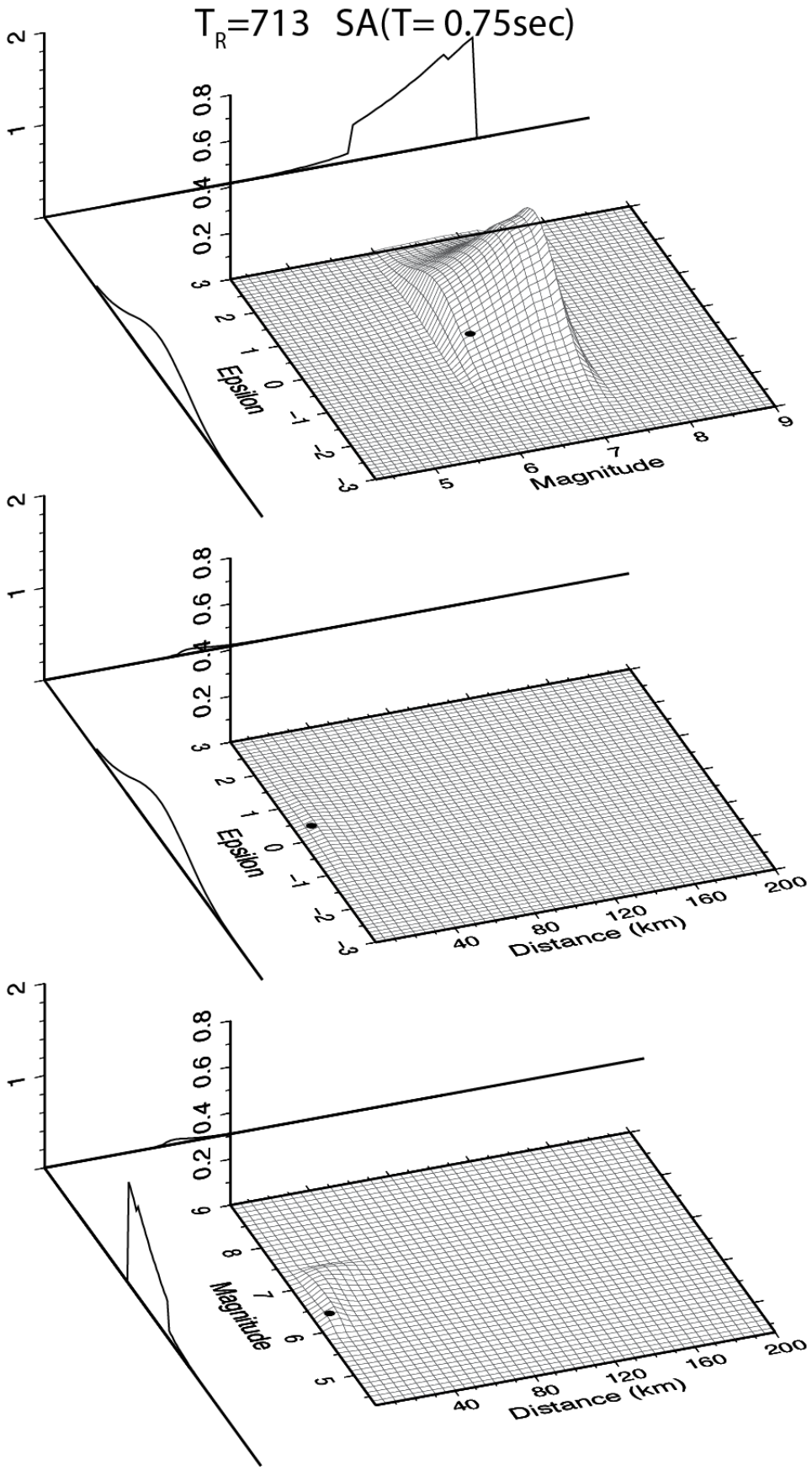

Figure 1.4.1.13. Disaggregation results expressed as contribution to 713 yr return period hazard for the target site. The central part of each panel shows the joint PDFs for the specific hazard variable pair for SA(T=0.75 sec). On the external axes the marginal PDFs obtained from the joint PDFs area also shown.

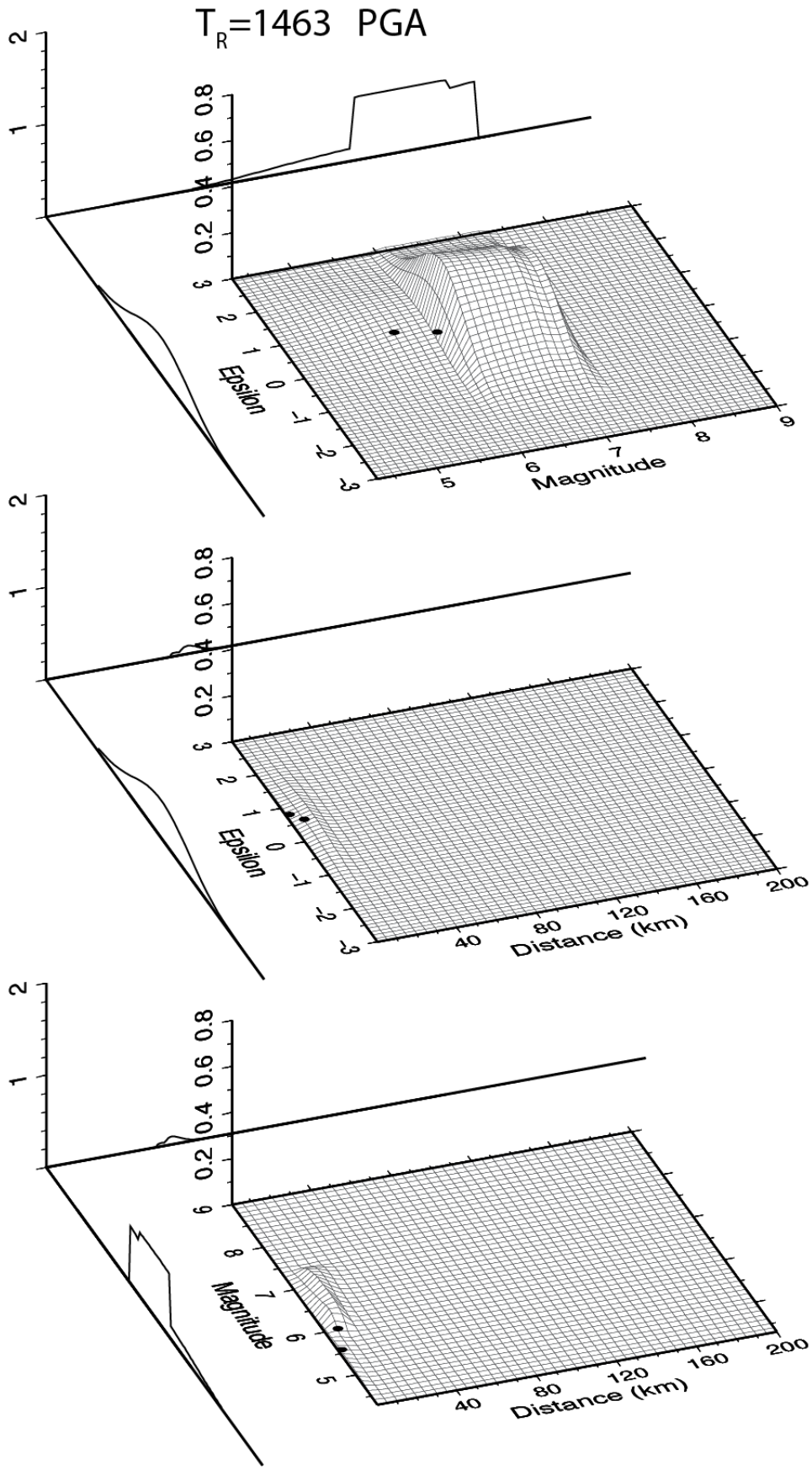

Figure 1.4.1.14. Disaggregation results expressed as contribution to 1463 yr return period hazard for the target site. The central part of each panel shows the joint PDFs for the specific hazard variable pair for PGA. On the external axes the marginal PDFs obtained from the joint PDFs area also shown.

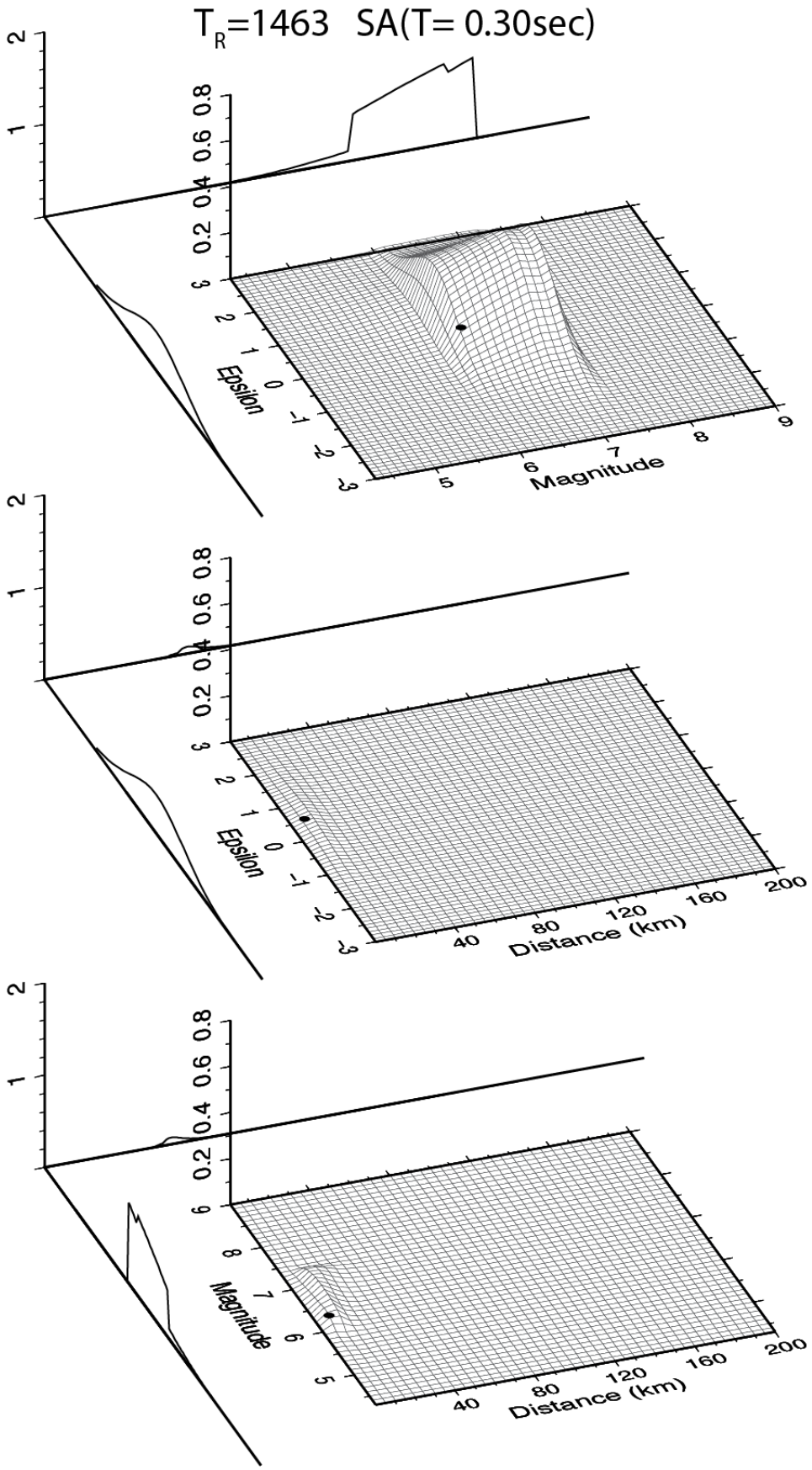

Figure 1.4.1.15. Disaggregation results expressed as contribution to 1463 yr return period hazard for the target site. The central part of each panel shows the joint PDFs for the specific hazard variable pair for SA(T=0.30 sec). On the external axes the marginal PDFs obtained from the joint PDFs area also shown.

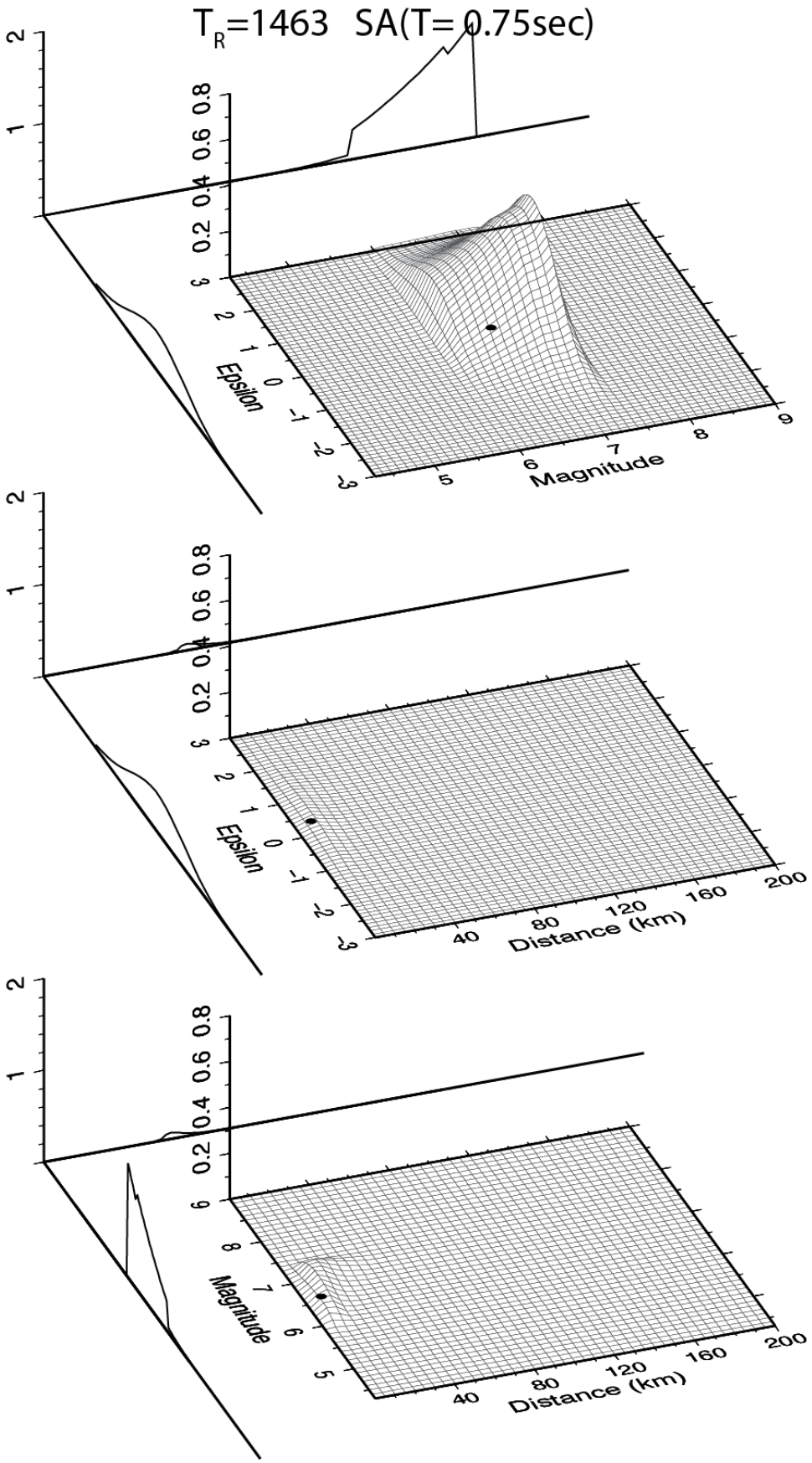

Figure 1.4.1.16. Disaggregation results expressed as contribution to 1463 yr return period hazard for the target site. The central part of each panel shows the joint PDFs for the specific hazard variable pair for SA(T=0.75 sec). On the external axes the marginal PDFs obtained from the joint PDFs area also shown.

1.4.2 Campobasso Hospital

For the sake of convenience was again reported the text of Chapter 1.4.1 (adapted for Campobasso Hospital).

The result of the probabilistic hazard analysis performed for the student house at University of Molise is reported in terms of Uniform Hazard Spectra (UHS) because, as discussed in Cap.1.4, from an engineering point of view it represents the better way to summarize the result of a seismic hazard analysis.

The UHS was computed in terms of PGA and Sa(T) for 47 different values of T (0.1-2.0 sec.) for a 200 years exposure period and for four different return periods (120, 201, 1898, 2475 years). The choice of return period (as described in Cap.1.4) is driven fundamentally by the regulation actually in force in the Italian territory about anti-seismic planning corresponding to the EC8 (Eurocode, 2003).

In Figure 1.4.2.1 are reported the UHSs corresponding to TR =120yr calculated at 47 vibration periods for the target site. In the same figure, the UHS retrieved from the INGV (black solid dashed line) are also shown. The latter UHS corresponds to the weighted mean of the UHSs at the four closest grid points to the target site, at which INGV computed PSHA (see cap.1.4 for more details).

For the selected sites, the disaggregation analysis was also performed. The figures 1.4.2.5-16 display the results of disaggregation for the student house obtained in the present study in terms of both joint and marginal PDFs, as described in Cap.1.4.

From disaggregation analysis was retrieved the mean and the first and second mode (where it exists) value of the triplet magnitude-distance-ε (M-R-ε) which is responsible for the ground motion exceedance. A second mode is not always present (Fig.1.4.2.10, Fig.1.4.2.11 or Fig.1.4.2.14), but when it exists it can provide useful information from the engineering point of view to perform the better non-linear dynamic analysis of a future build.

The results for the student house, in terms of mean and modal values, obtained from the joint PDFs, are given in Table1.4.2.1. In particular, $(\bar{M}, \bar{R}, \bar{\varepsilon})$ refers to the mean values, and (R*, M*, ε*) refers to the modal values.

As expected, disaggregation shows different results at different periods and return period (unimodal and bimodal shape) due to different contribution to hazard of each SZ. As a consequence, for the selected spectral ordinate and return period, at least two design earthquakes do exist and must be considered during the engineering structures design.

Table 1.4.2.1: **Table 1.4.1.1**: Modal and mean values for the hazard variables for the target site; for PGA, Sa(T= 0.50 sec) and Sa (T= 1.50 sec)*

	R* (Km)	M*	ε*	$\overline{R}$ (km)	$\overline{M}$	$\overline{\varepsilon}$
	Tr=120yr					
PGA	3/14	4.33/6.03	0.6/0.2	14.8	5.98	0.5
T= 0.50 sec	14/6	6.03/5.43	0.4/0.6	23.4	6.39	0.6
T= 1.50 sec	12/18	6.03/6.28	0.2/0.4	31.3	6.61	0.5
	Tr=201yr					
PGA	12/3	6.03/4.48	0.2/0.8	13.1	6.10	0.6
T= 0.50 sec	12/6	6.03/5.73	0.4/0.6	20.1	6.49	0.6
T= 1.50 sec	10/10	6.03/6.03	0.4/0.4	25.8	6.68	0.5
	Tr=1898yr					
PGA	6/6	6.03/6.03	0.6/0.6	8.1	6.57	0.6
T= 0.50 sec	7/7	6.48/6.48	0.4/0.4	10.4	6.73	0.7
T= 1.50 sec	10/10	6.93/6.93	0.4/0.4	12.2	6.84	0.7
	Tr=2475yr					
PGA	6/6	6.13/6.13	0.6/0.6	7.7	6.61	0.7
T= 0.50 sec	7/7	6.63/6.63	0.4/0.4	9.7	6.75	0.8
T= 1.50 sec	10/10	6.98/6.98	0.4/0.4	11.3	6.86	0.7

The values have been retrieved from the joint PDFs. $\overline{M}, \overline{R}, \overline{\varepsilon}$ refer to the mean values, and M, R*and ε*to the modal values.

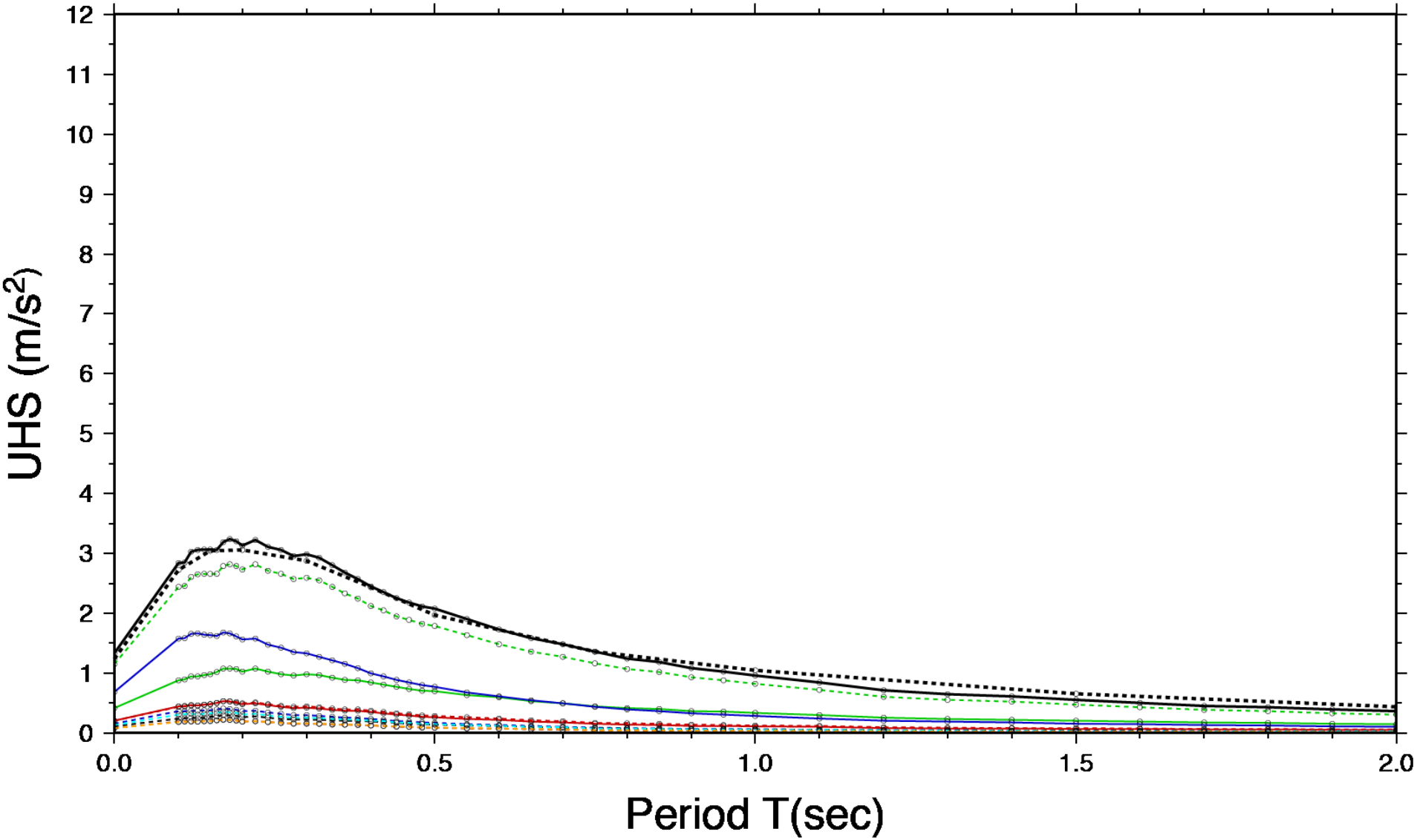

Figure 1.4.2.1. Uniform hazard spectra in m/s² for the target site and 120 yr return period. Lines represent the uniform hazard spectra computed considering the contribution of all seismogenic zones (black), SZ 918 (red), SZ 923 (green), SZ 924 (blue), SZ 925 (red dashed), SZ 927 (green dashed), SZ 928 (blue dashed),SZ 917 (black dashed), SZ 920 (cyan dashed), SZ922 (brown dashed), SZ 926 (orange dashed). The black dashed line represents the INGV uniform hazard spectrum.

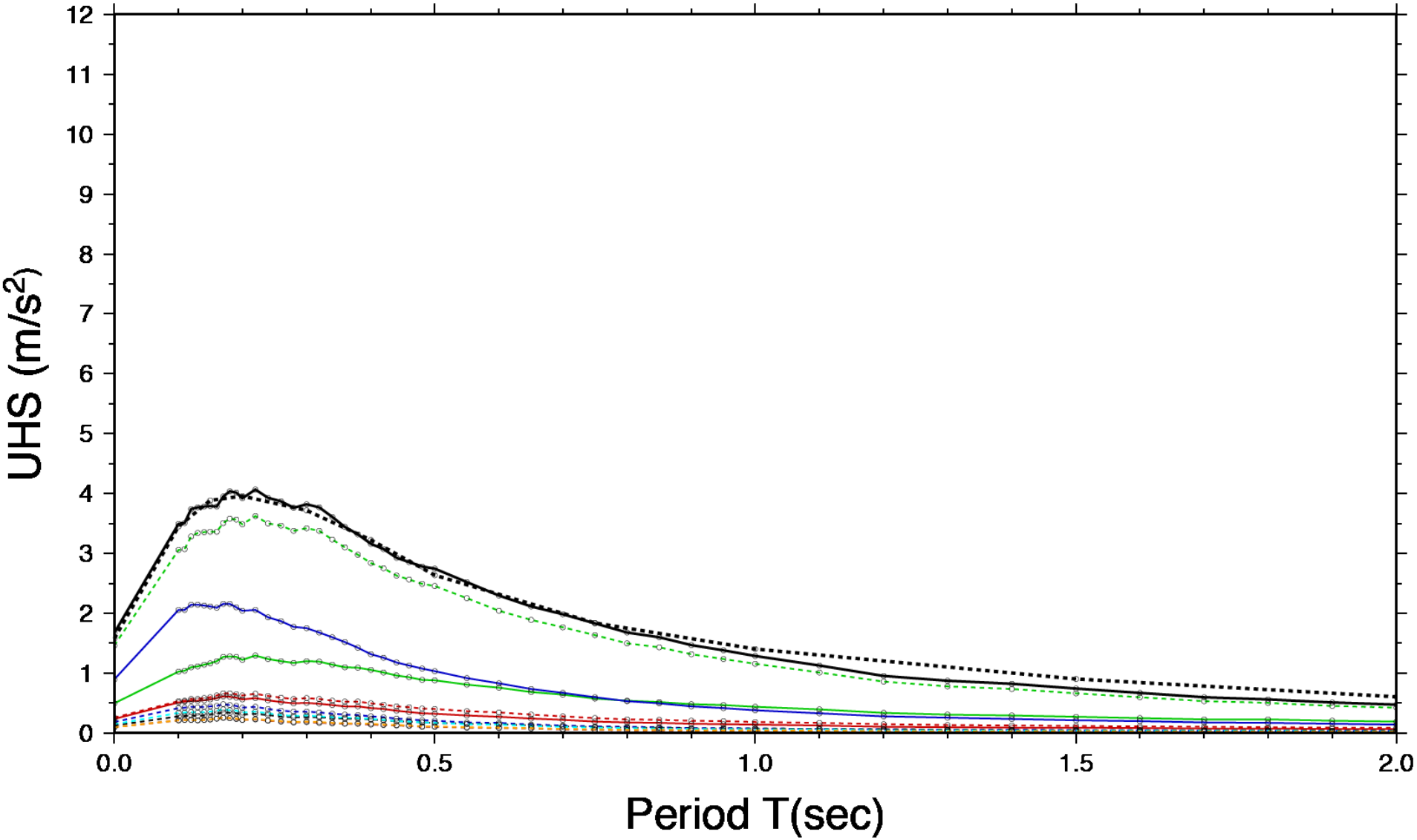

Figure 1.4.2.2. Uniform hazard spectra in m/s² for the target site and 201 yr return period. Lines represent the uniform hazard spectra computed considering the contribution of all seismogenic zones (black), SZ 918 (red), SZ 923 (green), SZ 924 (blue), SZ 925 (red dashed), SZ 927 (green dashed), SZ 928 (blue dashed),SZ 917 (black dashed), SZ 920 (cyan dashed), SZ922 (brown dashed), SZ 926 (orange dashed). The black dashed line represents the INGV uniform hazard spectrum.

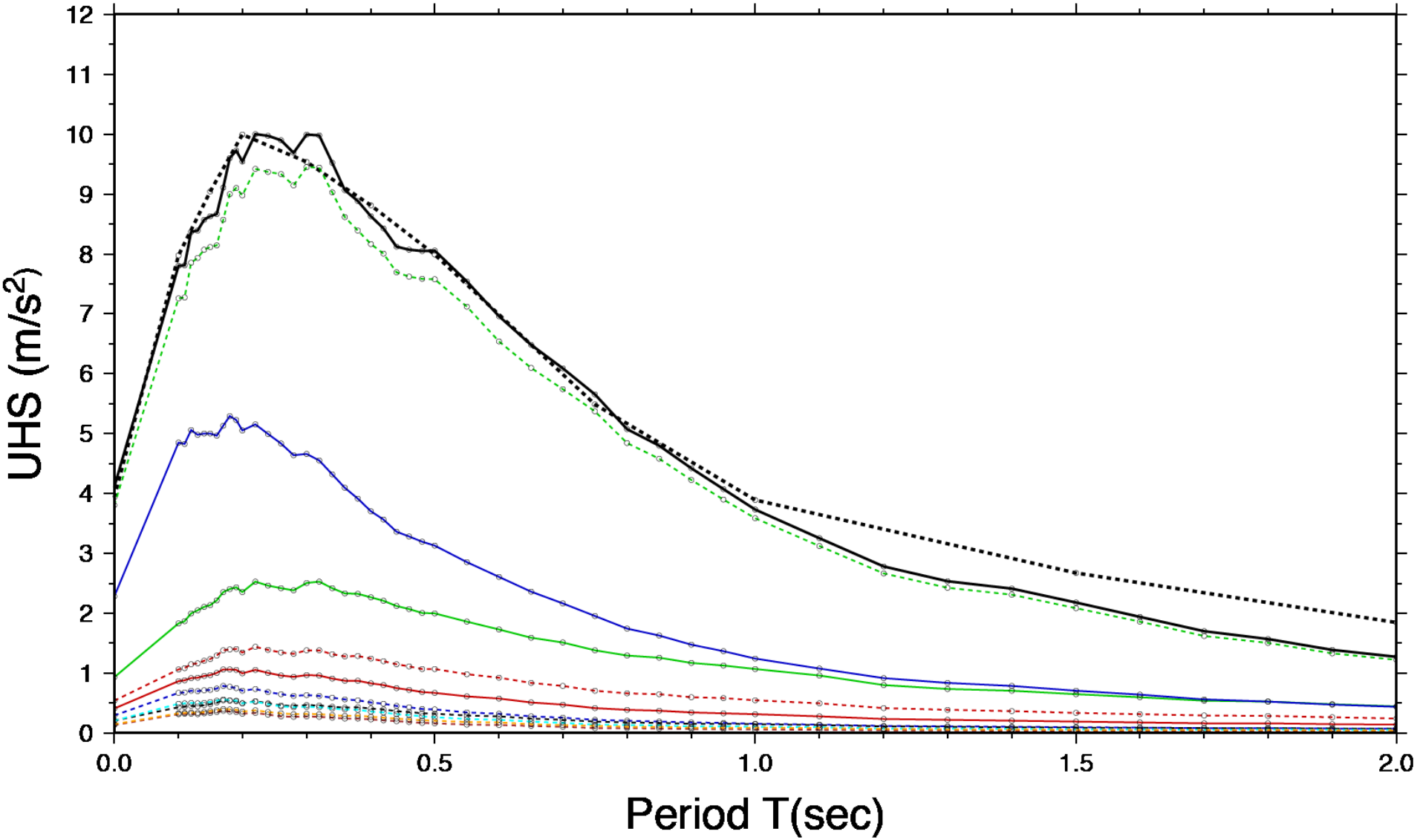

Figure 1.4.2.3. Uniform hazard spectra in m/s² for the target site and 1898 yr return period. Lines represent the uniform hazard spectra computed considering the contribution of all seismogenic zones (black), SZ 918 (red), SZ 923 (green), SZ 924 (blue), SZ 925 (red dashed), SZ 927 (green dashed), SZ 928 (blue dashed),SZ 917 (black dashed), SZ 920 (cyan dashed), SZ922 (brown dashed), SZ 926 (orange dashed). The black dashed line represents the INGV uniform hazard spectrum.

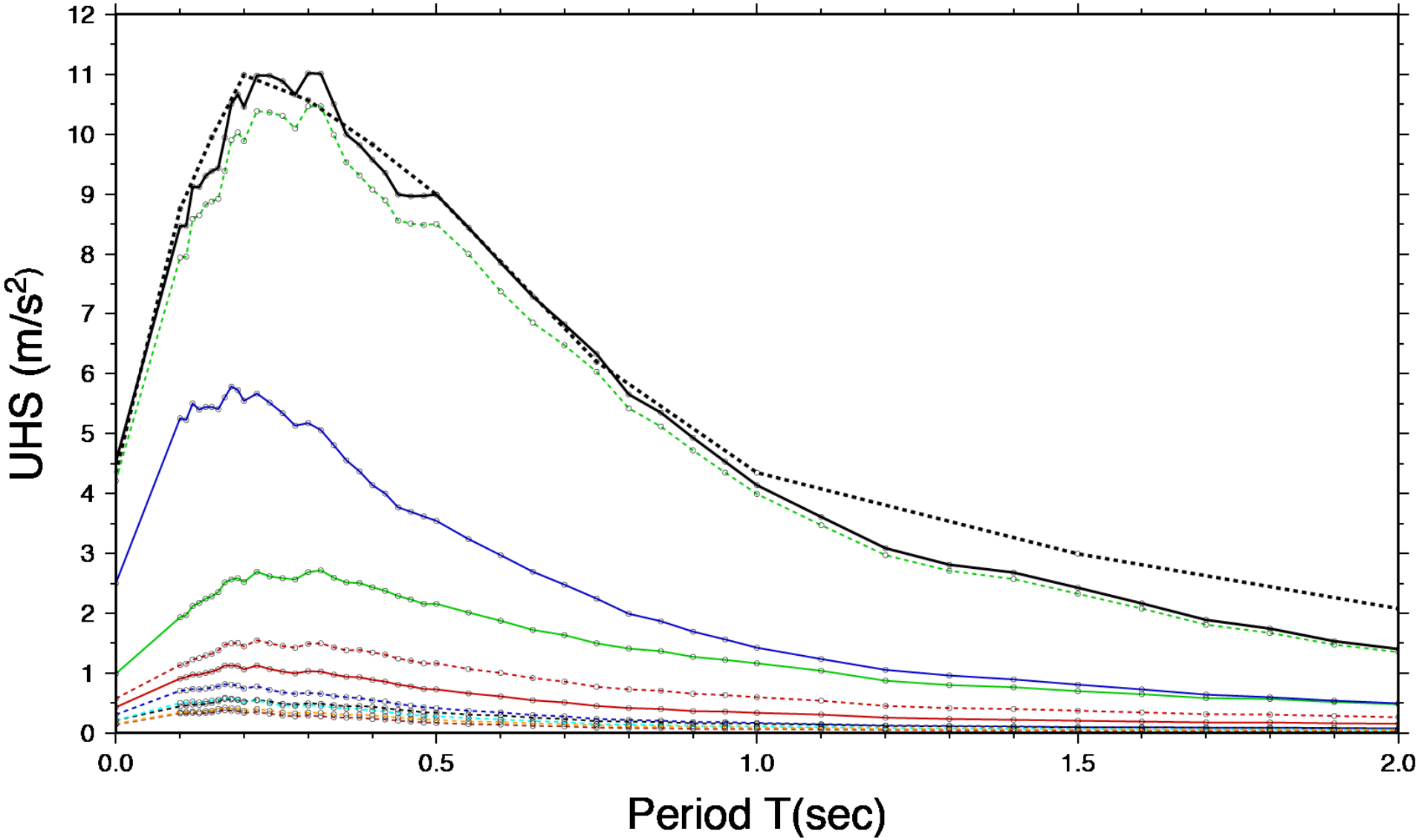

Figure 1.4.2.4. Uniform hazard spectra in m/s² for the target site and 2475 yr return period. Lines represent the uniform hazard spectra computed considering the contribution of all seismogenic zones (black), SZ 918 (red), SZ 923 (green), SZ 924 (blue), SZ 925 (red dashed), SZ 927 (green dashed), SZ 928 (blue dashed),SZ 917 (black dashed), SZ 920 (cyan dashed), SZ922 (brown dashed), SZ 926 (orange dashed). The black dashed line represents the INGV uniform hazard spectrum.

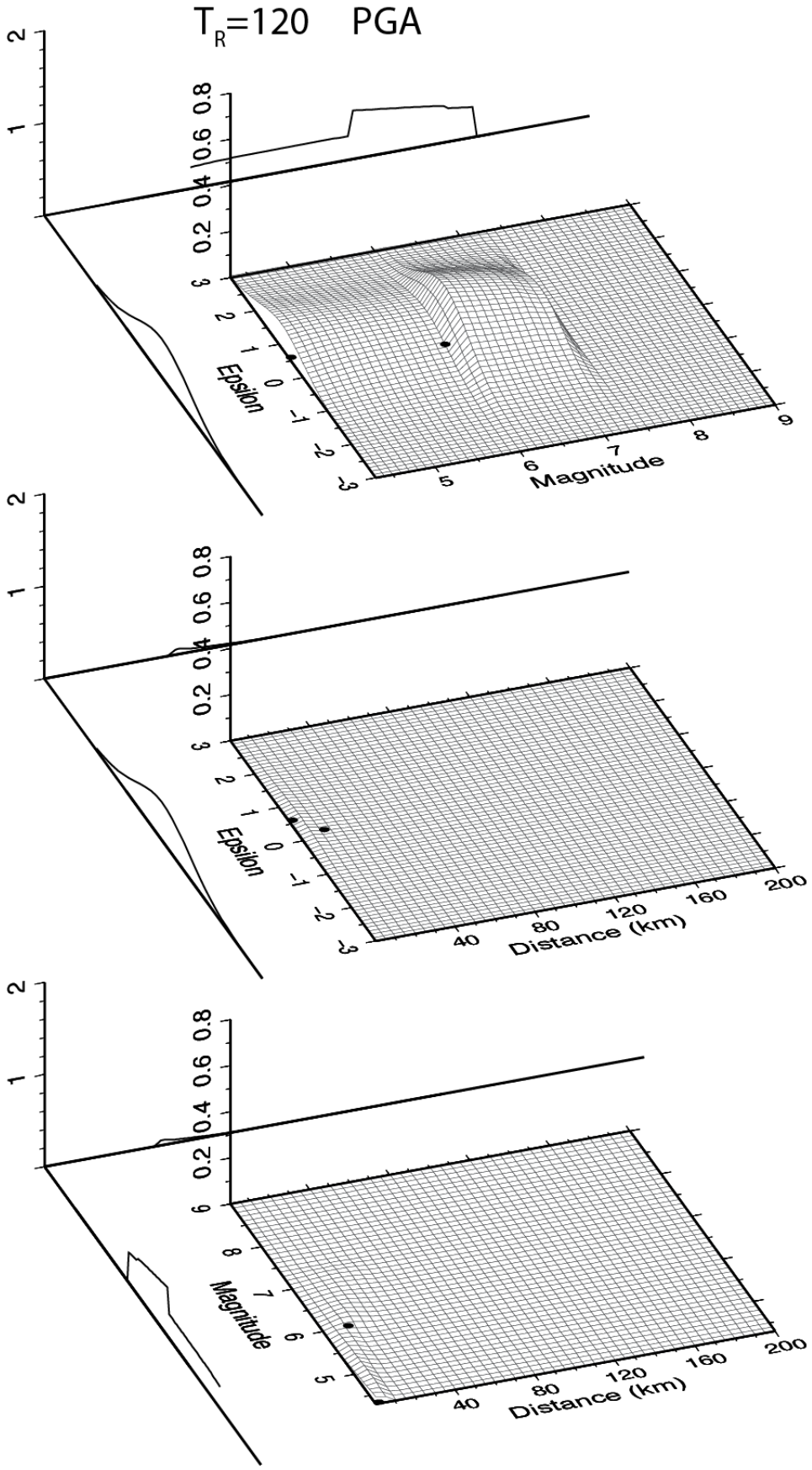

Figure 1.4.2.5. Disaggregation results expressed as contribution to 120 yr return period hazard for the target site. The central part of each panel shows the joint PDFs for the specific hazard variable pair for PGA. On the external axes the marginal PDFs obtained from the joint PDFs area also shown.

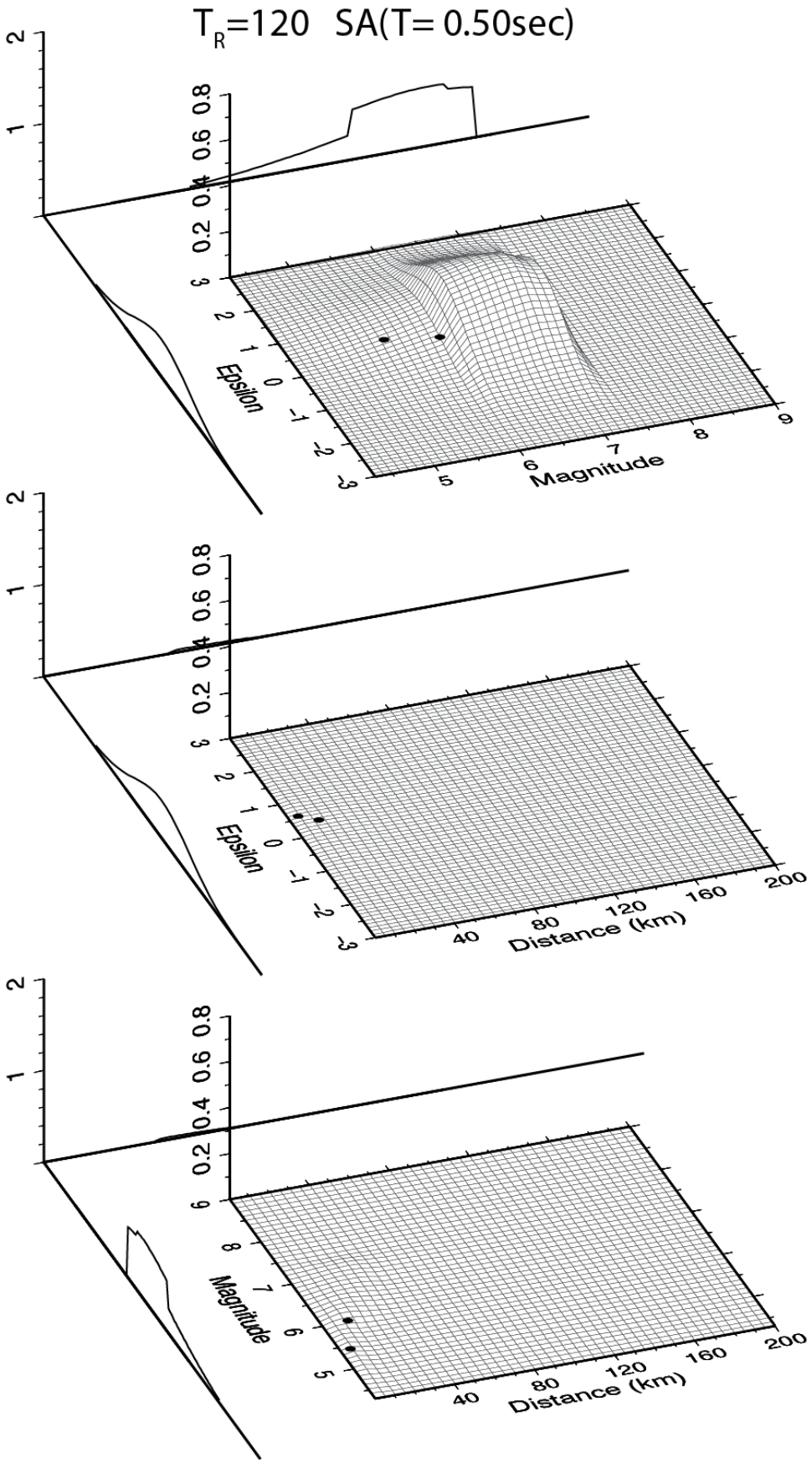

Figure 1.4.2.6. Disaggregation results expressed as contribution to 120 yr return period hazard for the target site. The central part of each panel shows the joint PDFs for the specific hazard variable pair for SA(T=0.50 sec). On the external axes the marginal PDFs obtained from the joint PDFs area also shown.

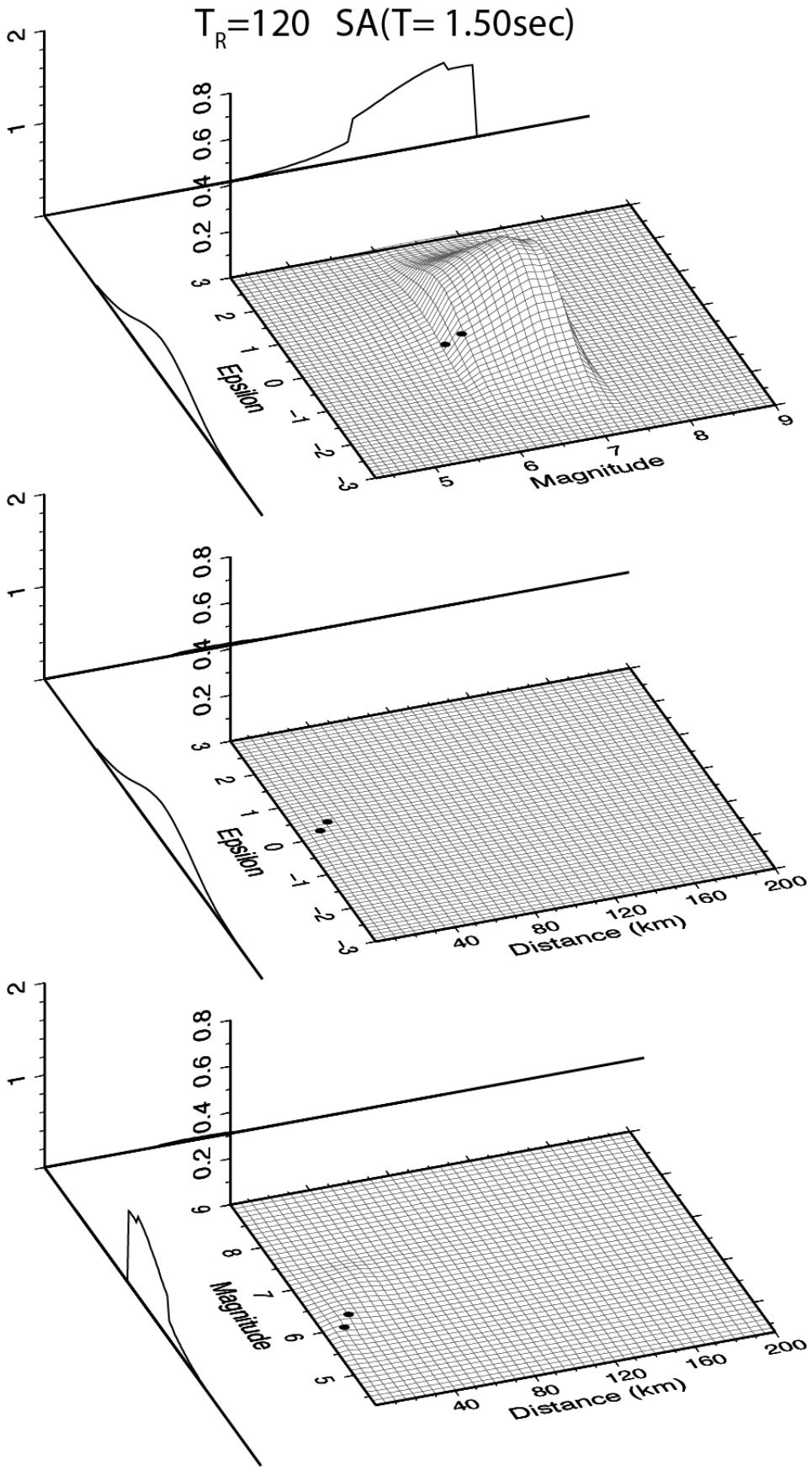

Figure 1.4.2.7. Disaggregation results expressed as contribution to 120 yr return period hazard for the target site. The central part of each panel shows the joint PDFs for the specific hazard variable pair for SA(T=1.50 sec). On the external axes the marginal PDFs obtained from the joint PDFs area also shown.

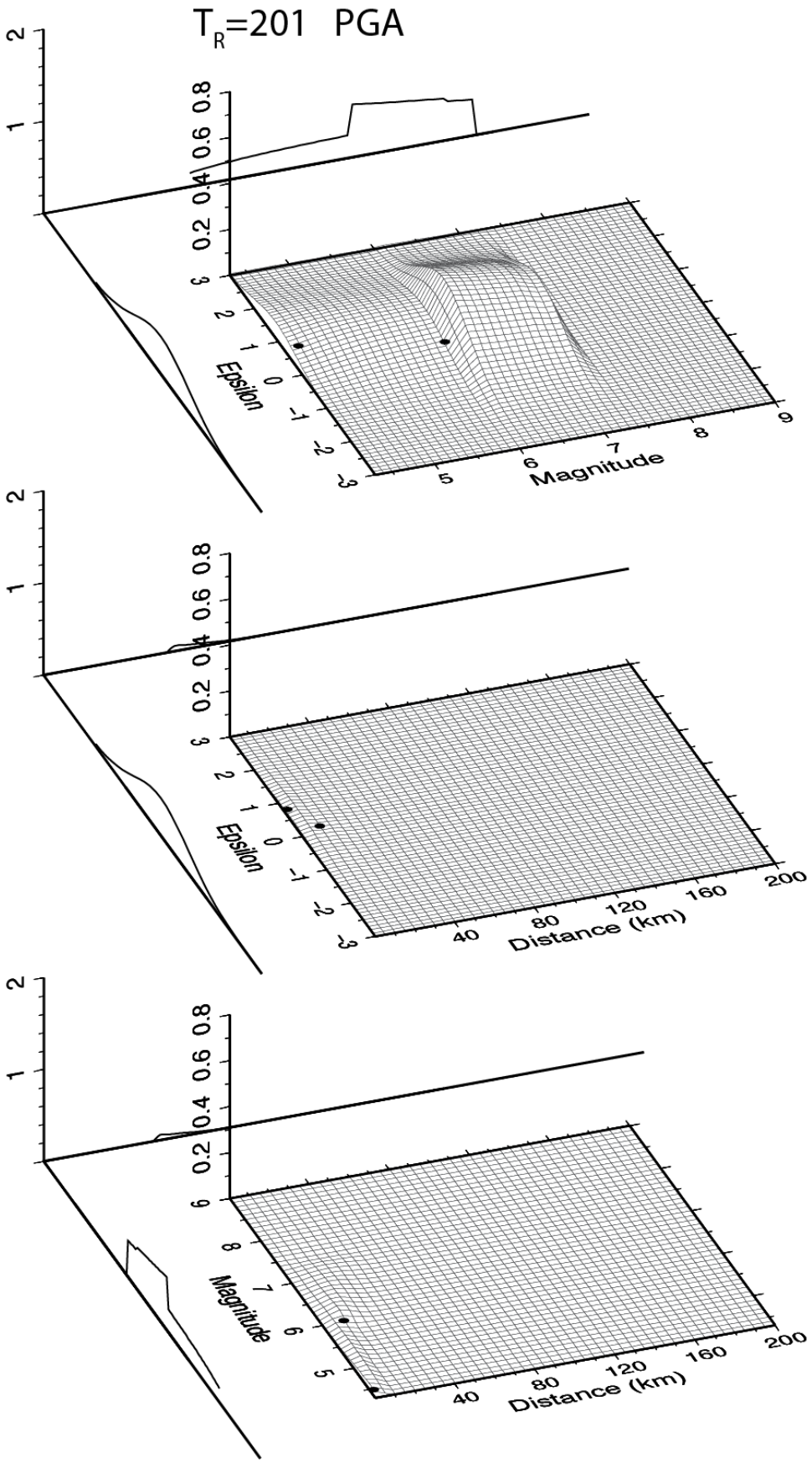

Figure 1.4.2.8. Disaggregation results expressed as contribution to 201 yr return period hazard for the target site. The central part of each panel shows the joint PDFs for the specific hazard variable pair for PGA. On the external axes the marginal PDFs obtained from the joint PDFs area also shown.

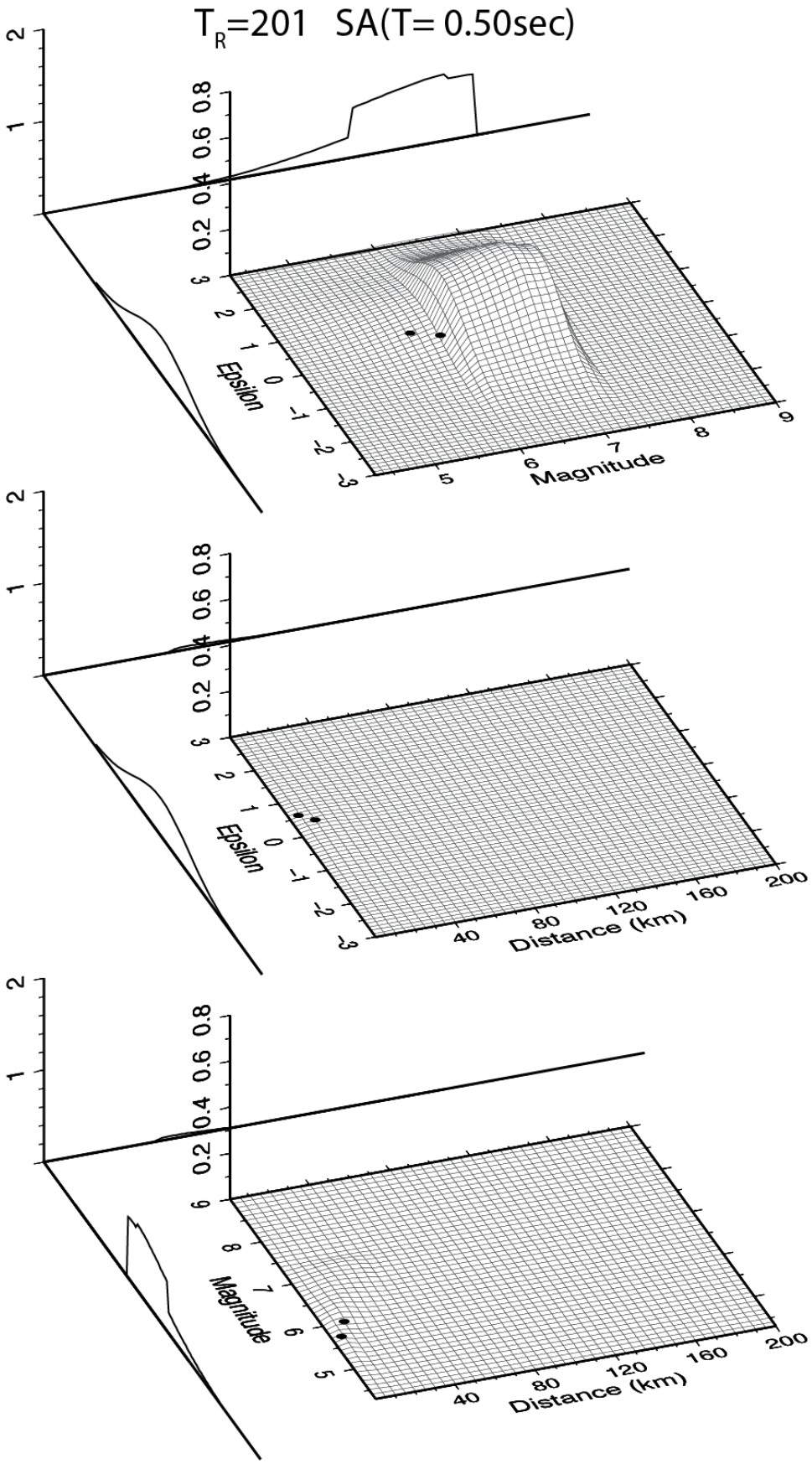

Figure 1.4.2.9. Disaggregation results expressed as contribution to 201 yr return period hazard for the target site. The central part of each panel shows the joint PDFs for the specific hazard variable pair for SA(T=0.50 sec). On the external axes the marginal PDFs obtained from the joint PDFs area also shown.

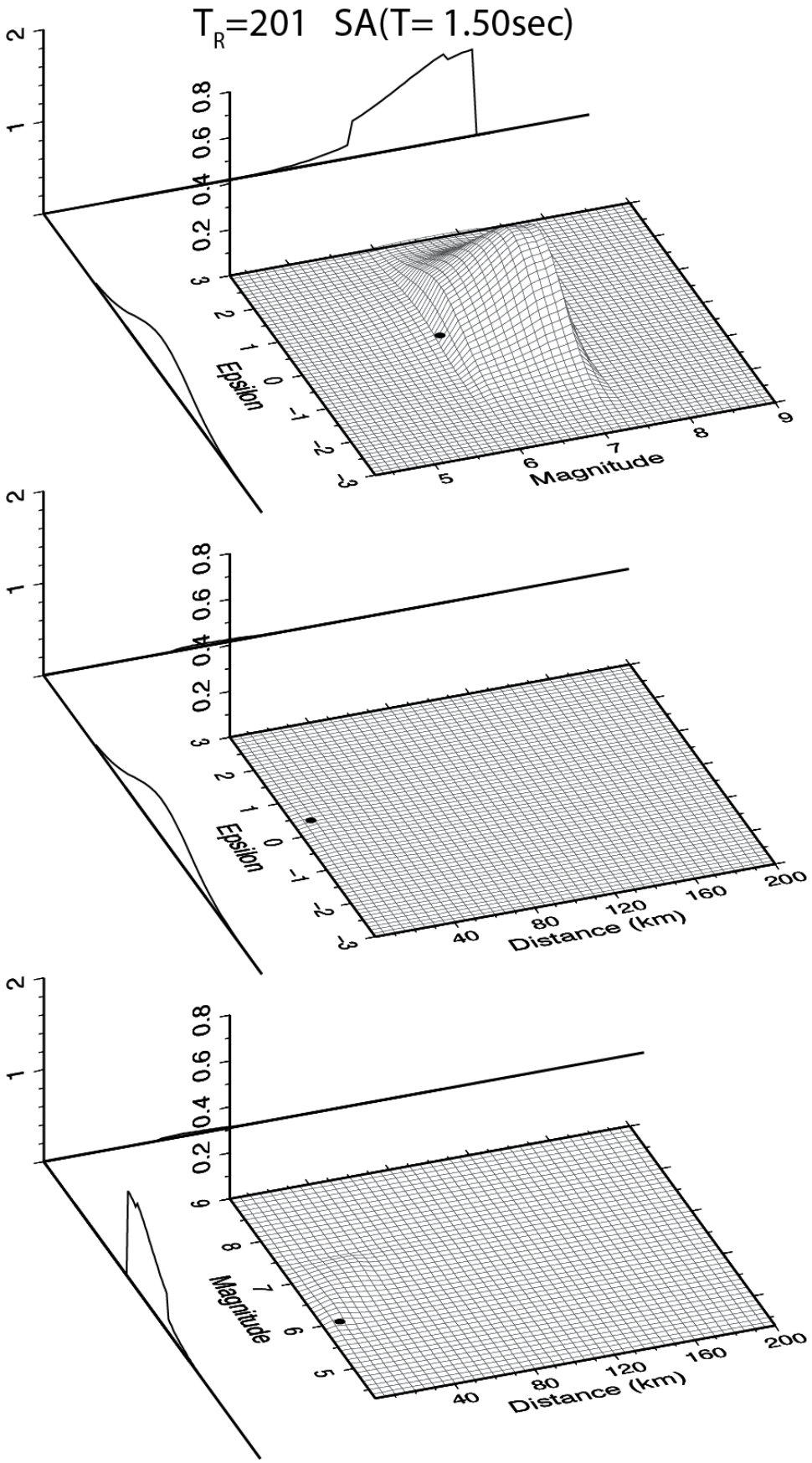

Figure 1.4.2.10. Disaggregation results expressed as contribution to 201 yr return period hazard for the target site. The central part of each panel shows the joint PDFs for the specific hazard variable pair for SA(T=1.50 sec). On the external axes the marginal PDFs obtained from the joint PDFs area also shown.

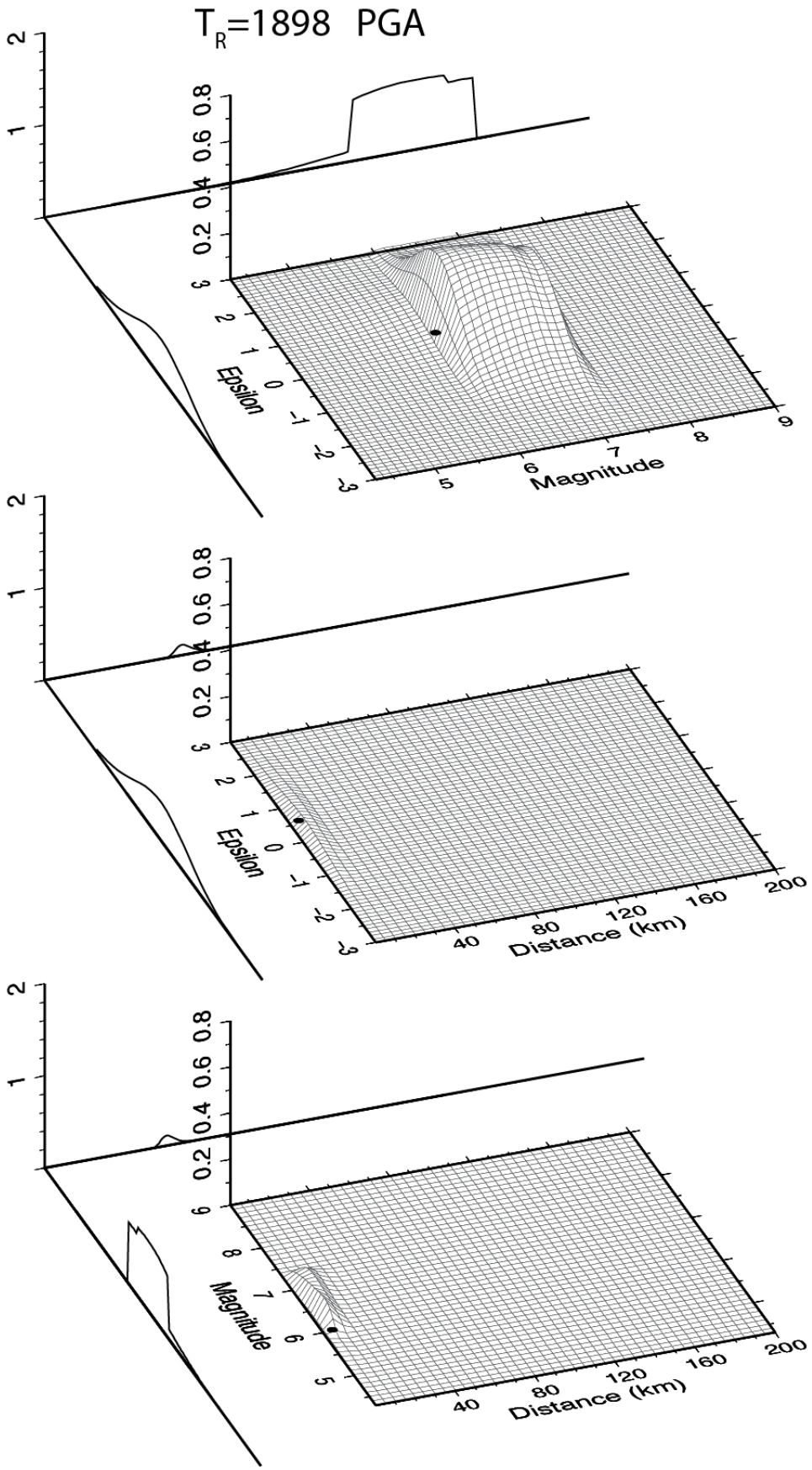

Figure 1.4.2.11. Disaggregation results expressed as contribution to 1898 yr return period hazard for the target site. The central part of each panel shows the joint PDFs for the specific hazard variable pair for PGA. On the external axes the marginal PDFs obtained from the joint PDFs area also shown.

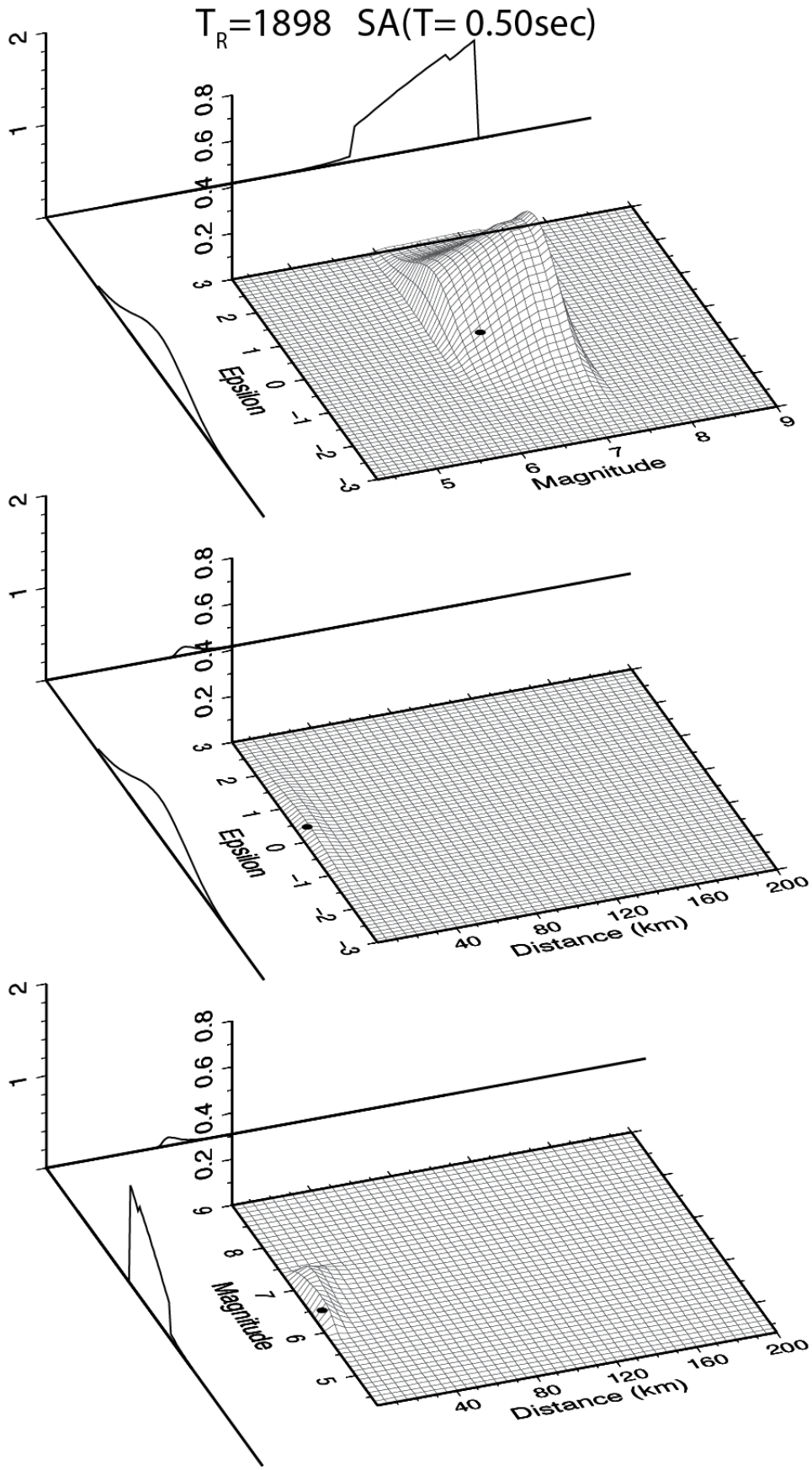

Figure 1.4.2.12. Disaggregation results expressed as contribution to 1898 yr return period hazard for the target site. The central part of each panel shows the joint PDFs for the specific hazard variable pair for SA(T=0.50 sec). On the external axes the marginal PDFs obtained from the joint PDFs area also shown.

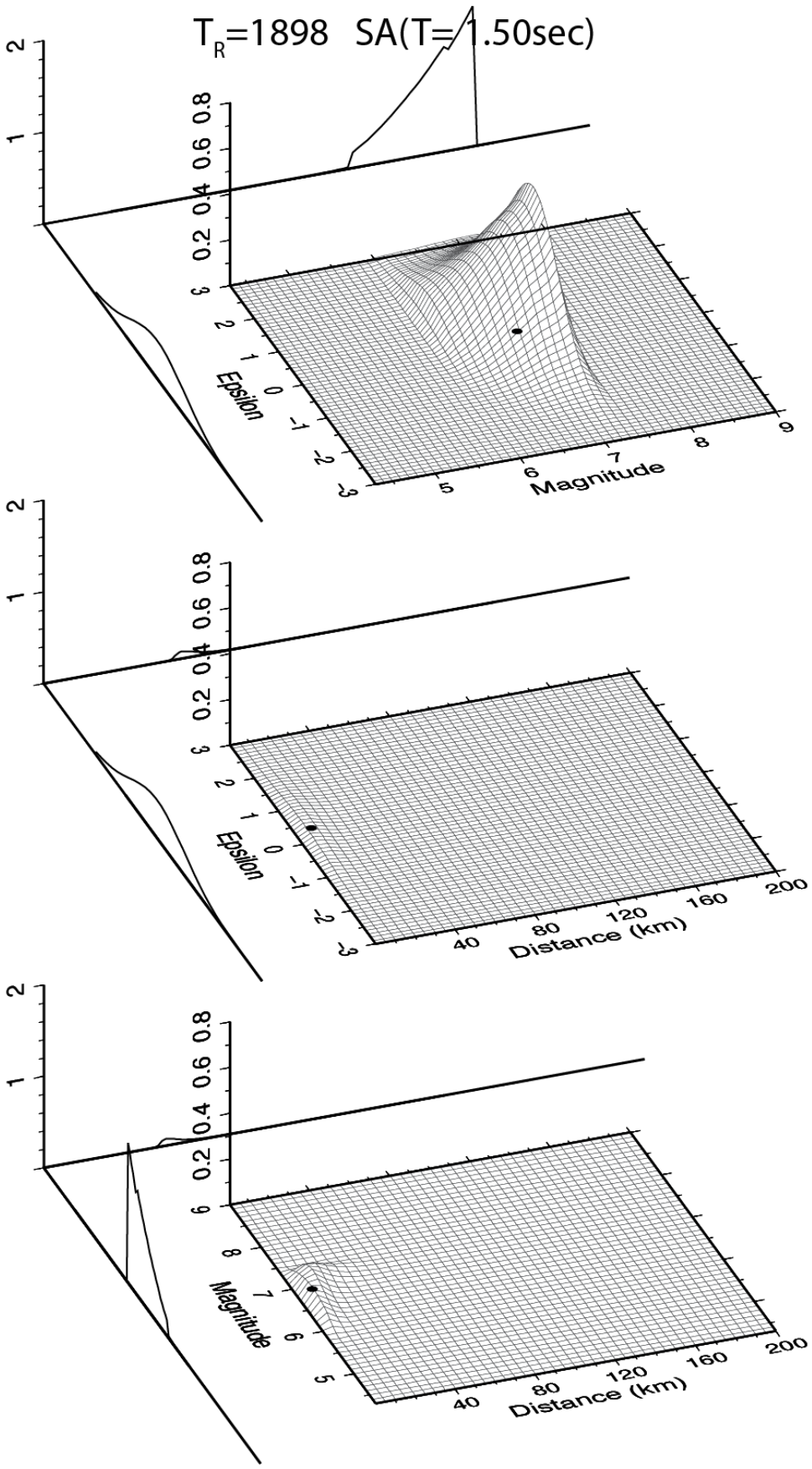

Figure 1.4.2.13. Disaggregation results expressed as contribution to 1898 yr return period hazard for the target site. The central part of each panel shows the joint PDFs for the specific hazard variable pair for SA(T=1.50 sec). On the external axes the marginal PDFs obtained from the joint PDFs area also shown.

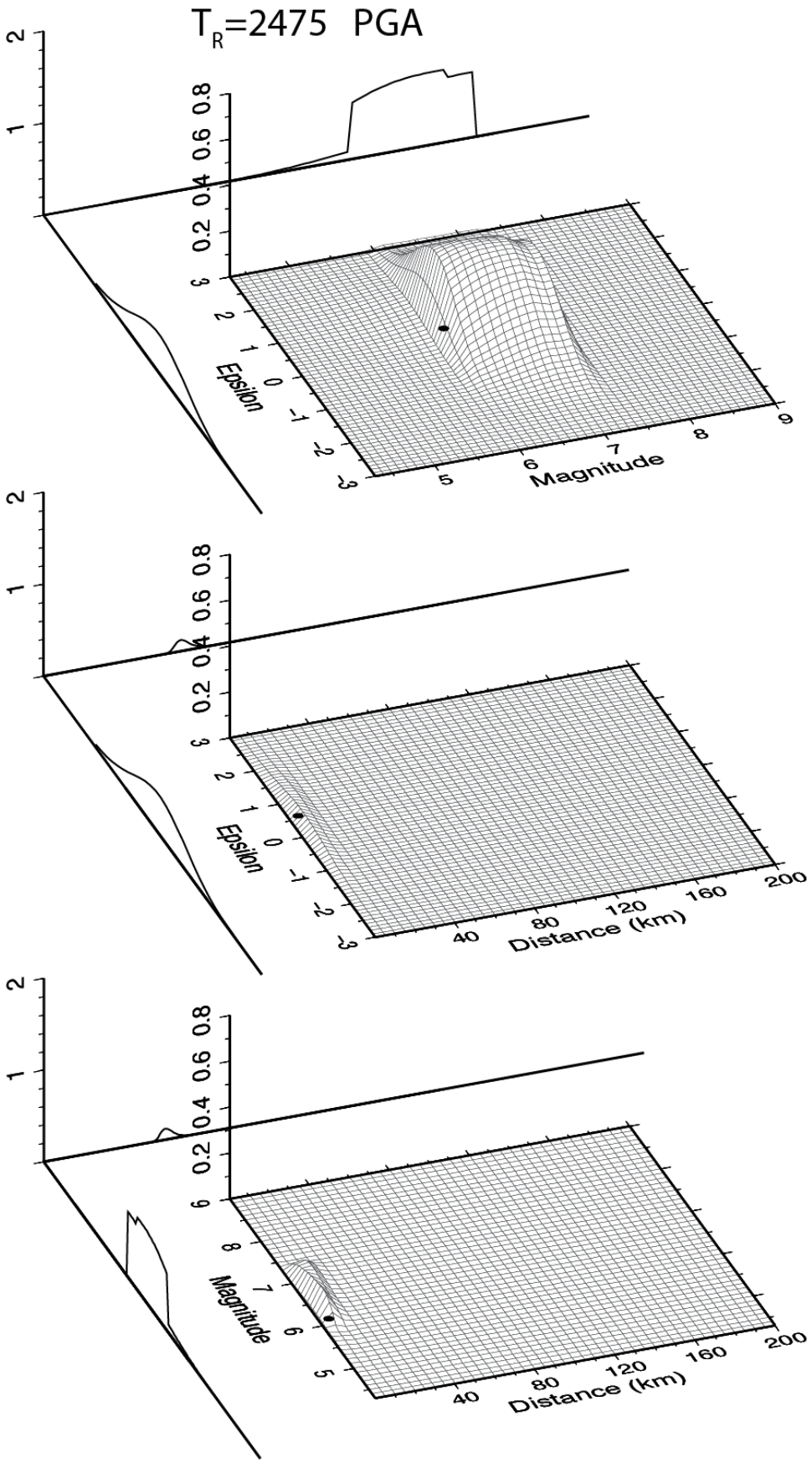

Figure 1.4.2.14. Disaggregation results expressed as contribution to 2475 yr return period hazard for the target site. The central part of each panel shows the joint PDFs for the specific hazard variable pair for PGA. On the external axes the marginal PDFs obtained from the joint PDFs area also shown.

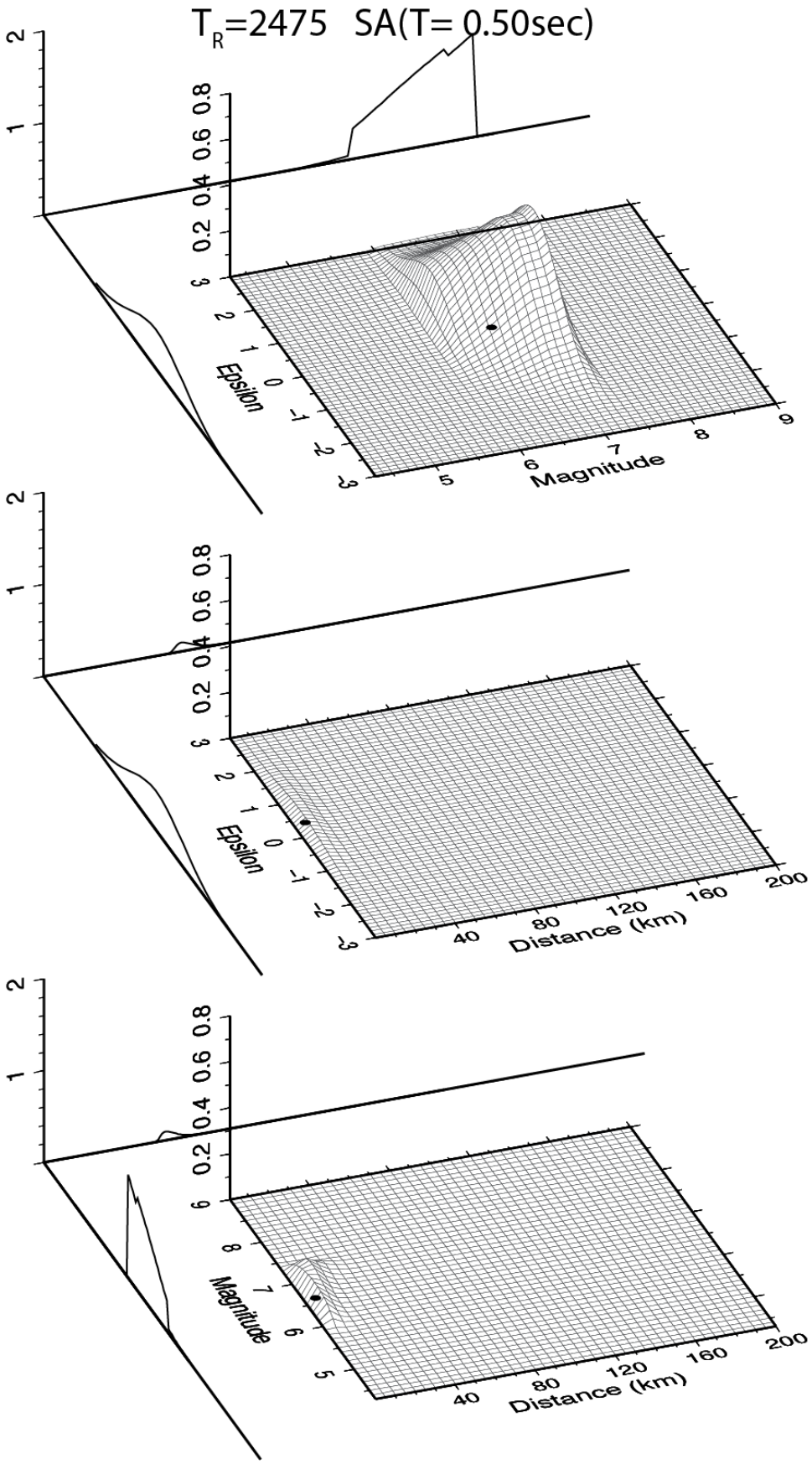

Figure 1.4.2.15. Disaggregation results expressed as contribution to 2475 yr return period hazard for the target site. The central part of each panel shows the joint PDFs for the specific hazard variable pair for SA(T=0.50 sec). On the external axes the marginal PDFs obtained from the joint PDFs area also shown.

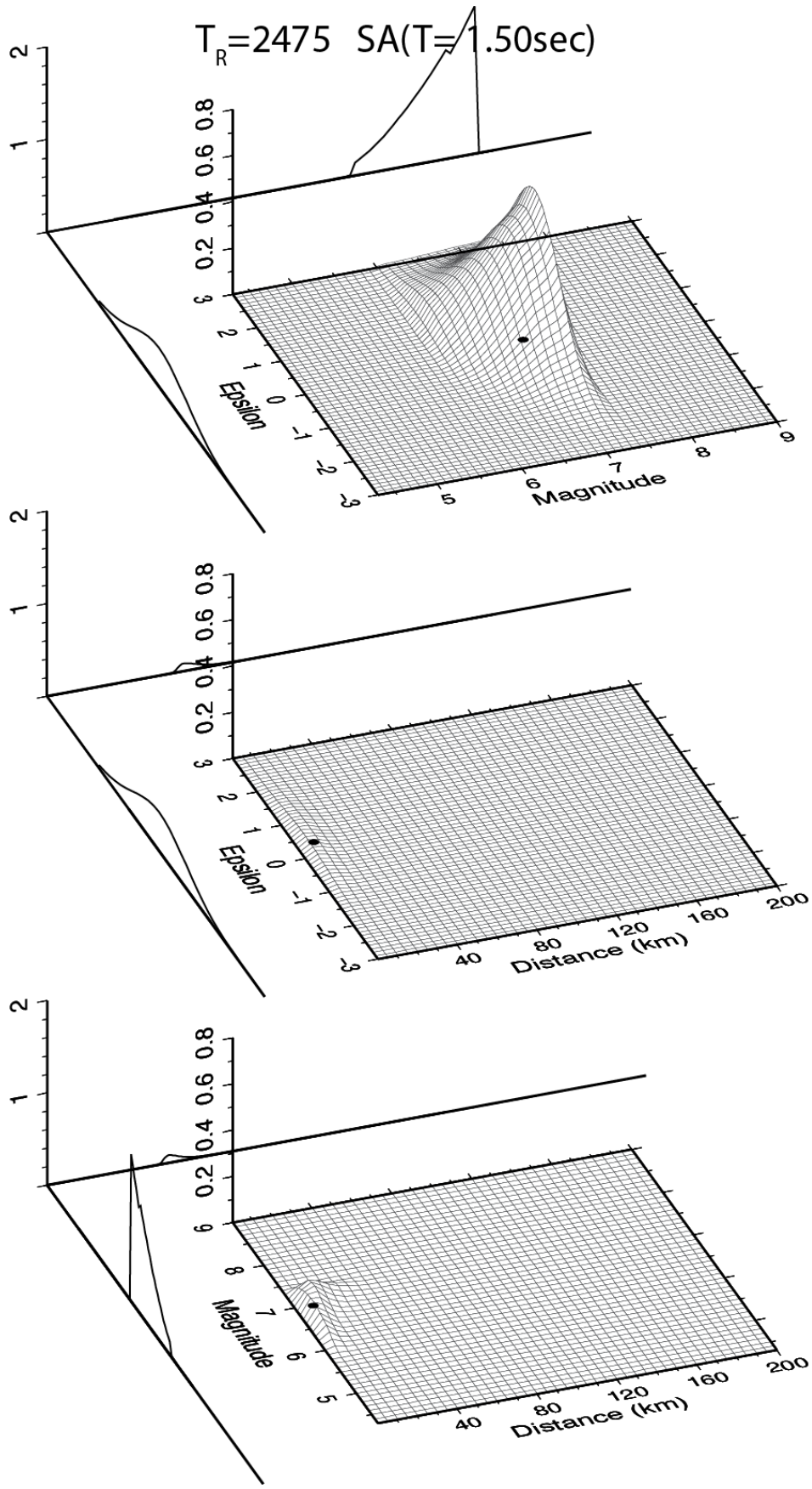

Figure 1.4.2.16. Disaggregation results expressed as contribution to 2475 yr return period hazard for the target site. The central part of each panel shows the joint PDFs for the specific hazard variable pair for SA(T=1.50 sec). On the external axes the marginal PDFs obtained from the joint PDFs area also shown.

1.6 Results

In the present chapter, some results of an interdisciplinary study are reported. In particular, the work represents a contribution to the development of an integrated structural and geotechnical monitoring system on structures located in a medium to high seismic hazard area in Italy. A site specific probabilistic hazard assessment has been carried out in order to provide refined information on relevant earthquakes expressed in terms of magnitude (M), distance (R) and ε that can affect the structure of interest. The uniform hazard spectrum at different structural periods (0.0-2.0sec) for 45, 75, 713, 1463 (Student house) and 120, 201, 1898, 2475 (Campobasso hospital) years return period was disaggregated for Molise region, Italy. For each of the disaggregated variables the shapes of both the joint and marginal probability density functions were studied and the first two modes of M, R and ε have been evaluated. In particular, the analysis showed that for the sites of interest and the selected return periods different design earthquake do exist and must be considered during the engineering structures design.

1.6 References

Ambraseys N.N., Simpson K.A., Bommer J.J.. Prediction of horizontal response spectra in Europe. Earthquake Engineering and Structural Dynamics 1996; 25:371–400.

Barani, S., Spallarossa, D. and Bazzurro, P. (2009). Disaggregation of Probabilistic Ground-Motion Hazard in Italy, Bull. Seismol. Soc. Am. 99,2638–2661.

Bazzurro, P., and Cornell, C. A. (1999). Disaggregation of seismic hazard, Bull. Seismol. Soc. Am. 89,501–520.

Benjamin, J. R., and Cornell, C. A. (1970). Probability, Statistics, and Decision for Civil Engineers, McGraw-Hill, New York.

Caccavale, M., Mancini, M., Convertito, V. and Fabbrocino, G. (2010). Seismic hazard disaggregation in the Molise region, Italy: the case study of Campobasso. 14th Eur. Conf. on Earthq. Eng., paper 1684.

Cornell, C. A. (1968). Engineering seismic risk analysis, Bull. Seismol. Soc. Am. 58,1583–1606.

Convertito V., Iervolino I. & Herrero A. (2009). Importance of mapping design earthquakes: Insights for the Southern Apennines. Bull. Seismol. Soc. Am. 99; 5; 2979-2991; DOI: 10.1785/0120080272

Eurocode 8 (2003). Design of structures for earthquake resistance CEN European Committee for Standardization, Bruxelles, Belgium.

Fabbrocino G., Laorenza C., Rainieri C., Santucci De Magistris F. & Visone C. (2009). Structural and geotechnical seismic monitoring of the new Student House in Campobasso, Italy, Int. Conf. on PBD in Earthquake Geotechnical Engineering - from case history to practice, Tsukuba, Japan.

Gruppo di lavoro Catalogo Parametrico dei Terremoti Italiani (CPTI) (2004). Catalogo Parametrico dei Terremoti Italiani, versione 2004 (CPTI04), INGV, Bologna.

Gutenberg, B. and Richter, C. R. (1944). Frequency of earthquakes in California, Bull. Seismol. Soc. Am. 34,185–188.

Iervolino I., Galasso C., Cosenza E. (2010), REXEL: Computer aided record selection for code base-seimic structural analysis. Bulletin of Earthquake Engineering.8:399-362.

Kramer. Geotechnical earthquake engineering. Prentice-Hall Civil Engineering and Engineering Mechanics Series, Upper Saddle River, NJ: Prentice Hall,| c1996 (1996)

McGuire, R. K. (1995). Probabilistic seismic hazard analysis and design earthquakes: Closing the loop, Bull. Seismol. Soc. Am. 85,1275–1284.

McGuire, R.K., and Arabasz, W.J. (1990). An introduction to probabilistic seismic hazard analysis, in S.H. Ward, ed. Geotechnical and Environmental Geophysics, Society of Exploration Geophysicists, Vol. 1, pp. 333-353.

Meletti, C., Galadini, F., Valensise, G., Stucchi, M., Basili, R., Barba, S., Vannucci, G., and Boschi, E. (2008). A seismic source zone model for the seismic hazard assessment of the Italian territory, Tectonophysics 450,85–108.

Mufti A., Guidelines for Structural Health Monitoring, University of Manitoba, ISIS, Canada, (2001), pp. 1-127, ISBN 0-9689006-0-7.

NTC (2008): Approvazione delle nuove norme tecniche per le costruzioni, Gazzetta Ufficiale della Repubblica Italiana, n. 29 del 4 febbraio 2008 – Suppl. Ordinario n. 30 http://www.cslp.it/cslp/index.php?option=comdocman&task=docdownload&gid=3269&Itemid=10 (in Italian).

Rainieri C., Fabbrocino G. & Cosenza E. (2008). Integrated systems for Structural Health Monitoring, Proceedings of the Fourth European Workshop on Structural Health Monitoring, Cracow, Poland.

Rainieri C., Lanzano G., Fabbrocino G., Santucci de Magistris F. (2010). Structural and Seismic Monitoring of Flexible Retaining Walls: opportunities and challenges, The 10th Int. Conf. CST2010, Valencia, Spain.

Sabetta, F., and Pugliese, A. (1996). Estimation of response spectra and simulation of non stationary earthquake ground motion, Bull. Seismol. Soc. Am. 86,337–352.

de Magistris. Beyond EC8: the new Italian seismic code. Geofizika (2011) Vol.28, pp.65-82

Silkorsky S., Development of a Health Monitoring System for Civil Structures using a Level IV Non-Destructive Damage Evaluation Method, Proceedings of the 2nd International Workshop on Structural Health Monitoring, Stanford, CA, USA, 1999.

Vallèe, M. and Di Luccio, F. (2005). Source analysis of the 2002 Molise, southern Italy, twin earthquakes (10/31 and 11/01), Geophysical Research Letters, 32,L12309.

Capitolo 2

Earthquake Hybrid scenarios for seismic hazard analysis at Campi Flegrei and Vesuvius volcanoes, in Campania region, southern Italy

2.1 Introduction

The magma migration, gas and hydrothermal fluid circulation as well as the induced fracturing phenomena or the local stress variations, are the principal causes of the earthquake in the volcanic areas.

The Campania region (southern Italy) is characterised by two different volcanic areas, Campi Flegrei caldera (Fig.2.1.1) and Mt. Vesuvius (Fig.2.1.2) that are both located in the same seismogenic zone (Fig.2.1.3) as individuated and adopted by INGV (Meletti et al., 2008). These areas represent a very particular interesting case-study for a seismic hazard analysis because Campi Flegrei and Mt. Vesuvius lies in high densely populated areas. For these areas the possible occurrence of a moderate seismic event represents a threat for the inhabitants and for the civil and/or industrial infrastructures. A seismic hazard analysis in these high dangerous zones is the first step for the seismic hazard mitigation.

The Campi Flegrei area extends about 400Km^2 on the west of the Napoli town and it is characterised by several active volcanoes. The main recent event in the area was an eruption leading to the formation of the Mt. Nuovo cone (1538). The eruption was preceded by 40 years of seismic activity that increased in the last 2 years before the main event (Convertito and Zollo, 2011).

In the last 40 years the volcanic activity was characterised by two main ground uplift episodes, in the 1970-72 and 1982-84, accompanied by intense microseismic activity. In the first period about three thousand shallow microearthquakes were recorded (Corrado et al. 1976). During the second one more than 10,000 shallow-depth microearthquakes with magnitudes less than 4.2 were recorded. As consequence of a persistent seismic activity and to preserve the population from possible structural failure of buildings, the local authorities evacuated the large districts of the town of Pozzuoli, located near the coast.

Mt. Vesuvius, the second study site, is located on the east side of Napoli town. This volcano is still active and the last eruption occurred in 1944. The Mt. Vesuvius is considered the most dangerous volcano in the world due to the high number of people living on its mountainside (approximately 700,000). The seismicity of the area is characterised by few hundreds shallow microearthquakes per year (about $M_L < 3.0$ and 5

Km of depth), prevalently localized beneath the crater (Convertito and Zollo, 2011). The main event recorded in the last years occurred on October 9th, 1999 and it was clearly felt from the population in the surround area. The magnitude of the event was low (M_L 3.6) but enough to cause panic in the population and attract the media attention.

The estimation of the hazard and the possible damage expected in a future eruption at Mt. Vesuvius and Campi Flegrei play a key role for the hazard mitigation in a strong populated area.

In the framework of the SPeeD[1] project a hybrid probabilistic-deterministic hazard analysis (Convertito et al., 2006) was performed for the Mt. Vesuvius and Campi Flegrei areas.

[1] http://speed.pi.ingv.it/

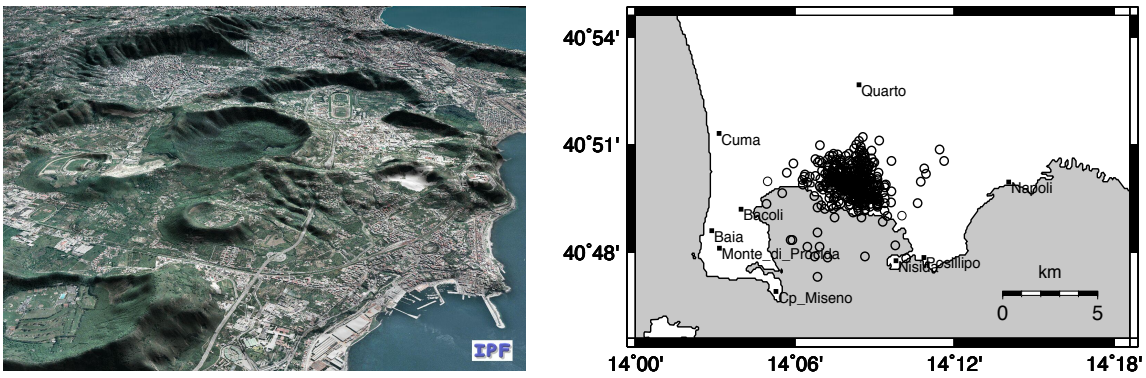

Figure 2.1.1. Earthquake source areas. Left panel, Digital Terrain Model of Campi Flegrei (http://ipf.ov.ingv.it/viste.html). Bottom Right panel, the Campi Flegrei area. Black circles represent the location of the earthquakes retrieved from the CPTI04 catalog (Gruppo di lavoro, 2004).

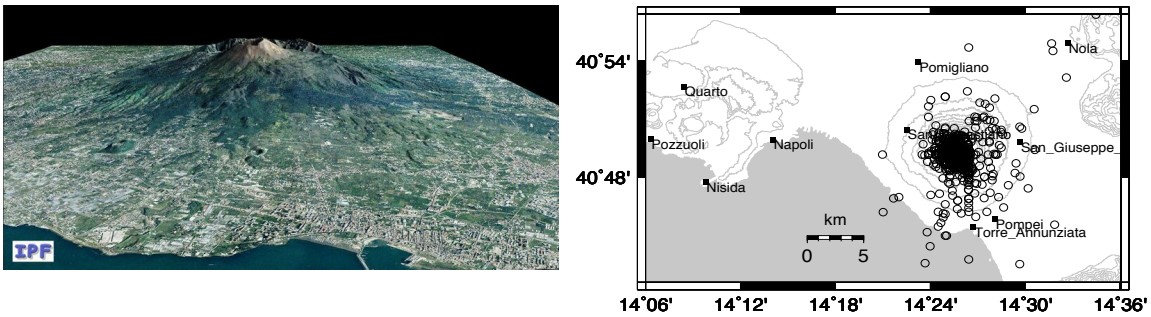

Figure 2.1.2. Earthquake source areas. Left panel, Digital Terrain Model of the Mt. Vesuvius (http://ipf.ov.ingv.it/viste.html). Right panel, the Mt. Vesuvius area. Black circles represent the location of the earthquakes retrieved from the CPTI04 catalogue (Gruppo di lavoro, 2004).

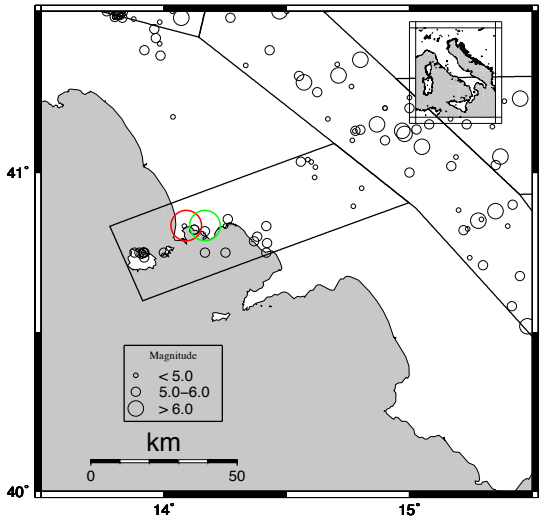

Figure 2.1.3. Seismic source zones configuration for the target zone. Location of the target area used in the analysis is identified by red and green circle for Campi Flegrei and Mt. Vesuvius, respectively. Black circles, whose radius is proportional to magnitude, represent the location of the earthquakes retrieved from the CPTI04 catalogue (Gruppo di lavoro, 2004).

2.2 Hybrid Seismic Hazard Analysis

The result of a Probabilistic Seismic Hazard Analysis (PSHA) is the frequency E(A≥A0) /probability of exceedance of a given ground motion parameter (Peak Ground Acceleration (PGA), Peak Ground Velocity (PGV), Spectral Acceleration (SA)) for a given time t, as shows in Cap.1. Due to the integral nature of PSHA, each value represents the combination of all the earthquakes of different sizes occurring in different seismic source zones with different probabilities of occurrence. As reported in the Cap.1 the PSHA is based on the Ground Motion Prediction Equations (GMPEs) that allows estimating PGA-V or SA as a function of the source, propagation medium and local site geology.

The application of the classical PSHA is not obvious when a single causative fault and an associated maximum earthquake is considered as the threat for the site of interest. One problem is represented by the formulation of a recurrence relationship and the computation of the activity rate. The hybrid approach is an original method that combines the probabilistic and the deterministic approaches in the hazard analysis (Convertito et al., 2006). This technique is designed to overcome some of the limitations inherent in the deterministic and Cornell (1968) classical approaches when a single causative fault is considered for a scenario-like hazard analysis. The classical PSHA approach is represented by the hazard integral:

$$E\,(A > A_0) = \int_{M_0}^{M_S} \int_{R_0}^{R_S} \int_{\varepsilon_0}^{\varepsilon_S} \alpha\,(m) P[A \geq A_0 | m, r, \varepsilon] f_M(m) f_R(r) f_\varepsilon(\varepsilon) dm dr d\varepsilon \qquad (2.2.1)$$

Where $\alpha(m)$ represents the seismicity rate from the seismic catalogue (CPTI04), $P[A \geq A_0|m,r,\varepsilon]$ is the conditional probability of exceedance, obtained through GMPEs (Fig.2.2.1). The $f_M(m)$ represents the Probability Density Function (PDF) on the magnitude as a function of *b-value*, M_{min} and M_{max} as shown in Figure 2.2.2. The $f_R(r)$ is the PDF on the distance and depends on the geometry of the source. The $f_\varepsilon(\varepsilon)$ represents the PDF accounting for the ground motion variability (ε_{min}, ε_{max}).

When a single fault is taken into account the (Eq.2.2.1) is modified in:

$$E\,(A > A_0) = \alpha_c \int_{M_c}^{m_c+\Delta m_2} \int_{\varepsilon_0}^{\varepsilon_s} P_a[A(m,\bar{r}) \geq A_0 | m,\bar{r},\varepsilon] f_{M_c}(m) f_\varepsilon(\varepsilon) dm d\varepsilon \qquad (2.2.2)$$

Where α_c represents the seismicity rate of the "characteristic earthquake", P[A≥A_0|m,$\bar{r}$,ε] is the conditional probability of exceedance, obtained through ground motion simulations (Fig.2.2.3). The $f_{Mc}(m)$ is the PDF of the "characteristic earthquake" (Fig.2.2.2).
The seismic rate for the "characteristic earthquake" (α_c) can be expressed as (Young and Coppersmith, 1985):

$$\alpha_c = \alpha_{nc} \frac{\beta \Delta m_2 e^{-\beta(m_{max}-m_0-\Delta m_1-\Delta m_2)}}{1 - e^{-\beta(m_{max}-m_0-\Delta m_2)}} \qquad (2.2.3)$$

with

$$\alpha_{nc} = \frac{\mu A_f \tilde{S}[1 - e^{-\beta(m_{max}-m_0-\Delta m_2)}]}{K M_0^{max} e^{-\beta(m_{max}-m_0-\Delta m_2)}} \qquad (2.2.4)$$

and

$$K = \frac{b10^{-c\Delta m_2}}{c-b} + \frac{be^{\beta\Delta m_1}(1 - 10^{-c\Delta m_2}]}{c} \qquad (2.2.5)$$

Where $\tilde{S}$ represents the slip rate, A_f is the fault area, μ represents the shear modulus, M_0^{max}represents the seismic moment, K is a constant and $\beta = b\ln(10)$ with b represents the slop of the regression equation. The variables m_{max} and m_{min} are the maximum and minimum magnitude of interest; the parameters Δm_1 and Δm_2 represent two intervals, respectively, below and above the magnitude level m_c that is considered as the characteristic earthquake magnitude (Fig. 2.2.3)

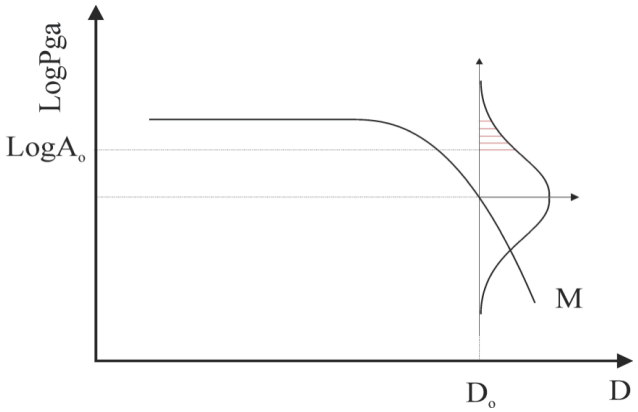

Figure 2.2.1. Variability of Ground Motion Parameter value predicted by Ground Motion Predictive Equation.

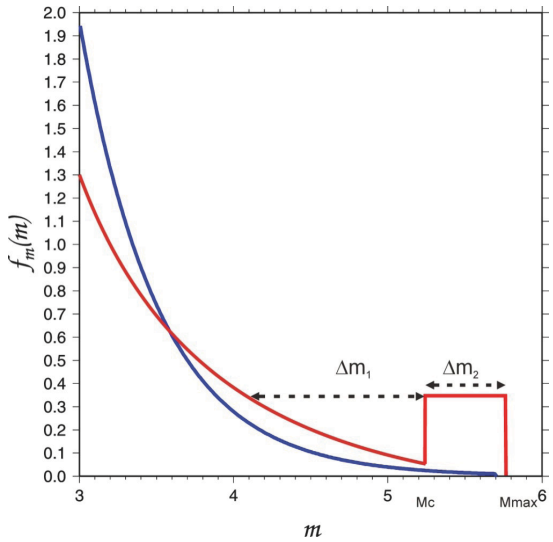

Figure 2.2.2. Probability Density Functions for magnitude.

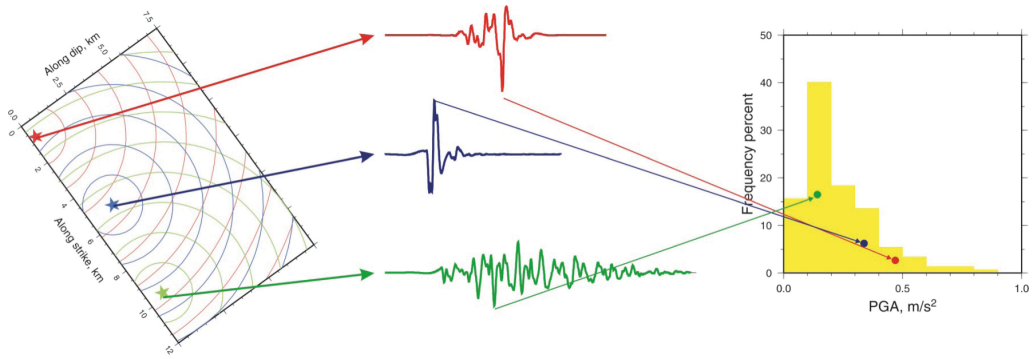

Figure 2.2.3. Distribution of Peak Ground Acceleration (PGA) for different ground motion simulation. Each colour represents a different simulation

The hybrid approach uses the "characteristic-earthquake" (Fig.2.2.2) model to compute the probability of occurrence of earthquakes (Schwartz and Coppersmith, 1984) and the approach proposed by Youngs and Coppersmith (1985) to compute the activity rate. The characteristic-earthquake model is based on the observation that during repeated rupture

episodes occurring on the same fault (or fault system), some characteristics, like fault geometry, source mechanism, and seismic moment, kept approximately constant over a large timescale. Under this hypothesis the PDF $f_{Mc}(m)$ is:

$$f_{M_c}(m) = 0 \qquad \begin{cases} \text{for } \mathrm{m} < \mathrm{m}_0 \\ \text{for } \mathrm{m} > \mathrm{m}_{\max} \end{cases} \tag{2.2.6}$$

or

$$f_{M_c}(m) = \begin{cases} \dfrac{\beta e^{-\beta(m - m_{0_2})}}{(1 - e^{-\beta(m_{max} - m_0 - \Delta m_2)})(1 + C)} \\ \dfrac{\beta e^{-\beta(m_{max} - m_0 - \Delta m_1 - \Delta m_2)}}{(1 - e^{-\beta(m_{max} - m_0 - \Delta m_2)})(1 + C)} \end{cases} \begin{cases} \text{for } \mathrm{m}_0 \le \mathrm{m} \le \mathrm{m}_c \\ \\ \text{for } \mathrm{m}_c = \mathrm{m} \le \mathrm{m}_{\max} \end{cases} \tag{2.2.7}$$

Where C is given by:

$$C = \frac{\beta e^{-(m_{max} - m_0 - \Delta m_1 - \Delta m_2)}]}{1 - e^{-\beta(m_{max} - m_{0-} \Delta m_2)}} \Delta m_2 \tag{2.2.8}$$

For both equations (2.2.1 and 2.2.2) $E(A>A_0)$ represents the frequency of exceedance or the probability of exceedance of a given threshold value A_0, under the hypothesis of Poissonian model for the earthquake recurrence (Eq.1.2.1).

The hybrid methodology allows overcoming the principal limitations of both the deterministic and classical probabilistic approach (Cornel, 1968) when a single fault is considered. The recurrence of a characteristic earthquake inferred by deterministic approach and seismic source parameters (radiation pattern, the fault geometry, and the directivity effect) inferred by Probabilistic approach can be account at same time.

The result of the hybrid approach is to compute the hazard curve for a fixed source once the magnitude m_c for the characteristic earthquake has been selected.

To determinate the level reached by a selected strong ground motion parameter and to evaluate the associated exceedance probability, a set of synthetic seismogram was generated (see cap.2.2.1 for more detail) for grid of stations to obtain a distribution of value for the selected parameter at each station (Fig.2.2.3).

2.2.1 Ground Motion Simulations Technique

Different methodology was developed in the last years to produce realistic strong ground motion simulations. This methodology can be classified in two main branches:

- Dynamic models
- Kinematic models

The dynamic models are complex; the specification of physical force is needed, and it is rarely used to generate synthetic seismogram Generally, dynamic model are of great complexity and required an expensive computational cost. The kinematic models represent the earthquake rupture process at fixed point over the fault. The different representations of the rupture process on an extended fault allows to classified the kinematic approaches in four groups:

- Integral
- Composite
- Stochastic
- Hybrid

The first approach resolves the integral in the representation theorem to calculate the radiated wave field. To perform this method the computation of Green's functions in a dense grid of point that cover the selected fault plan is required.
The composite method is characterized by few sub-sources or sub-events and the result wave field is represented by the sum of each of them opportunely filtered to obtain the proper seismic moment and spectral shape.
The stochastic approach is based on the observation that the accelerograms of the strong shaking appears random and incoherent. The high frequency is reproduced in a purely stochastic way and isn't based on physical background.
The hybrid technique is represented by a combination of the different approach proposed. The combination was performed usually without related the different approaches used.

To generate synthetic seismograms for the Campi Flegrei and Vesuvius volcanoes areas a hybrid methodologies that related low- and high-frequency model was used (Gallovič and Brokěsová, 2007). This approach was performed overlapping the results from integral method for low frequency (up to f_2) and composite method for high frequency (from f_1) as shows in figure 2.2.1.1. This methodology was used to perform a full waveform simulation in 1D crustal model (Tab. 2.2.1), using a finite fault model with heterogeneous rupture description.

Concerning the low frequency (integral approach), the representation theorem is applied, assuming radial slip pulse propagation with relatively simple slip velocity function; the slip at a fault point is obtained summing up slips of all the sub-sources.

For the high frequency part (composite approach) the sub-sources are treated as individual point sources with isotropic source function (Brune, 1970), time-shifted according to their rupture time; their corner frequencies are inverse proportional to the length of the fault.

For the overlapping zone (between f_1 and f_2 in figure 2.2.1.1, to simulate smooth transition between deterministic and chaotic styles of faulting, a weighted summation of the synthetics is applied in the cross-over frequency band. The bounding frequencies are $f=1/2\tau$ and $f=2/\tau$, being τ the slip pulse duration (Gallovič and Brokěsová, 2007). The Green's functions were computed by the discrete wave numbers technique (Bouchon, 1981) in a layered crustal model (Tab. 2.2.1).

This approach is based on the decomposition of the faulting process into sub-sources (Fig.2.2.1.2). The rupture nucleation points were distributed in the centre and in the deepest part of the fault, according to hypocentral determinations of the selected main event.

A family of synthetic acceleration records is obtained by simulating a large number of rupture scenarios for a given fault plane and from each it was possible to obtain the distribution of different structural periods. Each rupture scenario has a different rupture nucleation point, final slip distribution and rupture velocity. Heterogeneous slip on the fault is computed according to the *k-square* model of Hanks (1982) and Herrero and Bernard (1994). Each computed slip distribution is such that the total seismic moment corresponds to that of the considered characteristic earthquake.

The maximum number of rupture scenarios to be simulated was chosen after having verified that no substantial differences in the estimation of mean values and standard deviations of the selected ground motion parameter were observed for each receiver, by

considering a larger number of simulations. For each rupture scenario we computed synthetic accelerograms on a regular grid of 865 receivers located in the selected area (Figure 2.2.1.3). The spacing between adjacent receivers was 1 km and the maximum frequency content of simulated accelerograms was 25 Hz.

The synthetic data was confronted with different Ground Motion Prediction Equations as a validation test (Figure. 2.2.1.4).

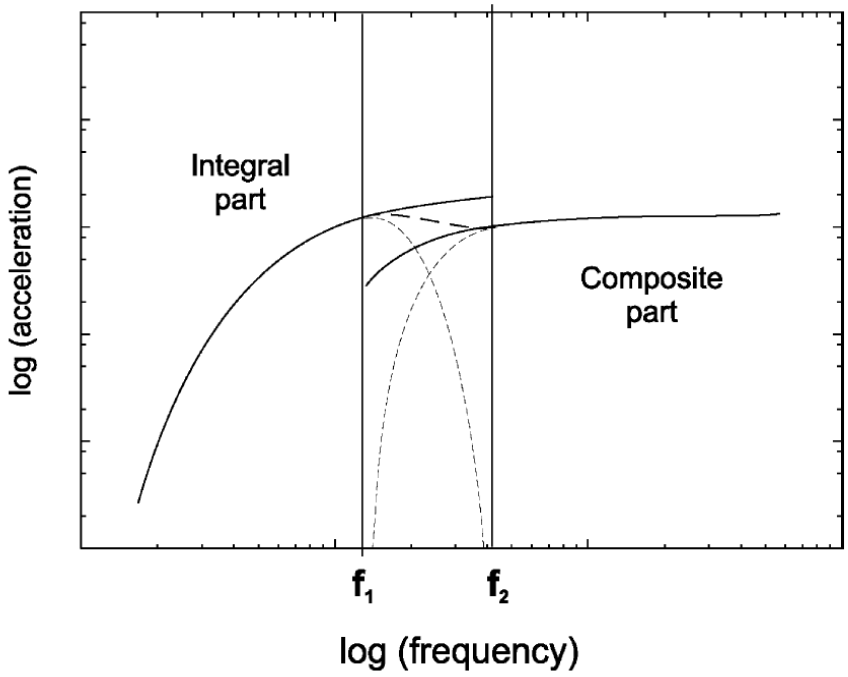

Figure 2.2.1.1. A sketch of the hybrid combination of the integral and composite synthetics (bold solid lines) in the frequency domain. In the cross-over frequency zone (between bounding frequencies f1 and f2) the synthetics are multiplied by weighting functions sin2(x) and cos2(x), with x = (π/2)((f − f1)/(f2 − f1)) (thin dashed lines) and summed up (bold dashed line). This operation is performed for both the real and imaginary parts of the spectrum. Note that the possible step in spectral levels in the cross-over zone depends mainly on the mutual amount of directivity in the integral and composite models. Moreover, the transition could be smoother due to propagation effects and/or may be masked by the oscillatory character of the Fourier spectra. Extracted from (Gallovič and Brokešová, 2007).

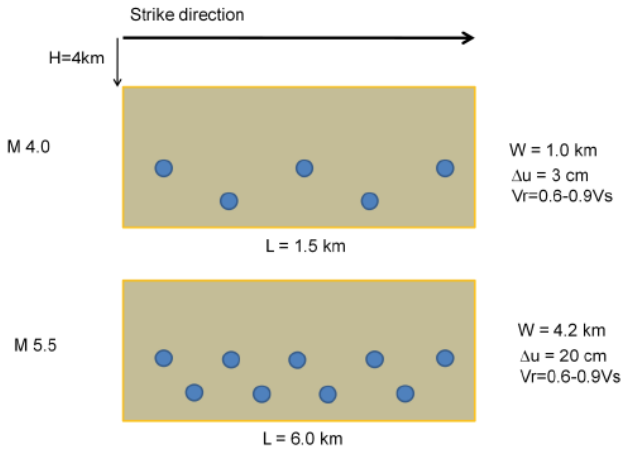

Figure 2.2.1.2. Distribution of nucleation points on the fault plan for magnitude 4.0 (top) and magnitude 5.5 (bottom). between adjacent receivers was 1 km and the maximum frequency content of simulated accelerograms was 25 Hz.

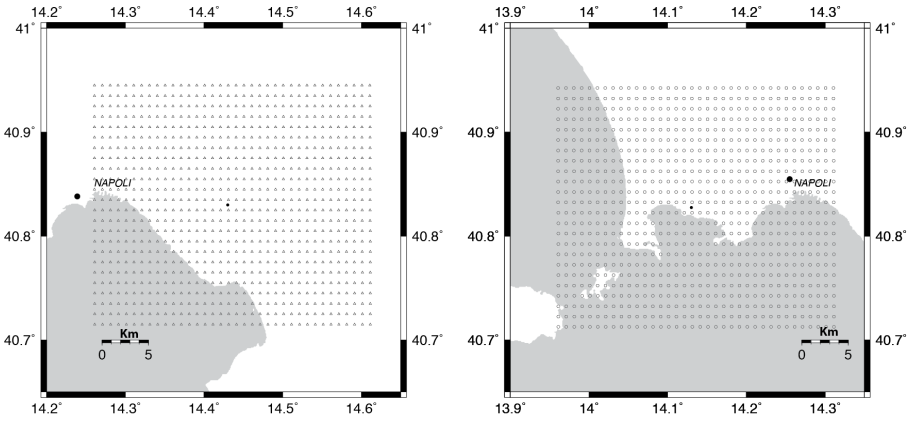

Figure 2.2.1.3. Distributions of stations (black circle) for synthetic seismogram calculation. For each target zone (Campi Flegrei on the left and Vesuvius on the right) a grid of 865 was considered

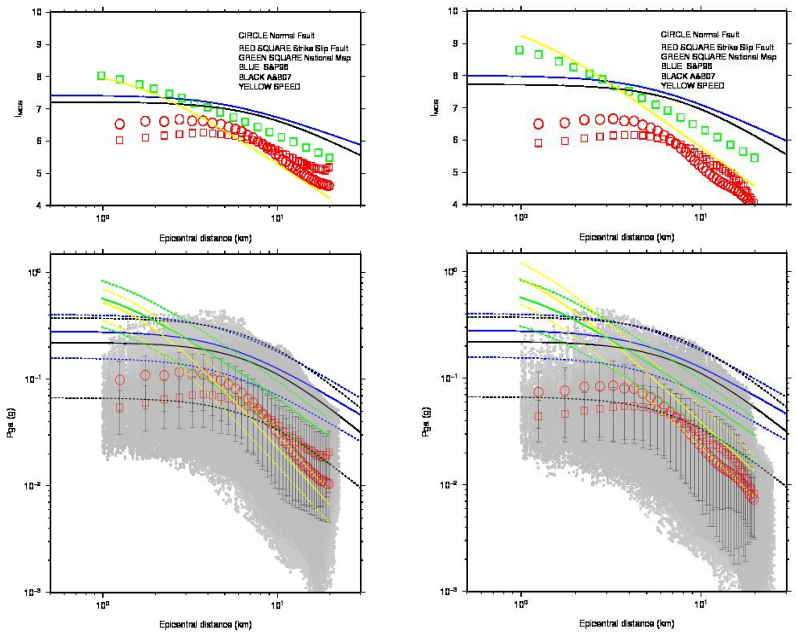

Figure 2.2.1.4. Analysis of synthetic seismogram and GMPE.

Table 2.2.1.1. Velocity model and characteristic for Vesuvius (top) and Campi Flegrei (bottom). Retrieved from Del Pezzo et al. (2006) and Zollo et al. (2008).

Vesuvius

z(km)	Vp(km/s)	Vs(km/s)	ρ(g/cm^3)
0.0	1.6	0.8	2.0
1.0	3.0	1.6	2.3
2.0	4.5	2.4	2.6
5.0	6.0	3.2	2.9

Campi Flegrei

z(km)	Vp(km/s)	Vs(km/s)	ρ(g/cm^3)
0.0	1.6	0.47	2.0
0.6	3.5	2.06	2.4
2.7	4.8	3.0	2.6
3.4	5.4	3.4	2.8
4.0	6.0	3.53	2.9
7.5	6.3	3.71	3.0

2.3 Hybrid seismic hazard maps

For both Mt Vesuvius and Campi Flegrei volcanoes the "characteristic earthquake" (See cap. 2.2) model was applied to a set of hypothetical causative faults corresponding to M 4.0 and M 5.5 recognized as maximum magnitude earthquake. The details about the source mechanism and the values of parameters (Eq. 2.2.7) for the "characteristic earthquake" are reported in Tab2.3.1.

Table2.3.1: Parameterization used to resolve the probability density function of magnitude for the characteristic earthquake (Eq.2.2.7) (Top). The values for Dip (δ) and Rake (λ) for the considered fault mechanism (Bottom).

M_c	M_{min}	Δm_1	Δm_2	A_f (km^2)
4.0	3.0	0.5	0.5	1
5.5	3.0	0.5	0.5	25.2

Mechanism	δ (°)	λ(°)
Normal Fault	45	90
Reverse Fault	45	-90
Strike Slip	90	0

The probability of occurrence of earthquakes (Schwartz and Coppersmith, 1984) was calculated and the activity rate was computed using the approach proposed by Youngs and Coppersmith (1985).

The Gallovič and Brokešhová (2007) (See Cap.2.2.1 for more details) hybrid simulation methodology was used to obtain synthetic seismograms that were relevant for the estimation of earthquake effects, the distance and azimuthal distribution of ground motion parameters and their expected ranges of variability.

For each single fault, the fault dimensions, the average slip-rate values and the b-value of the region where the fault is embedded were used as parameter of the Youngs and Coppersmith (1985) method to define the value of activity rate. The surface projection of the faults identified at both Campi Flegrei and Mt Vesuvius areas are shown in Figure 2.3.1. For M 4.0 earthquake, a 1.0km^2 fault area has been used while for M 5.5 earthquake the fault area was 25.2km^2. Concerning the slip-rate and b-values the adopted

parameterization has been retrieved from the DISS[1] database and the seismic catalogue (CPTI04), respectively, and is reported in Table 2.3.2.

Table2.3.2: Parameterization used for computing the return periods for the two selected magnitude values.

	Numerical		Geological (DISS[1])	
Slip-rate (mm/yr)	**Avg**	**Max**	**Min**	**Max**
	1.12	**1.542**	**0.4**	**0.6**
	Hyst. Comp. (CPTI04)	Stat. Comp. (CPTI04)	Instrumental Seismicity Mt. Vesuvius	Instrumental Seismicity Campi Flegrei
***b*-value**	**1.04**	**0.66**	**2.0**	**1.05**

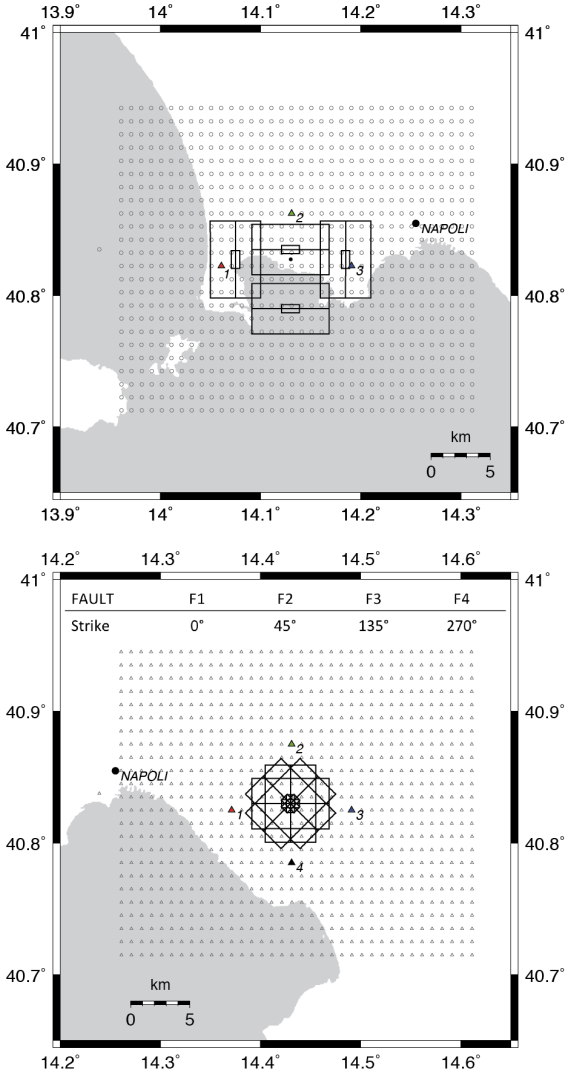

Figure 2.3.1: surface faults projections used in the simulation study at Campi Flegrei (Top panel) and Vesuvius (Bottom panel). The circles represent the virtual stations at which are calculated synthetic seismograms

[1] http://diss.rm.ingv.it/diss/

For each magnitude, different return periods were selected to perform the analysis. In the present thesis are reported the results of seismic hazard calculated for Tr=20000yrs for M 5.5 with normal/reverse and strike slip mechanism, corresponding to a probability to be exceeded of 0.25% in 50yrs.

For each single fault at both Campi Flegrei and Mt. Vesuvius areas, was generated a database of accelerometric recordings obtained by varying rupture velocity, nucleation point location and final slip map from which it were possible to obtain the distribution of the PGA (Peak Ground Acceleration) and Spectral Acceleration (SA(T)) for structural periods T=0.3sec and T=1.0sec, at a set of 865 sites in the area.

Deterministic distributions of simulated ground-motion values have been used to calculate hybrid scenario hazard maps for the selected faults.

2.3.1 Mt. Vesuvius area

The result of the hazard analysis for the Mt. Vesuvius is reported in terms of mean peak ground parameters (PGA, PGV and Sa) and associated CoV (Fig. 2.3.1.1-6) and hazard maps (Fig. 2.3.1.7-9) for an event of magnitude 5.5, four different strike values and for Direct/Revers (DR) and Strike Slip (SS) mechanism.
The CoV coefficient is defined as:

$$CoV = 100\left(\frac{STD}{\overline{Par}}\right) \qquad (2.3.1.1)$$

Where STD represents the standard deviation of the selected parameter distribution and $\overline{\text{Par}}$ represents the mean value of this parameter.
The deterministic maps represent the spatial distribution of mean values calculated for 81 different scenarios. Each scenario was obtained varying the nucleating point on fault plane, the rupture velocity and the final slip map.
The CoV (Eq.2.3.1.1) map has to be discussed together with the deterministic map. The regions where the CoV is higher indicate that the PGA values can vary strongly, depending on how the rupture nucleates, propagates and stops during the faulting process.
As an example, in Figure 2.3.1.1 (Top) the distribution of PGA in unit of g at VS area for M 5.5 and normal fault mechanism are shown. The distributions of CoV values at VS area for the PGA and the four selected fault was also reported (Figure 2.3.1.1, bottom).
Figure 2.3.1.5 shows the distributions of Sa(T=0.3s) at VS area for the four selected fault. Figure 2.3.1.5 (Top) reports the distribution of Sa(T=0.3s) in unit of g at VS area for M 5.5. The strike slip fault mechanism is shown and the distributions of CoV values at VS area for the PGA and the four selected fault are also reported (Bottom).
From the pictures is possible to note the complexity of the different slip map used to generate the synthetic seismogram. The maps are not isotropic, but show a directivity effect particular for finite faults.
The hybrid scenario hazard maps for the selected faults (Fig. 2.3.1.7-9) were calculated from the deterministic distributions of simulated ground-motion values.

It can be observed that, due to the adopted methodology, hybrid hazard maps show a quite complex pattern with respect to the classical hazard maps that generally feature symmetry in the ground motion distribution. In fact, hybrid maps can account for focal mechanism, for hanging-wall versus foot-wall effect and directivity effects that cannot be accounted for in the classical approach.

Figures (2.3.1.7-9) shows the PGA and SA(T=0.3s) and Sa(T=1.0s) for normal (Top) and strike slip (Bottom) fault mechanisms having a probability of 0.25% to be exceeded in 50 years (Standard buildings) respectively or 0.5% to be exceeded in 100 years (Strategic infrastructure: bridges, dams).

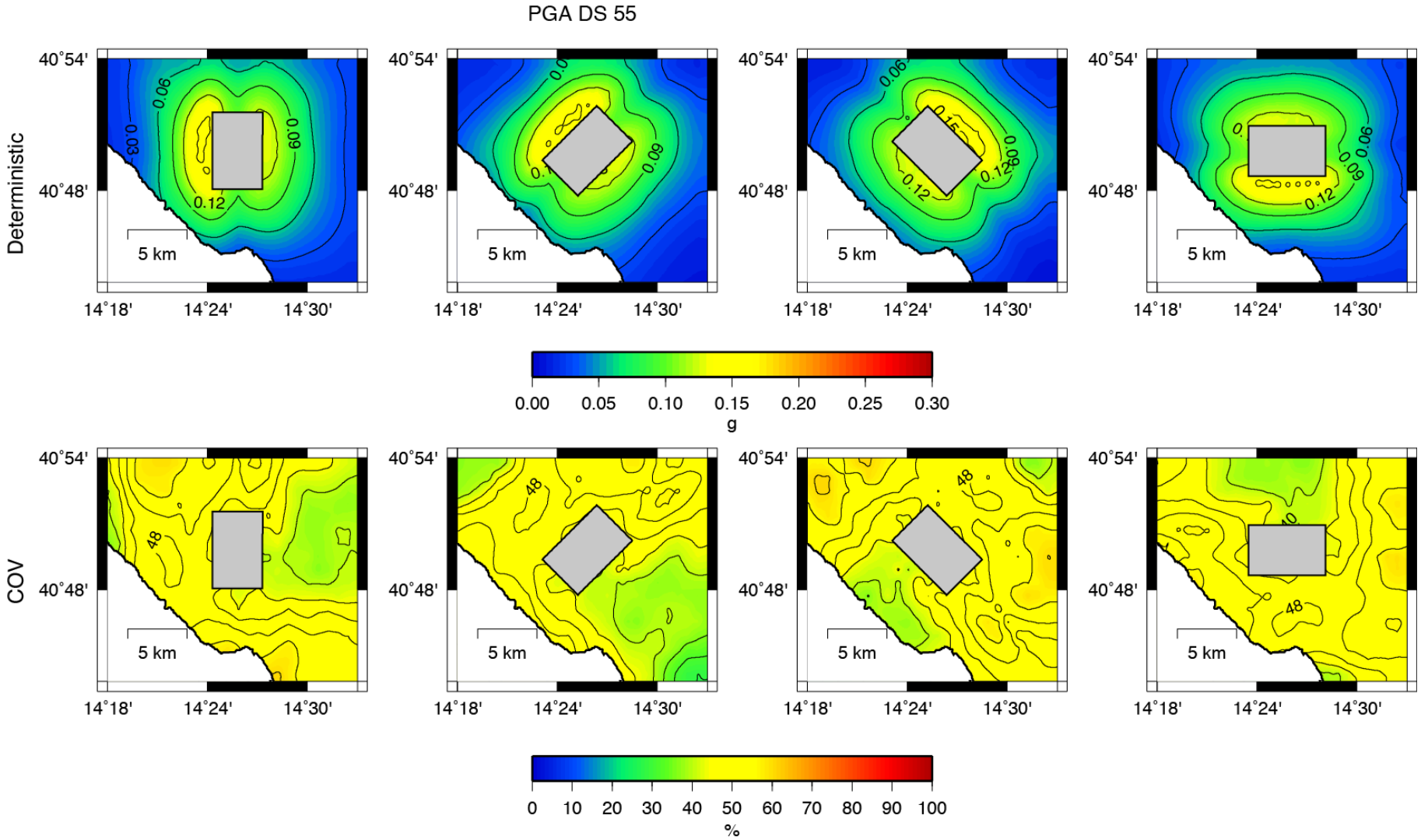

Figure 2.3.1.1. Distribution of PGA in unit of g at VS area for M 5.5 and normal fault mechanisms for 4 strike values (0°, 45°, 135° and 270°) (Top). CoV map of PGA (See text for more details) at VS area for M 5.5 and normal fault mechanisms for 4 strike values (90°, 180°, 270° and 360°) (Bottom).

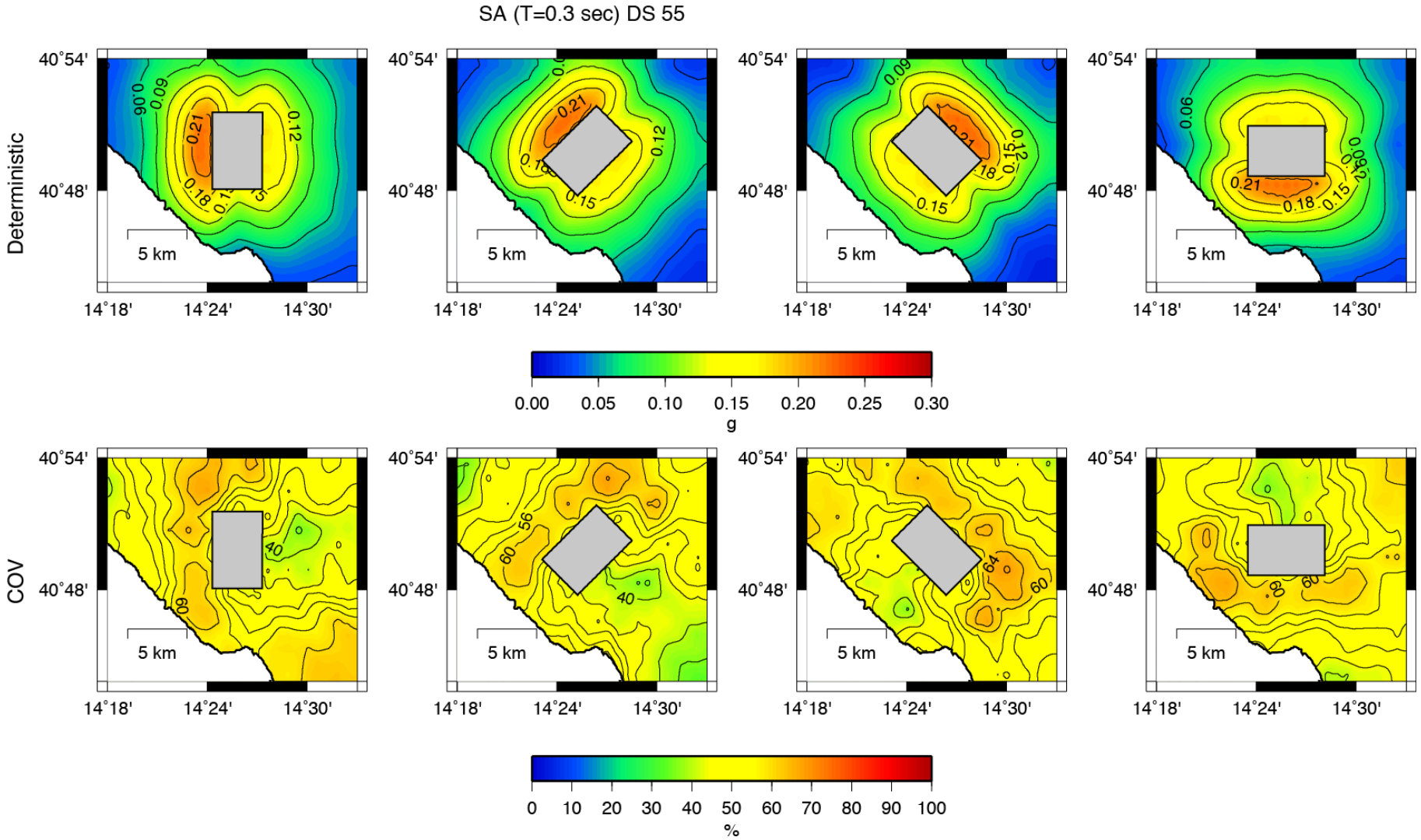

Figure 2.3.1.2. Distribution of Sa(T=0.3s) in unit of g at VS area for M 5.5 and normal fault mechanisms for 4 strike values (0°, 45°, 135° and 270°) (Top CoV map of PGA (See text for more details) at VS area for M 5.5 and DS fault mechanisms for 4 strike values (90°, 180°, 270° and 360°) (Bottom).

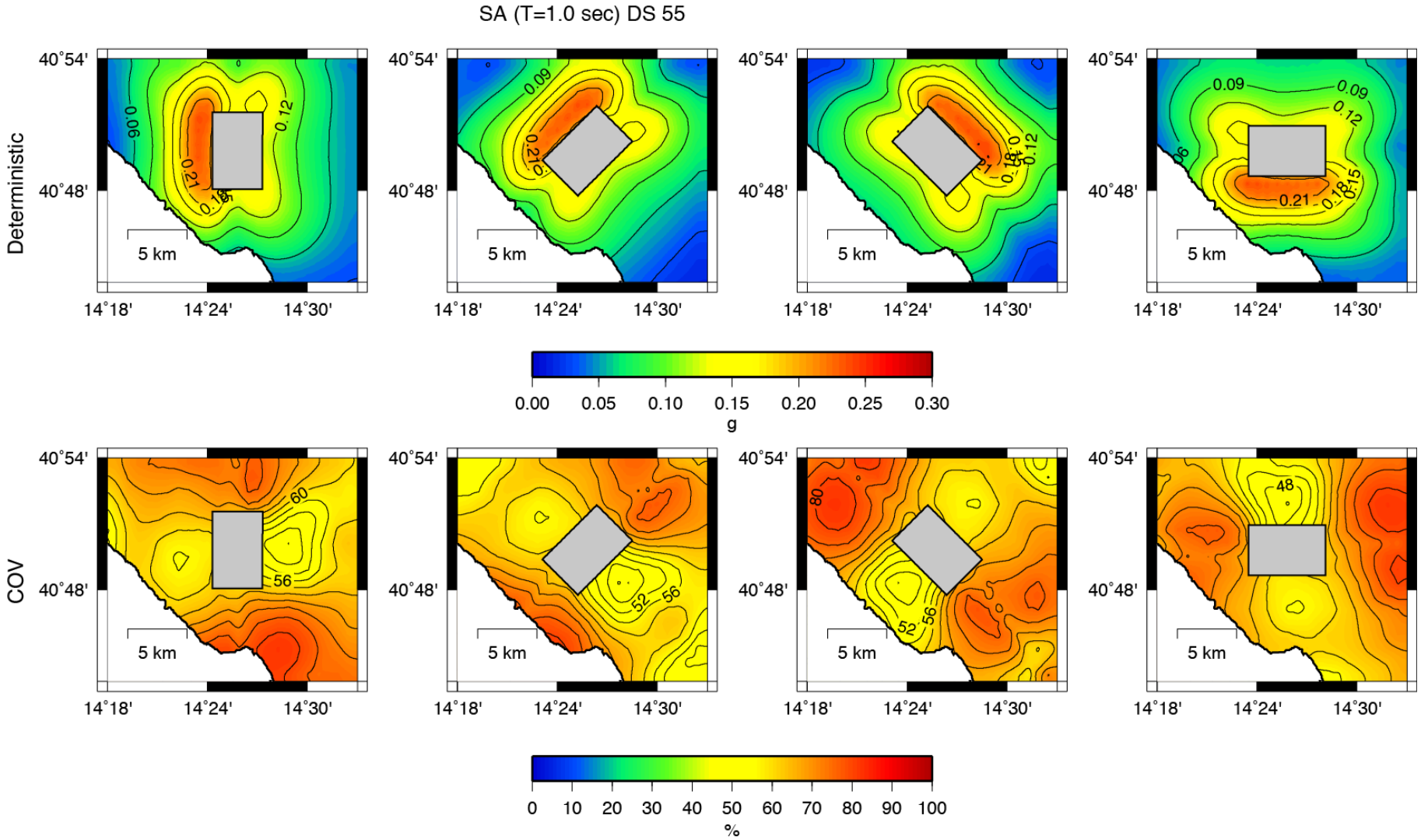

Figure 2.3.1.3. Distribution of Sa(T=1.0s) in unit of g at VS area for M 5.5 and normal fault mechanisms for 4 strike values (0°, 45°, 135° and 270°) (Top). CoV map of PGA (See text for more details) at VS area for M 5.5 and normal fault mechanisms for 4 strike values (90°, 180°, 270° and 360°) (Bottom).

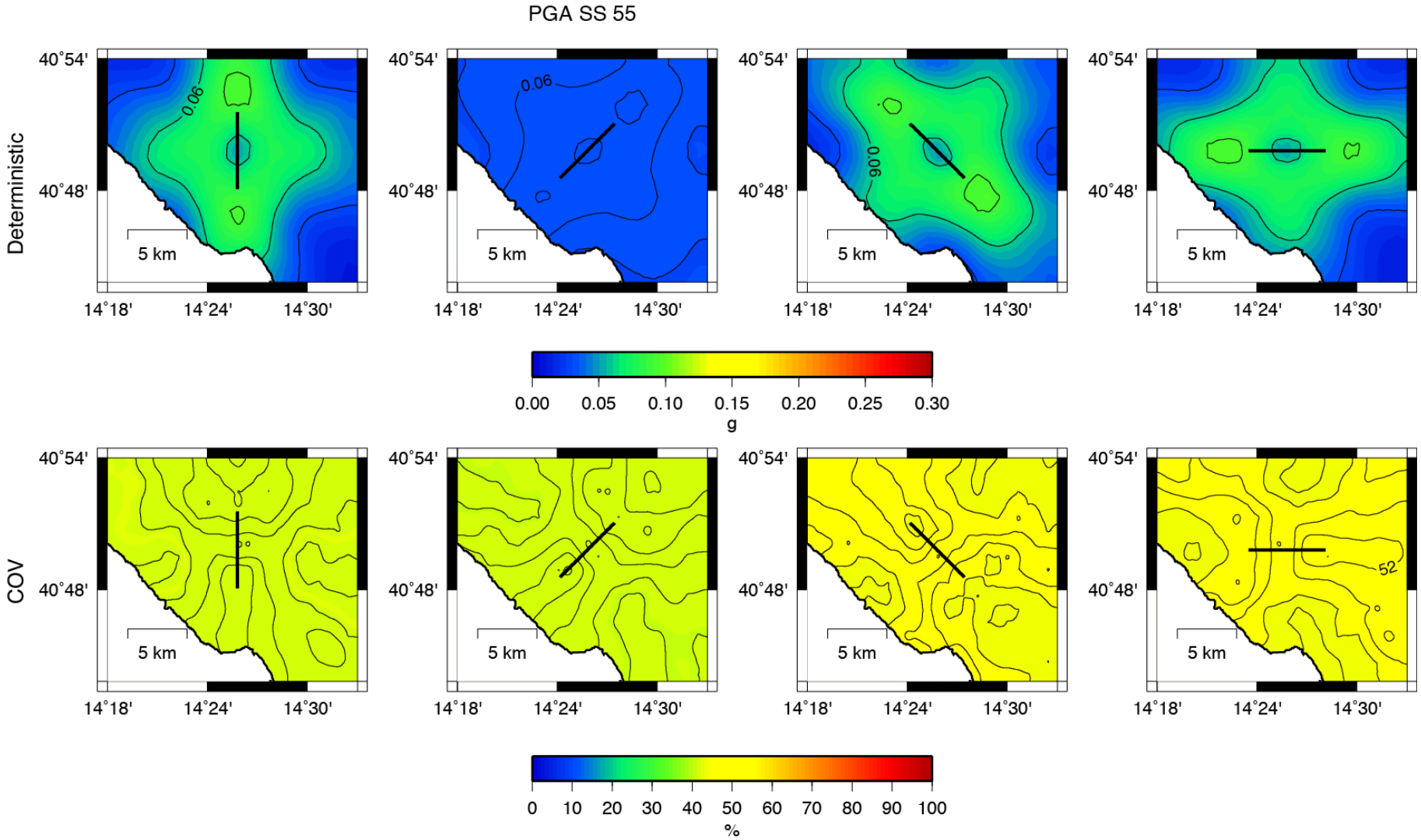

Figure 2.3.1.4. Distribution of PGA in unit of g at VS area for M 5.5 and strike slip fault mechanisms for 4 strike values (0°, 45°, 135° and 270°) (Top). CoV map of PGA (See text for more details) at VS area for M 5.5 and strike slip fault mechanisms for 4 strike values (90°, 180°, 270° and 360°) (Bottom).

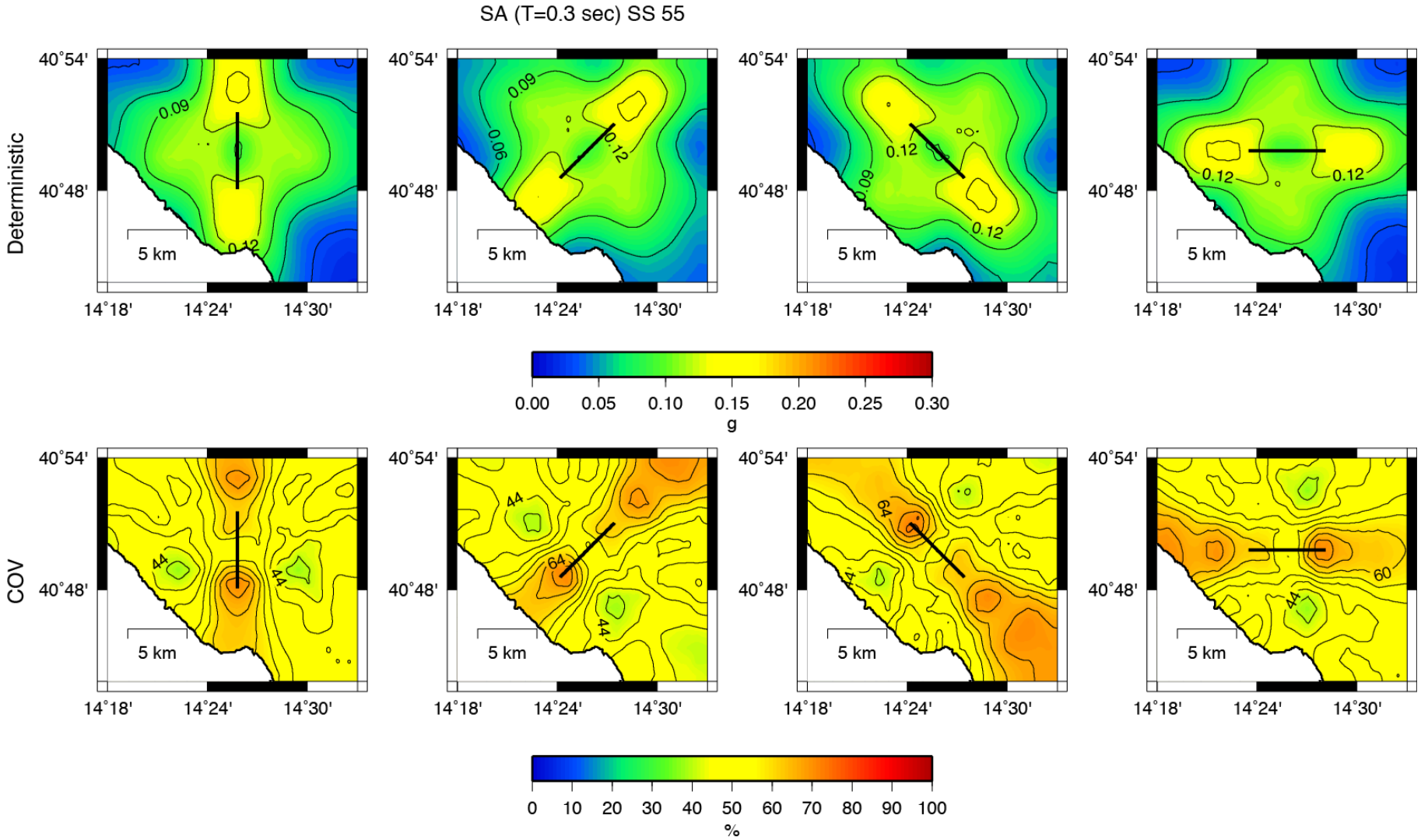

Figure 2.3.1.5. Distribution of Sa(T=0.3s) in unit of g at VS area for M 5.5 and strike slip fault mechanisms for 4 strike values (0°, 45°, 135° and 270°) (Top). CoV map of PGA (See text for more details) at VS area for M 5.5 and strike slip fault mechanisms for 4 strike values (90°, 180°, 270° and 360°) (Bottom).

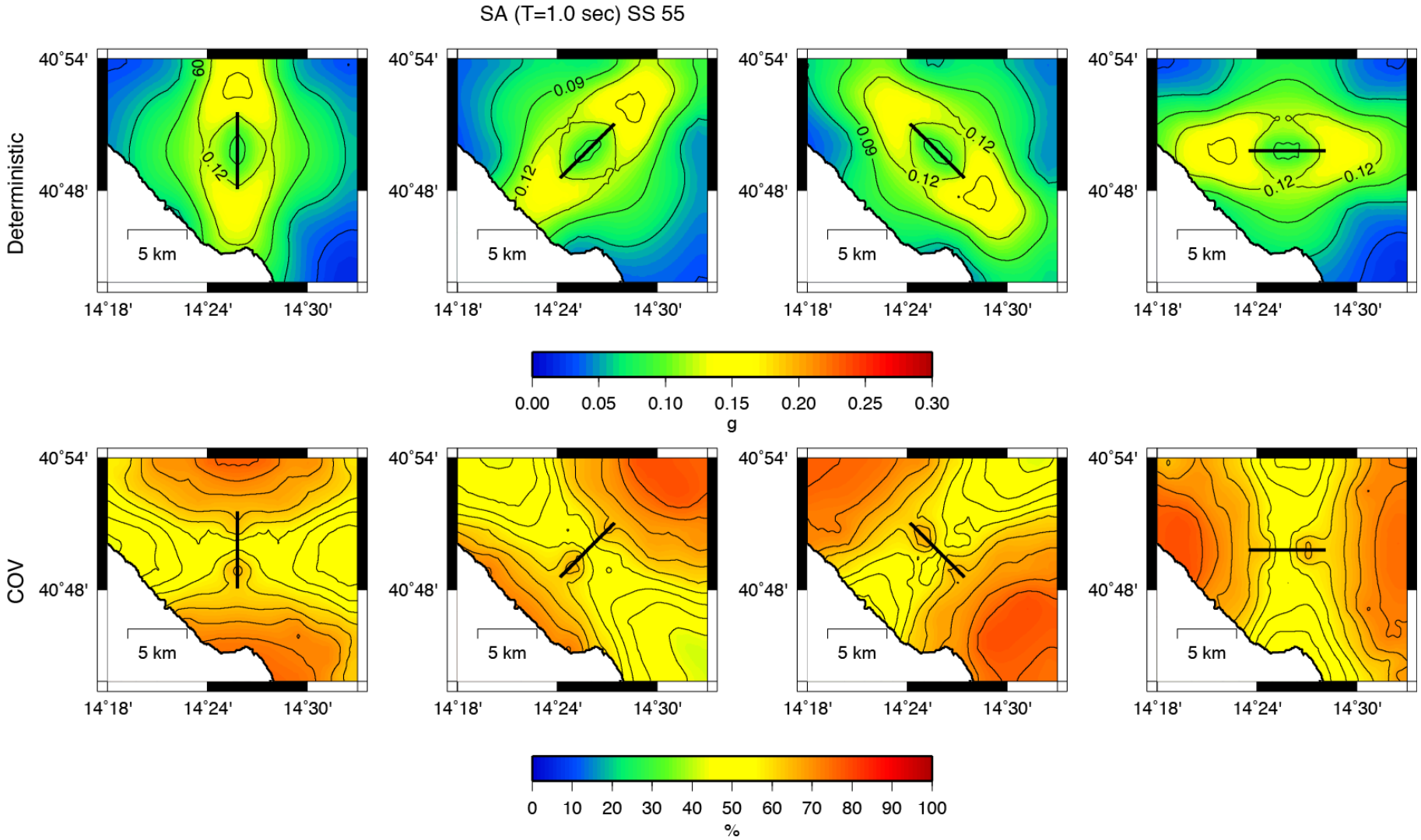

Figure 2.3.1.6. Distribution of Sa(T=1.0s) in unit of g at VS area for M 5.5 and strike slip fault mechanisms for 4 strike values (0°, 45°, 135° and 270°) (Top). CoV map of PGA (See text for more details) at VS area for M 5.5 and strike slip fault mechanisms for 4 strike values (90°, 180°, 270° and 360°) (Bottom).

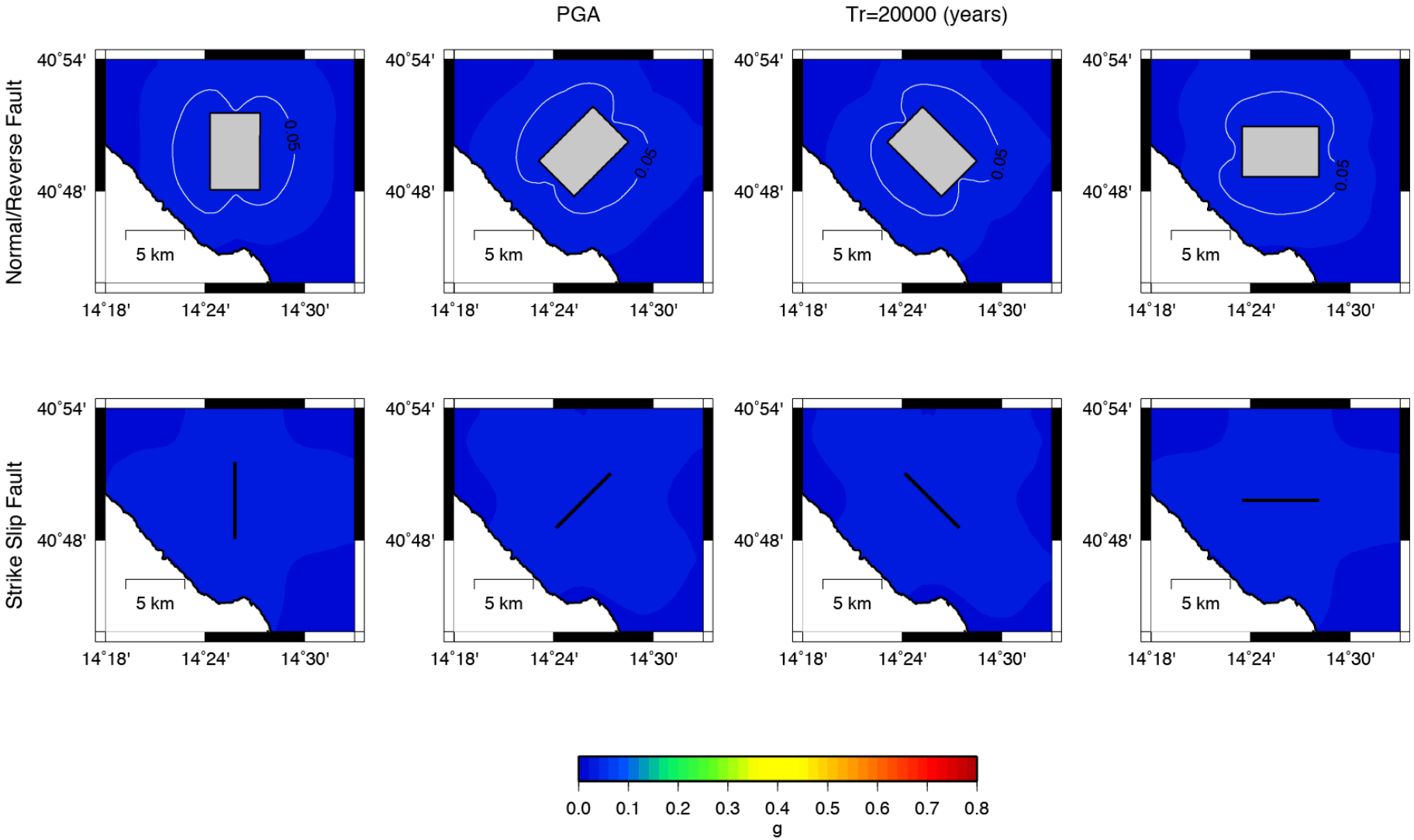

Figure 2.3.1.7. Upper panels: hybrid hazard maps in unit of g at VS area for M 5.5 and normal fault mechanisms for a 20000 yr return period for PGA. Lower panels: same as upper panels but for strike slip fault machanisms.

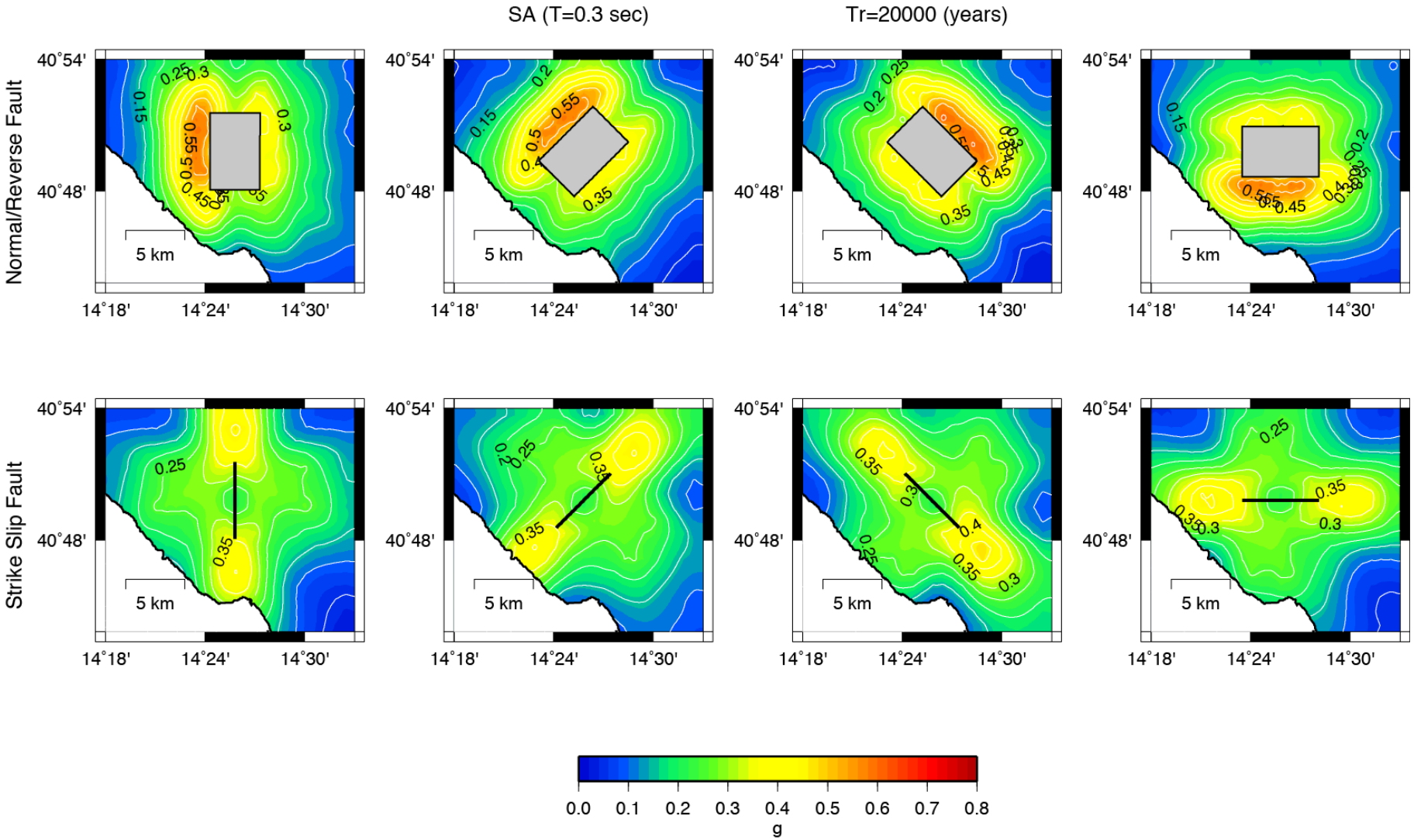

Figure 2.3.1.8. Upper panels: hybrid hazard maps in unit of g at VS area for M 5.5 and normal fault mechanisms for a 20000 yr return period for Sa(T=0.3sec). Lower panels: same as upper panels but for strike slip mechanisms.

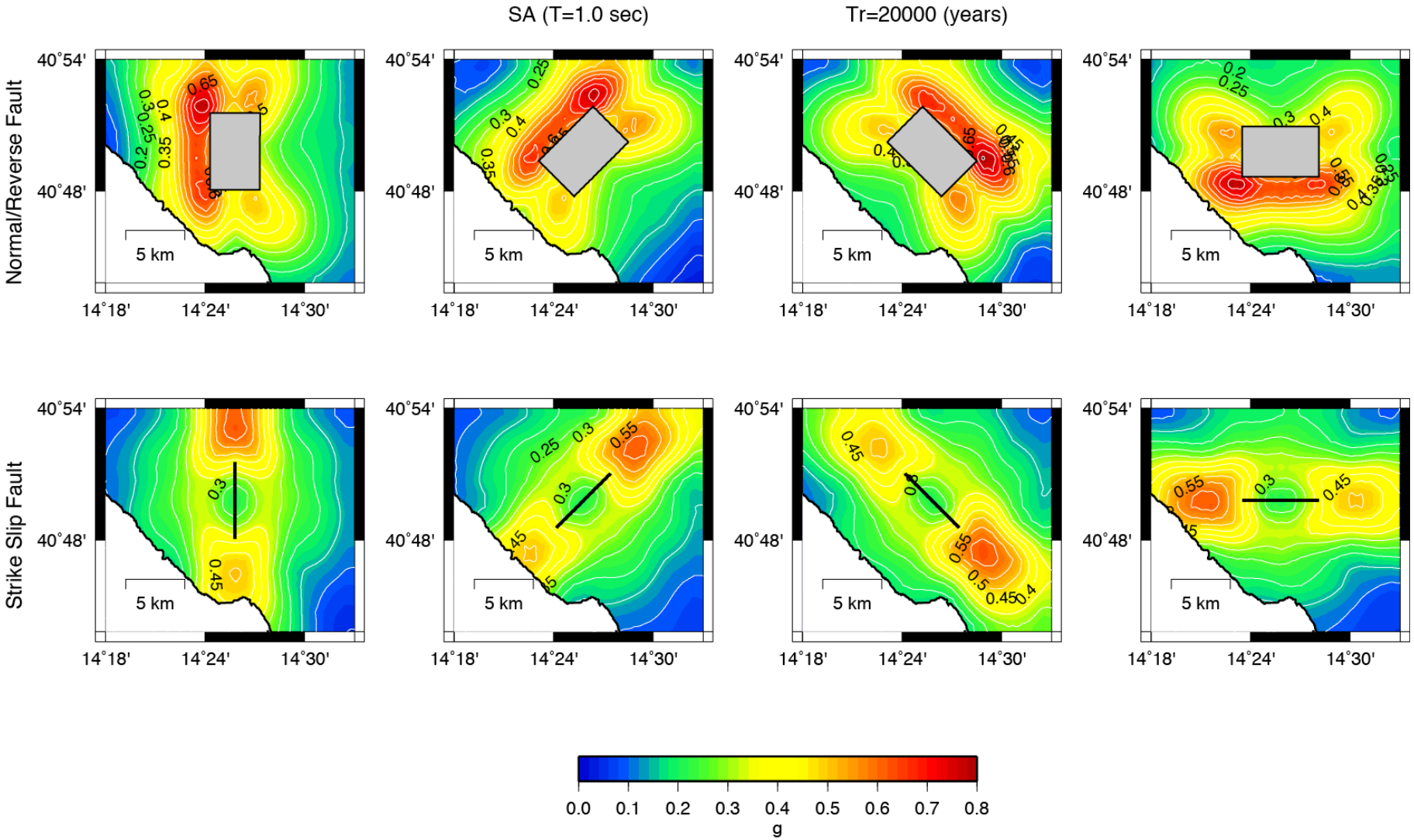

Figure 2.3.1.9. Upper panels: hybrid hazard maps in unit of g at VS area for M 5.5 and normal fault mechanisms for a 20000 yr return period for Sa(T=1.0sec). Lower panels: same as upper panels but for strike slip mechanisms.

2.3.2 Campi Flegrei area

For the sake of clarity was here reported again the text of Chapter 2.3.1 (adapted for Campi Flegrei area).

The result of the hazard analysis for the Campi Flegrei is reported in terms of mean peak ground parameters (PGA, PGV and Sa) and associated CoV (Fig. 2.3.2.1-6) and hazard maps (Fig. 2.3.2.7-9) for an event of magnitude 5.5, four different strike values and for Direct/Revers (DR) and Strike Slip (SS) mechanism.

The CoV coefficient is defined as:

$$CoV = 100\left(\frac{STD}{\overline{Par}}\right) \qquad (2.3.1.1)$$

Where STD represents the standard deviation of the selected parameter distribution and $\overline{\text{Par}}$ represents the mean value of this parameter.

The deterministic maps represent the spatial distribution of mean values calculated for 81 different scenarios. Each scenario was obtained varying the enucleating point on fault plane, the rupture velocity and the final slip map.

The CoV (Eq.2.3.2.1) map was reported to be evaluated with the deterministic map. The regions where the CoV is higher indicate that the PGA values can vary strongly, depending on how the rupture nucleates, propagates and stops during the faulting process.

As an example, in Figure 2.3.2.1 (Top) the distribution of PGA in unit of g at VS area for M 5.5 and normal fault mechanism are shown. The distributions of CoV values at VS area for the PGA and the four selected fault was also reported (Figure 2.3.2.1, bottom).

Figure 2.3.2.5 shows the distributions of Sa(T=0.3s) at VS area for the four selected fault. Figure 2.3.2.5 (Top) reports the distribution of Sa(T=0.3s) in unit of g at VS area for M 5.5. The strike slip fault mechanism is shown and the distributions of CoV values at VS area for the PGA and the four selected fault are also reported (Bottom).

From the pictures is possible to note the complexity of the different slip map used to generate the synthetic seismogram. The maps are not isotropic, but show a directivity effect particular for finite faults.

The hybrid scenario hazard maps for the selected faults (Fig. 2.3.2.7-9) were calculated from the deterministic distributions of simulated ground-motion values.

It can be observed that, due to the adopted methodology, hybrid hazard maps show a quite complex pattern with respect to the classical hazard maps that generally feature symmetry in the ground motion distribution. In fact, hybrid maps can account for focal mechanism, for hanging-wall versus foot-wall effect and directivity effects that cannot be accounted for in the classical approach.

Figures (2.3.2.7-9) shows the PGA and SA(T=0.3s) and Sa(T=1.0s) for normal (Top) and strike slip (Bottom) fault mechanisms having a probability of 0.25% to be exceeded in 50 years (Standard buildings) respectively or 0.5% to be exceeded in 100 years (Strategic infrastructure: bridges, dams).

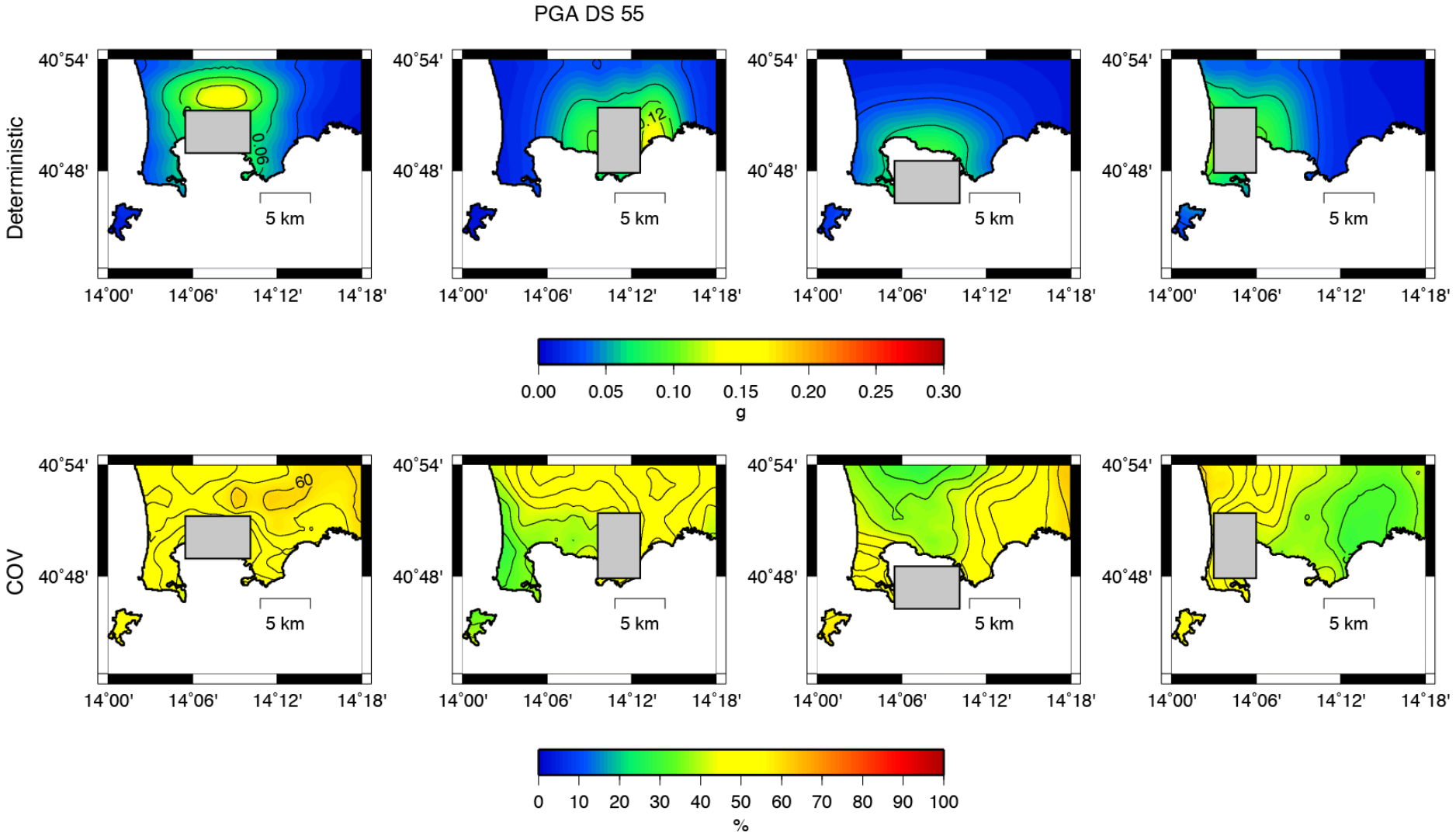

Figure 2.3.2.1. Distribution of PGA in unit of g at CF area for M 5.5 and normal fault mechanisms for 4 strike values (0°, 45°, 135° and 270°) (Top). CoV map of PGA (See text for more details) at CF area for M 5.5 and normal fault mechanisms for 4 strike values (90°, 180°, 270° and 360°) (Bottom).

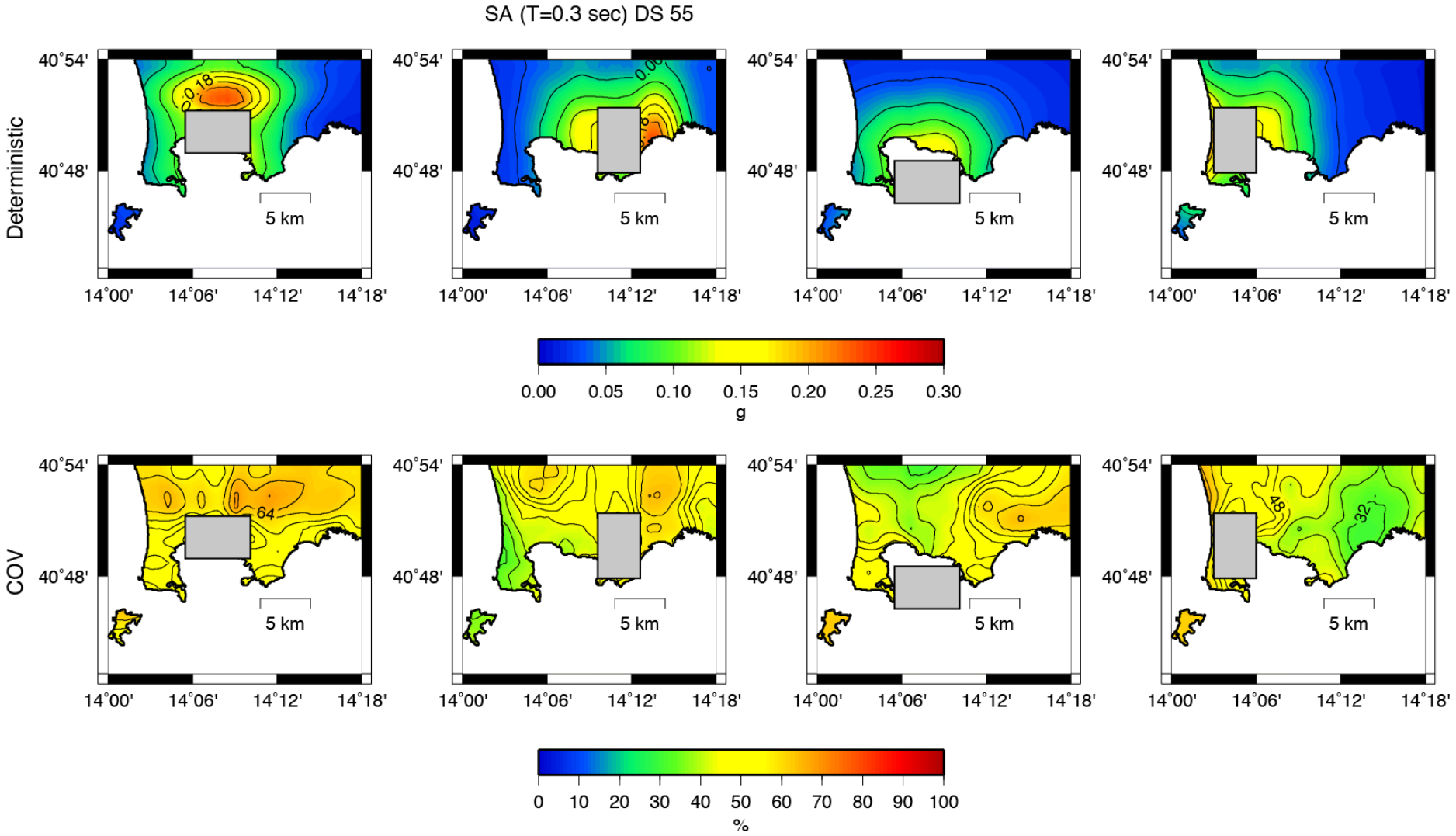

Figure 2.3.2.2. Distribution of Sa(T=0.3s) in unit of g at CF area for M 5.5 and normal fault mechanisms for 4 strike values (0°, 45°, 135° and 270°) (Top CoV map of PGA (See text for more details) at CF area for M 5.5 and DS fault mechanisms for 4 strike values (90°, 180°, 270° and 360°) (Bottom).

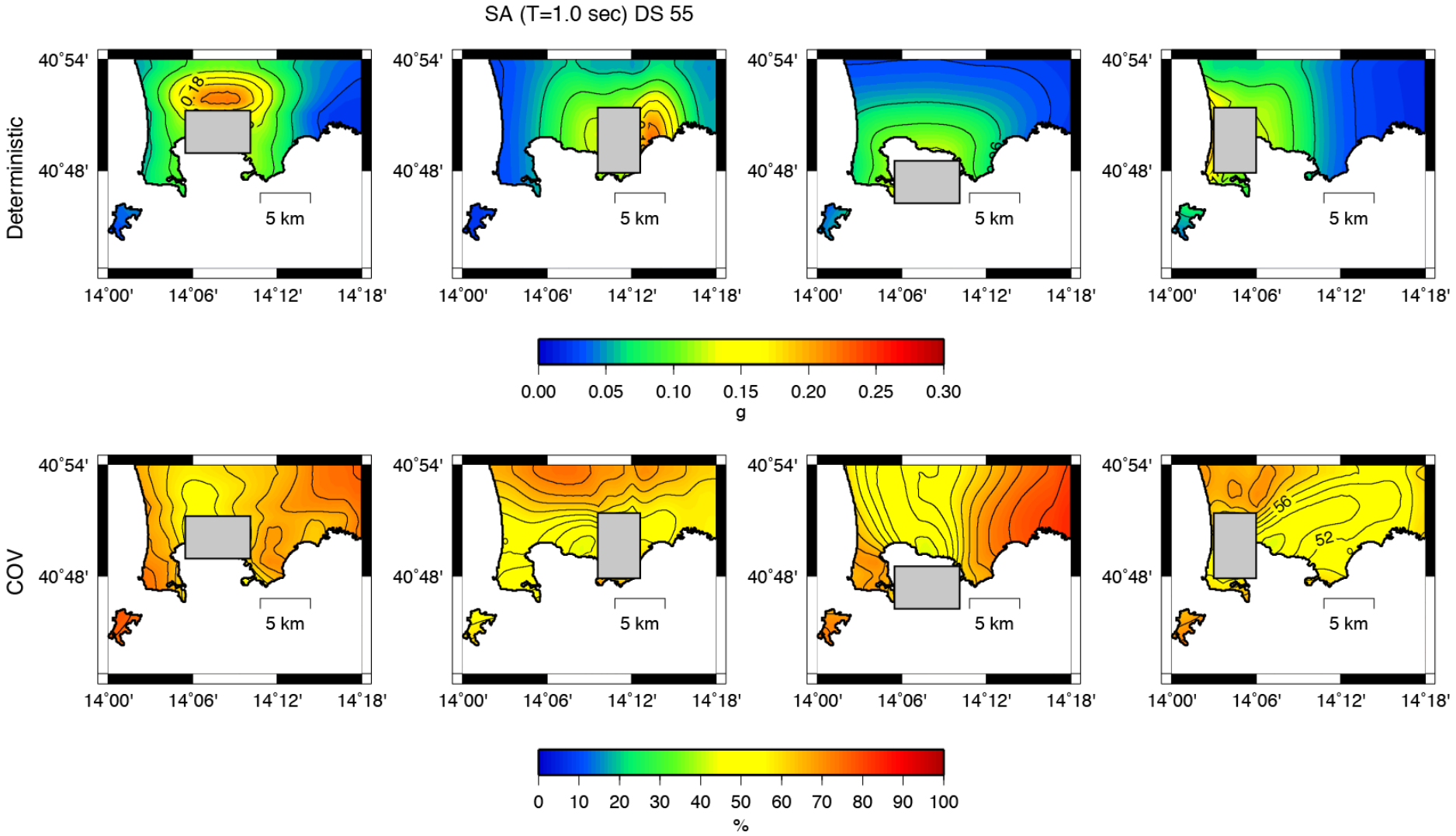

Figure 2.3.2.3. Distribution of Sa(T=1.0s) in unit of g at CF area for M 5.5 and normal fault mechanisms for 4 strike values (0°, 45°, 135° and 270°) (Top). CoV map of PGA (See text for more details) at CF area for M 5.5 and normal fault mechanisms for 4 strike values (90°, 180°, 270° and 360°) (Bottom)

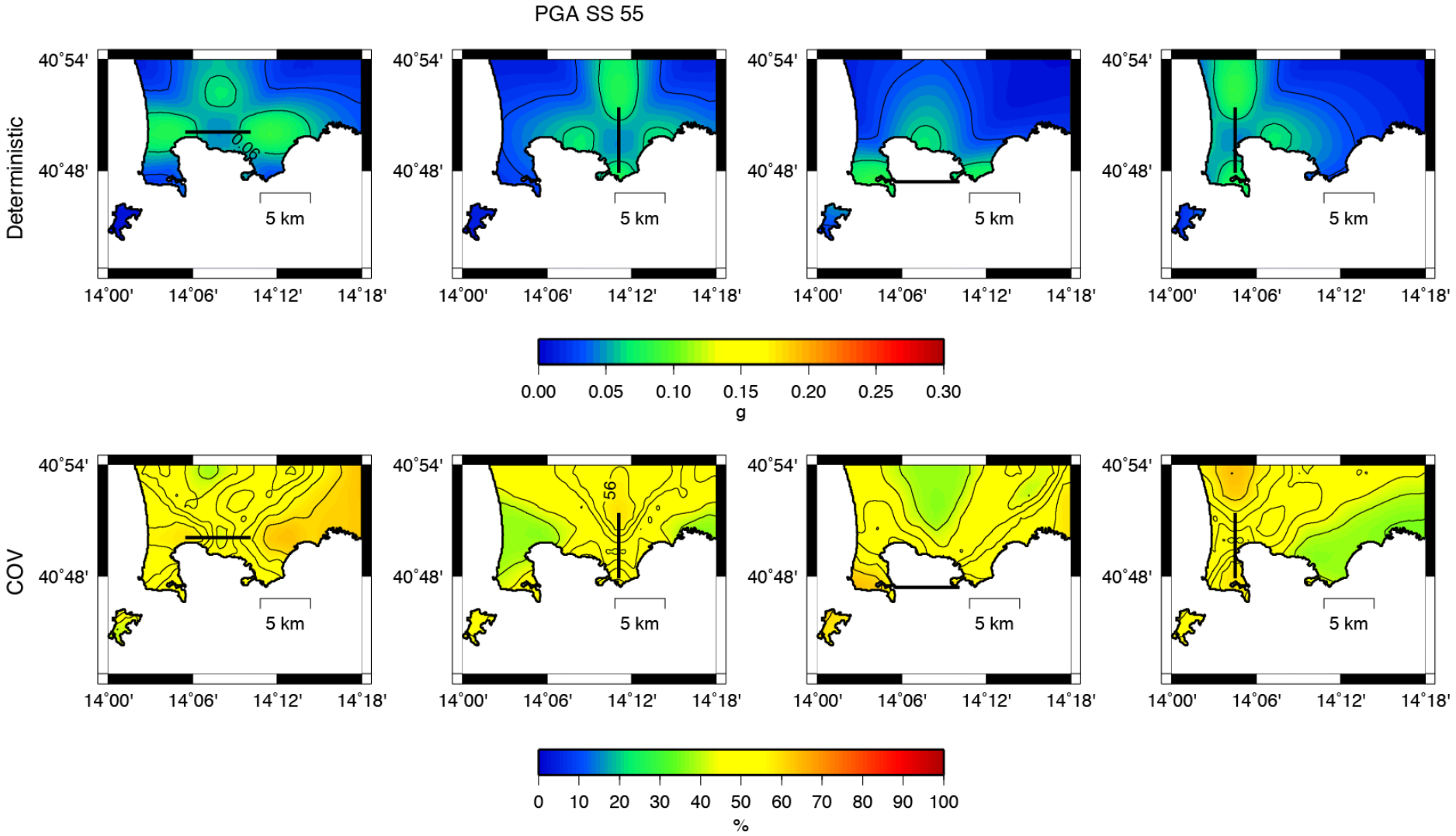

Figure 2.3.2.4. Distribution of PGA in unit of g at CF area for M 5.5 and strike slip fault mechanisms for 4 strike values (0°, 45°, 135° and 270°) (Top). CoV map of PGA (See text for more details) at CF area for M 5.5 and strike slip fault mechanisms for 4 strike values (90°, 180°, 270° and 360°) (Bottom).

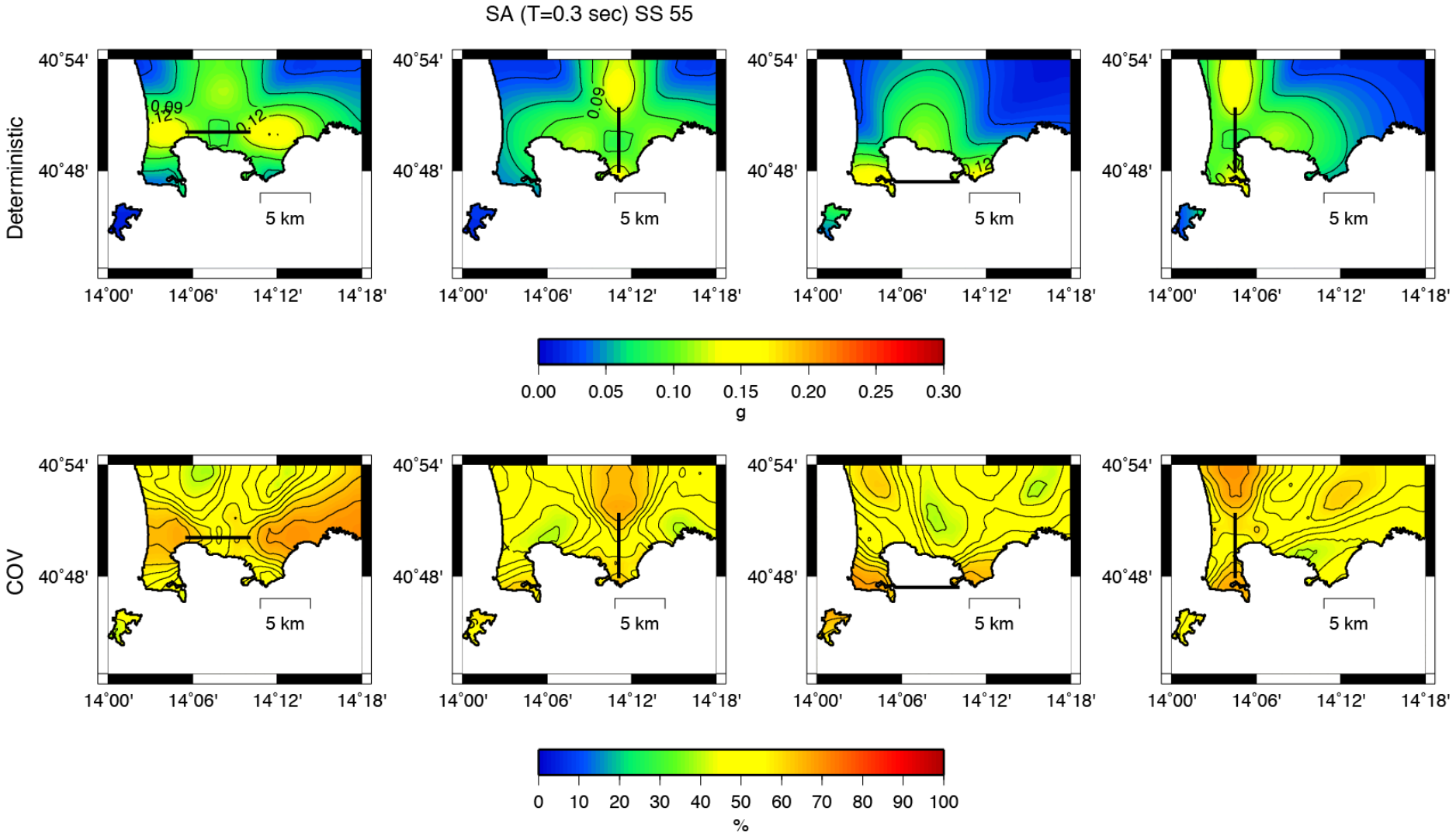

Figure 2.3.2.5. Distribution of Sa(T=0.3s) in unit of g at CF area for M 5.5 and strike slip fault mechanisms for 4 strike values (0°, 45°, 135° and 270°) (Top). CoV map of PGA (See text for more details) at CF area for M 5.5 and strike slip fault mechanisms for 4 strike values (90°, 180°, 270° and 360°) (Bottom).

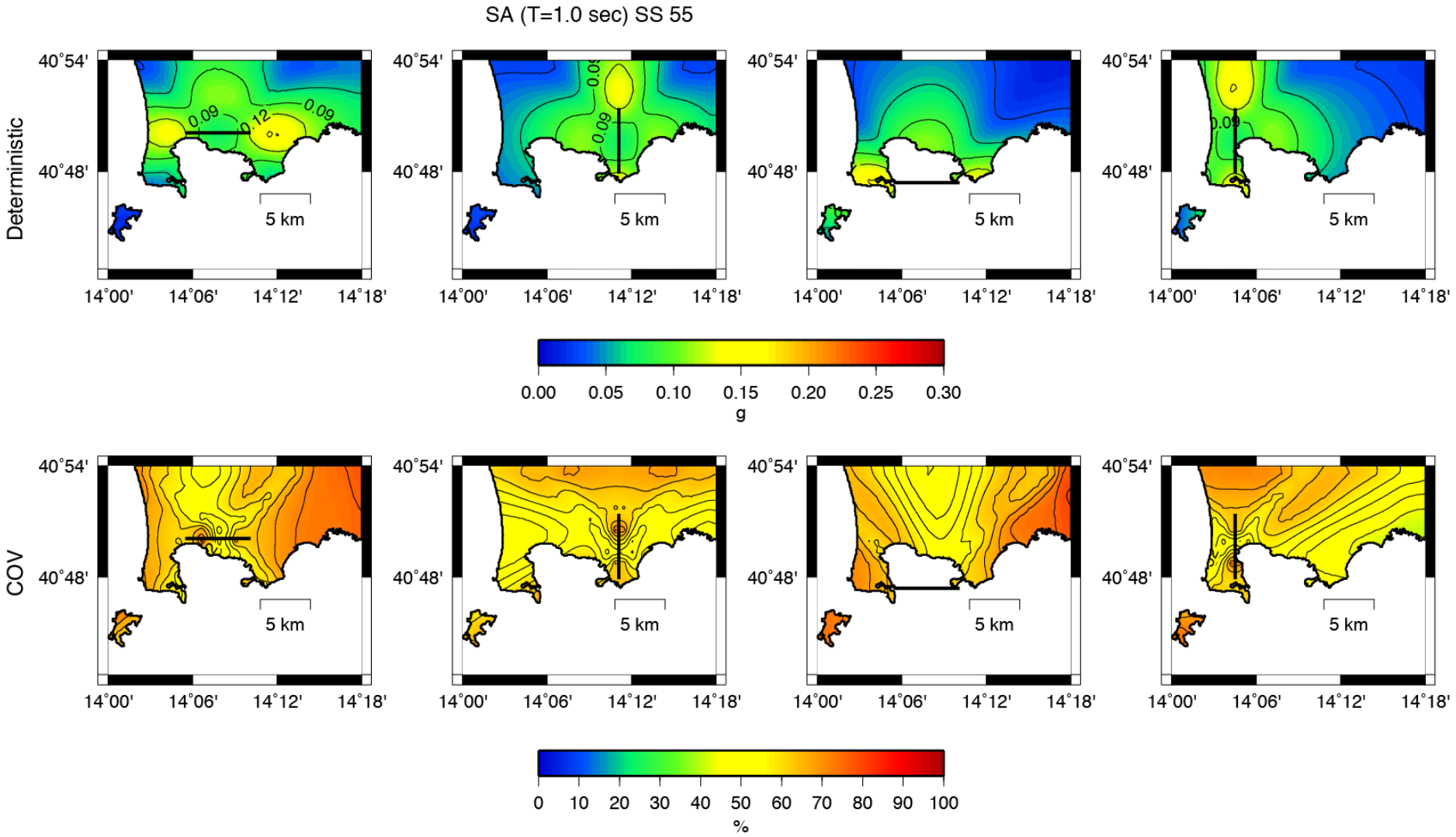

Figure 2.3.2.6. Distribution of Sa(T=1.0s) in unit of g at CF area for M 5.5 and strike slip fault mechanisms for 4 strike values (0°, 45°, 135° and 270°) (Top). CoV map of PGA (See text for more details) at CF area for M 5.5 and strike slip fault mechanisms for 4 strike values (90°, 180°, 270° and 360°) (Bottom).

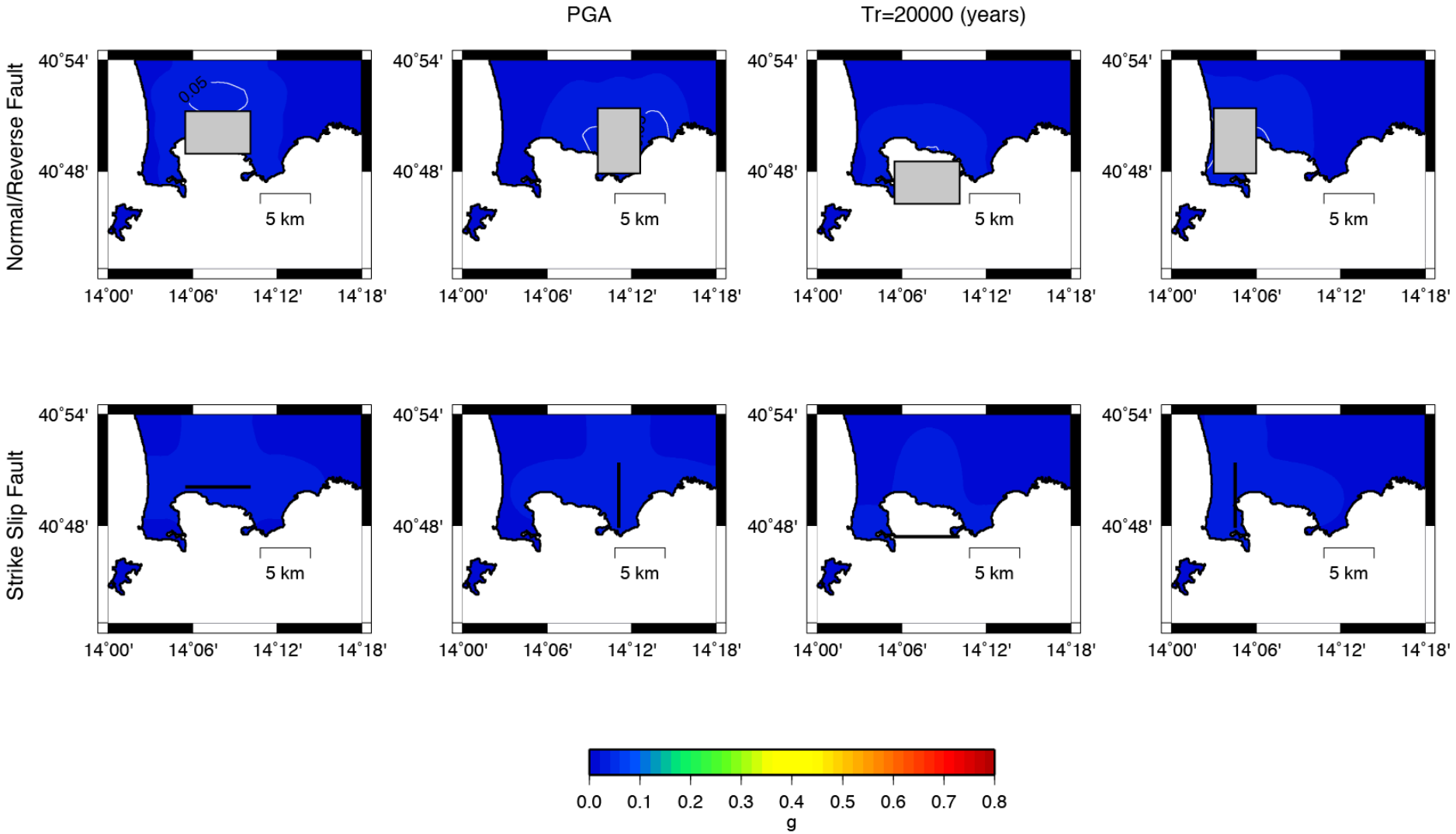

Figure 2.3.2.7. Upper panels: hybrid hazard maps in unit of g at CF area for M 5.5 and normal fault mechanisms for a 20000 yr return period for PGA. Lower panels: same as upper panels but for strike slip fault machanisms.

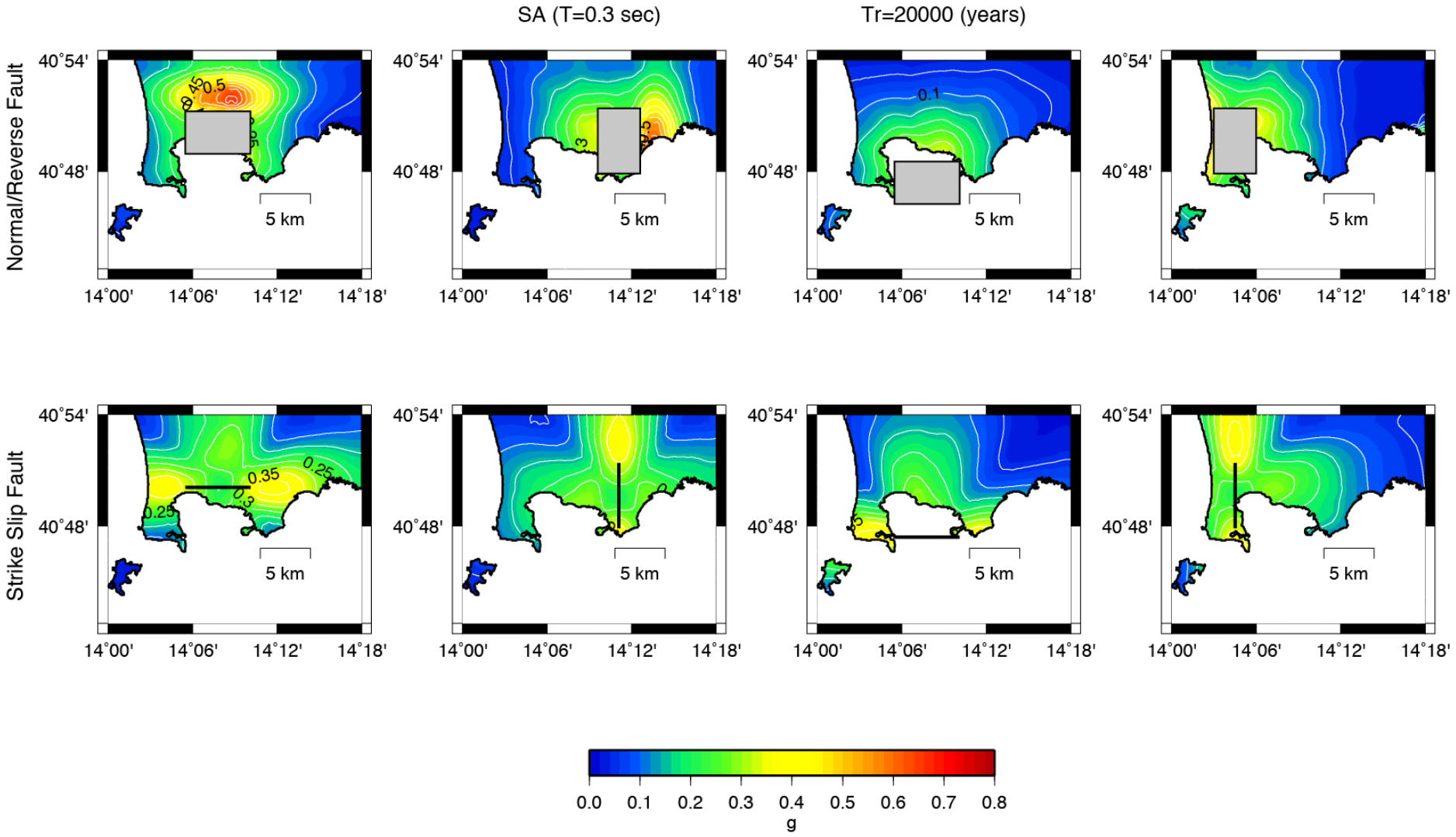

Figure 2.3.2.8. Upper panels: hybrid hazard maps in unit of g at CF area for M 5.5 and normal fault mechanisms for a 20000 yr return period for Sa(T=0.3sec). Lower panels: same as upper panels but for strike slip mechanisms.

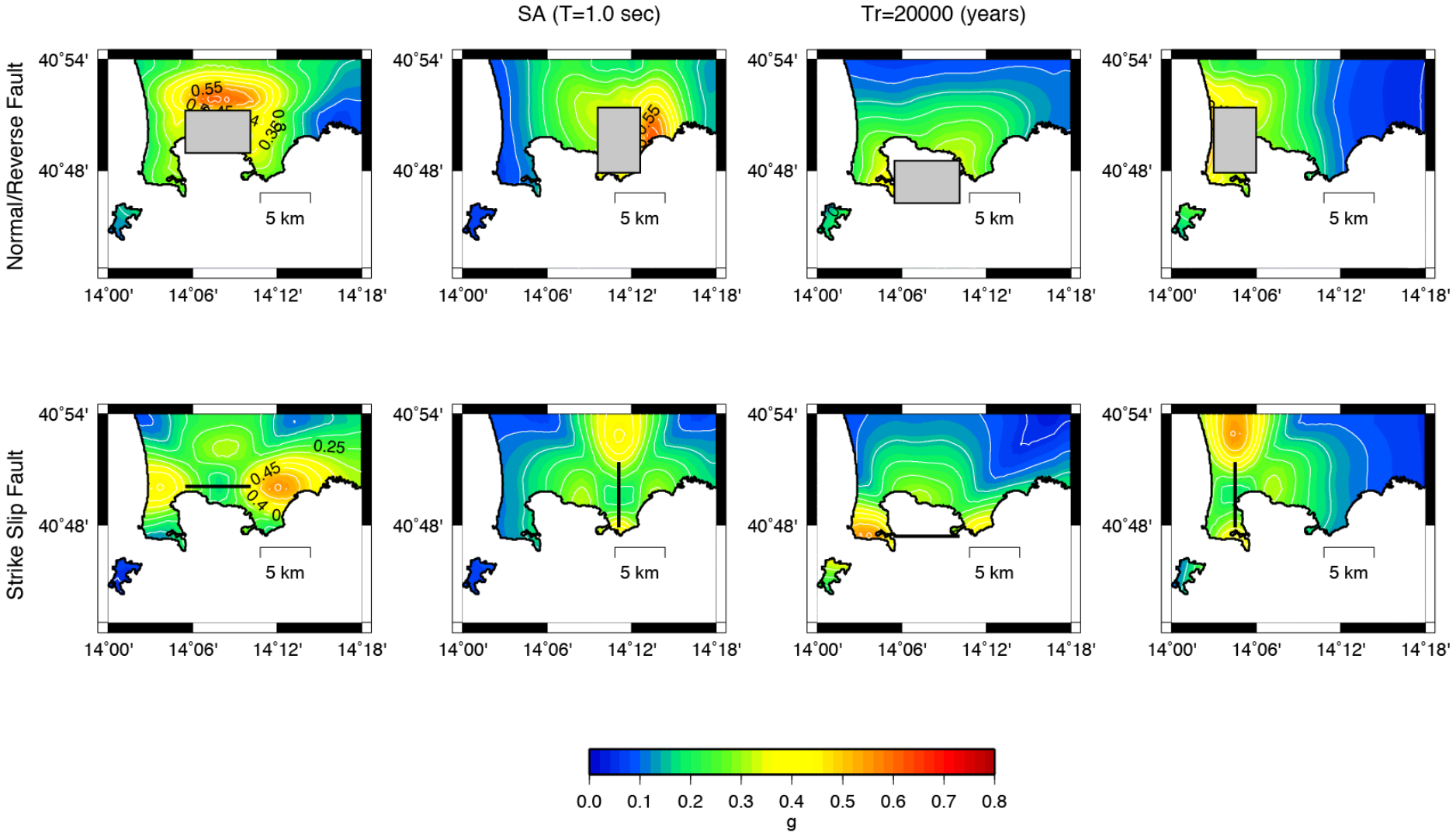

Figure 2.3.2.9. Upper panels: hybrid hazard maps in unit of g at CF area for M 5.5 and normal fault mechanisms for a 20000 yr return period for Sa(T=1.0sec). Lower panels: same as upper panels but for strike slip mechanisms.

2.4 Site specific Uniform Hazard Spectra

From an engineering point of view, as was describe in Cap.1.4, the UHS (Uniform Hazard Spectra) represent the better way to summarize the result of a seismic hazard analysis. The UHS represents the acceleration amplitude for different structural periods with the same probability of exceedance in the period of interest. Each period represents a fundamental period of the civil structure modelled as a simple oscillator (Reiter, 1990). Under this simplification the final result for a complete hazard assessment is represented by an elastic response spectrum (commonly, 5% critically damped) that is derived from the analysis of the PSHA at the site (e.g., Reiter 1990).

The UHS is obtained by solving the hazard integral (Eq.2.2.1) for each structural period with a fixed probability of exceedance.

For Campi Flegrei and Mt. Vesuvius, three and four sites with different locations with respect to the source zones were selected and the time-dependent hazard was computed in terms of Sa(T) for 15 different values of T (0.0-4.0 sec.).

2.4.1 Mt. Vesuvius area

The result of the hazard analysis for the Mt. Vesuvius is reported in terms USH (Uniform Hazard Spectra) to better way to summarize the result of a seismic hazard analysis.
Four sites (Fig.2.4.1.1) at different locations with respect to the source zones was selected for Mt. Vesuvius and the time-dependent hazard was computed in terms of Sa(T) for 15 different values of T (0.0-4.0 sec.). For each site (S1, S2, S3, S4) the UHS corresponding to an earthquake of M 5.5 with normal/reverse mechanism acting on one of the faults (F1, F2, F3, F4) was computed. This analysis allows understanding which fault gives the greater contribute to the hazard, in terms of acceleration amplitude, of each site. In this case, all faults are overlapped each other, is possible to note that contribute to the hazard of the each fault is about the same then other. F or examples the UHS for the site 2 (Figure 2.4.1.3) shows that the contribute of faults F2, F3, F4 is not so different than the contribute of F1.
However the complexity of the seismic sources, able to reproduce directivity and hanging-wall versus foot-wall effect, contribute to the different shape of the UHS curves the periods ranging from 0.5 to 1.0 and from 1.5 to 4.0 seconds.
In these intervals it is possible to note a considerable increment of the acceleration values, at same site, as a function of the selected fault. In particular it has been observed that for site number 1 at about 0.15 seconds the acceleration value for fault F1 is greater than for acceleration for fault F2 (Fig.2.4.1.2), independently from source to site distance.

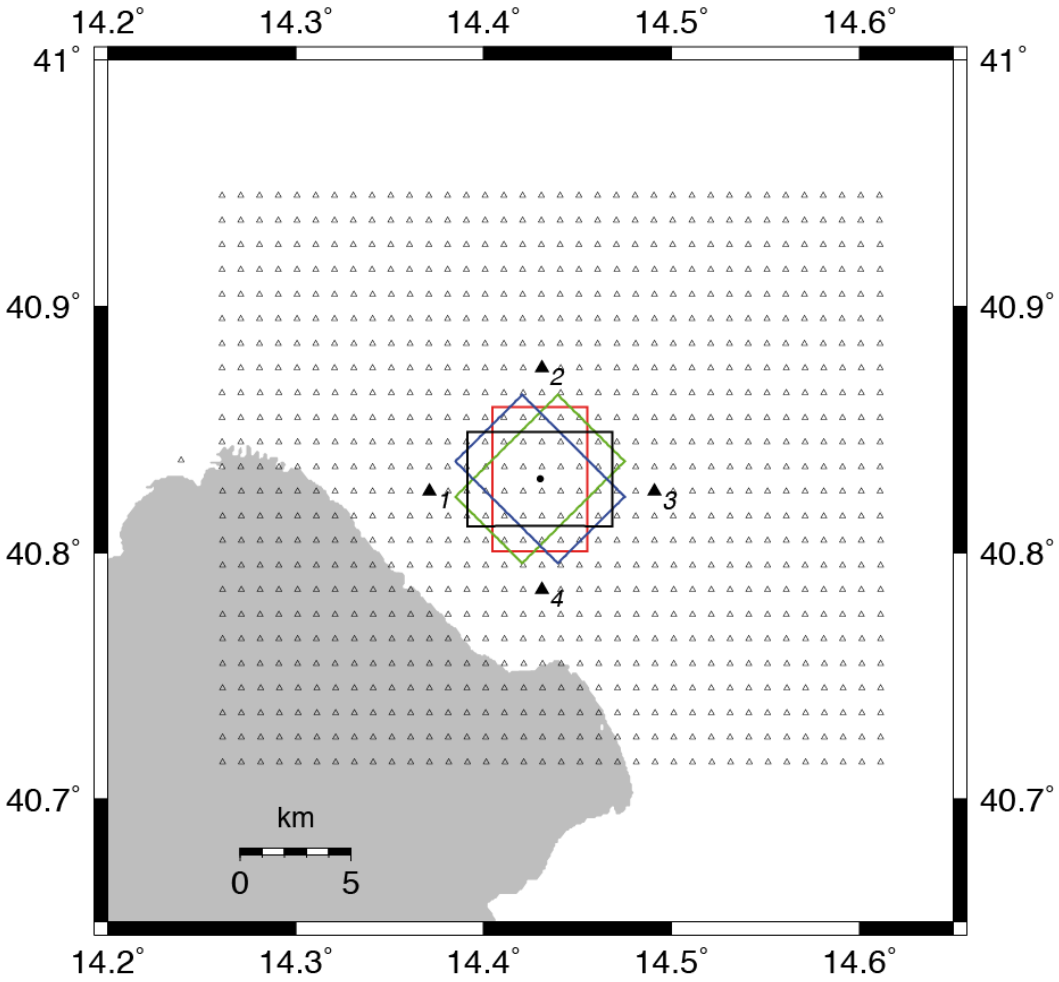

Figure 2.4.1.1 Identified surface fault projections at CF, the colours boxes represent the surface projection of fault plane for M5.5 event (each colour identify a strike value). The black triangles represent the site at which was calculated the UHS.

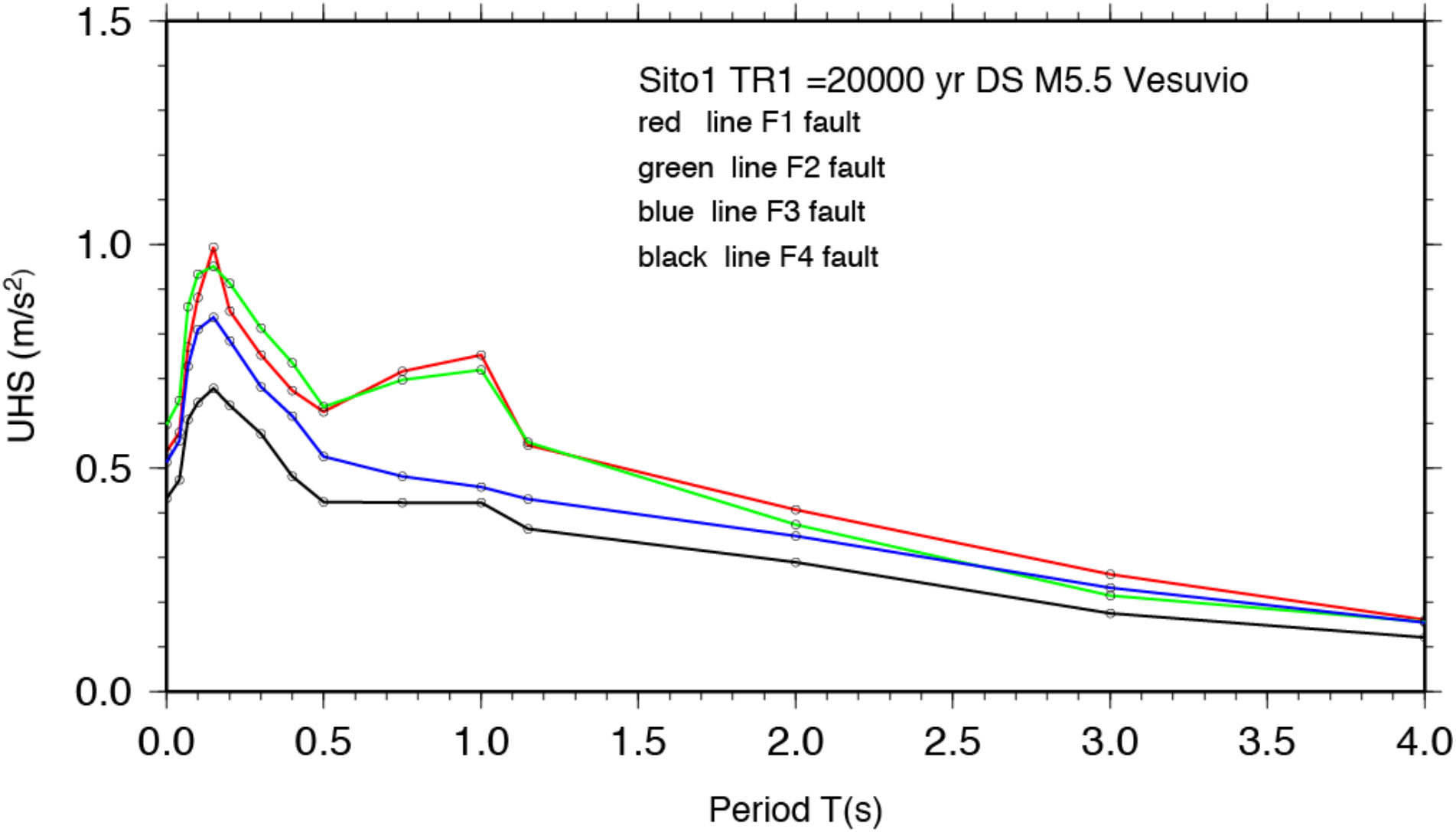

Figure 2.4.1.2. Uniform Hazard Spectra for VS area at Site 1 for a return period of 20000yr and an earthquake of magnitude M5.5

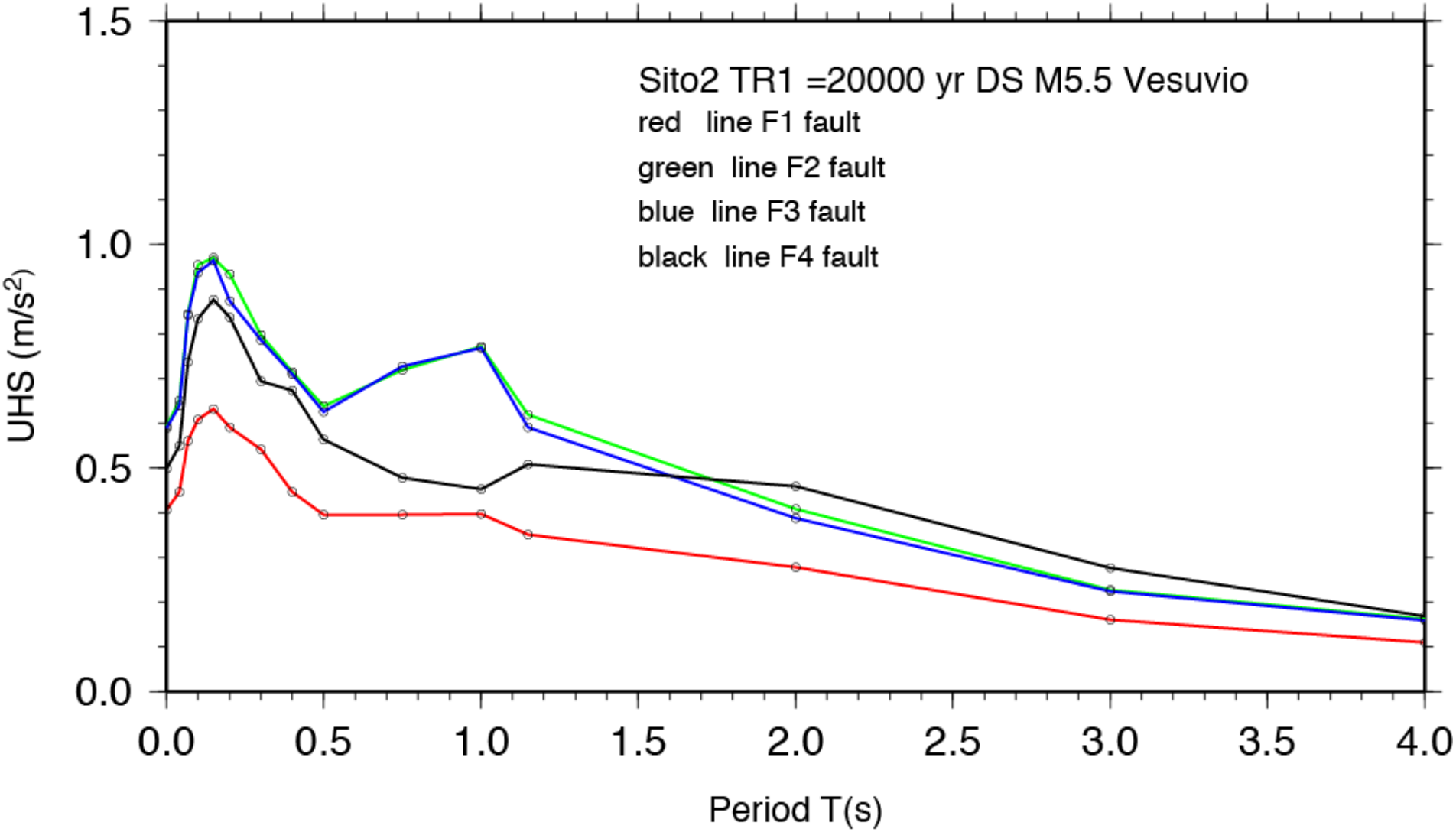

Figure 2.4.1.3. Uniform Hazard Spectra for VS area at Site 2 for a return period of 20000yr and an earthquake of magnitude M5.5

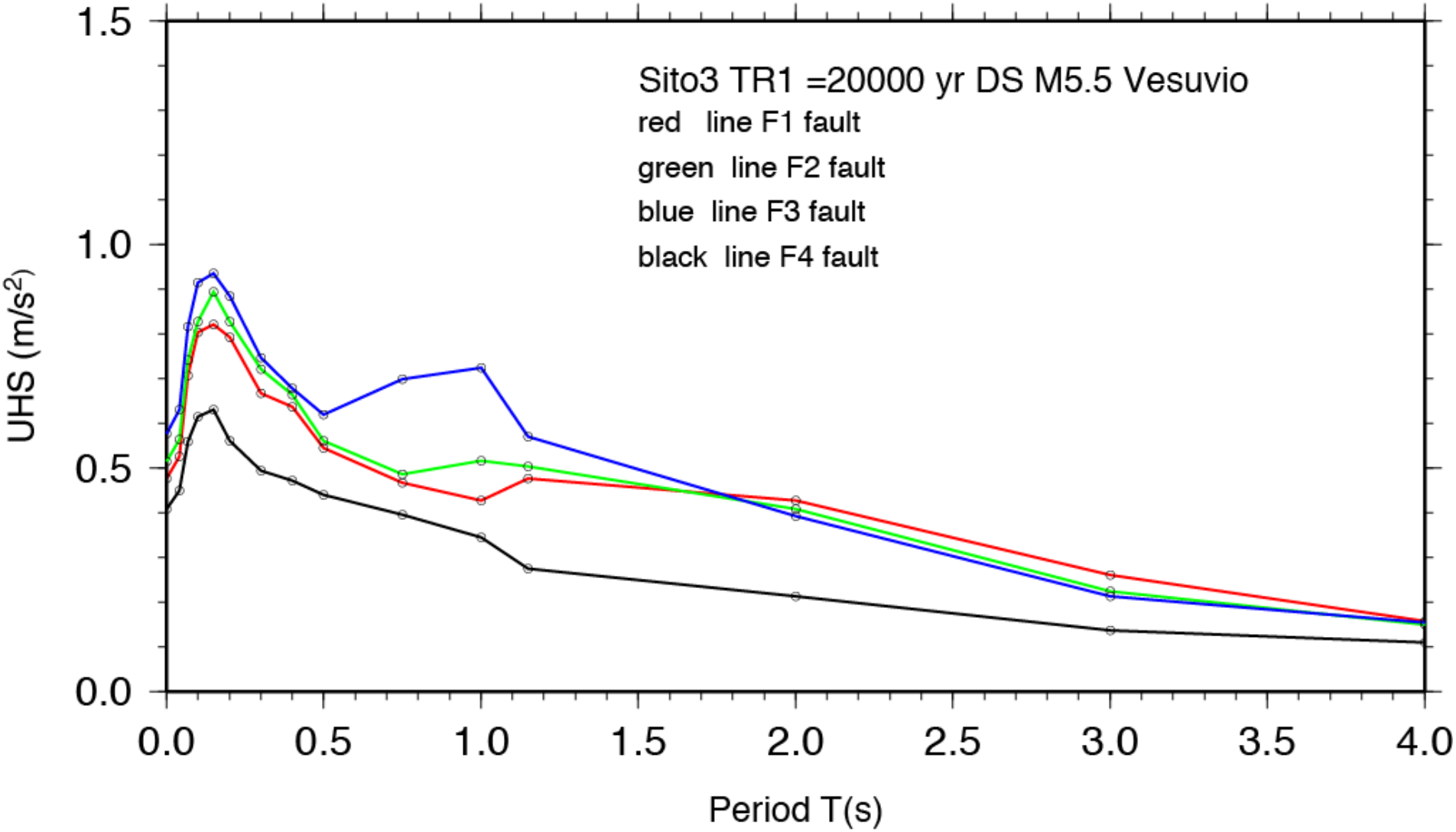

Figure 2.4.1.4. Uniform Hazard Spectra for VS area at Site 3 for a return period of 20000yr and an earthquake of magnitude M5.5

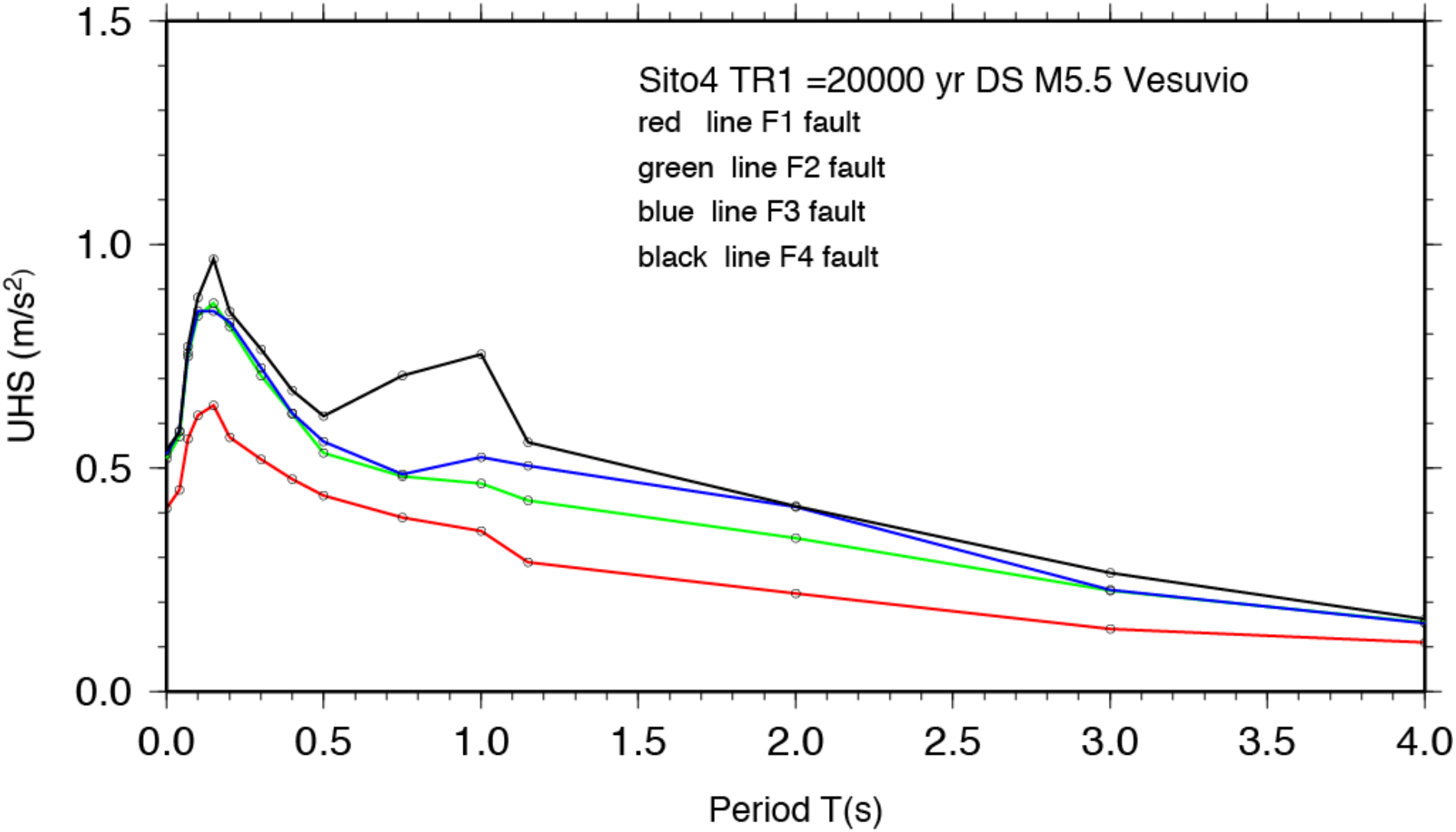

Figure 2.4.1.5. Uniform Hazard Spectra for VS area at Site 4 for a return period of 20000yr and an earthquake of magnitude M5.

2.4.2 Campi Flegrei

For the sake of convenience was again reported the text of Chapter 2.4.1 and adapted for Campi Flegrei area.

The result of the hazard analysis for the Campi Flegrei is reported in terms USH (Uniform Hazard Spectra) because from an engineering point of view its represent the better way to summarize the result of a seismic hazard analysis.

Three sites (Fig.2.4.2.1) at different locations with respect to the source zones were selected for Campi Flegrei area and the time-dependent hazard was computed in terms of Sa(T) for 15 different values of T (0.0-4.0 sec.). For each site (S1, S2, S3) the UHS corresponding to an earthquake of M 5.5 with normal/reverse mechanism acting on one of the faults (F1, F2, F3, F4) was computed. This analysis allows understanding which fault gives the greater contribute to the hazard, in terms of acceleration amplitude, of each site. For all site is possible to observe that contribute to the hazard of the closest fault is always greater than other. It is evident for site 2 (Figure 2.4.2.3) that the contribute of fault F1 (the closest one) is greater than the contribute of F2, F3, F4.

However the complexity of the seismic sources, able to reproduce directivity and hanging-wall versus foot-wall effect, contribute to the different shape of the UHS curves the periods ranging from 0.1 to 1.2 and from 2.5 to 4.0 seconds.

In the first interval it is possible to observe an increment of the acceleration values, in particular for site number 2 and fault F1 (Figure 2.4.2.3).

In the second interval the figures (2.4.2.2-4) shows that the more distant fault have a high contribute for long periods than others.

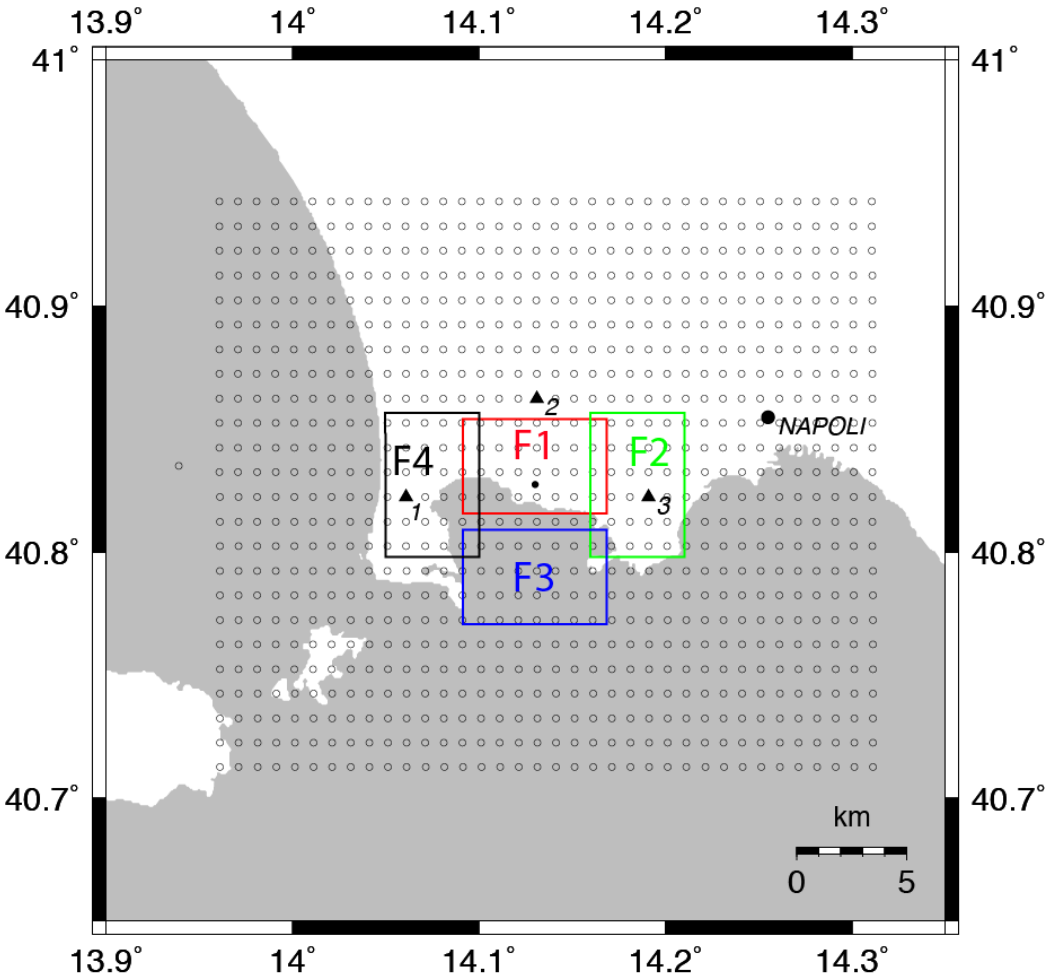

Figure 2.4.2.1 Identified surface fault projections at VS, the colours boxes represent the surface projection of fault plane for M5.5 event (each colour identify a strike value). The black triangles represent the site at which was calculated the UHS.

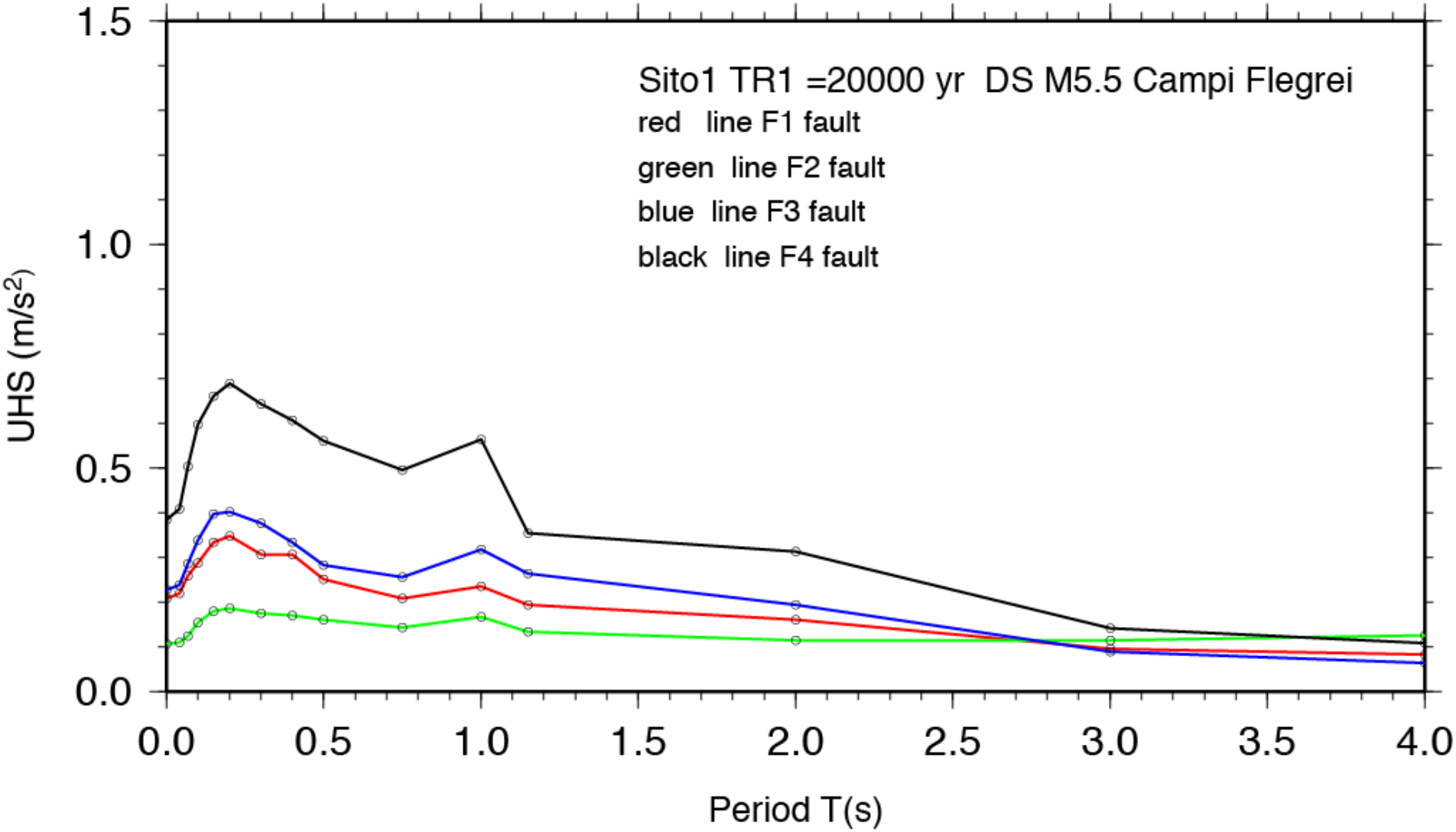

Figure 2.4.2.2. Uniform Hazard Spectra for CF area at Site 1 for a return period of 20000yr and an earthquake of magnitude M5.5

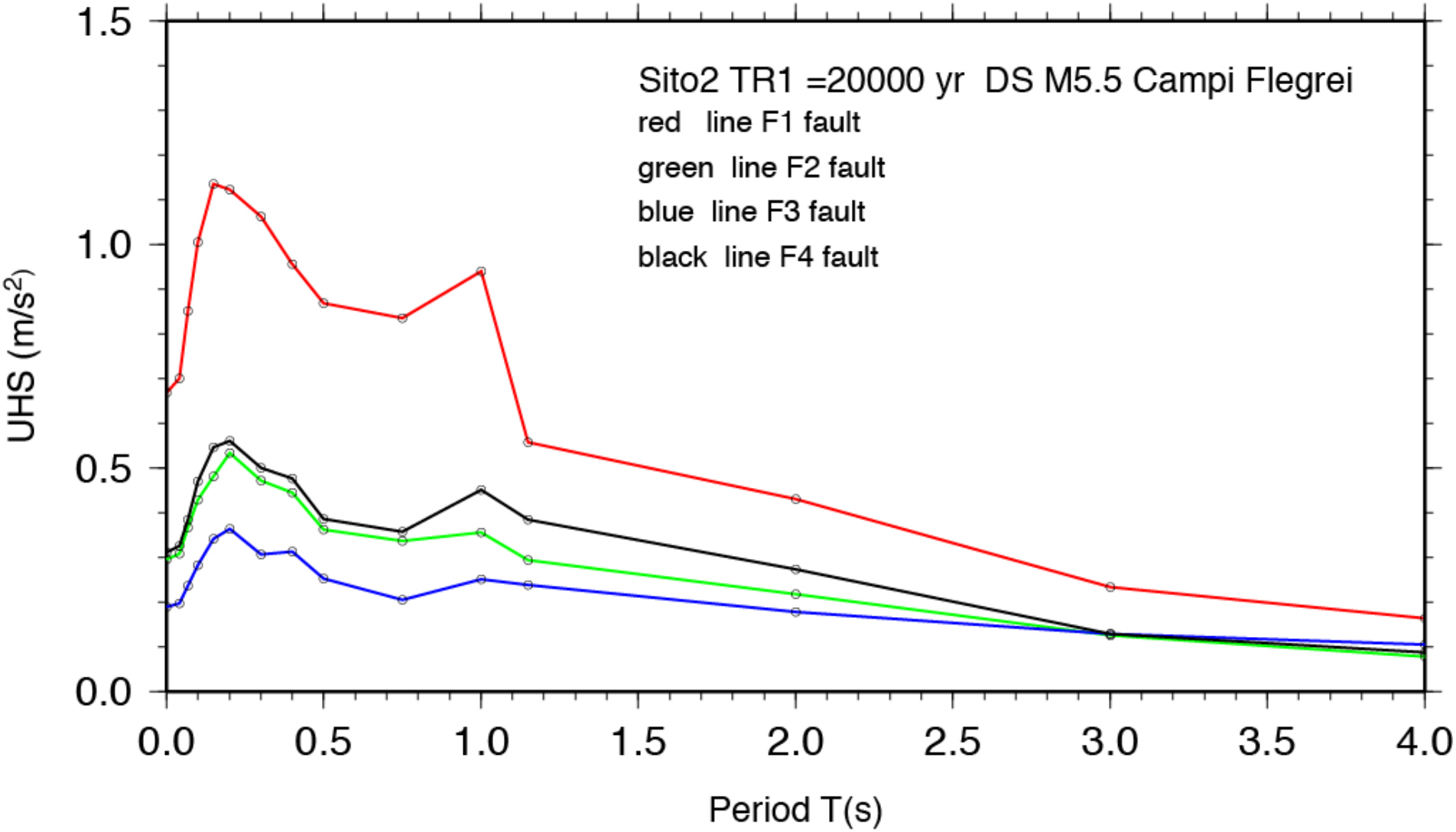

Figure 2.4.2.3. Identified Uniform Hazard Spectra for CF area at Site 2 for a return period of 20000yr and an earthquake of magnitude M5.5

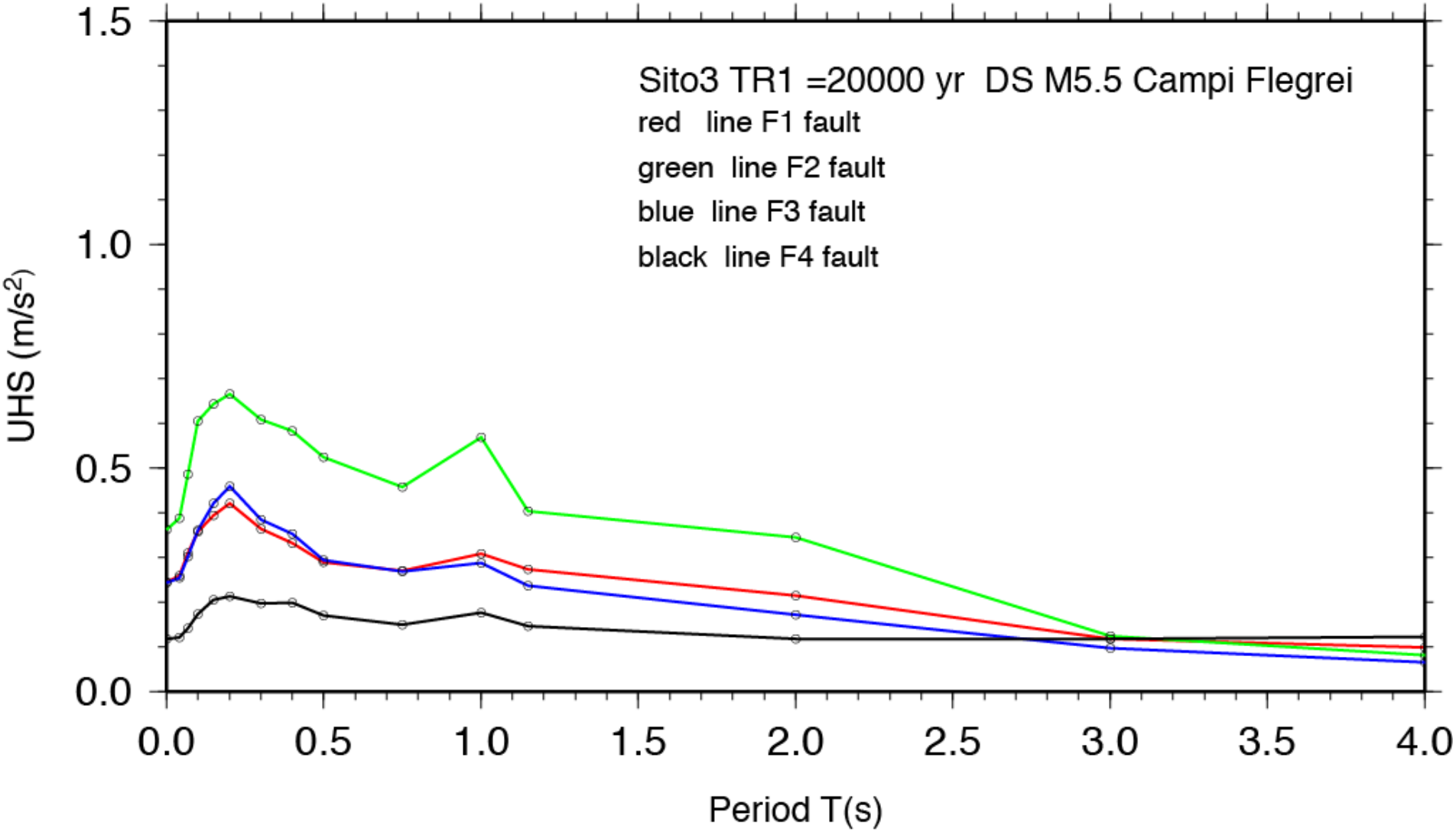

Figure 2.4.2.4. Identified Uniform Hazard Spectra for CF area at Site 3 for a return period of 20000yr and an earthquake of magnitude M5.5

2.5 Results

A hybrid approach has been applied for overcoming some of the limitations of both PSHA and deterministic techniques when applied to a single fault for a scenario-like description of the hazard. For both Mt. Vesuvius and Campi Flegrei volcanoes a set of causative faults corresponding to M 4.0 and M 5.5 were identified. The "characteristic earthquake" model was applied to compute the probability of occurrence of earthquakes (Schwartz and Coppersmith, 1984) and the approach proposed by Youngs and Coppersmith (1985) was applied to compute the activity rate. Full-waveform ground-motion simulation using finite fault models rather than GMPEs has been used to calculate ground motion parameters and their expected ranges of variability (Convertito et al., 2006). For both volcanoes the deterministic maps and the seismic hazard maps and the site specific Uniform Hazard Spectra (UHS) have been calculated.

The hybrid approach uses the seismic simulation, that provides a more realistic and robust peak-ground motion field compared with GMPEs, and the characteristic earthquake scenario to account for focal mechanism, for hanging-wall versus foot-wall effect and directivity effects.

The results show a quite complex pattern with respect to the classical hazard maps that generally feature symmetry in the ground motion distribution. In fact, as an example, hybrid maps can account for focal mechanism and directivity effects.

The analysis performed highlight lower values for PGA than for Sa(T=0.3 and T=1.0 sec) at the same probability of exceedance and return period. This result is important because it confirms that the only PGA is too limitative for describing in exhaustive way the hazard.

The UHS show for both Campi Flegrei and Mt. Vesuvius a different contributes to the hazard as a function of the selected fault at the same site. The analysis of the hazard maps and UHS allows to conclude that the Campi Flegrei and Mt.Vesuvius have to be considered "necessarily" in a separate way whereas for INGV (Meletti et al., 2008) they are located in the same seismogenic zone.

2.6 References

Bouchon, M., 1981. A simple method to calculate Green's functions for elastic layered media. Bull. Seism. Soc. Am. 71, 959–971.

Brune, J., 1970. Tectonic stress and the spectra of seismic shear waves from earthquakes. J. Geophys. Res. 75, 4997–5009 (correction, J. Geophys. Res. 76, 5002, 1971).

Cornell C.A. (1968) Engineering seismic risk analysis. Bull Seism Soc Am 58: 1583-1606

Convertito V., Emolo A. and A. Zollo (2006). Seismic-Hazard Assessment for a Characteristic Earthquake Scenario: An Integrated Probabilistic-Deterministic Method. Bull. Seism. Soc. Am. vol. 96 (2) pp. 377-391

Convertito V., and A. Zollo (2010). Assessment of pre- and syn-crisis seismic hazard at Mt. Vesuvius and Campi Flegrei volcanoes, Campania region southern Italy. In review

Corrado G, Guerra I, Lo Bascio A, Luongo G, Rampoldi R (1976) Inflation and microearthquake activity of Phlegraen Fields, Italy. Bull Volcanol 40:169–188

CPTI04 - Gruppo di lavoro Catalogo Parametrico dei Terremoti Italiani (CPTI) (2004). Catalogo Parametrico dei Terremoti Italiani, versione 2004 (CPTI04), INGV, Bologna.

De Natale G, Iannaccone G, Martini M, Zollo A (1987) Seismic sources and attenuation properties at Campi Flegrei volcanic area. Pure Appl Geophys 125: 883-917

Del Pezzo E., Bianco F., De Siena L., Zollo A. (2006). *Small scale shallow attenuation structure at Mt.Vesuvius, Italy*. Physics of the Earth and Planetary Interiors, **157**: 257-268

Del Pezzo, E., Bianco, F. and Zaccarelli, L.(2006). *Separation of Qi and Qs from passive data at Mt. Vesuvius: a reappraisal of seismic attenuation*. Physics of the Earth and Planetary Interiors, **159**, 202- 212

Gallovic, F., and J. Brokesova (2007), Hybrid k-squared source model for strong ground motion simulations: Introduction, Phys. Earth Planet. Inter., 160, 34 – 50.

Gruppo di lavoro Catalogo Parametrico dei Terremoti Italiani (CPTI) (2004). Catalogo Parametrico dei Terremoti Italiani, versione 2004 (CPTI04), INGV, Bologna.

Hanks, T. C. (1982). fmax, Bull. Seism. Soc. Am. 72, 1867–1880.

Herrero, A., and P. Bernard (1994). A kinematic self-similar rupture process for earthquakes, Bull. Seism. Soc. Am. 84, 1216–1229.

Meletti, C., Galadini, F., Valensise, G., Stucchi, M., Basili, R., Barba, S., Vannucci, G., and Boschi, E. (2008). A seismic source zone model for the seismic hazard assessment of the Italian territory, Tectonophysics 450,85–108.

Reiter L (1990) Earthquake hazard analysis. Columbia University Press, New York

Schwartz, D. P., and J. Coppersmith (1984). Fault behaviour and characteristic earthquakes: examples from Wasatch and San Andreas faults, J. Geophys. Res. 89, 5681–5698.

Youngs, R. R., and K. Coppersmith (1985). Implications of fault slip rates and earthquake

Zollo et al. Seismic reflections reveal a massive melt layer feeding Campi Flegrei caldera. Geophys. Res. Lett. (2008) vol. 35 (12) pp. L12306

Capitolo3

Real-time Fault Extent Estimation methodology to calculate realistic Ground Shaking Map

3.1 Introduction

The generation of ground shaking maps (ShakeMaps) (Wald *et al.*, 1999) after moderate-to-large earthquakes can be crucial for recognizing the areas most affected by the strongest shaking, and can provide useful support for emergency response and planning. Usually, for near-real time applications, the initial source model is assumed to be a point source and, as a consequence, the predicted ground-motion field will feature an isotropic shape (at bedrock) that, for large earthquakes, may underestimate the ground-motion at the closest sites to the fault. In fact, these sites could be affected by fault finiteness effects. Thus, for moderate-to-large earthquakes, rapid estimation of the main seismic source parameters, such as fault geometry, focal mechanism and directivity, can help to refine ground-motion predictions, particularly in those areas where seismic recordings are not available. For example, when information about surface fault projection are available, a more appropriate source-to-site metric, such as the Joyner and Boore (1981) distance definition, can be used instead of the epicentral or hypocentral distance. This can be particularly important for codes aimed at predicting peak ground-motion distributions soon after the occurrence of an earthquake as, for example, ShakeMap implemented world-wide (Wald *et al.*, 1999) or GRSmap implemented in the Campania-Lucania region, in southern Italy (Convertito *et al.*, 2010).

In this context, during last years, several techniques aimed at estimating fault geometry and dominant rupture direction have been proposed and applied on different time scales. The most general technique is the one proposed by Dreger and Kaverina (2000), Their approach uses broadband data to retrieve the seismic moment tensor and slip distribution over a planar surface, and by so to predict peak ground velocities. In contrast, Miyake *et al.* (2001) analyzed amplitude spectra ratios between mainshock and aftershocks, used as empirical Green's function, to estimate both rupture propagation direction and the area on the fault characterized by the largest slip velocity release defined as strong-motion generation area by the authors. Although efficient, due to the large number of parameters and the need for aftershock Green's functions, this technique could not be valuable for near-real time applications. More recently, Yamada and coauthors, in two different papers (Yamada *et al.*, 2007; Yamada and Heaton, 2008) have extended the work proposed by Cua and Heaton developed in the framework of the Virtual Seismologist method (Cua,

2005) to large earthquakes where point source approximation may not be appropriate. The technique is based on the analysis of peak ground-motion parameters and uses a discriminant function to classify records into near-source and far-source (Yamada and Heaton, 2008). Next, they proposed a two step strategy aimed at estimating the slip distribution on the fault in time and space by using high-frequency ground-motion waveform envelopes and assuming a 1D line-source model to account for fault finiteness. For small events, Zollo and de Lorenzo (2001) and de Lorenzo and Zollo (2003) proposed a method to estimate the radius, dip, and strike of a circular seismic rupture through the inversion of first *P*- and *S*-wave pulse widths measured on microearthquake records. The method is based on quite general, numerically calibrated, relationships relating source and attenuation parameters under the assumption that the waves are radiated by a circular crack propagating at a constant rupture velocity. More recently, Frez *et al.* (2010) proposed different techniques for estimating the rupture direction for low-magnitude earthquakes, by assuming a 1D linear-source model with rupture propagating horizontally and analyzing the directivity effect affecting the pulse width of the *P*-wave arrivals and the amplitude spectrum recorded in near-source distances range.

The basic idea of the present thesis generalizes the approach proposed by Boatwright (2007) for small earthquakes to moderate and large events. The proposed approach investigates the possibility of estimating rupture extent and direction by studying the information contained in the peak ground-motion parameters, analyzing how the directivity effect influences these parameters. This issue has been investigated in several papers present in the literature that mainly deal with problem of introducing the directivity effect into Ground Motion Predictive Equations (GMPEs). The approaches proposed by Somerville *et al.* (1997), and more recently by Rowshandel (2010), aim at providing corrective coefficients for existing GMPEs. More sophisticated techniques have been proposed by Spudich *et al.* (2004) and Spudich and Chiou (2008) which provided a functional form for directivity effects derived from isochrone theory and by Venkataraman and Kanamori (2004) aiming to analyze the directivity effect on the radiated seismic energy.

However, as reported by Boatwright (1982), theoretical dynamic models predict that high-frequency acceleration radiated by a set of incoherent sub-sources is correlated to the square root of the rupture area. Additionally, Hanks and McGuire (1981) modeled the magnitude dependence of high-frequency ground motion as a result of a longer duration of large earthquakes rather than to their intrinsic power. As a consequence of those

observations, peak acceleration carries information on the rupture length and can be considered as independent of the amount of slip.

In the analyses that follow, observed Peak Ground acceleration (PGA) and Peak Ground Velocity (PGV) represent the data. The model parameters consist of the dimensions of the surface projection of the fault and additional quantities that account for the directivity of the source, that are described in detail in the next section. The inverse problem is solved through a grid-search approach aimed at maximizing a Probability Density Function (PDF) of the residuals of observed and estimated (by a GMPE) peak parameters. The model space to be investigated is defined through a Bayesian approach.

The proposed technique has been applied to three different earthquakes featuring different source mechanisms. More specifically, the 17 August 1999 Mw 7.5 Kocaeli (Turkey) earthquake has been selected for its strike-slip fault mechanism, the 6 April 2009 Mw 6.3 L'Aquila (Italy) earthquake represents normal faulting, and the 17 January 1994 Mw 6.7 Northridge (California) earthquake provides an example of thrust faulting.

3.2 Theory Framework

For a line-source model in a homogeneous propagation medium characterized by a bilateral rupture and far-field approximation, based on the original formulation of Hirazawa and Stauder (1965), Boatwright (2007) proposed a generalization of the directivity function C_d to account for ground motion amplitude variation, whose formulation is:

$$C_d = \frac{1}{2}\sqrt{\frac{(1+e)^2}{(1-\alpha cos\vartheta)^2} + \frac{(1-e)^2}{(1+\alpha cos\vartheta)^2}} \tag{3.2.1}$$

where $\alpha = v_r / \beta$ is the Mach number, v_r is the rupture velocity, β is the shear-wave velocity and ϑ is the angle between the ray leaving the source and the direction of rupture propagation (Joyner, 1991). In the original formulation, this coefficient is applied as a factor to *P*- and *S*-direct waves. In the present thesis it is assumed that it can be also applied to peak-ground motion quantities that, particularly at large distances, could be associated to different seismic phases. Bilateral rupture propagation on the fault line is accounted by the coefficient *e* denoted as "percent unilateral rupture" (Boatwright, 2007) and defined as:

$$e = \frac{2L' - L}{L} \tag{3.2.2}$$

where L is the whole fault length and L' is assumed to be the prevalent rupture direction (Fig.3.1.1). As a consequence, the *e* value ranges between 0, for a bilateral rupture and 1 for a unilateral rupture. Using the C_d coefficient reported in equation (3.2.1), it is thus possible in principle to constrain the dominant rupture direction, unless other effects (e.g., site effect, travel path attenuation) perturbing the peak-amplitudes are not adequately corrected. Once the other fault dimension, *W*, is introduced (as discussed in detail in the next section), the best surface fault projection could be obtained by maximizing a PDF which accounts for the difference between recorded peak-ground motion parameters, in

particular PGA and PGV, and theoretical predictions that include the directivity factor C_d. More specifically, predicted peak motion values are obtained by using a proper GMPE where the minimum distance from the fault is used as the source-to-site distance. Here, the fault distance is defined as the R_{JB}-distance, that is the shortest distance between the recording station and the surface projection of the fault rupture (Joyner and Boore, 1981). The measured peak-ground motion values correspond to the maximum of the two horizontal components. As a consequence, in order to achieve compatibility among GMPEs which use different peak-ground motion definitions, the relationships proposed by Beyer and Bommer (2006) have been used with their recommended modifying factors.

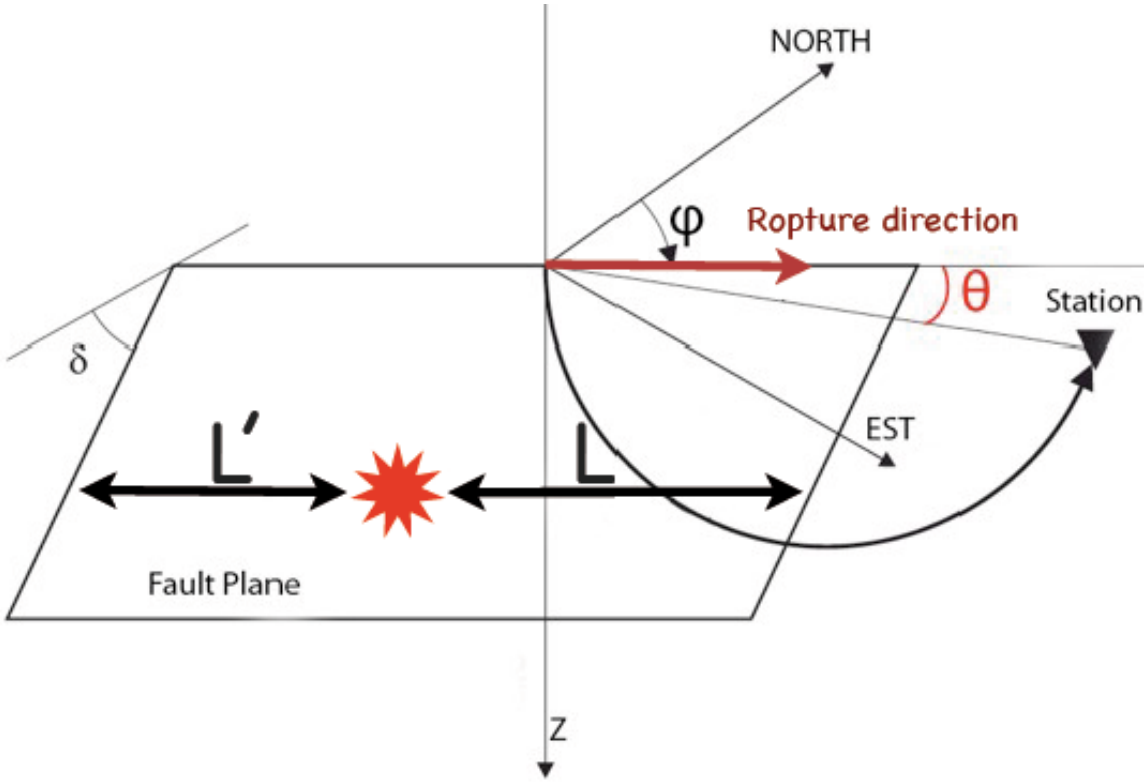

Fig.3.1.1: Graphic construction of fault plane with the variables L, L', e and θ (see the text for more details).

3.2.1 Parametric analysis of the C_d coefficient

Before performing the data inversion, the C_d function has been investigated in order to study possible correlations among the parameters that enter its definition. As reported in equation (3.2.1), the parameters of interest are essentially the Mach number α, the angle ϑ, and the percent of unilateral rupture e. However, due to its definition, $e=(2L'-L)/L$, an obvious correlation between e and L does exist hence this pair of parameters is not investigated. Figure 3.2.1 shows the C_d function plotted as function of the parameters e and α for three values of ϑ corresponding to directive (ϑ =0°), non-directive (ϑ =90°) and anti-directive (ϑ =180°) rupture-to-station location, respectively.

The analysis of the results shown in Figure 3.2.1 allowed us to conclude that the model does not allow to resolve the parameters e and α independently from each other.

In addition to the model resolution, further insights can be obtained from the analysis of the results shown in Figure 3.2.2 where, for the three earthquakes considered in the present thesis, C_d is plotted as function of ϑ for seven α values together with the relative azimuth of the stations (black arrows) with respect to the fault strike. The plots have been elaborated by using for each earthquake the reference value for L and e (see Tables 3.4.1.1, 3.4.2.1 and 3.4.3.1). From the figure it can be noted that the distribution of the stations at which data are available will only allow discrimination of directivity or anti-directivity directions but will not allow estimation of the value of C_d (and its parameters).

Finally, the results of the analysis of the model resolution and the data distribution together with the data errors suggests that parameter α must be set during data inversion. In the applications presented in this study α has been set to 0.8 which is a reasonable value for sub-shear ruptures (Aki and Richards, 2002).

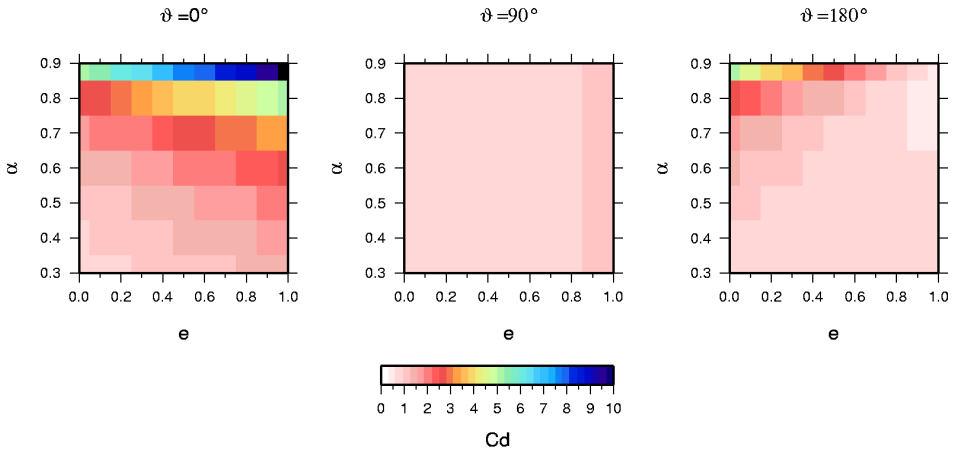

Fig.3.2.1: Resolution analysis of the C_d function for the pair of parameters (e, α) inverted for estimating best surface rupture projection.

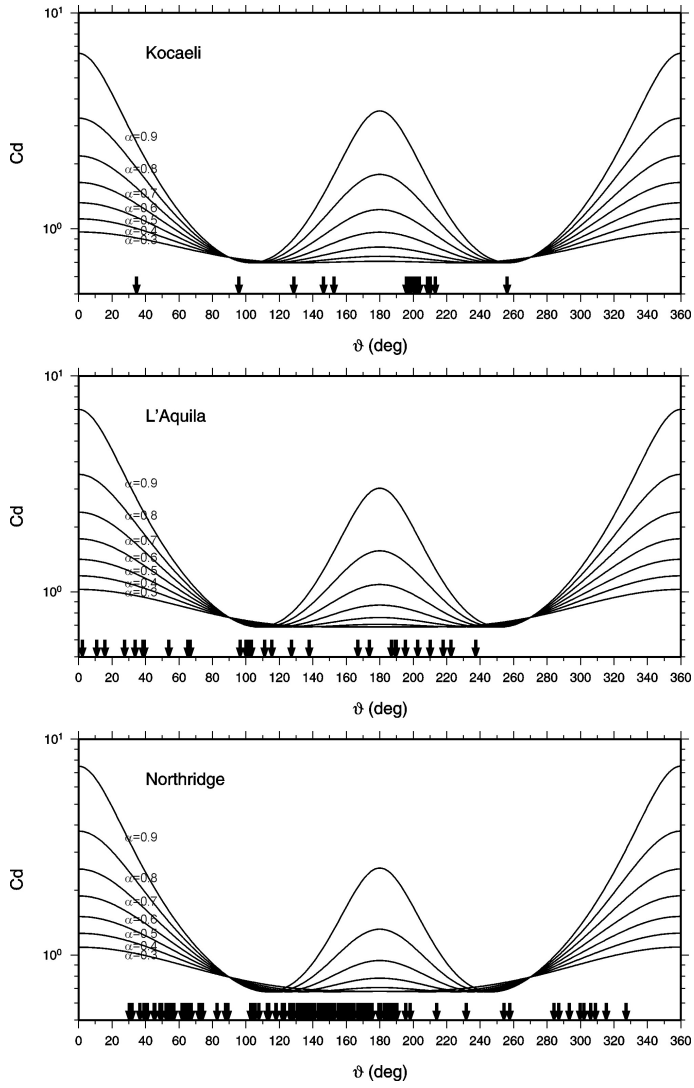

Fig.3.2.2: The C_d plot as a function of the angle ϑ between the ray leaving the source and the rupture propagation for the three earthquakes considered in the applications. The black arrows indicate the stations azimuth relative to the fault strike.

3.3 Inversion scheme and model space definition

A grid-search technique is used for determining the best model which is defined through a Bayesian approach. Each model is defined by four parameters $\boldsymbol{x}$=(L, W, e, ϕ) corresponding to: the fault length (L), the width of the fault (W), the percent unilateral rupture with respect to the fault length (e) and the dominant direction of the rupture (ϕ). By definition, the e parameter ranges between (0, 1), ϕ ranges between (0, 2π).

The approach used to select the intervals of exploration for L and W is described as follows. *A-priori* estimates of fault length, width, and area (A), as well as their standard error and associated PDFs, are computed from the Wells and Coppersmith (1994) relationships assuming a log-normal distribution. In order to optimize the grid search, the range of variation for W is conditioned to the L value by using the Bayesian approach. In particular, for a given l value in the range of variation of L, the PDF for the fault width, conditioned to fault length, is obtained by using Bayes' theorem

$$f_{w|l}(w|l) = \frac{f(l|w)g_W(w)}{\int_W f(l|w)g_W(w)\,dw} \tag{3.3.1}$$

where $g_W(w)$ is a log-normal distribution whose parameters are obtained from the Wells and Coppersmith (1994) relationships. The PDF of l given w, $f(l|w)$, is assumed to be uniform

$$f(l|w) = \frac{1}{L_2 - L_1} \tag{3.3.2}$$

Where $L_2 = \frac{A+\sigma_A}{w}$, $L_1 = \frac{A-\sigma_A}{w}$ and $A\pm\sigma_A$ corresponds to the mean fault area A value obtained from the Wells and Coppersmith (1994) relationships plus/minus one standard deviation. Finally, the intervals of variation for l and w are obtained by selecting two percentiles, p_1 and p_2, and retrieving the corresponding value from the cumulative PDF. Specifically for w, using a large p_2 value, allows the width obtained by using the Wells

and Coppersmith (1994) relationships (that corresponds to the downdip width of the fault) to be commensurate with the width of the surface fault projection that, depending on the dip-angle value, is smaller or equal to the actual width. As an example, Figure 3.3.1 shows both the PDF and cumulative PDF for L and W obtained for the application to the 17 August 1999 Mw 7.5 Kocaeli (Turkey) earthquake. Moreover, during the model space exploration the constraint $0 < W \leq L$ is imposed. W values close to zero can be used for large-magnitude strike-slip events with very long aspect-ratios. A control is also performed in order to account for sparseness of azimuthal coverage of stations around the epicenter, which plays a fundamental rule on the degree of uncertainty of the estimated parameters. Sparseness is measured by dividing the whole azimuthal range in sectors centered in the epicenter, counting the number of stations in each sector. The arithmetic sum of the angular sectors having zero stations provides the degree of sparseness (Γ). When the sparseness value Γ exceeds a given threshold, the retrieved rupture direction is considered as not reliable. As result of some preliminary tests, in the applications presented in this study, 8 sectors of 45 deg wide and a threshold of 90 deg were selected. Moreover, when the sampled rupture direction lies in a sector that does not contain stations, the condition e=0, corresponding to a bilateral rupture, is cautiously imposed. For each rupture model $\boldsymbol{x}$, the residuals between observed and predicted PGA and PGV values are estimated. In particular, the theoretical predictions are obtained by using GMPEs, accounting for the site effect through their appropriate coefficients and are corrected for the C_d factor corresponding to the sampled model. Given a model $\boldsymbol{x}$, a function $f(\boldsymbol{x})$ is defined as

$$f(\boldsymbol{x}) = k_1 e^{-misfit} \tag{3.3.3}$$

where k_1 is a constant of normalization used for $f(\boldsymbol{x})$ to be a PDF and *misfit* is given by

$$misfit = \sum_{i=1}^{Ns} \left\{ \log\left(Y_i^{obs}\right) - \log\left[Y_i^{pred} \cdot C_d(e, \vartheta_i)\right] + k_2 \right\}^2 \tag{3.3.4}$$

where Y_i corresponds to either PGA or PGV, C_d is reported in equation (3.2.1) and N_s is total number of stations. k_2 is a constant tuning parameter accounting for uncertainties on magnitude estimates, earthquake mislocation and/or site effects which may not be

properly accounted by the directivity function and GMPE. Its value ranges between plus/minus a fixed percentage of the standard error of the selected GMPE and is estimated through preliminary tests. The logarithm can be either the common logarithm or natural logarithm, depending on the selected GMPE. The dependence on *L* and *W* parameters is implicit in the Y_i^{pred} term because it is obtained by using a GMPE formulated in terms of the R_{JB}-distance. Of course, it requires that the geometry of the surface fault projection should be defined.

The function ***f(x)*** reported in equation (3.3.3) corresponds to a PDF and, as a consequence, the best model $\boldsymbol{x}_{best}$ corresponds to the model that maximizes it. The main advantage of computing ***f(x)*** as a PDF is that it provides a complete description of parameters' uncertainties and resolutions, mapping the PDF in the whole parameter space. This is particularly important for inverse problems where non-unique solutions are expected, as may be for the cases analyzed in the present thesis.

Note that, because the proposed technique has to be applied in near-real time, the only available observed quantities could be the measured PGA and PGV values, the epicentral location and the earthquake magnitude. As a consequence, in order to properly use GMPEs that adopt the R_{JB}-distance, an empirical conversion that allows to obtain the R_{JB}-distance from the epicentral distance is needed. To this aim, as proposed by Montaldo *et al.* (2005) for seismic hazard map calculation for Italy, the strong-motion database compiled in the framework of the PEER project (Chiou *et al.*, 2008) has been accessed and the following linear relationship between R_{JB}-distance and epicentral distance (R_{epi}) has been retrieved

$$R_{JB} = a + bR_{epi} \tag{3.3.5}$$

The coefficients *a* and *b* have been retrieved by a linear weighted regression, considering five different magnitude classes ranging from 5.0 to 8.0. Figure 3.3.2 shows the dataset used for the analysis, the lines corresponding to the best-fit (black lines) those corresponding to plus/minus one standard error (dashed lines). In particular, for each magnitude class, data have been grouped in bins 5km wide in R_{epi} distances. The coefficients and associated uncertainties obtained from regression are listed in Table 3.3.1. The linear correlation between the two distances decreases with both magnitude increasing and epicentral distance decreasing where the effect of fault finiteness cannot

be neglected. This is in agreement with the observation that the closest distance to the surface projection of the fault is approximately equal to the epicentral distance, for M < 6 events (Boore and Atkinson, 2008). For the sake of simplicity in the numerical implementation, we decided to use a simpler conversion modeling compared to that proposed by Wald *et al.* (2008) which uses a non-linear relationship among the two metrics and differentiates not for magnitude classes but for the ground-motion parameters. The PDF $f(\boldsymbol{x})$ reported in equation (3.3.3) allowed us to estimate parameters uncertainties through the model covariance matrix given by

$$C_M^{ij}(\boldsymbol{x}) = \int_{\boldsymbol{X}} (x_i - \langle x_i \rangle)\big(x_j - \langle x_j \rangle\big) f(\boldsymbol{x}) d\,\boldsymbol{x}\,, for\ i, j = 1,\ldots,4 \qquad (3.3.6)$$

where $\langle x_i \rangle$ and $\langle x_j \rangle$ correspond to the mean value of the parameters x_i and x_j, respectively, defined over the model space. Additionally, the covariance matrix has been also used to compute the correlation matrix in order to analyze the *a-posteriori* correlation among the parameters.

Table 3.3.1: Regression coefficients and relative uncertainty of equation (3.3.5).

Magnitude Class (Mw)	a	σ_a	b	σ_b	σ_Y	R^2
5.0-6.0	-2.406	0.709	0.936	0.007	1.282	0.999
6.0-6.5	-3.411	1.129	0.939	0.014	1.858	0.999
6.5-7.0	-10.024	2.103	1.000	0.018	6.586	0.996
7.0-7.5	-9.527	3.033	1.015	0.032	8.542	0.994
7.5-8.0	-8.566	1.028	0.691	0.019	4.978	0.989

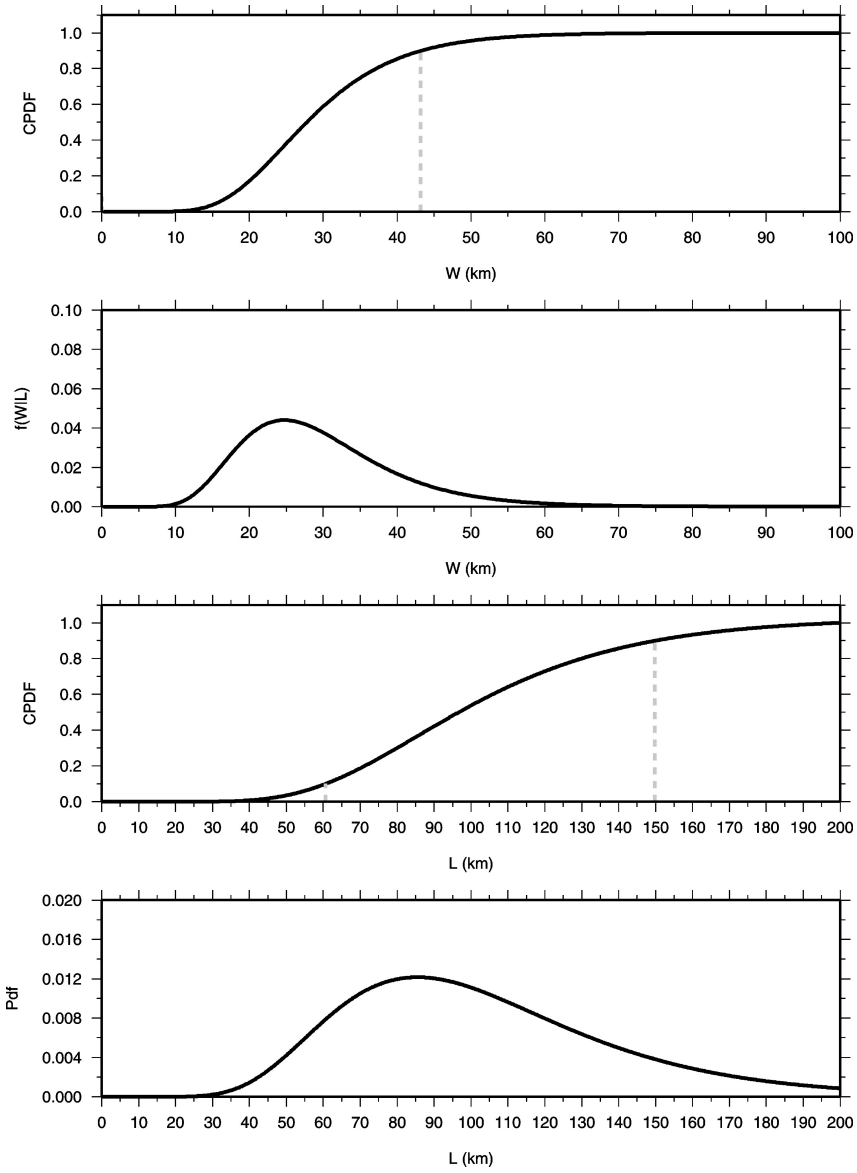

Fig.3.3.1: (Panels a and b) Conditional PDF and associated cumulative PDF governing the *W* obtained by the Bayesian approach proposed in the present thesis. Dashed lines identify the 90th percentile for *W*. (Panels c and d) PDF and cumulative PDF governing the *L* parameter obtained for the application to the 17 August 1999 Mw 7.5 Kocaeli (Turkey) earthquake (black lines) using the Wells and Coppersmith (1994) relationships. Dashed lines identify the *L* values corresponding to 10th and 90th percentile for *L*.

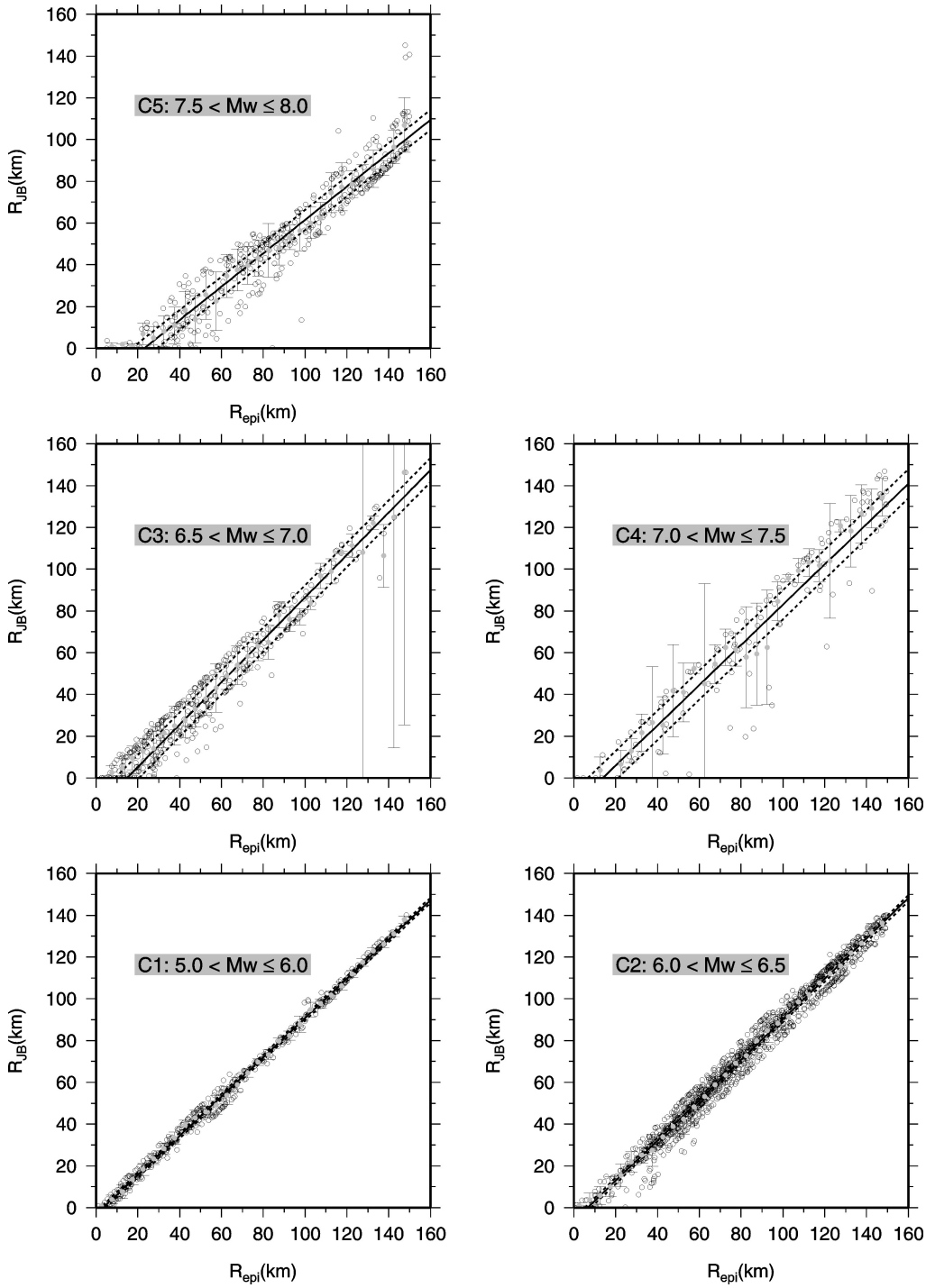

Fig.3.3.2: Relationships between epicentral distance (R_{epi}) and R_{JB}-distance for the five magnitude classes reported in each panel. Open circles correspond to the data retrieved from the PEER database while grey circles and black bars correspond to average values and associated standard errors obtained by using a 5.0 km sampling interval on the epicentral distance. Continuous black lines refer to the weighted best fitting while black dashed lines refer to $\pm 1\sigma$.

3.4 Application

The technique proposed in this thesis has been applied to three different earthquakes, which occurred in different seismotectonic settings, characterized by different fault mechanisms, and recorded by seismic networks with variable number of stations and azimuthal coverage with respect to each event location.

3.4.1 Kocaeli

The first application concerns the 17 August 1999 Mw 7.5 Kocaeli (Turkey) earthquake which was characterized by strike-slip fault mechanism Sekiguchi and Iwata (2002), The station distribution and epicenter of the Kocaeli earthquake are shown in the lower panels of Figure 3.4.1.1. The data used were retrieved from the PEER strong-motion database (Chiou *et al.*, 2008) which, for each station, also provides the NEHRP site class based on the average shear-wave velocity over the uppermost 30m (V_{S30}). PGA and PGV values were available at 31 stations. However, we selected subset of these data based on epicentral distance (ranging between 0.0 and 180.0 km) and n_σ the number of standard deviations (set at n_σ=2 in the present application) for which each data is allowed to deviate from the median value of the selected GMPE. The resulting number of stations was 20 for PGA and 16 for PGV. Open triangles in the lower panels of Figure 3.4.1.1 identify those stations that were excluded from the inversion.

For the present application, theoretical PGAs have been obtained by using the GMPE proposed by Akkar and Bommer (2007a) while PGVs were obtained by using the GMPE proposed by Akkar and Bommer (2007b). Both the GMPEs were retrieved from a European strong-motion database. The results obtained from the PGA and PGV inversion

were compared with the fault model adopted by Sekiguchi and Iwata (2002), listed in Table 3.4.1.1, which was assumed as the reference model.

In the central panels of Figure 3.4.1.1, a zoom of the maps reported in the lower panels is shown. The black line represents the assumed reference surface fault projections that, due to the vertical strike-slip fault mechanism, corresponds to a line, while grey rectangles and arrows correspond to fault projection and rupture direction, respectively, retrieved by using the technique proposed in the present thesis. In the upper panels the logarithm residuals distribution both for PGA and PGV and for both reference and estimated models, are reported. The analysis of the residuals shows that, although the dimensions of the retrieved models, that is, the surface fault projection, are different from the ones assumed as reference, they are characterized by lower residuals values. Likewise, the retrieved rupture direction well agrees with the true rupture with an approximately eastward direction. Reference and estimated parameters are listed in Table 3.4.1.1. For each parameter, the retrieved value corresponds to the value that maximizes the PDF in equation (3.3.3), while the uncertainty is obtained from the covariance matrix (equation 3.3.6). It should be noted that, for each parameter, the best model does not correspond to the average model used to compute the covariance matrix as a consequence of the fact that the function $f(\boldsymbol{x})$ does not correspond to a Gaussian PDF and may be multimodal. Additionally, in Figure 3.4.1.2, the correlation matrices for both PGA and PGV are shown. Except for L and W, for which the correlation has been imposed through the Bayes' theorem, the other two parameters are characterized by very poor positive correlation which means that each of them can be estimated independently of the respective values of the other parameters. Moreover, in this case, the uncertainty affecting one single parameter does not affect the uncertainty of the other parameters (Tarantola, 1987). On the other hand, as reported in Table 2, each parameter is characterized by a different level of uncertainty. In particular, in the present application, the largest uncertainties are on W and ϑ as a consequence of the stations distribution and several other factors, such as the space sampling adopted (in the case for the rupture direction) or the selected GMPE and its associated standard error.

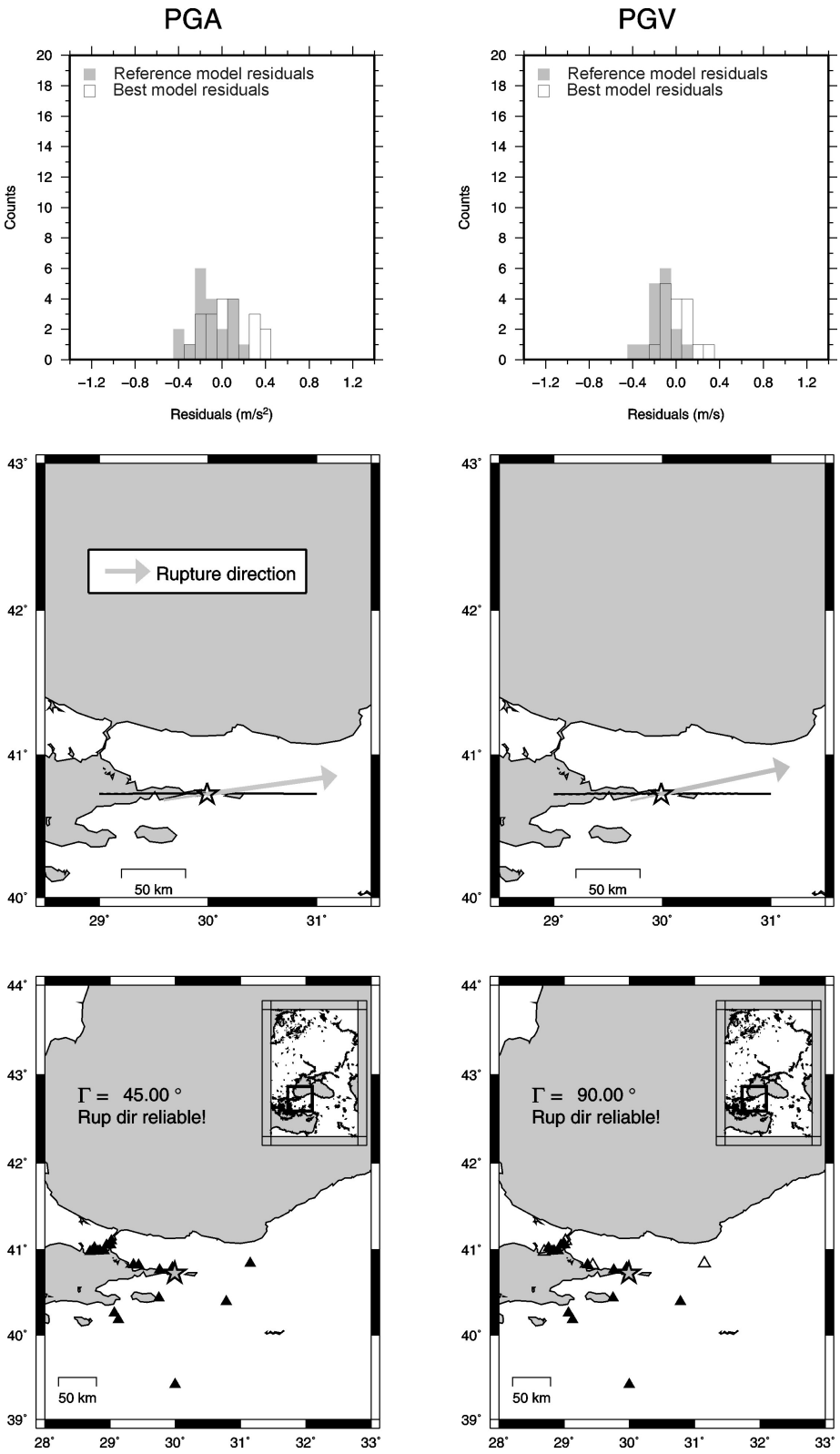

Fig.3.4.1.1: Results for the 17 August 1999 Mw 7.5 Kocaeli (Turkey) earthquake. Stations distribution (triangles) and epicentral location (star) are shown in the lower panels for both PGA and PGV. In the lower panels is also reported the sparseness value (Γ) (see text). Reference and retrieved fault surface projections, along with retrieved rupture directions are shown in the central panels. The reference model is after Sekiguchi and Iwata (2002). The logarithm residual distributions obtained by using reference and retrieved models, for both PGA and PGV, are shown in the upper panels. In particular, empty black bars refer to best model while grey bars refer to reference model.

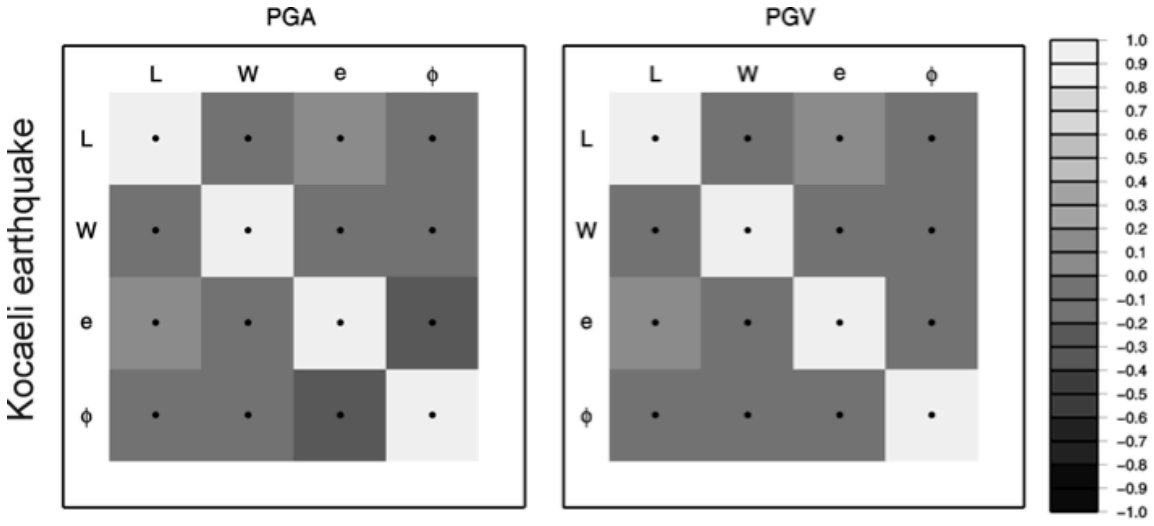

Fig.3.4.1.2: Correlation matrices for PGA (left) and PGV (right) for the 17 August 1999 Mw 7.5 Kocaeli (Turkey) earthquake.

Table 3.4.1.1: Retrieved model, for both PGA and PGV data, for the 17 August 1999 Mw 7.5 Kocaeli (Turkey) earthquake compared with the reference model. The reference model is after Sekiguchi and Iwata (2002).

	Best Model		
Parameter	PGA (m/s^2)	PGV (m/s)	Reference Model
L (km)	83±32	91 ±32	145
W (km)	0.1±15	0.1 ± 15	0
e	0.4±0.2	0.6±0.3	0.3
ϕ(deg)	82±99	78±109	------

3.4.2 L'Aquila

As second application, the proposed technique has been applied to the data recorded during the 6 April 2009 Mw 6.3 L'Aquila earthquake, in Central Italy. The used dataset consisted of PGAs and PGVs recorded at 48 stations by both Rete Accelerometrica Nazionale (RAN), managed by the Italian Department of Civil Protection (DPC) and Istituto Nazionale di Geofisica e Vulcanologia (INGV), disseminated through the online ITACA database (http://itaca.mi.ingv.it). For each station, the site classifications, retrieved from the same databases, are based on the V_{S30} following the Eurocode8 classification (CEN, 2003). The theoretical PGA and PGV values have been obtained by using the GMPE proposed by Akkar and Bommer (2007a) and Akkar and Bommer (2007b), respectively, and setting n_σ=2. The results obtained from the PGA and PGV inversions have been compared with respect to the fault model used by Cirella *et al.* (2009) as specified in Table 3.4.2.1. The results of the inversion are shown in Figure 3.4.2.1 and the parameters corresponding to the best model are provided in Table 3.4.2.1 along with their uncertainties. In contrast to the results obtained for the Kocaeli earthquake, described in the previous section, as the number of available data increases, the uncertainties on the estimated parameters decrease, particularly for W and ϑ.

In the lower panels in Figure 3.4.2.1, stations having an epicentral distance ranging from 1.0 to 100.0 km are shown. In the same figure, open triangles indicate stations that were not considered in the inversion, because the logarithm of recorded peak ground-motion value exceeded the predicted value for more than $\pm 2\sigma$, σ being the standard error of the selected GMPE. The final number of stations used in the analysis was 40 for PGA and 44 for PGV. Reference and retrieved surface fault projections for both PGA and PGV are shown in the central panels of Figure 3.4.2.1. In this example, the surface fault projections retrieved are different from the reference model and, moreover, the model obtained from PGA data is different from PGV one. This discrepancy can be partially explained by the different frequency content associated to PGA and PGV which, thus, carry information about different radiation length-scales on the fault plane as viewed by different frequency bandwidths. Additional effects represented by the hanging-wall versus foot-wall effect or peculiar site effects that cannot be fully explained by the

coefficients used in the GMPE are also likely to complicate the matter. However, the geometry obtained inverting the PGAs is fairly consistent with the position and dimension of the main slip patch retrieved by Cirella *et al.* (2009). Moreover, the retrieved rupture directions are consistent with those derived by Ameri *et al.* (2009), Atzori *et al.* (2009) and Cirella *et al.* (2009) modeling different kinds of data (strong-ground motion, co-seismic ground displacements, and GPS data). In the upper panels of Figure 3.4.2.1 the residuals distributions are shown for both the best model retrieved in the present study and the assumed reference model. As an additional feature, in the Figure 3.4.2.2, a representation of the correlation matrices is shown. As for the Kocaeli earthquake, there is very poor correlation among the parameters.

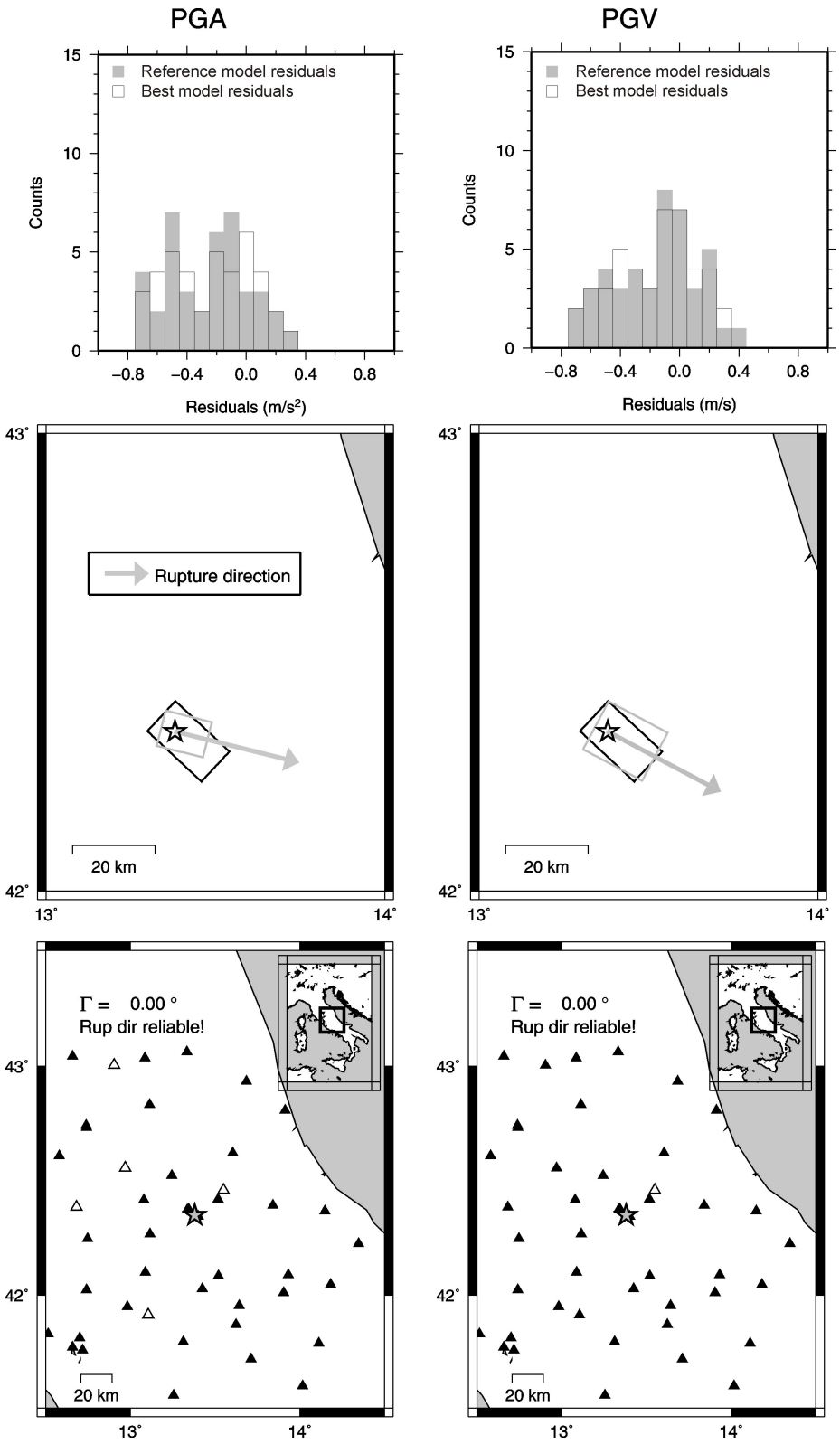

Fig.3.4.2.1: Same as Figure 3.4.1.1 but for the 6 April 2009 Mw 6.3 L'Aquila (Italy) earthquake. The reference model is after Cirella *et al.* (2009).

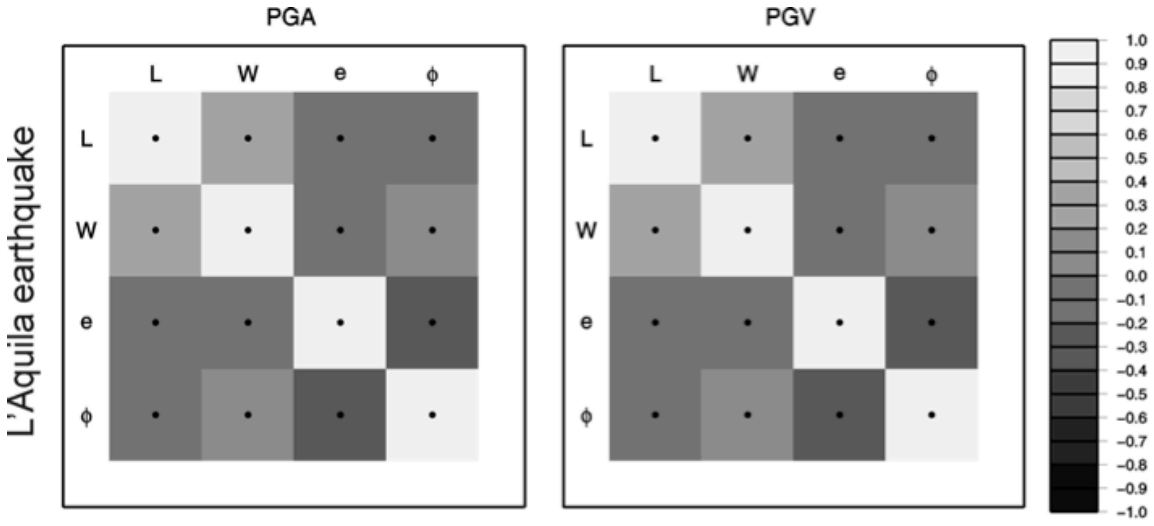

Fig.3.4.2.2: Correlation matrices for PGA (left) and PGV (right) for 6 April 2009 Mw 6.3 L'Aquila (Italy) earthquake.

Table 3.4.2.1: Same as Table 1 but for the 6 April 2009 Mw 6.3 L'Aquila (Italy) earthquake. The reference model is after Cirella *et al.* (2009).

	Best Model		
Parameter	PGA (m/s^2)	PGV (m/s)	Reference Model
L (km)	12 ± 6	16 ± 6	18
W (km)	9± 6	13 ± 6	11
e	0.4 ± 0.2	0.6 ±0.3	0.4
ϕ(deg)	104±83	118±64	------

3.4.3 Northridge

The last application is to the 17 January 1994 Mw 6.7 Northridge (California) earthquake, which represents an example of reverse faulting mechanism. Moreover, it is a very well instrumented earthquake. Recorded PGAs and PGVs and V_{S30} at 157 stations been retrieved from the PEER strong-motion database (Chiou *et al.*, 2008). The reference model has been retrieved from Wald *et al.* (1996) while the GMPE selected for the application is that proposed by Boore and Atkinson (2008). Also for this earthquake n_σ was set to 2 and stations used for the inversion resulted in 147 for PGA and 144 for PGV. As reported by Wald *et al.* (1996), the ground motion field north of the epicenter of the Northridge earthquake is mostly dominated by up-dip source directivity. As a consequence, it is expected that the proposed technique would be able to identify correctly the dominant rupture direction in that area. The results of the analysis are shown in Figure 3.4.3.1 and listed in Table 3.4.3.1. It can be noted that the retrieved rupture direction agrees with the observation of Wald *et al.* (1996) for both PGA and PGV. On the other hand, the retrieved geometries have some differences with respect to that assumed as reference model, although the residuals distributions, particularly for PGV, feature a quite similar shape. Thus, from ground-motion prediction point of view, the retrieved models provide the same results compared with the reference model. Additionally, compared with the case of the Kocaeli and L'Aquila earthquakes, a further increase of the number of stations and a more uniform distribution results in lower parameters' uncertainties.

The correlation matrices are shown in Figure 3.4.3.2. Note that the parameters have a larger anti-correlation with respect to the results obtained for the Kocaeli and L'Aquila earthquakes as a possible consequence of the difference between rupture direction and fault strike.

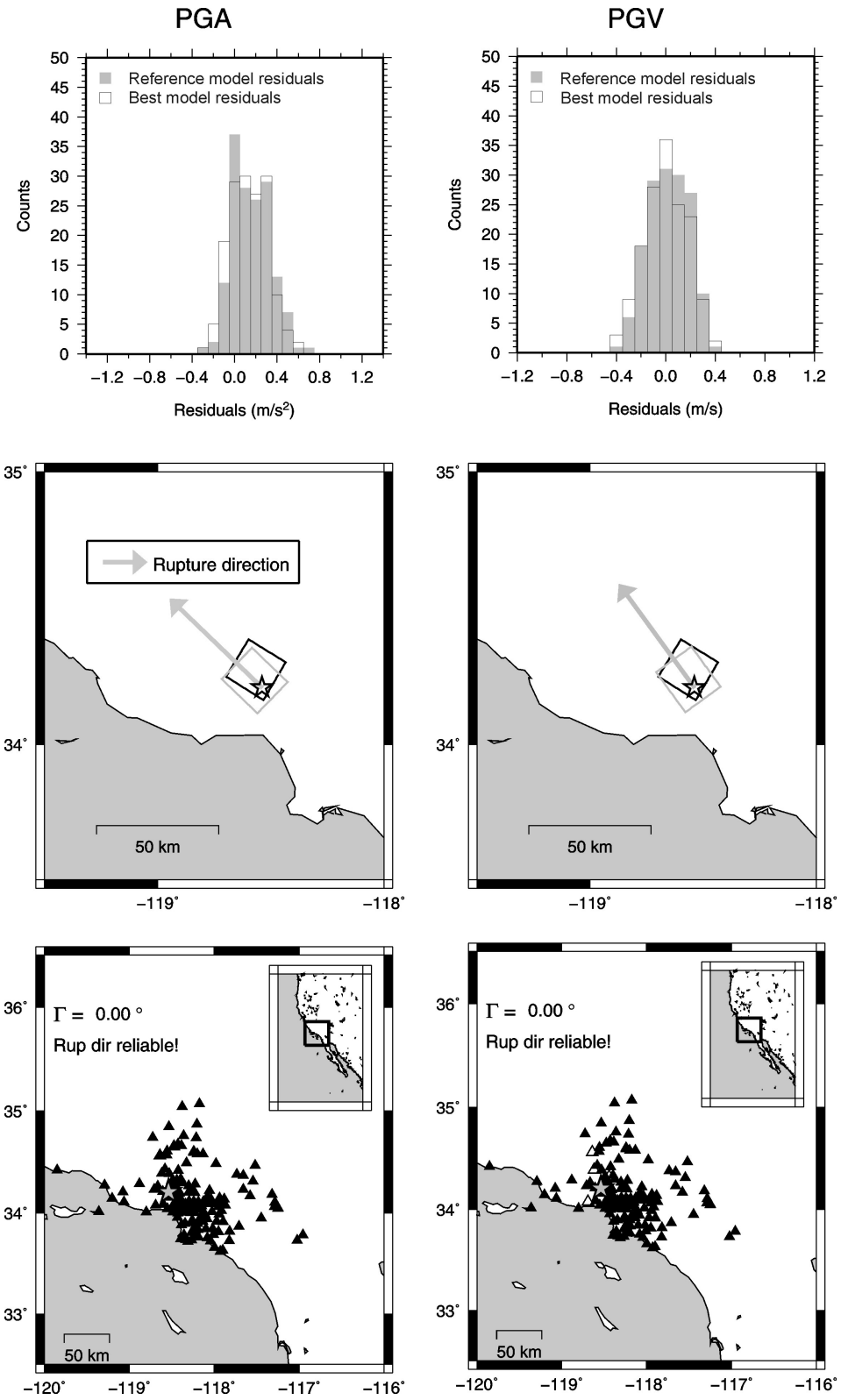

Fig.3.4.3.1: Same as Figure 3.4.1.1 but for 17 January 1994 Mw 6.7 Northridge (California) earthquake. The reference model is after Wald *et al.* (1996).

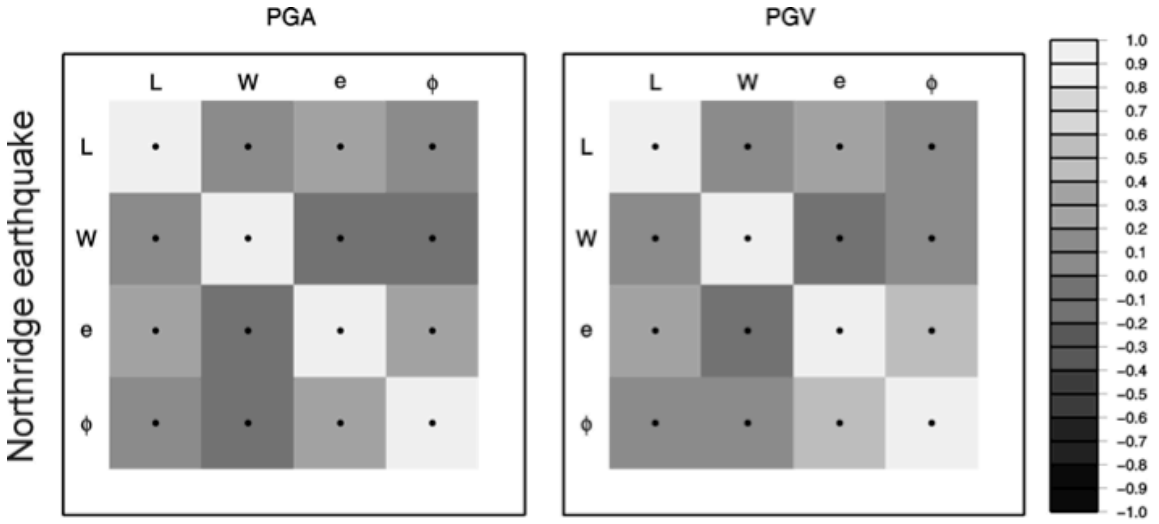

Fig.3.4.3.2: Correlation matrices for PGA (left) and PGV (right) for the 17 January 1994 Mw 6.7 Northridge (California) earthquake.

Table 3.4.3.1: Same as Table 3.4.1.1 but for 17 January 1994 Mw 6.7 Northridge (California) earthquake. The reference model is after Wald *et al.* (1996).

	Best Model		
Parameter	PGA (m/s^2)	PGV (m/s)	Reference Model
L (km)	20±10	20±10	18
W (km)	18±7	18±7	24
e	0.4± 0.1	0.4±0.2	0.5
ϕ(deg)	314±37	324±67	------

3.5 ShakeMap® computation and validation test

The final goal of the technique proposed in the present thesis is to estimate fault surface projection to be used in conjunction with GMPEs for better reproducing the recorded PGA and PGV fields in the framework of ground-shaking map calculation. Due to different sources of uncertainties, the best models retrieved in the applications described in the previous sections, show some differences with respect the models assumed as reference. In order to assess the effect of the differences between the models, for each of the three selected earthquakes, an additional validation test has been performed. In particular, for each earthquake and for both PGA and PGV, ground-shaking maps for the best models and the reference models have been calculated by using the ShakeMap code (Wald *et al.*, 1999; Wald *et al.*, 2005). The maps, expressed in percent of the acceleration of gravity *g* for PGA and in cm/s for PGV, have been computed by setting the same configuration parameters value for all the earthquakes and both reference and best models. The parameters of concern are: L1-norm for measuring the differences between observed data (reduced to bedrock) and estimated data for the bias correction, *dtresh*, *ctresh* and the final gridding step value (Wald *et al.*, 1999). On the other hand, for each earthquake, a specific GMPE and the V_{S30} map appropriate for the region of interest, have been selected to account for site effect in ShakeMap.

Once the maps have been produced, a bootstrap test similar to the one proposed by Convertito *et al.* (2010) has been performed. The test is based on the exclusion of an increasing number of stations from the initial dataset. Next, all the maps have been re-calculated and PGA and PGV values at the grid nodes closest to the excluded stations are extrapolated from the map. At each station, for both the reference and retrieved models, the residuals, defined as the difference of the natural logarithm of the observed data and extrapolated data from the ground-shaking maps, indicated as Δ(logPGA) and Δ(logPGV), are evaluated. The analysis of the residuals allowed us to quantify how the differences in the models can affect the calculated ground shaking maps. This issue is of particular relevance for those areas not covered by seismic network. In the applications proposed in the present thesis, the test has been performed by excluding 10%, 20% and 30% of initial

number of stations in each 45 deg wide (0 deg corresponding to the North) sector. The results of the bootstrap tests are shown in Figures 3.5.1, 3.5.2, and 3.5.3 for the Kocaeli, L'Aquila, and Northridge earthquakes, respectively. In each figure, the upper panels show the computed ground-shaking maps when all the stations are used, with panels a and b referring to reference model and panels c and d to the best models retrieved by using the technique proposed in the present thesis. Additionally, the arrows shown in panels c and d, indicate the best rupture directions. In the same figures, lower panels show the residuals as function of the epicentral distance when 10%, 20% and 30% of the whole stations are excluded.

As a general comment, for each of the selected earthquakes, the results of the bootstrap tests show that the ground-motion fields obtained by the reference and retrieved models do not differ significantly, providing very similar PGA and PGV distributions in areas where seismic station would not be available. This result represents an important innovation to calculate a faster and reliable spatial distribution of PGA and PGV to improve the emergency dislocation and response.

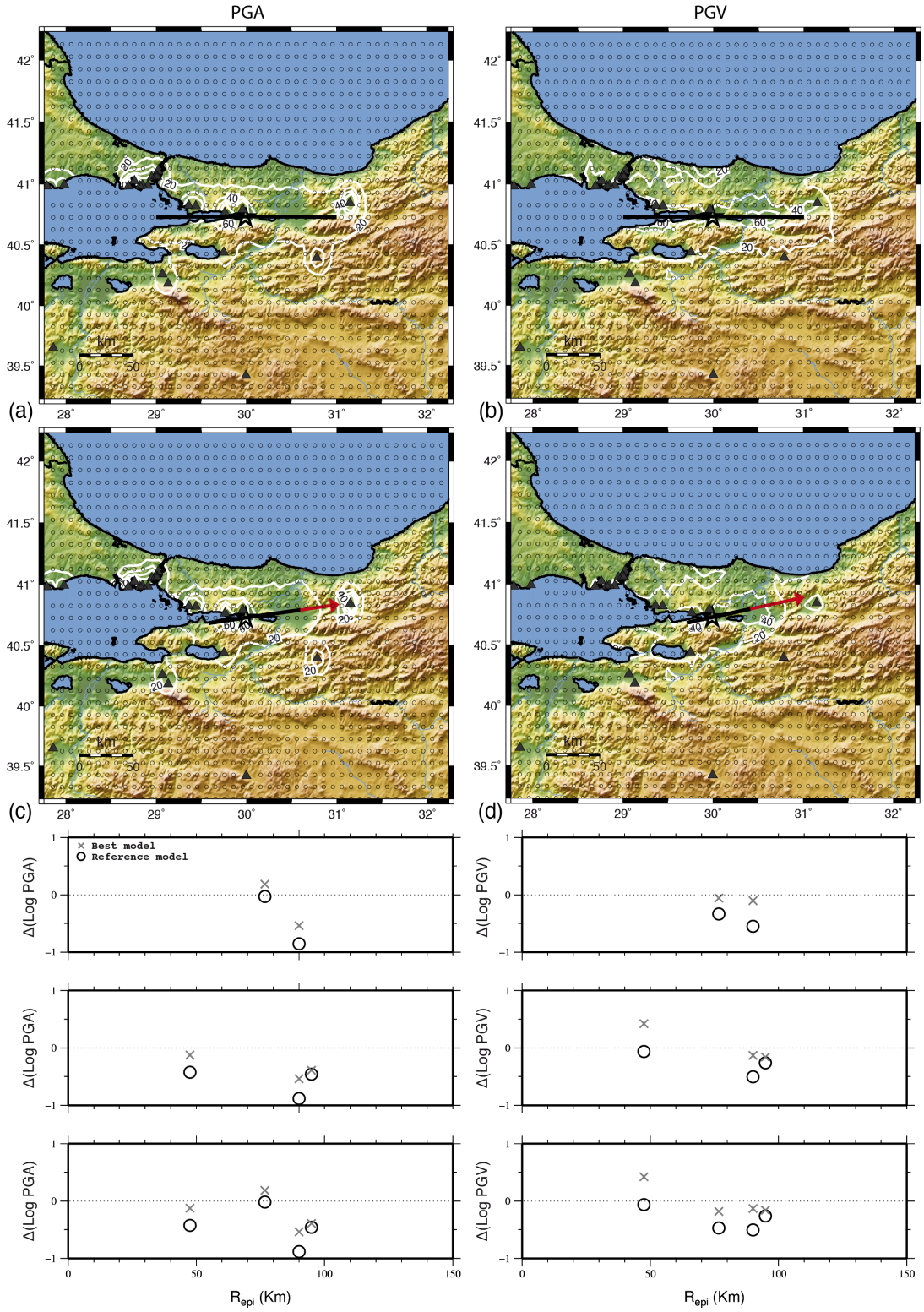

Fig.3.5.1: (Top) Ground-shaking maps for PGA and PGV for the 17 August 1999 Mw 7.5 Kocaeli (Turkey) earthquake (a, b, c, d). Black lines in panels a and b represent surface fault projections assumed as reference model, while in the panels c and d the best models obtained from PGA and PGV respectively, are shown. The star represents the epicenter, the triangles seismic stations and the circles the phantom stations used in ShakeMap. Red arrows shown in the panels c and d represent the best model rupture direction. In the bottom panel it is represented the natural logarithm residual analysis for PGA (left) and PGV (right) values, excluding the 10% (top), 20% (center) and 30% (bottom) of initial stations. Black circles refer to data extracted from the maps obtained by using the reference model, grey crosses refer to the best models.

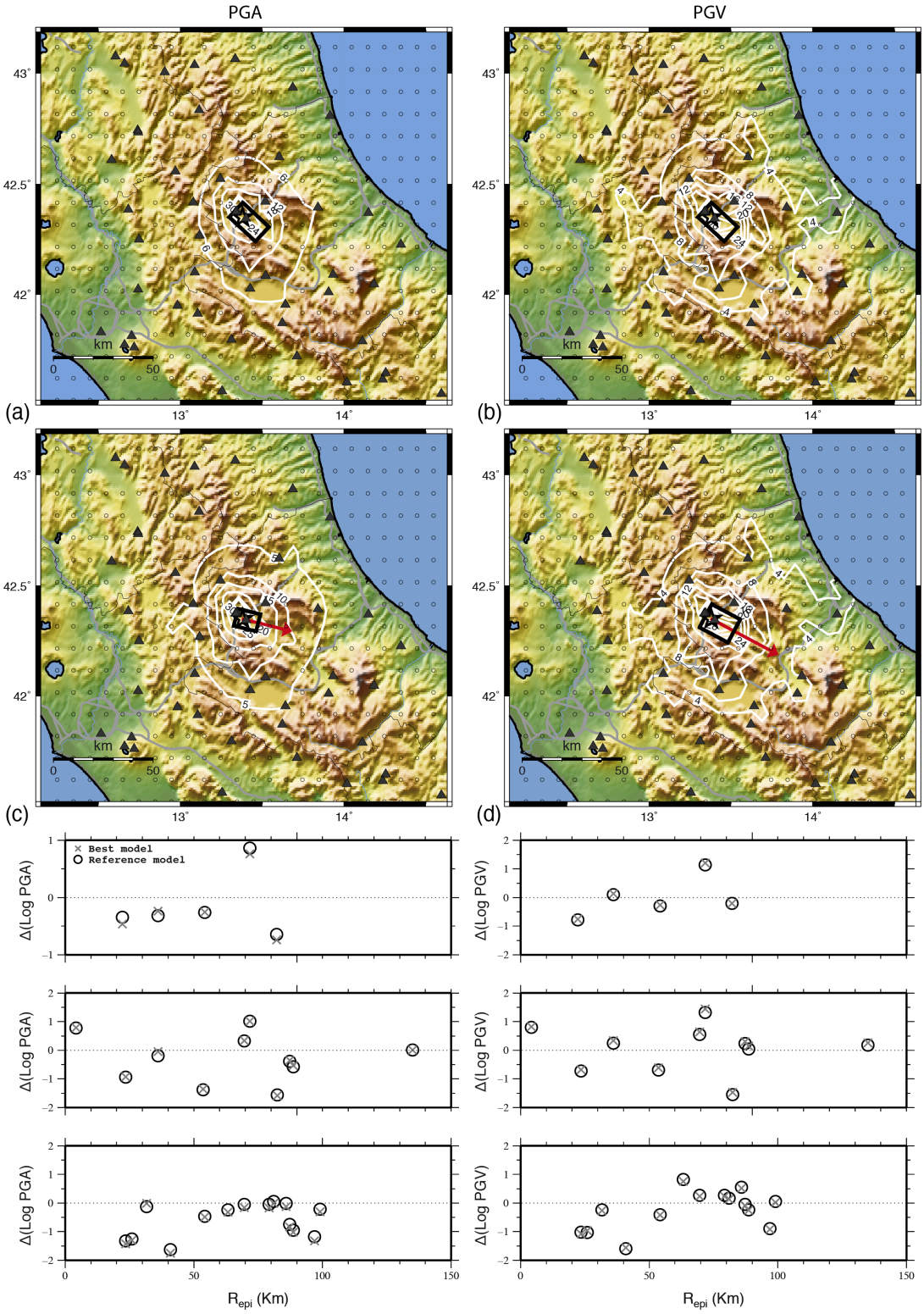

Fig.3.5.2: Same as Figure 3.5.5 but for the 6 April 2009 Mw 6.3 L'Aquila (Italy) earthquake.

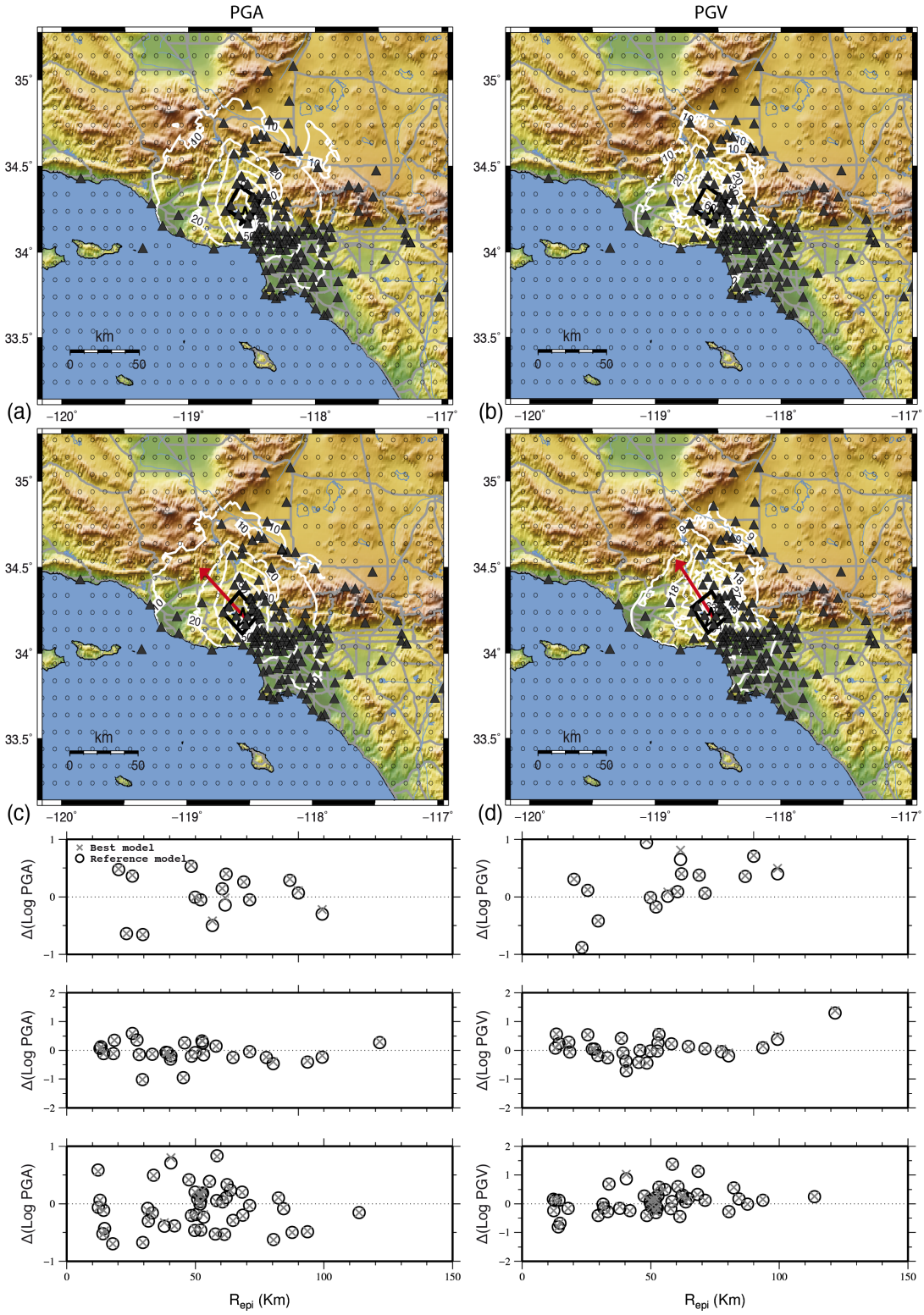

Fig.3.5.3: Same as Figure 3.5.1 but for the 17 January 1994 Mw 6.7 Northridge (California) earthquake.

3.6 Results

In the present thesis, a technique for estimating surface fault projection and source rupture direction for moderate-to-large earthquakes is presented. The technique, based on the analysis of the directivity effect on peak ground-motion parameters, can be applied in near-real time applications to improve the emergency service and and to plan the emergency actions. It uses only magnitude estimation, hypocentral or epicentral location and peak ground-motion quantities, such as PGAs and PGVs recorded during earthquakes, for retrieving surface fault projection and dominant rupture direction through a simple grid-searching exploration of the space parameter defined through a Bayesian approach. The grid-searching exploration for the case studies reported in the present thesis, on a Linux PC equipped with a 2.93GHz Intel Core2 CPU, required a processing time ranging from less than 1 minute (Kocaeli earthquake) to 2-3 minutes (Northridge earthquake).

The proposed technique has been validated using data from three different earthquakes which, occurring in different seismotectonic environments are characterized by different fault mechanisms. In particular, the 17 August 1999 Mw 7.5 Kocaeli (Turkey) earthquake was selected for application to strike-slip fault mechanism, whereas the 6 April 2009 Mw 6.3 L'Aquila (Italy) and the 17 January 1994 Mw 6.7 Northridge (California) earthquakes were selected for application in the case of normal fault and thrust fault mechanisms, respectively.

For each earthquake, the results obtained from the inversion of peak quantities are compared with respect to an *a-priori* reference model. It has to be noted that the reference model is constrained by using more comprehensive data sets (e.g., co-seismic displacement, GPS, full-waveform inversion, and so on) and information coming from moment tensor inversion and/or field observations when available. These models can substantially differ from the models retrieved by using peak-ground motion parameters. In fact, peak-ground motion parameters can carry information on the areas of largest energy radiation, which rarely coincide with the entire fault plain. In this study, depending on the complexity of the earthquakes in terms of rupture history, the results show that the models retrieved provide residuals smaller than or comparable with those obtained by using the reference models.

Additionally, as confirmed by the obtained results it should be stressed that the uncertainty level of the estimated parameters depends on the seismic network coverage, on the accuracy of the GMPE, and on the availability of information concerning site conditions at the recording stations.

Due to the goal of the technique proposed in the present thesis, i.e., to provide finite fault model to be used in ground-shaking map calculation, the ShakeMap code by Wald *et al*. (1999) has been used to obtain PGA and PGV maps and a bootstrap-like test has been performed to infer their reliability. The results of the bootstrap test confirm that, independently from the source mechanism, the retrieved models provide peak ground-motion fields at least similar to those obtained when the reference models are used. Although a test on a larger number of earthquakes could enforce and confirm the obtained results, the technique seems to be reliable to be applied in near-real time for improving the ground-shaking maps computation.

3.7 References

Ameri, G., M. Massa, D. Bindi, E. D'Alema E., A. Gorini, L. Luzi, S. Marzorati, F. Pacor, R. Paolucci, R. Puglia, and C. Smerzini (2009). The 6 April 2009 Mw 6.3 L'Aquila (Central Italy) Earthquake: Strong-motion Observations, *Seismol. Res. Lett.* **80**, 6, 951-966; doi:10.1785/gssrl.80.6.951.

Aki, K. and P. Richards (2002). Quantitative Seismology - Theory and Methods, second edition, Freeman.

Akkar, S., and J. J. Bommer (2007a). Empirical prediction equations for peak ground velocity derived from strong-motion records from Europe and the Middle East, *Bull. Seismol. Soc. Am.* **97**, 511-530, doi:10.1785/0120060141.

Akkar, S., and J. J. Bommer (2007b). Prediction of elastic displacement response spectra in Europe and the Middle East, *Earthquake Engng Struct Dyn*, **36**, 1275-1301, doi:10.1002/eqe.679.

Atzori, S., I. Hunstad, M. Chini, S. Salvi, C. Tolomei, C. Bignami, S. Stramondo, E. Trasatti, A. Antonioli, and E. Boschi (2009). Finite fault inversion of DInSAR coseismic displacement of the 2009 L'Aquila earthquake (central Italy), *Geophys. Res. Lett.* **36**, L15305, doi:10.1029/2009GL039293.

Beyer, K., and J. J. Bommer (2006). Relationships between median values and between aleatory variabilities for different definitions of the horizontal component of motion, *Bull. Seismol. Soc. Am.* **96**, 1512–1522, doi:10.1785/0120050210.

Boatwright, J. (1982). A dynamic model for far-field acceleration, *Bull. Seismol. Soc. Am.* **72**, 1049–1068.

Boatwright, J. (2007). The persistence of directivity in small earthquakes, *Bull. Seismol. Soc. Am.* **97**, 1850–1861, doi:10.1785/0120050228.

Boore, D. M., and G. M. Atkinson (2008). Ground-motion prediction equations for the average horizontal component of PGA, PGV, and 5%-damped PSA at spectral periods between 0.01 s and 10.0 s, *Earthq. Spectra* **24**, 1, pp. 99-138, doi:10.1193/1.2830434.

CEN, European Committee for Standardisation (2003), Eurocode 8: design provisions for earthquake resistance of structures, Part 1.1: general rules, seismic actions and rules for buildings, prEN 1998-1.

Chiou, B. S. J., R. Darragh, and W. Silva (2008). An overview of the NGA database, *Earthq. Spectra* **24**, 23-44.

Cirella, A., A. Piatanesi, M. Cocco, E. Tinti, L. Scognamiglio, A. Michelini, A. Lomax, and E. Boschi (2009). Rupture history of the 2009 L'Aquila (Italy) earthquake from non-linear joint inversion of strong motion and GPS data, *Geophys. Res. Lett.* **36**, L19304, doi:10.1029/2009GL039795.

Convertito, V., R. De Matteis, L. Cantore, A. Zollo, G. Iannaccone, and M. Caccavale (2010). Rapid estimation of ground-shaking maps for seismic emergency management in the Campania Region of southern Italy, *Nat Hazards* **52**, 97-115, doi:10.1007/s11069-009-9359-2.

Cua, G. (2005). Creating the virtual seismologist: developments in earthquake early warning and ground motion characterization, *Ph. D. Thesis*, Department of Civil Engineering, California Institute of Technology.

de Lorenzo, S., and A. Zollo (2003). Size and geometry of microearthquake seismic ruptures from P and S pulse width data, *Geophys. J. Int.* **155**, 422-442.

Dreger, D., and A. Kaverina (2000). Seismic remote sensing for the earthquake source process and near-source strong shaking: a case study of the October 16, 1999 Hector Mine earthquake, *Geophys. Res. Lett.* **25**, 13, 1941-1944.

Eurocode 8 (2003). Design of structures for earthquake resistance CEN European Committee for Standardization, Bruxelles, Belgium.

Frez, J., F. A. Nava, and J. Acosta (2010). Source rupture plane determination from directivity doppler effect for small earthquakes recorded by local networks, *Bull. Seismol. Soc. Am.* **100**, 289–297, doi:10.1785/0120090139.

Hanks, T. C., and R. K. McGuire (1981). The character of high-frequency strong ground motion, *Bull. Seismol. Soc. Am.* **71**, 2071-2095.

Hirazawa, T., and W. Stauder (1965). On the seismic body waves from a finite moving source, *Bull. Seismol. Soc. Am.* **55,** 237-262.

Joyner, W. B. (1991). Directivity for non-uniform ruptures, *Bull. Seismol. Soc. Am.* **81**, 1391-1395.

Joyner, W. B., and D. M. Boore (1981). Peak horizontal acceleration and velocity from strong-motion records including records from the 1979 Imperial Valley, California, earthquake, *Bull. Seismol. Soc. Am.* **71**, 2011-2038.

Miyake, H., T. Iwata, and K. Irikura (2001). Estimation of rupture propagation direction and strong motion generation area from azimuth and distance dependence of source amplitude spectra, *Geophys. Res. Lett.* **28**, 14, 2727-2730.

Montaldo, V., E. Faccioli, G. Zonno, A. Akinci, and L. Malagnini (2005). Treatment of ground-motion predictive relationships for the reference seismic hazard map of Italy, *J. Seismol.* **9**, 295-316.

Rowshandel, B. (2010). Directivity Correction for the Next Generation Attenuation (NGA) Relations, *Earthq. Spectra* **26**, 525-559; doi:10.1193/1.3381043.

Sekiguchi, H., and T. Iwata (2002). Rupture process of the 1999 Kocaeli, Turkey, earthquake estimated from strong-motion waveforms, *Bull. Seismol. Soc. Am.* **92**, 300-311.

Somerville, P.G., Smith, N.F., Graves, R.W., and N.A Abrahamson, (1997). Modification of empirical strong ground motion attenuation relations to include the amplitude and duration effects of rupture directivity, *Seismol. Res. Lett.* **68**, 199-222.

Spudich, P., B.S.J. Chiou, Graves, R.W., Collins, N. and P. Somerville, (2004). A Formulation of Directivity for Earthquake Sources Using Isochrone Theory, U.S. Geological Survey Open-File Report 2004–1268, 54p.

Spudich, P., and B.S.J. Chiou, (2008). Directivity in NGA earthquake ground motions: Analysis using isochrone theory, *Earthq. Spectra* **24**, 279 -298, doi:10.1193/1.2928225.

Tarantola, A. (1987). Inverse problem theory: methods for data fitting and model parameter estimation, Elsevier Science Publisher, Amsterdam, 1987, 613 pp.

Venkataraman, A., and H. Kanamori (2004). Effect of directivity on estimates of radiated seismic energy, *J. Geophys. Res.* **109**, B04301, doi:10.1029/2003JB002548.

Wald, D. J., T. H. Heaton, and K. W. Hudnut (1996). Rupture history of the 1994 Northridge, California earthquake from strong-motion, GPS, and leveling data, *Bull. Seismol. Soc. Am.* **86**, S49-S70.

Wald, D. J., V. Quitoriano, T. H. Heaton, H. Kanamori, C. W. Scrivner, and C. B. Worden (1999). TriNet ShakeMaps: Rapid generation of instrumental ground motion and intensity maps for earthquakes in southern California, *Earthq. Spectra* **15**, 537-555.

Wald, D. J., B. C. Worden, K. Lin, and K. Pankow (2005). "ShakeMap manual: technical manual, user's guide, and software guide." U. S. Geological Survey, Techniques and Methods 12-A1, 132 pp.

Wald, D. J., K. Lin, and V. Quitoriano (2008). Quantifying and qualifying ShakeMap uncertainty, U.S. Geological Survey Open-File Report 2008-1238, 27p.

Wells, D. L., and K. J. Coppersmith (1994). New empirical relationships among magnitude, rupture length, rupture width, rupture area, and surface displacement, *Bull. Seismol. Soc. Am.* **84**, 974-1002.

Wessel, P., and W. H. F. Smith (1991). Free software helps map and display data, EOS Trans. AGU **72**, 441, 445-446.

Yamada, M., and T. H. Heaton (2008). Real-time estimation of fault rupture extent using envelopes of acceleration, *Bull. Seismol. Soc. Am.* **98**, 2, 607-619, doi:10.1785/0120060218.

Yamada, M., T. Heaton, and J. Beck (2007). Real-time estimation of fault rupture using near-source versus far-source classification, *Bull. Seismol. Soc. Am.* **97**, 6, 1890-1910, doi:10.1785/0120060243.

Zollo, A., and S. de Lorenzo (2001). Source parameters and 3-D attenuation structure from the inversion of microearthquake pulse width data: Method and Synthetic tests, *J. Geophys. Res.* **106**, B8, 16287-16306.

Capitolo 4

Project of a stand alone Earthquake early warning system

4.1 Introduction

The occurrence of a seismic event always induces a strong socio-economic impact for the involved areas. The strong ground-shaking effects, due to the propagation of elastic waves, strongly stimulate the interdisciplinary research (physical, seismology, mathematics, geology, engineering, etc.) with the aim to mitigate the seismic hazard.

The Earthquake Early Warning Systems (EEWS) plays a relevant role for an effective and efficient protection from catastrophic consequences of the occurrence of a serious seismic event.

In the last two decades the technological innovations allows developing and implementing EEWS in many active seismic region of the world, due to seismic hazard.

The EEWS represents a technological challenge because in the real time scale it is not possible perform the signal analysis to define all the seismic parameters. Moreover the warning times necessary to start manual or automatic operations to reduce the collateral damages are of the order of few seconds.

An EEWS can be represented as an instrument or a more complex system able to identify an earthquake and produce a rapid notification of the potential damaging effects due to the incoming seismic waves. A simple buzzer or light can be useful for a rapid notification, for prevention or emergency, but EEWS is able to perform also automatic procedure like shutdown of critical systems such as lifts, high-speed trains, start-up generators.

A relevant aspect of an EEWS is the social preparedness associated with a sufficient warning time. In this case few seconds are enough to reach a safer position, to avoid panic and to improve rescue operations.

Furthermore, if the EEWS is designed to share information with a monitor centre, within seconds after an earthquake it is possible to know the spatial distributions of the ground shaking intensity and possible damage. This information is the base for a more efficient emergency response and rescue activity.

The idea of EEWS was developed by Cooper in 1868 for San Francisco, California. Cooper proposed to install a network of seismic detectors in the epicentral area, located outside the San Francisco area. In case of earthquake in the epicentral area an electric signal would be sent to San Francisco by telegraph line. The signal received in the City

Hall activates the ring of a bell to alert the population. Unfortunately, the first EEWS was design and implemented only about 100 years later.

The EEWS are based on physical characteristic of seismic and electromagnetic waves that travel with different velocity. An electric impulse sent by air, satellite or wire to transmit information about incoming earthquake, travel faster (about 300000Km/s) than seismic wave (about 3-7Km/s). Therefore an alert signal is potentially able to reach a strategic site before the seismic tremor. In addiction, between the first seismic wave identified (P-waves) and the most energetic once (S-waves) there is a velocity gap (about 3-4 Km/s) (Figure.4.1.1) that can be exploited as the time interval in which it is possible to activate the safe procedure.

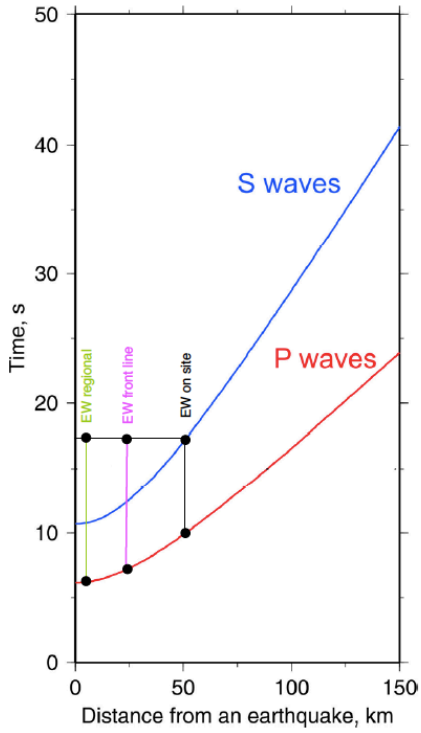

Figure 4.1.1. P and S-wave arrival time as a function of the distance from an earthquake.

The EEWS works in the real-time seismology and must be able to collect and analyse the seismic data as fast as possible to recognize and inform about an incoming earthquake. As reported by Kanamori (2004) for EEWS the “regional” and “on-site” (or site-specific) approaches are possible.

A “regional” EEWS is based on seismic stations network covering a seismogenic area. The event location and magnitude are estimated using the first second of recorded signal and are used to estimate the ground motion intensity at a target structure located at a

distant site. On the other hand an “on-site” EEWS is based on a single seismic station or an array of stations located at target structure. For this configuration the peak ground motion amplitude (acceleration, velocity or displacement) and/or predominant period on the initial *P*-wave motion are used to predict the peak ground motion at the same site.

A fine EEWS must be able to identify an earthquake before the arrival of the damaging waves, send an alert notification and at same time to reduce the error of peak ground motion estimation (Zollo et al., 2009a,b)

The Japanese Railway developed in 1960’s a system to avoid trains derailment during strong earthquake that at the present represents the most important EEWS in the world (Nakamura, 1988). The main characteristic of this EEWS is its configuration. The system is constituted by a large number of seismometers collocated along and connected with the railway to control the train operation during an earthquake.

A technological aspect of the earthquake early warning considered in the framework of this PhD thesis concerns the development of an EEWS able to integrate both regional and on-site approaches (Fig.4.1.2) based on the real-time measurement of peak displacement and predominant period on early P-wave signals (see Cap.4.2 for more details). Using the threshold-based method (Zollo *et al*., 2010) the system can provide a rapid estimation of the PDZ, by-passing the magnitude estimation for ground motion prediction. Moreover it can be easily integrated with a more standard regional method (e.g. PRESTo; Satriano et al., 2010).

The most critical issue for an EEWS is the choice of the data transmission system. It is well known that the satellite transmission is slow (Time delay ≈ 2s) for early warning purpose, expensive and difficult to be implemented; moreover the radio links are not suitable for streaming due to band limitations. Proprietary WI-FI and/or GPRS/UMTS are the preferred solutions because they are able to reduce the time transmission and to increase the lead-time (the time between the alert notification and the arrival time of potentially destructive waves at a given target site). Another critical issue like the sensor and Analog-to-Digital Converter (ADC) choice should be taken into account for the realization of an EEWS. The last year of this PhD thesis was devoted to the development of a prototype node for an EEWS based on Micro-Electro-Mechanical Systems (MEMS) sensor technology. Three different axial accelerometers have been tested in combination with several ADC (12, 14, 16, 18, 24 bit) to define the optimum hardware configuration in terms of cost, energy consumption, size, dynamic range, to detect events of moderate-strong intensity ($I_{MM} \geq$ VI-VII).

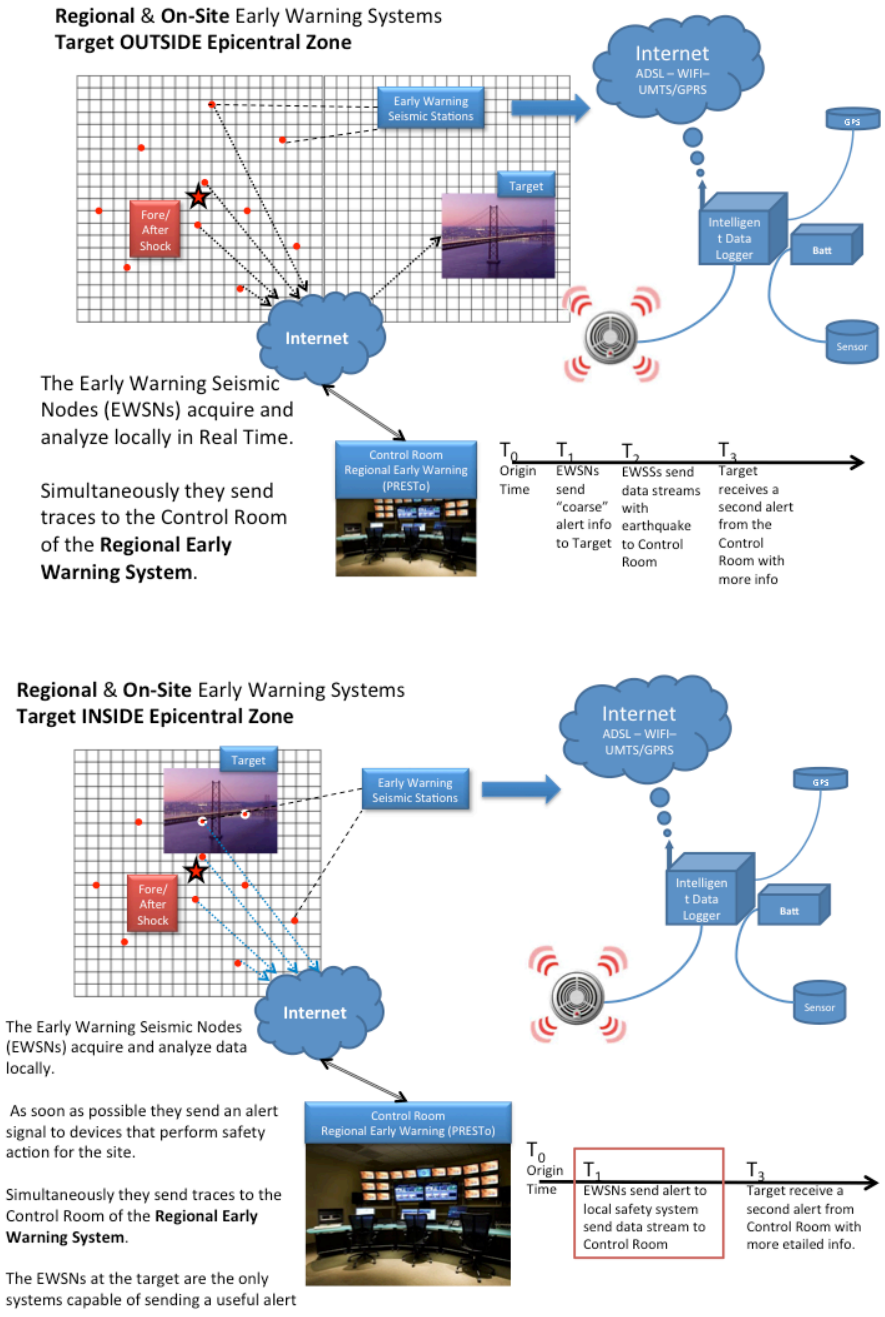

Figure 4.1.2 Example of Regional and On-Site Early Warning System. The scenario with the target outside the epicentral zone (top): during earthquake each node (red point) acquire and analyse data in real-time and send an "coarse" alert signal to the target. Simultaneously they send traces to the control room of the regional early warning system. The control room send a second alarm to the target with more information. The scenario with the target inside the epicentral zone (bottom): during earthquake each node (red point) acquire and analyse data in real-time and send an alert signal to the target. Simultaneously they send traces to the control room of the regional early warning system.

4.2 EEWS-Box project study

In the last two decades a lot of systems were developed to recognize an earthquake within the first seconds of the incoming signal and to activate the necessary operations. In this case the timeliness is a fundamental requirement to contribute to the mitigation of casualties and damages. The set up of a system able to operate in real time is not an easy task because the algorithms must be robust and moreover up to now the hardware is not cheap enough to permit a large diffusion over a large area. The timeliness, diffusion and costs are the main concerns of all EEWS and the relationship of these three variables can vary as a function of the plan target (seismic study or alert system).

The EEWS-Box project comes from the necessity to understand the possibility to develop a stand alone EEWS with a "strong" hardware and cheap. A target for the EEWS-Box in terms of magnitude (M) and distance (R) of the earthquake recognized by the system should be defined, in order to select the suitable hardware, that represents a key point for the development of the EEWS-BOX. To perform a real time analysis it is necessary to assembly a DSP (Digital Signal Processing) and a CPU (Central Process Unit) in combination with an ADC (Analogue to Digital Converter) to convert the continuous seismic signal in a digital one with enough bits. The most important hardware component of an EEWS is the sensor that must be able to record weak and strong earthquakes, but it should not be expensive or big.

The problem of the right ADC, in terms of number of bit, and the sensor selection are coupled. For instance the use of a very sensitive sensor, able to recognize very weak motions, coupled with the digitalization of this information with a large bin[1] (low bit) is meaningless because it represents a waste of information for the system.

A set of analysis was performed on an earthquakes database in order to define the M-R target and the proper ADC/sensor coupling.

The seismic signal dataset was formed by a relevant numbers of events recorded by ISNet[2] and Kik-net[3] seismic networks with a large range of magnitude and epicentral

[1] Interval between two different amplitude level.
[2] http://isnet.na.infn.it/cgi-bin/isnet-events/isnet.cgi
[3] http://www.kik.bosai.go.jp

distance (Fig.4.2.1 and Fig.4.2.2).

The first analysis performed consists in the re-quantitation of seismic signal recorded at 24 bit. The results of this analysis represent an approximation of the seismogram recorded with a different number of bit. An example of seismic signal converted from 24 to 14, 16 and 18 bit, for an earthquake of magnitude 2.6 M_w recorded at 8.99 Km, is reported in Figure (4.2.3). From the Figure it is possible to note the information loss due to a low bit number. For this specific case (low distance and magnitude) it is possible to observe that the first part of the two signal appears to be very similar, but the tail results too much degenerated to retrieve information.

A qualitative test was performed by analysing the cross-correlation plots between the real seismic signal (24 bit) and the re-quantitated signal (14, 16 and 18 bit) reported in this thesis only for three stations for each earthquakes. For sake of brevity only the results for three different earthquakes [4] were reported. The test has evidenced that a signal degeneration occurs with the distance; this trend is more evident at low magnitude.

For each signal (24, 14, 16 and 18 bit) the PSD (Power Spectral Density) in decibel was calculated and plotted in terms of frequency with respect to low and high global noise level (Peterson, 1993). The analysis shows that for magnitude grater than 2.5/3.0 and for distance up to 200 Km (for M_w 7.2) the PSD decibel values (14, 16, 18, 24 bit) are lower than the global high noise curve and the shape looks like not flat as usually observed for seismic amplitude correctly recorded. As a consequence of this evidence the low bit seismic signal appears equivalent to the original signal (24 bit). For magnitude lower than 2.5 the same consideration are still valid only at very short distance as shown in Figure (4.2.34-37), where the PSD at 16 bit for different distance and fixed magnitude or different magnitude and fixed distance are reported.

At least a double integration was performed for the 24 and 16 bit signal to pick out the information loss due to the signal elaborations. Also in this case the degeneration of the signal appears evident at great distance and/or at low magnitude.

Two different sensors were considered during the preliminary study for the EEWS-BOX. The first one was a Guralp[5] accelerometer, a professional and expensive sensor, while the second one was an experimental multi MEMS system[6]. These sensors was used to record 24h of ambient seismic noise in a quite site located at Physic Department of University of

[4] Iwate-Miyagi (Japan) 2005/12/17 (Fig.4.2.4-13); Laviano (Italy) 2008/05/27 (Fig.4.2.14-23); Iwate-Miyagi (Japan) 2008/06/14 (Fig.4.2.24-33);

[5] http://www.guralp.com/products/5TC/

[6] No details available

Naples. The data acquired at 24 bit was converted to 16 bit and the PSD (16 and 24 bit) for 2h of signal (in different times) was reported in Figure (4.2.38-41).

The analysis performed shows that, independently from seismic sensor (Guralp or MEMS) the PSD decibel values are lower than the global high noise curve. In addition can be noted that the MEMS signal appears flat and without significant variation at different times and/or at different number of bit. It can be concluded that the low bit seismic signal is not a good candidate for the seismic noise study.

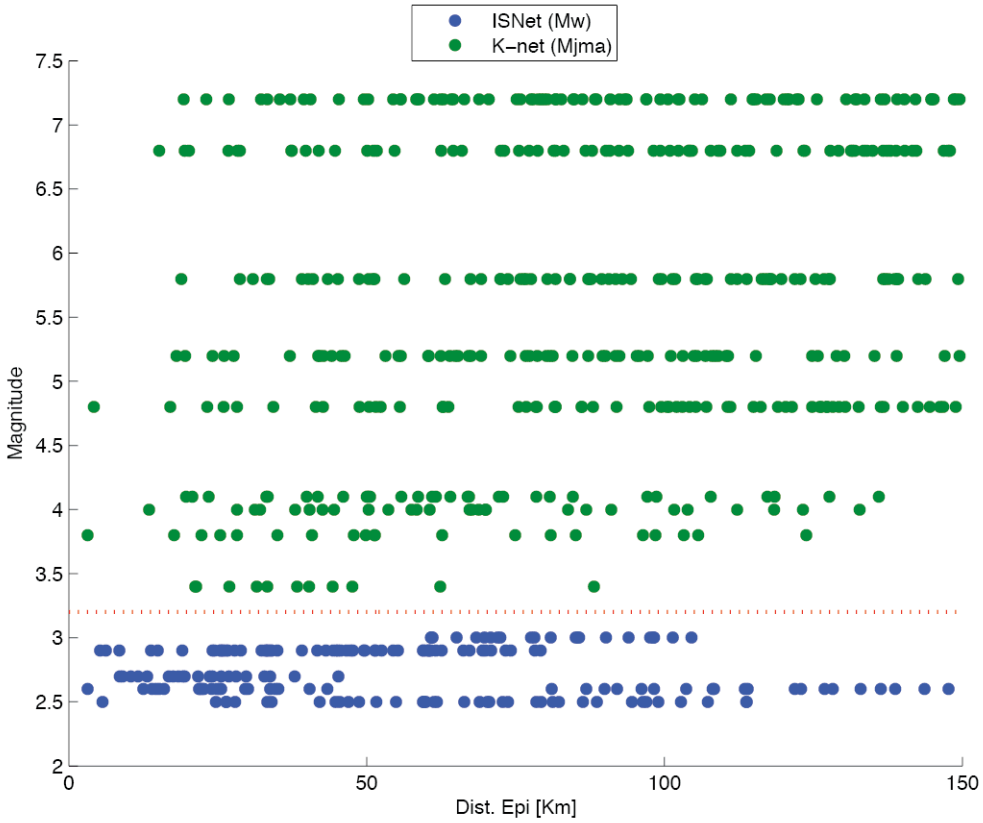

Figure 4.2.1. Distribution of earthquakes database as functions of magnitude and epicentral distance (Dist. Epi). The blue circles represent the ISNet records and the green circles represent the Kik-net records.

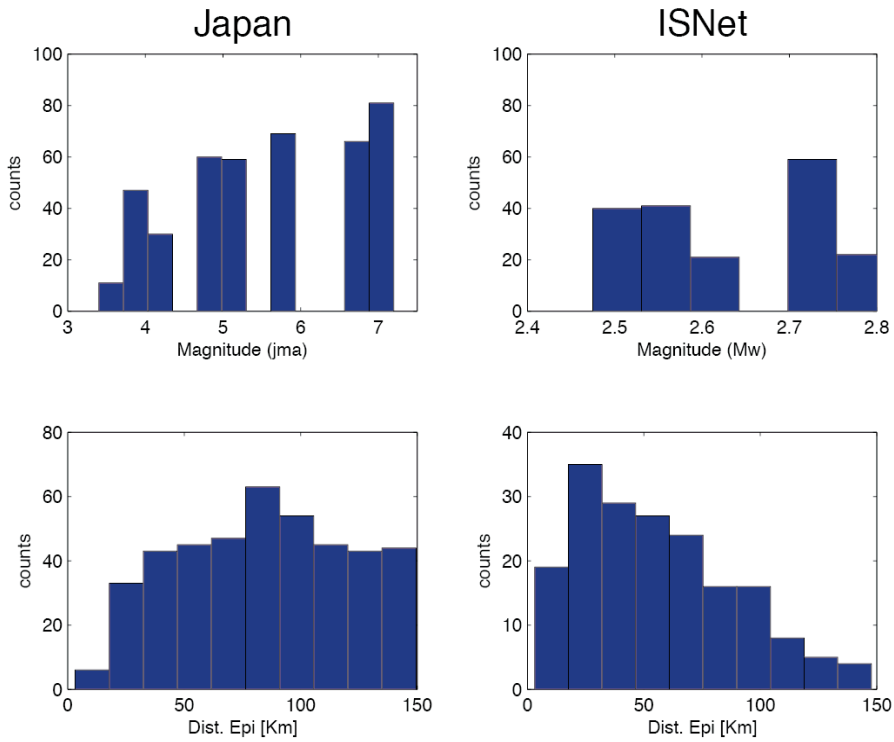

Figure 4.2.2. Magnitude (Top) and epicentral distance (Bottom) distributions histograms for the analysed earthquake retrieved from kik-net database (Left) and ISNet database (Right).

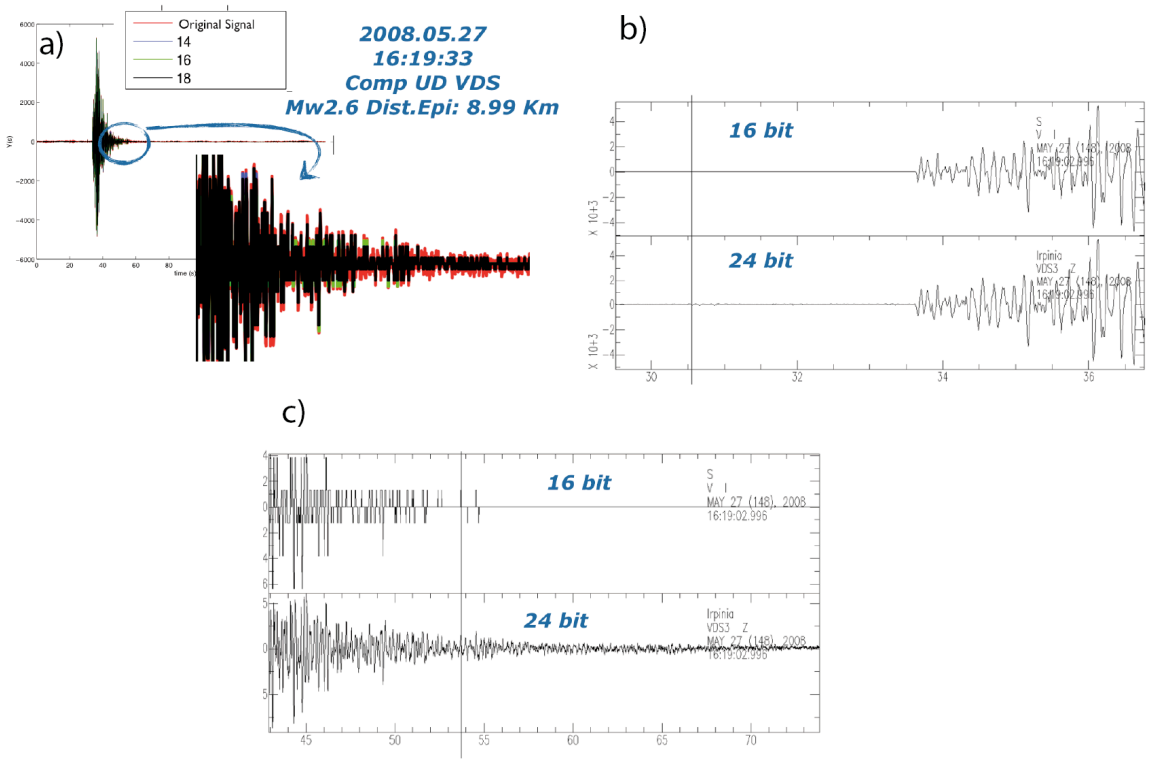

Figure 4.2.3. a) Seismograms at different number of bit (14, 16, 18) and the original signal for the vertical component (UD) of VDS station. b) Seismograms at 16 and the original signal (24 bit) for the vertical component (UD) of VDS station; zoomed on first P wave arrive. c) Seismograms at 16 and the original signal (24 bit) for the vertical component (UD) of VDS station; zoomed on the signal tail.

Iwate-Miyagi (Japan) 2005/12/17

The first application concerns the 17 December 2005 M_{jma} 3.8 Iwate-Miyagi (Japan) earthquake. The station distribution and epicenter of the Iwate-Miyagi earthquake are shown in Figure 4.2.4. The data used were retrieved from the Kik-net database.

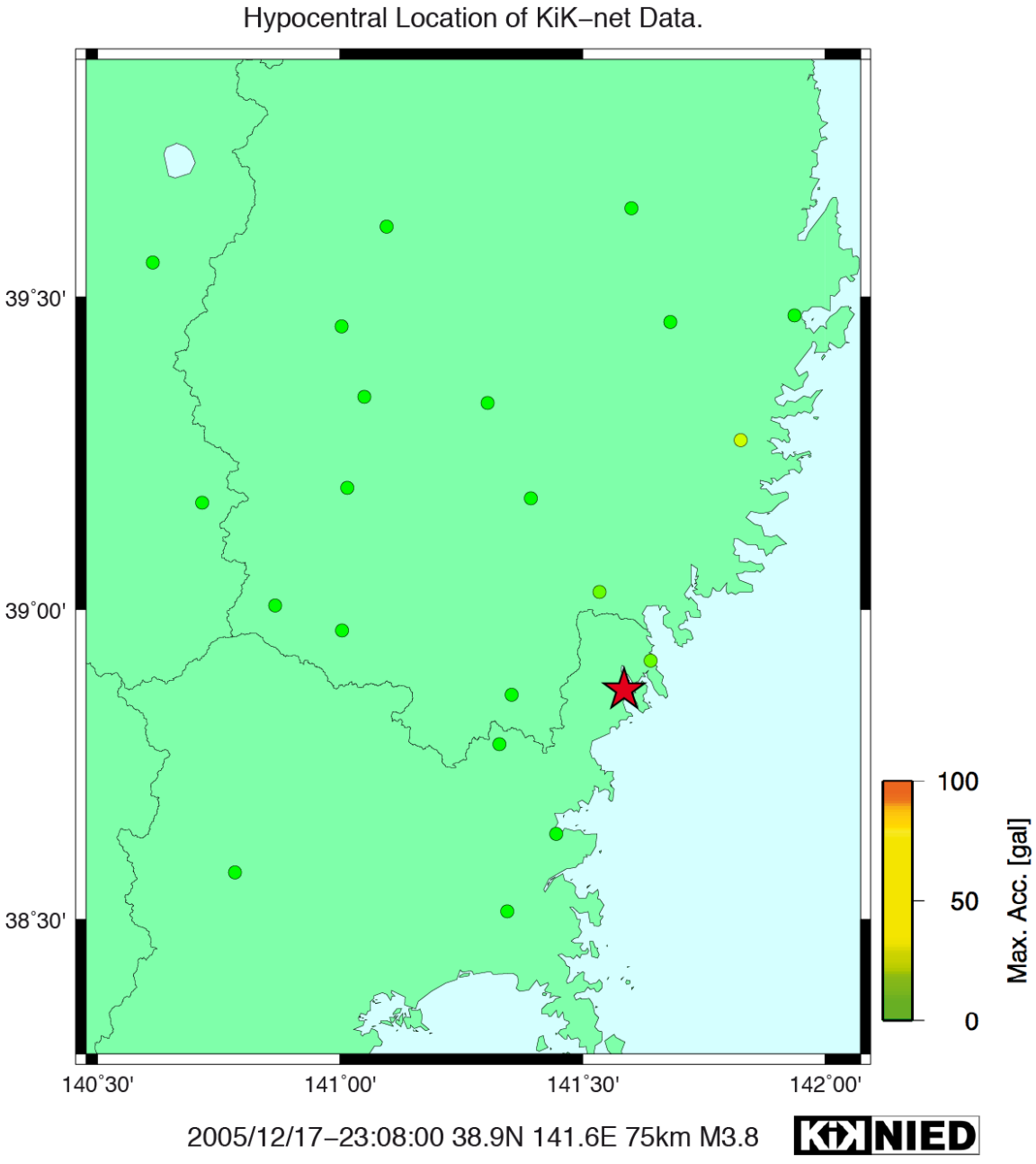

Figure 4.2.4. Hypocentral localization and acceleration map for Iwate-Miyagi (2008/12/17) earthquake retrieved from http://www.kik.bosai.go.jp

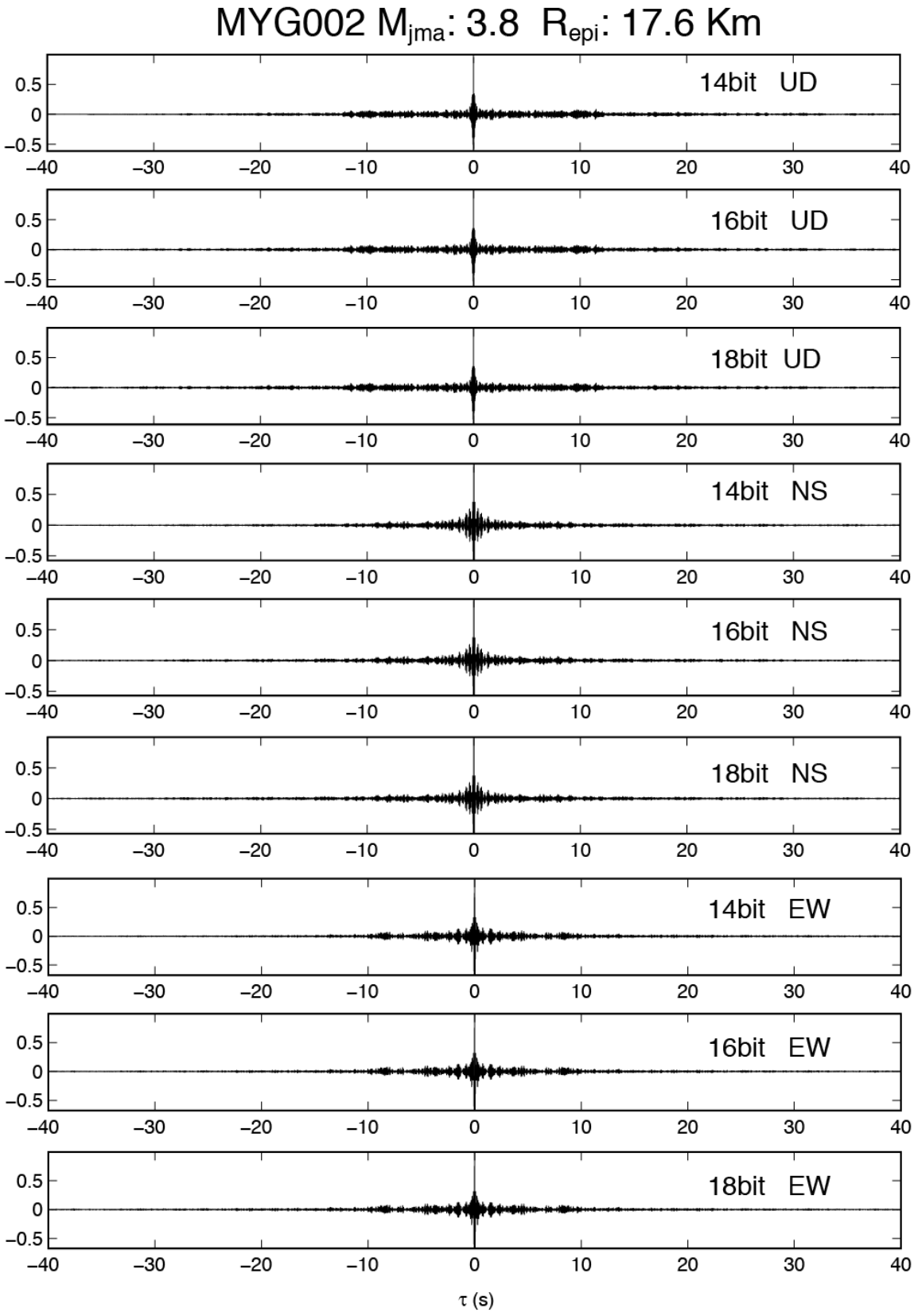

Figure 4.2.5. Cross-correlation plots at different number of bit (14, 16, 18) for the vertical (UD), North-South and East-West horizontal components for station MYG002.

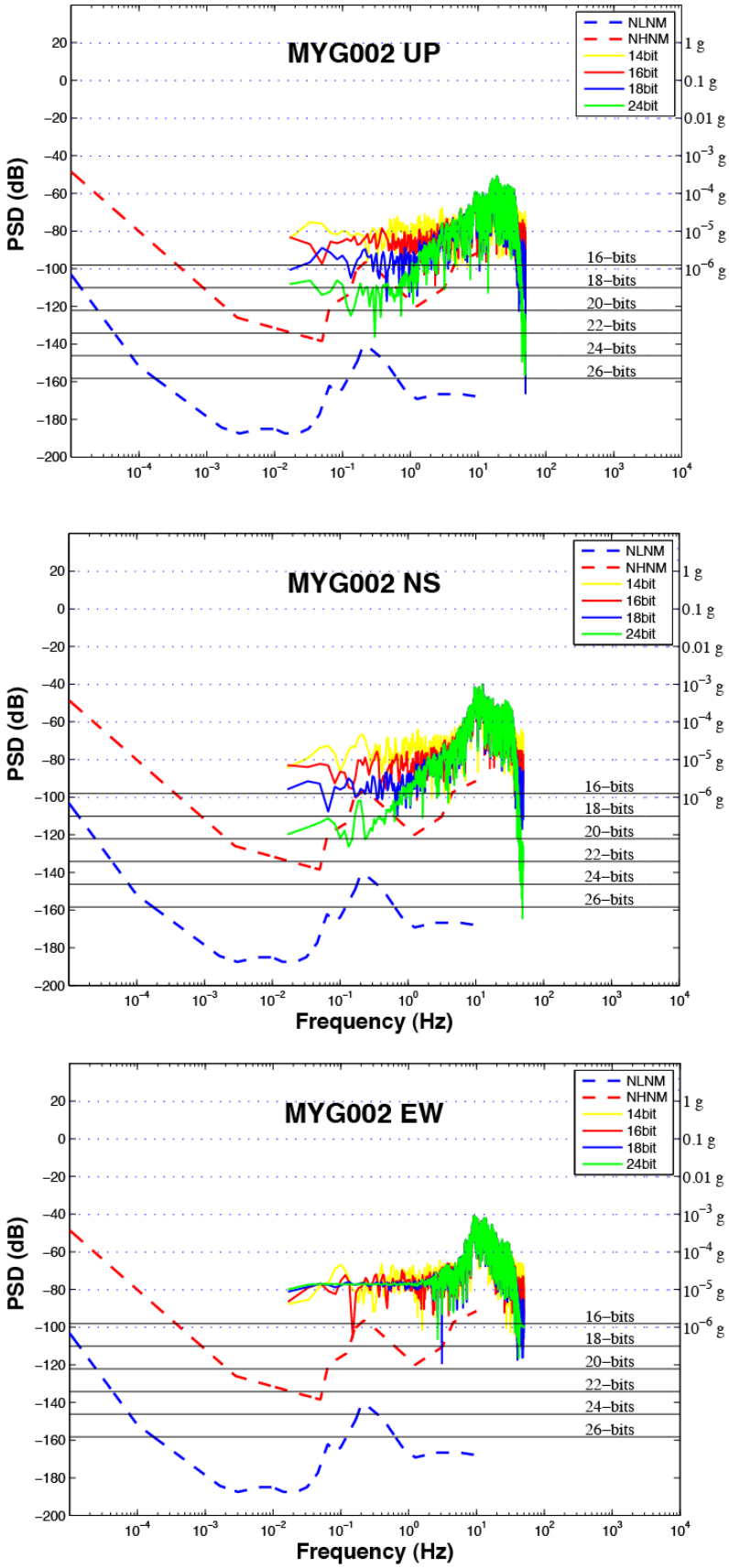

Figure 4.2.6. Power Spectral Density at different number of bit (14, 16,18,24) for the station MYG002. Top: vertical component (UD). Centre: North-South horizontal component (NS). Bottom: East-West horizontal component (EW). The red and blue dashed line represent the high and low global noise level respectively. The black horizontal lines represent the theoretical dynamic range of a data acquisition.

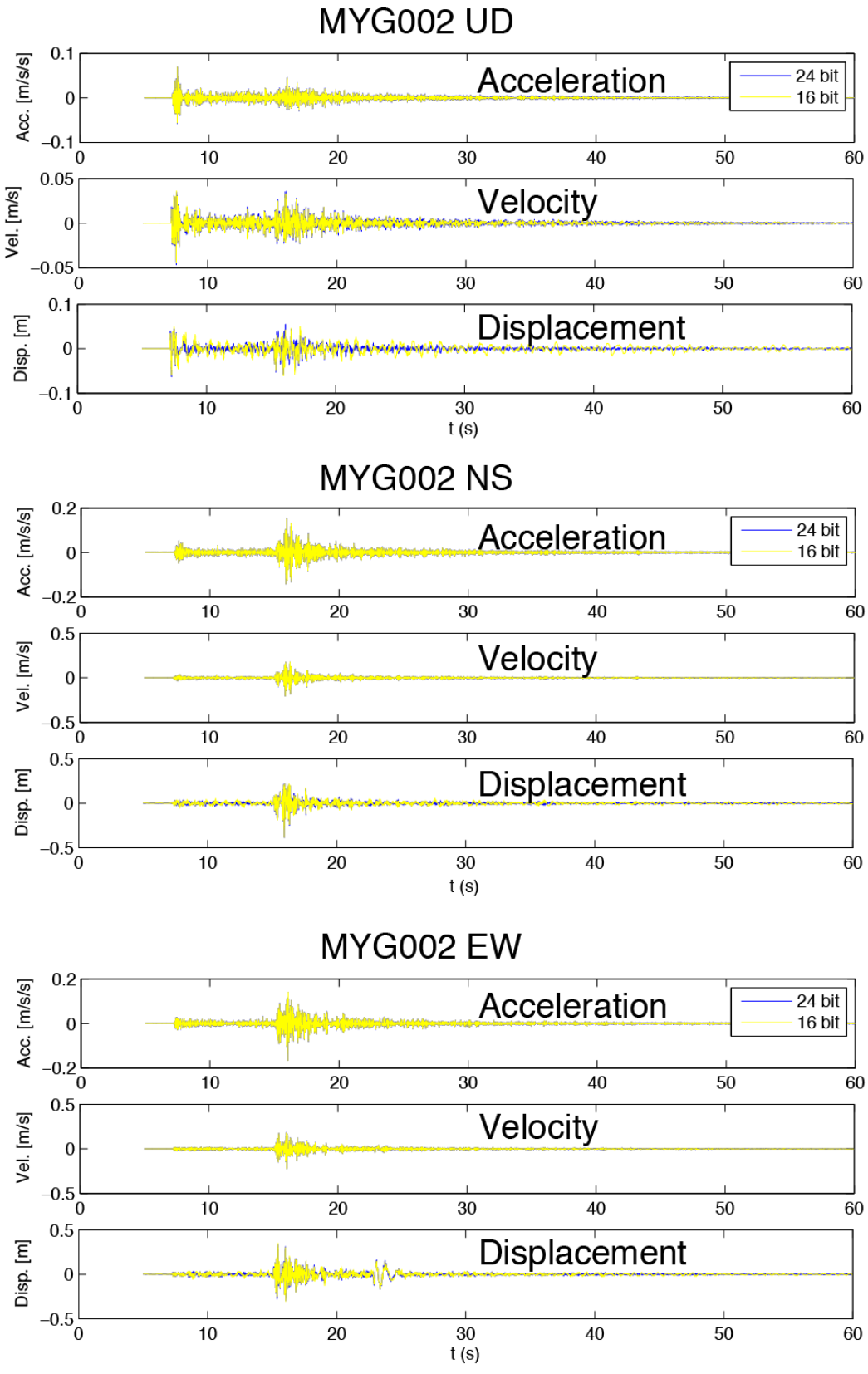

Figure 4.2.7. Seismograms at different number of bit (16 and 24) for the station MYG002. Top: vertical component (UD). Centre: North-South horizontal component (NS). Bottom: East-West horizontal component (EW). For each plot are reported the accelerogram (Top), the velocity (Centre) and the displacement (Bottom).

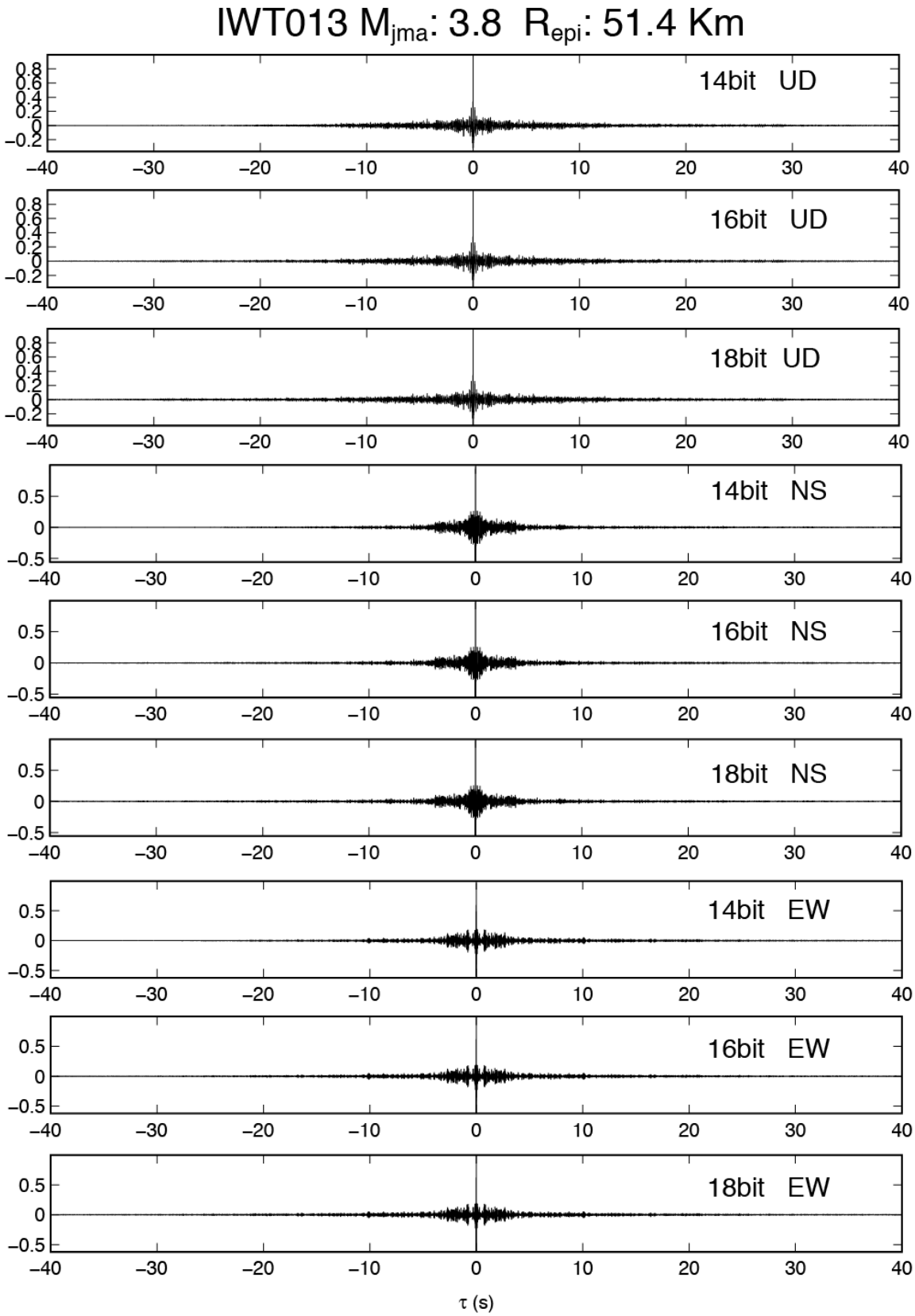

Figure 4.2.8. Same as Figure 4.2.5 but for station IWT013.

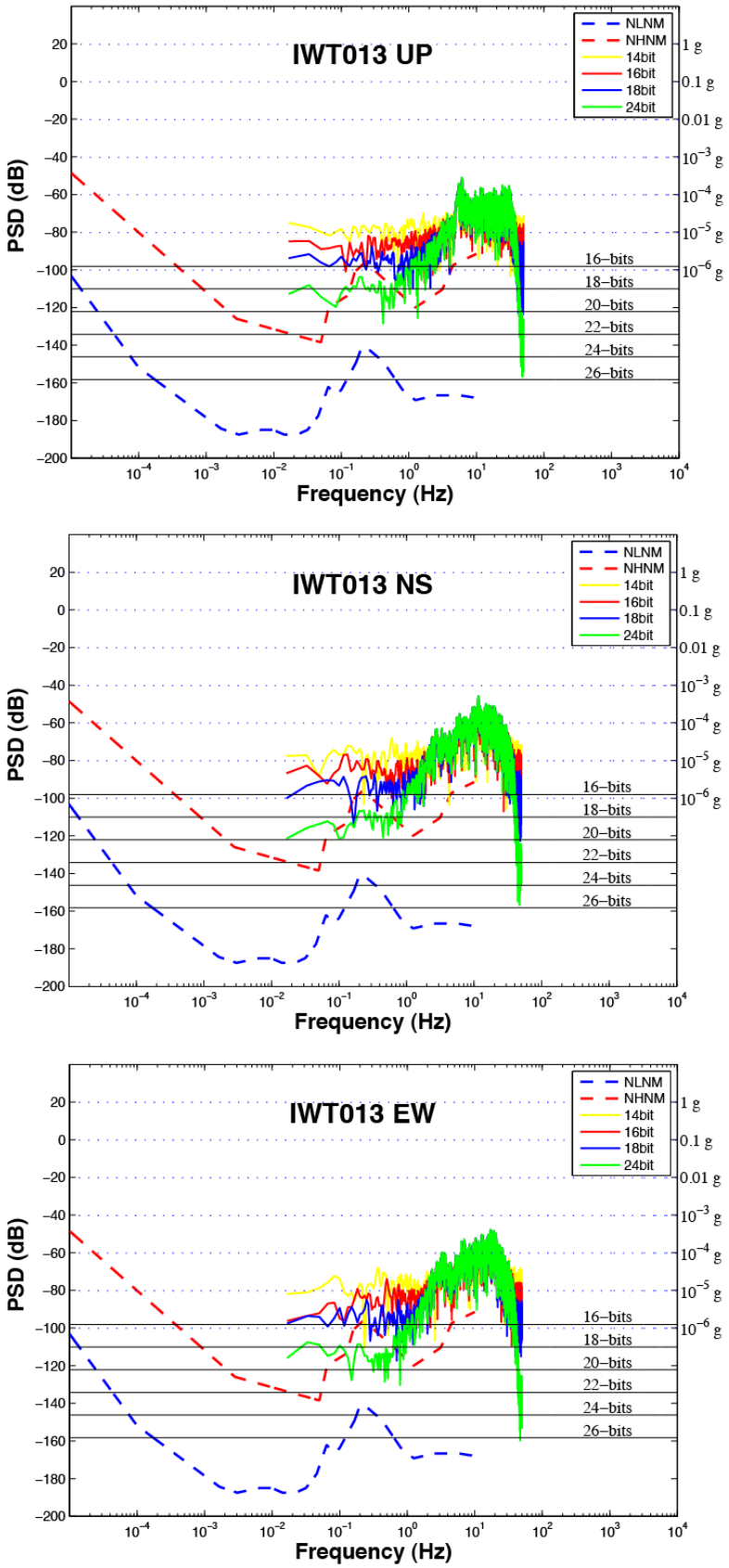

Figure 4.2.9. Same as Figure 4.2.6 but for station IWT013.

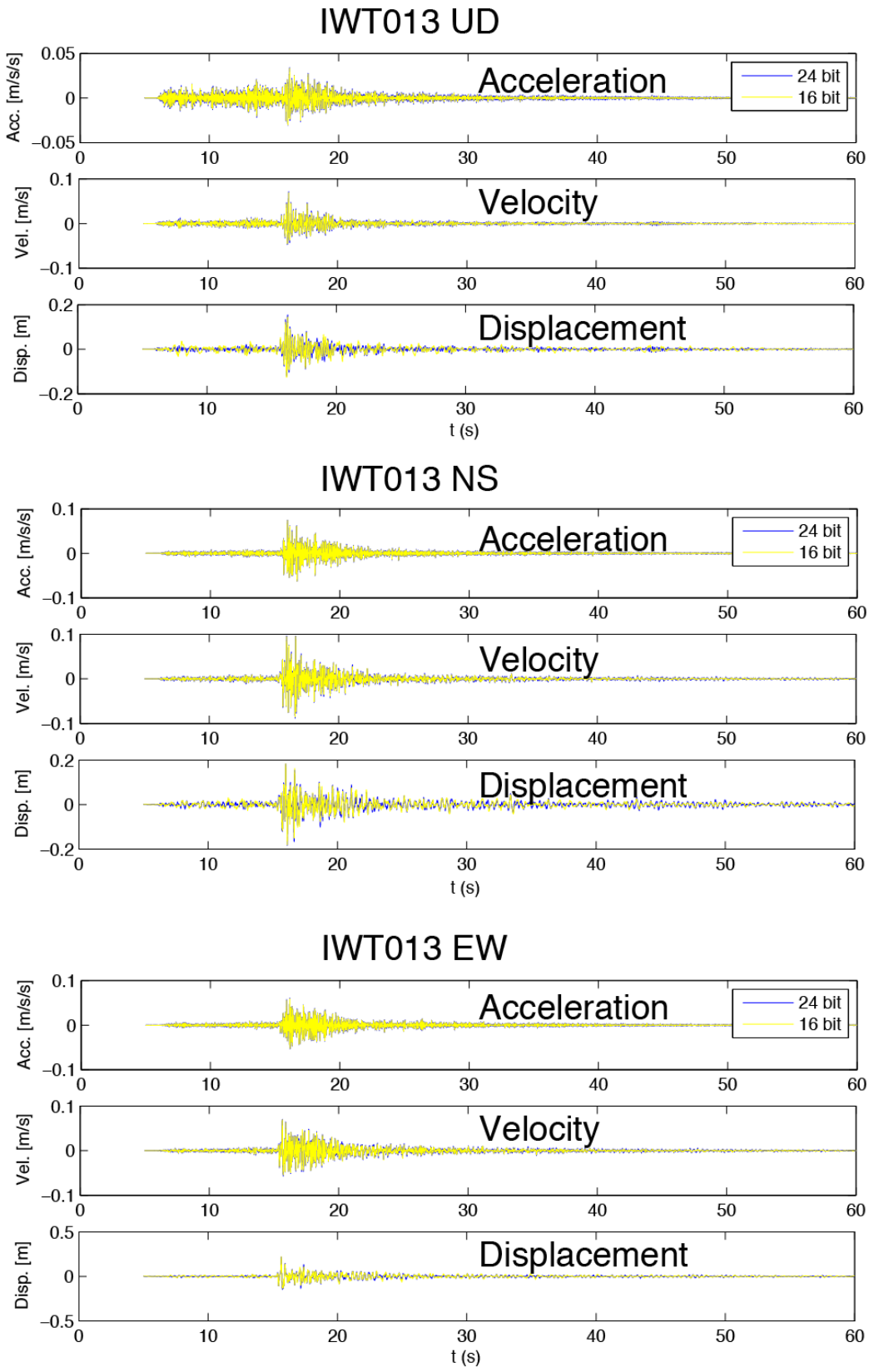

Figure 4.2.10. Same as Figure 4.2.7 but for station IWT013.

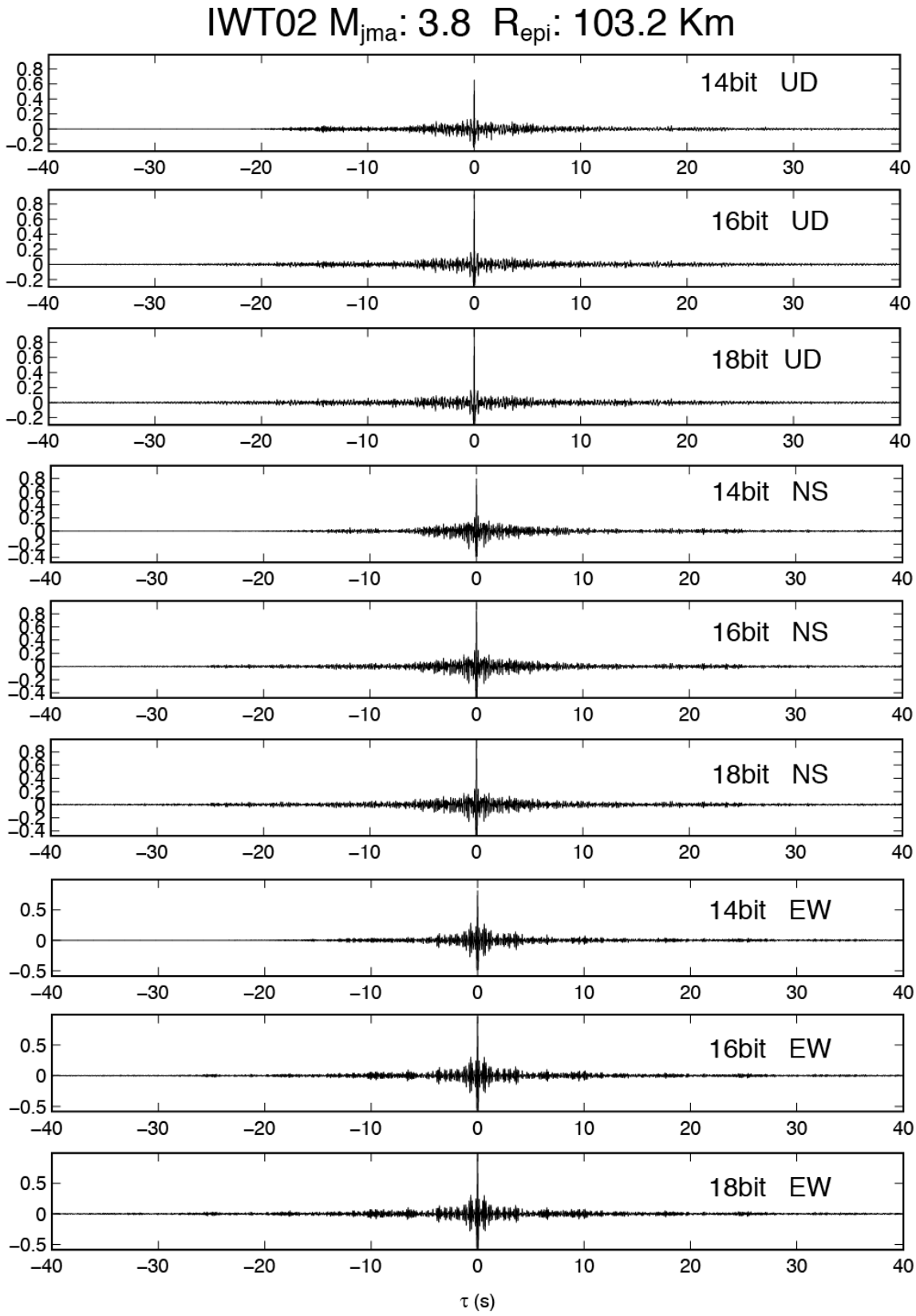

Figure 4.2.11. Same as Figure 4.2.5 but for station IWT013.

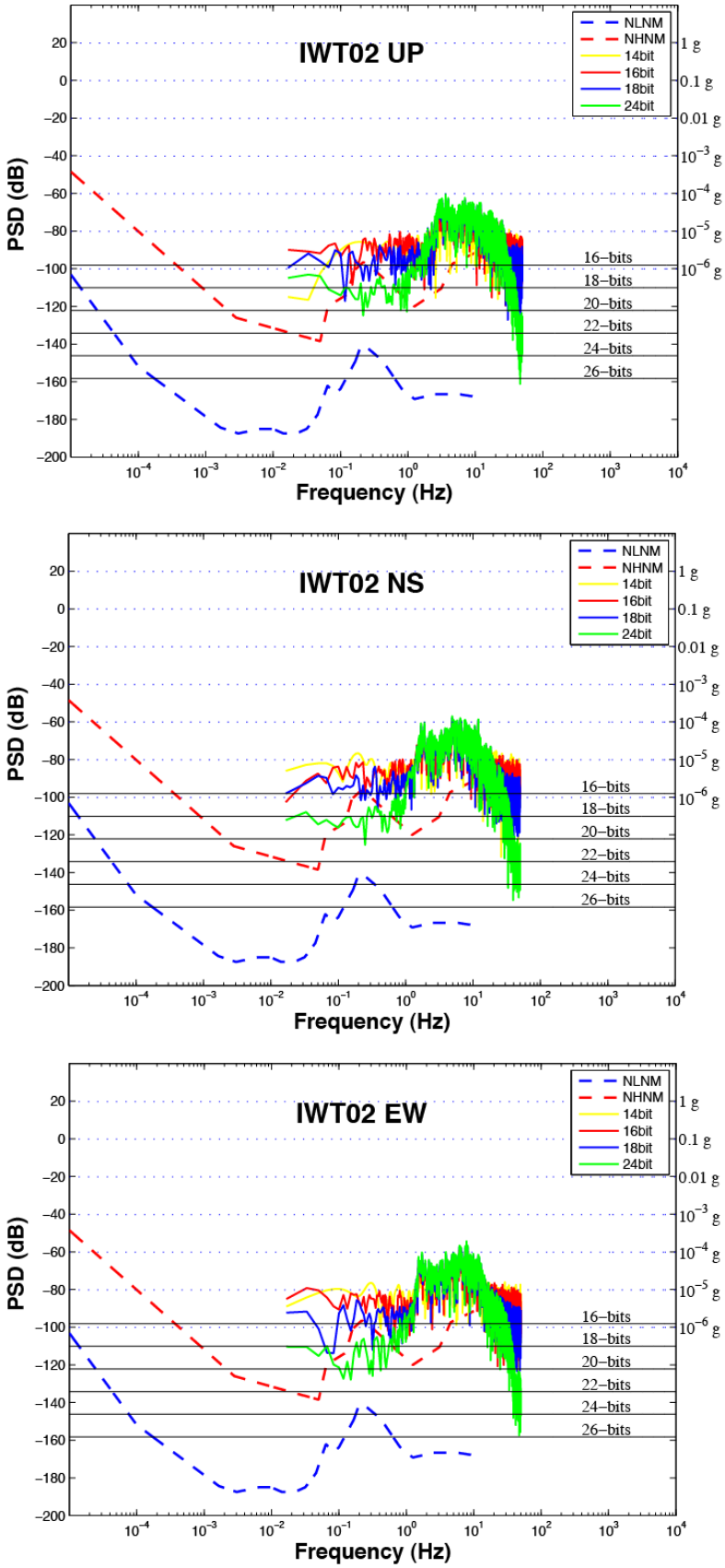

Figure 4.2.12. Same as Figure 4.2.6 but for station IWT02.

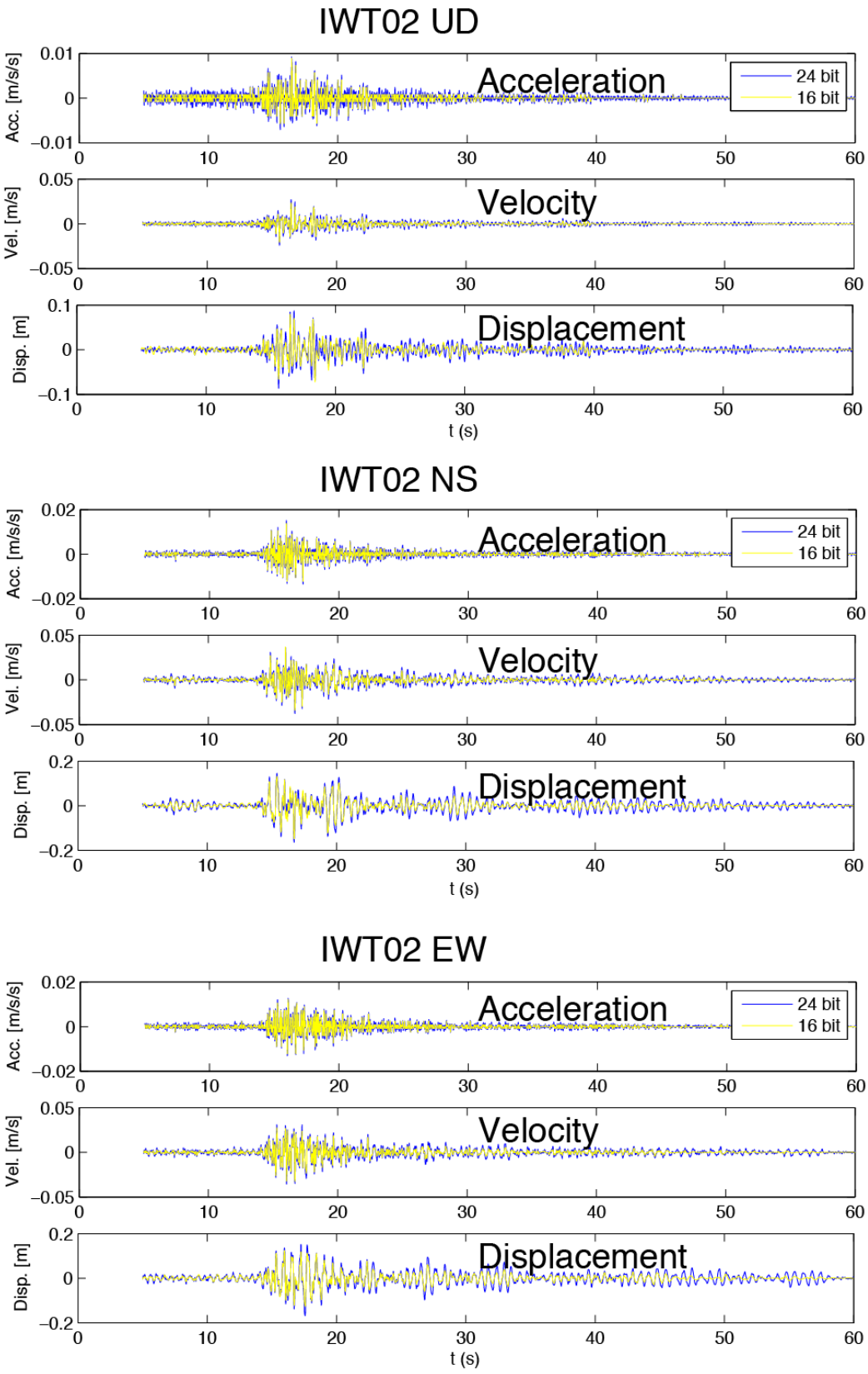

Figure 4.2.13. Same as Figure 4.2.7 but for station IWT02.

Laviano (Italy) 2008/05/27

The first application concerns the 27 May 2008 M_L 2.7 Laviano (Italy) earthquake that was characterized by normal fault mechanism. The station distribution and epicenter of the Laviano earthquake are shown in Figure 4.2.14. The data used were retrieved from the ISNet database.

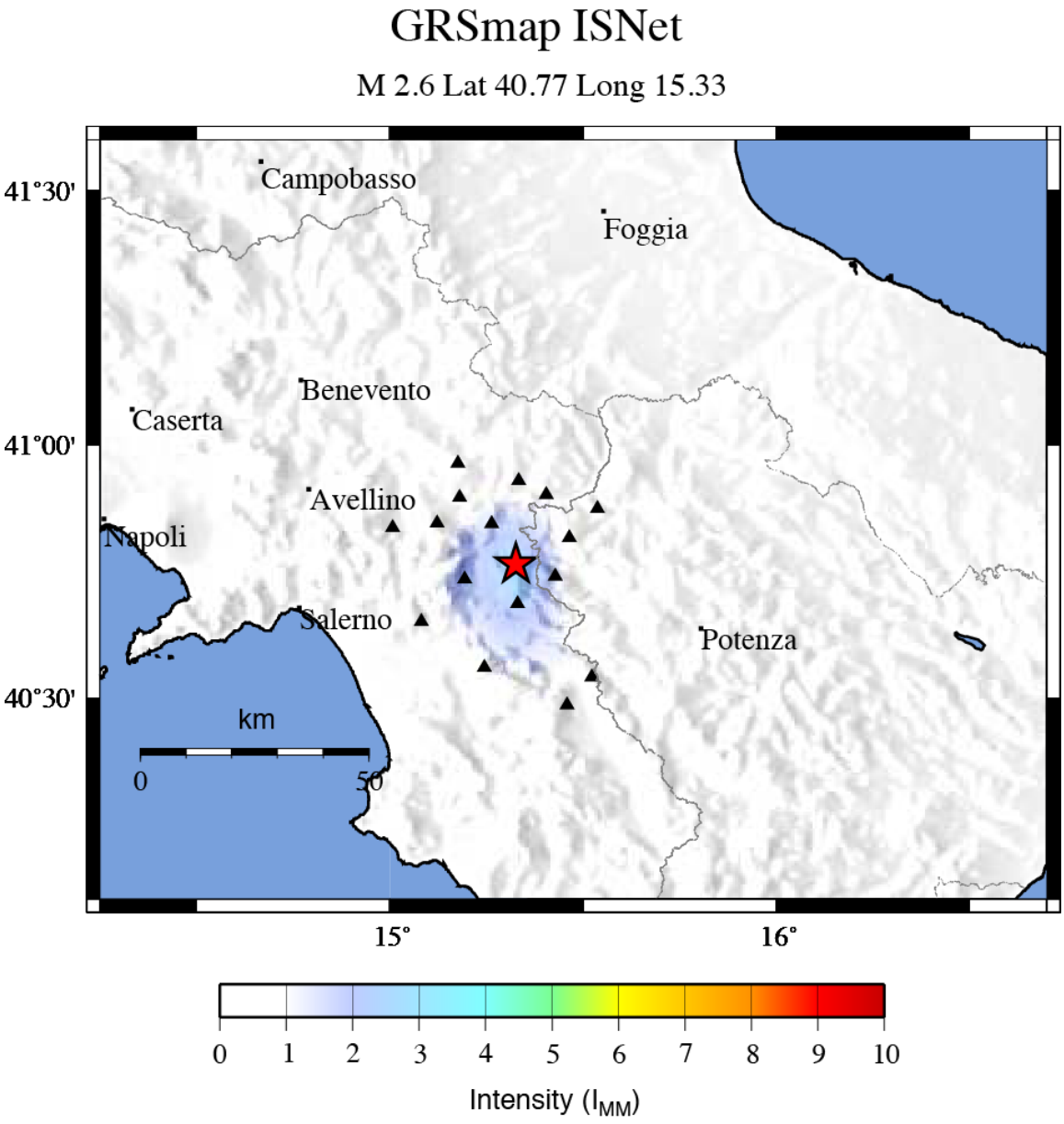

Figure 4.2.14. Epicentrer localization and intensity map, calculated by GRSMap code (Convertito et al., 2010), for Laviano (SA) earthquake 2008/05/27.

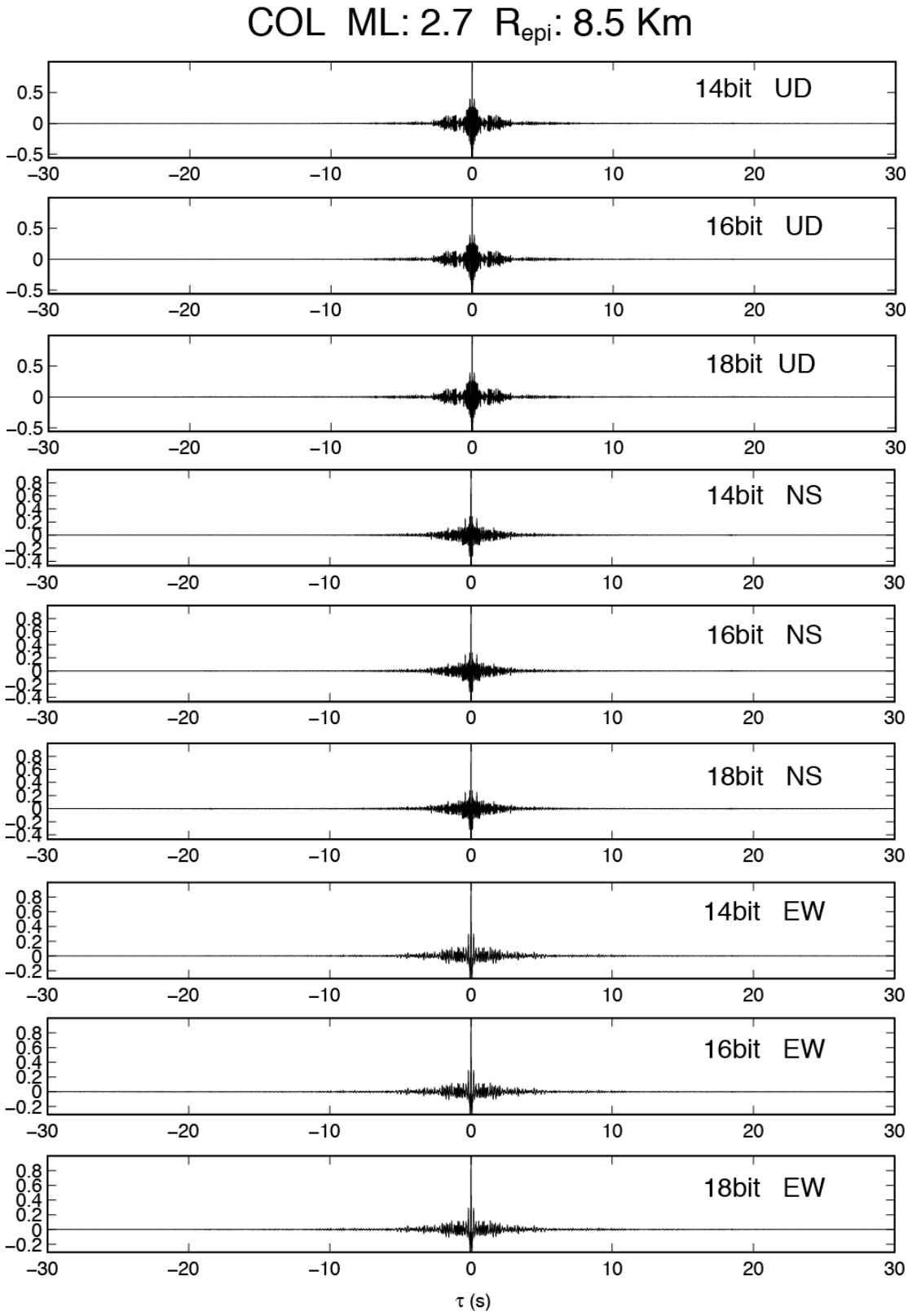

Figure 4.2.15. Cross-correlation plots at different number of bit (14, 16, 18) for the vertical (UD), North-South and East-West horizontal components for station COL.

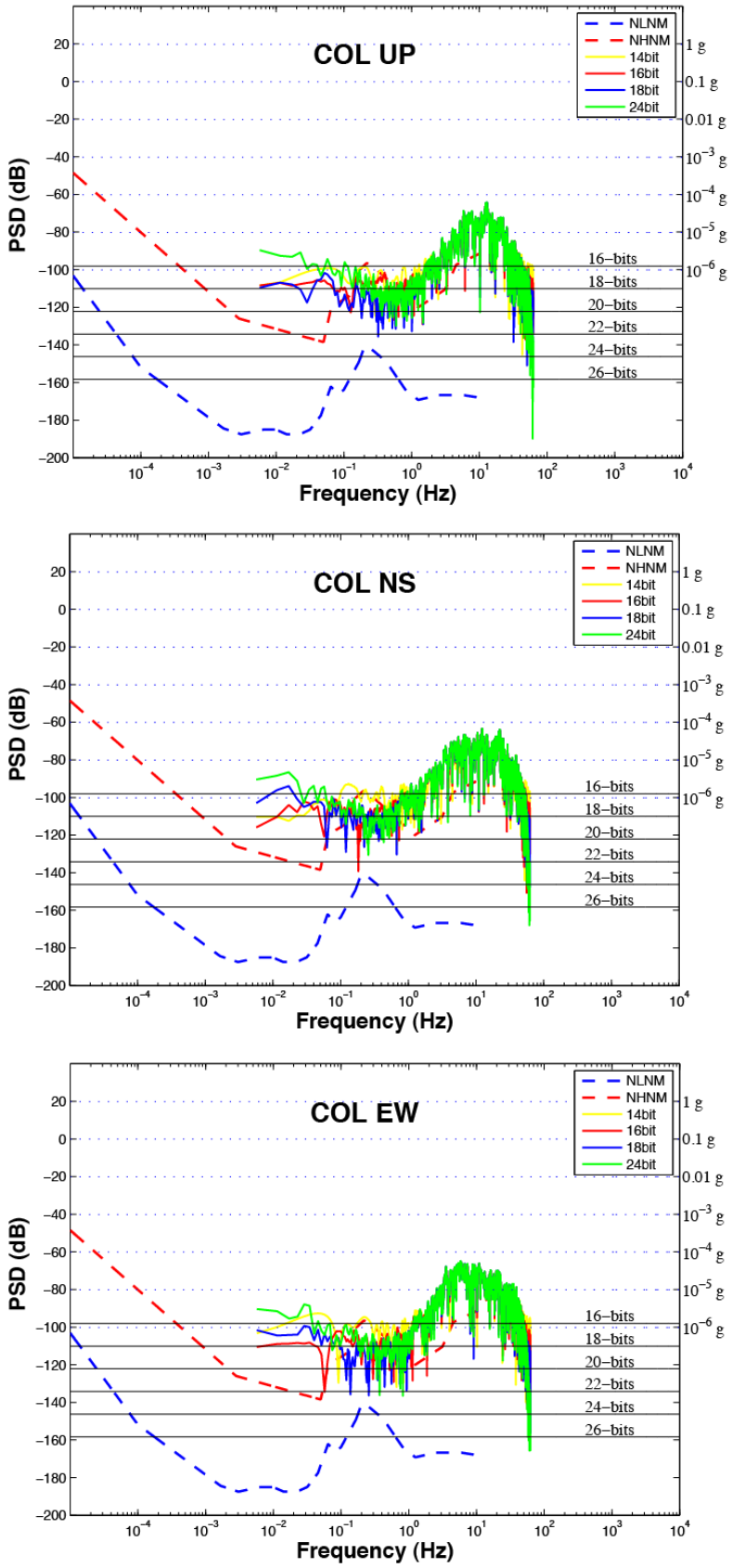

Figure 4.2.16. Power Spectral Density at different number of bit (14, 16,18,24) for the station COL. Top: vertical component (UD). Centre: North-South horizontal component (NS). Bottom: East-West horizontal component (EW). The red and blue dashed line represent the high and low global noise level respectively. The black horizontal lines represent the theoretical dynamic range of a data acquisition.

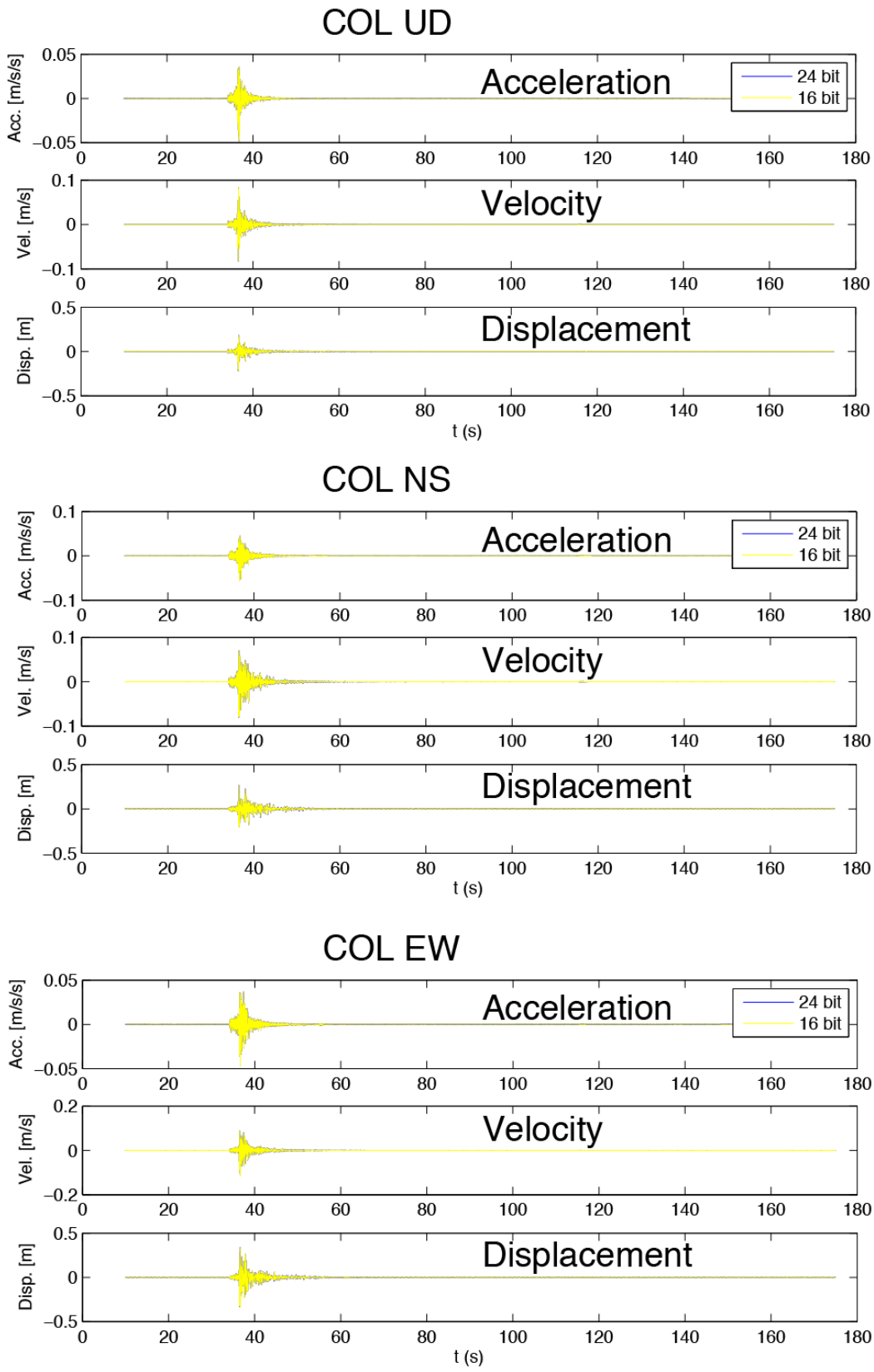

Figure 4.2.17. Seismograms at different number of bit (16 and 24) for the station MYG002. Top: vertical component (UD). Centre: North-South horizontal component (NS). Bottom: East-West horizontal component (EW). For each plot are reported the accelerogram (Top), the velocity (Centre) and the displacement (Bottom).

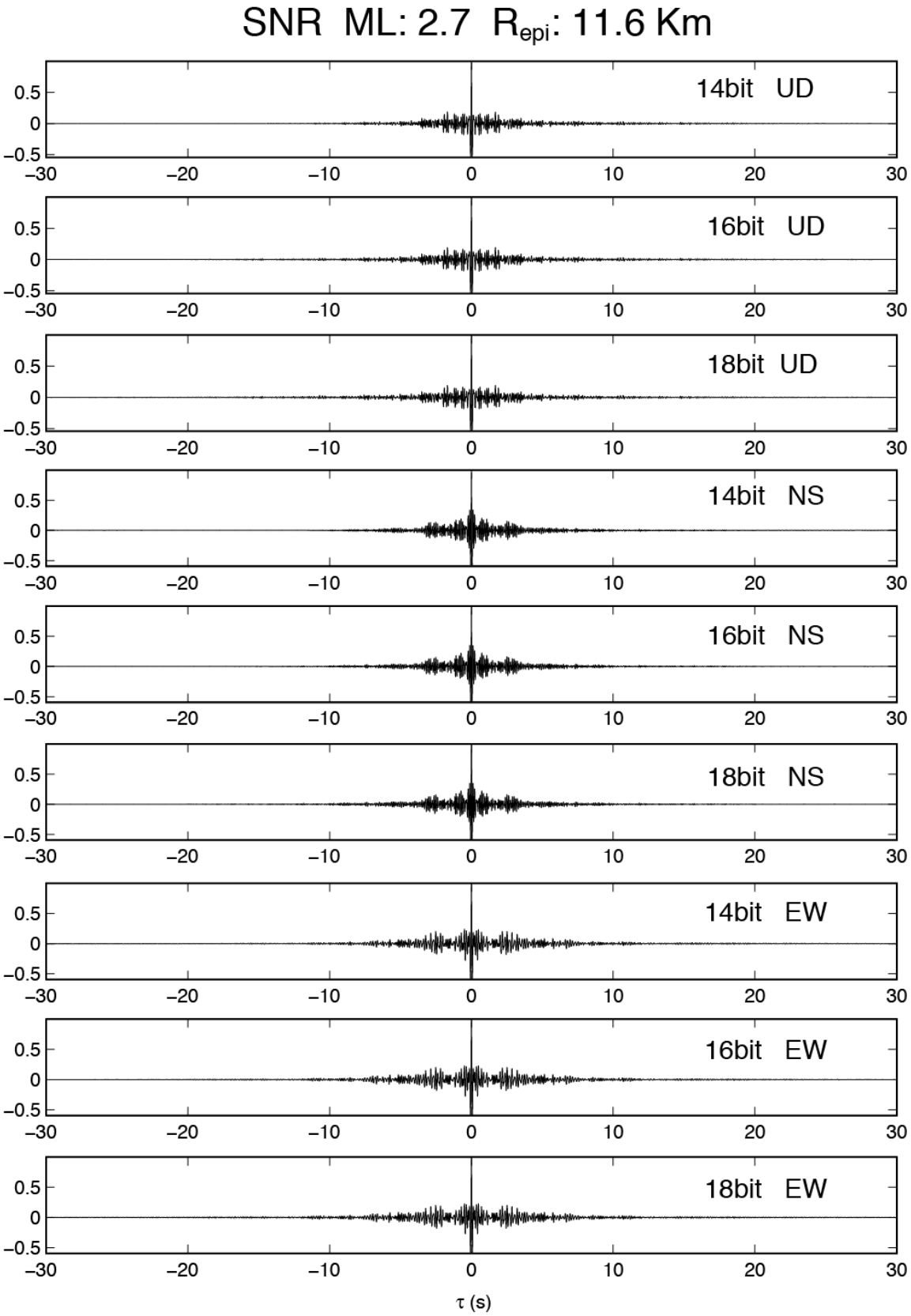

Figure 4.2.18. Same as Figure 4.2.15 but for station SNR.

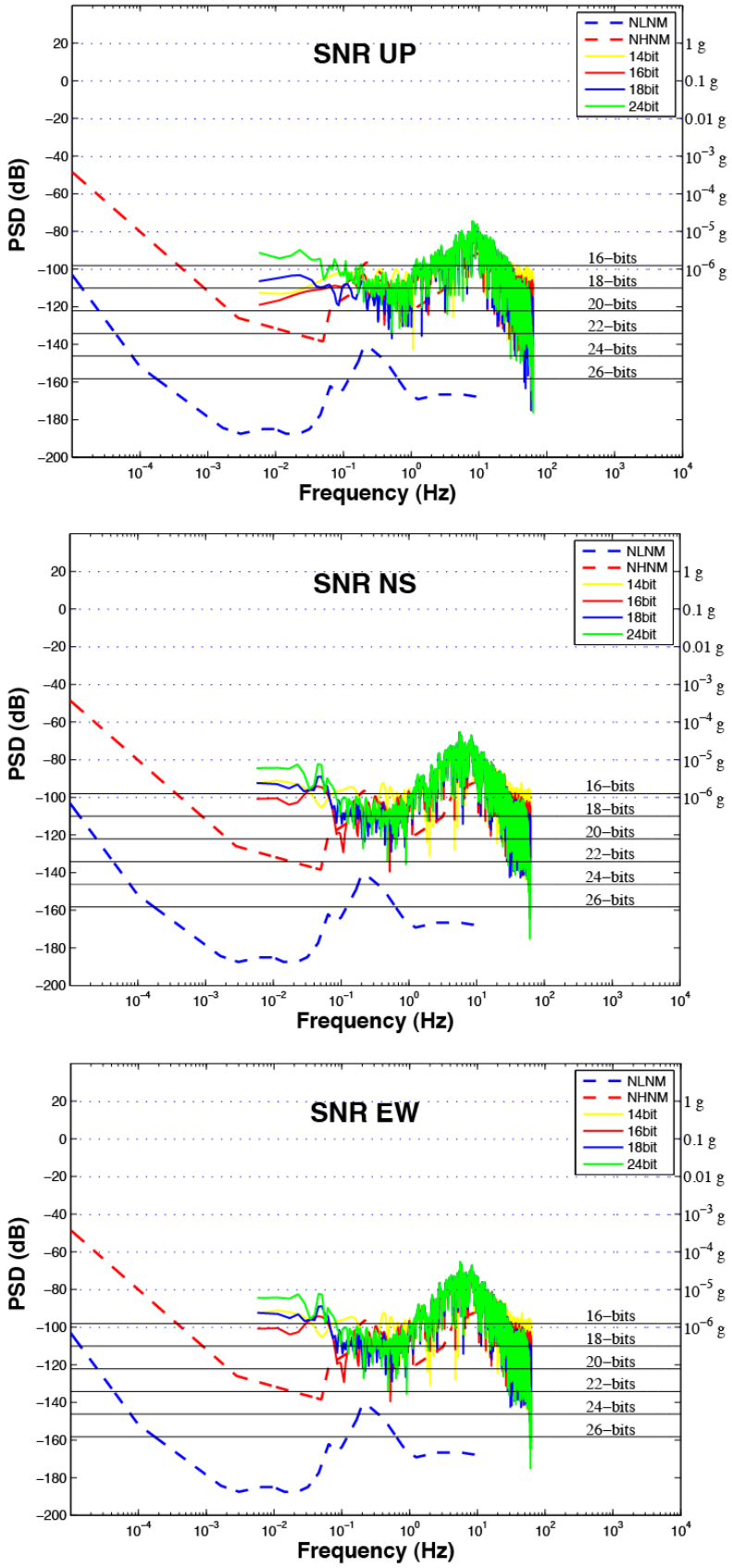

Figure 4.2.19. Same as Figure 4.2.16 but for station SNR.

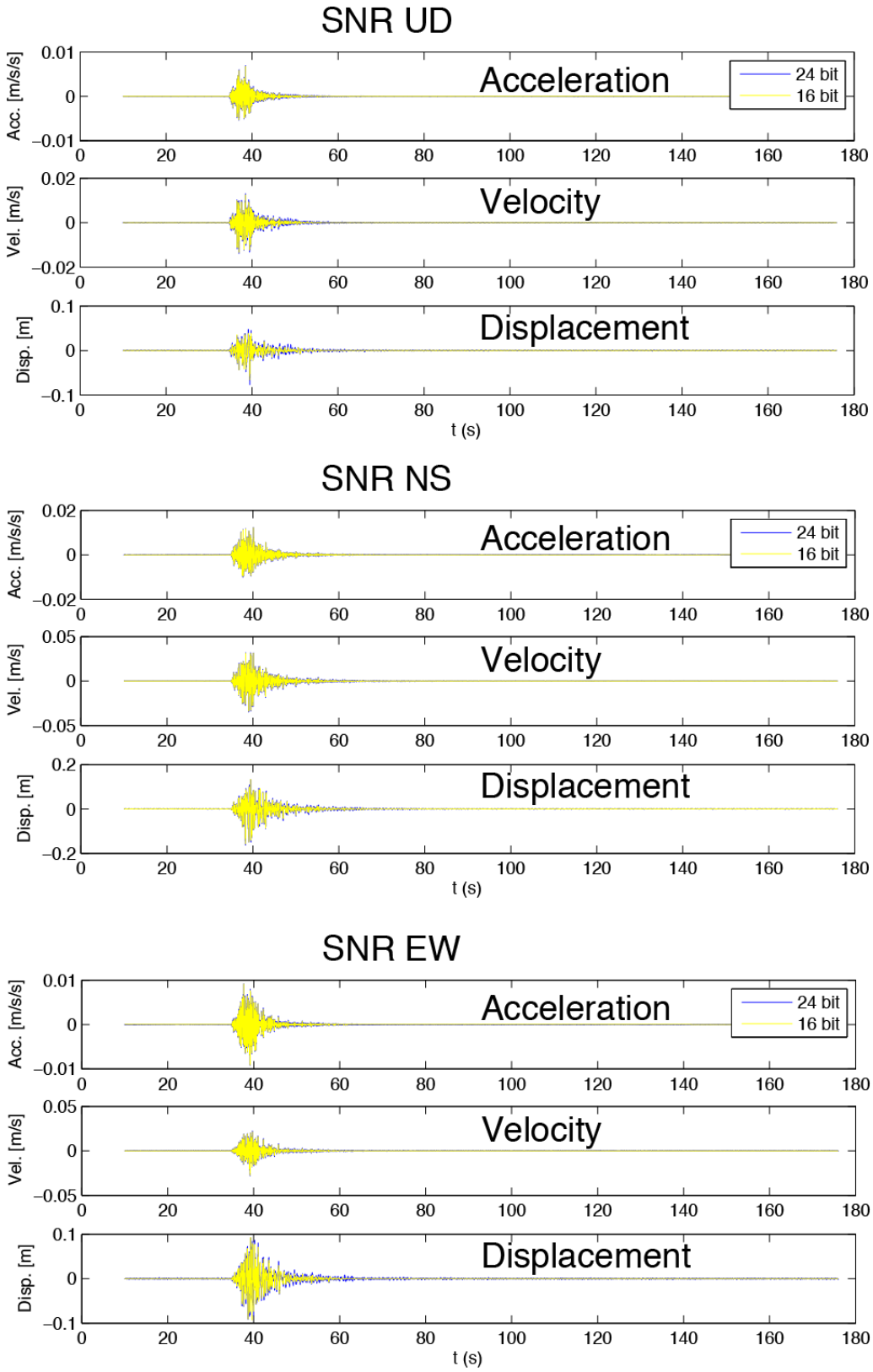

Figure 4.2.20. Same as Figure 4.2.17 but for station SNR.

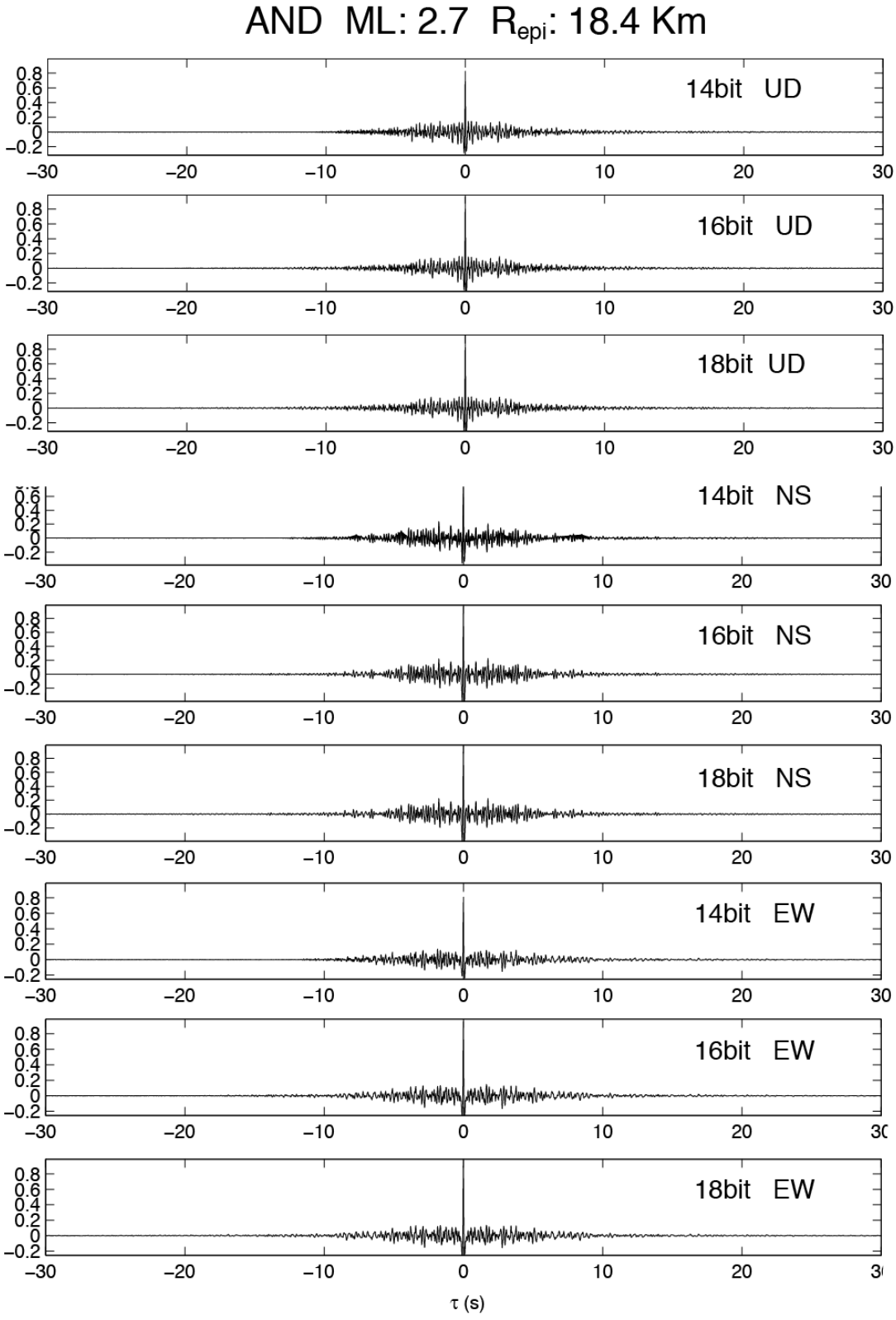

Figure 4.2.21. Same as Figure 4.2.15 but for station AND.

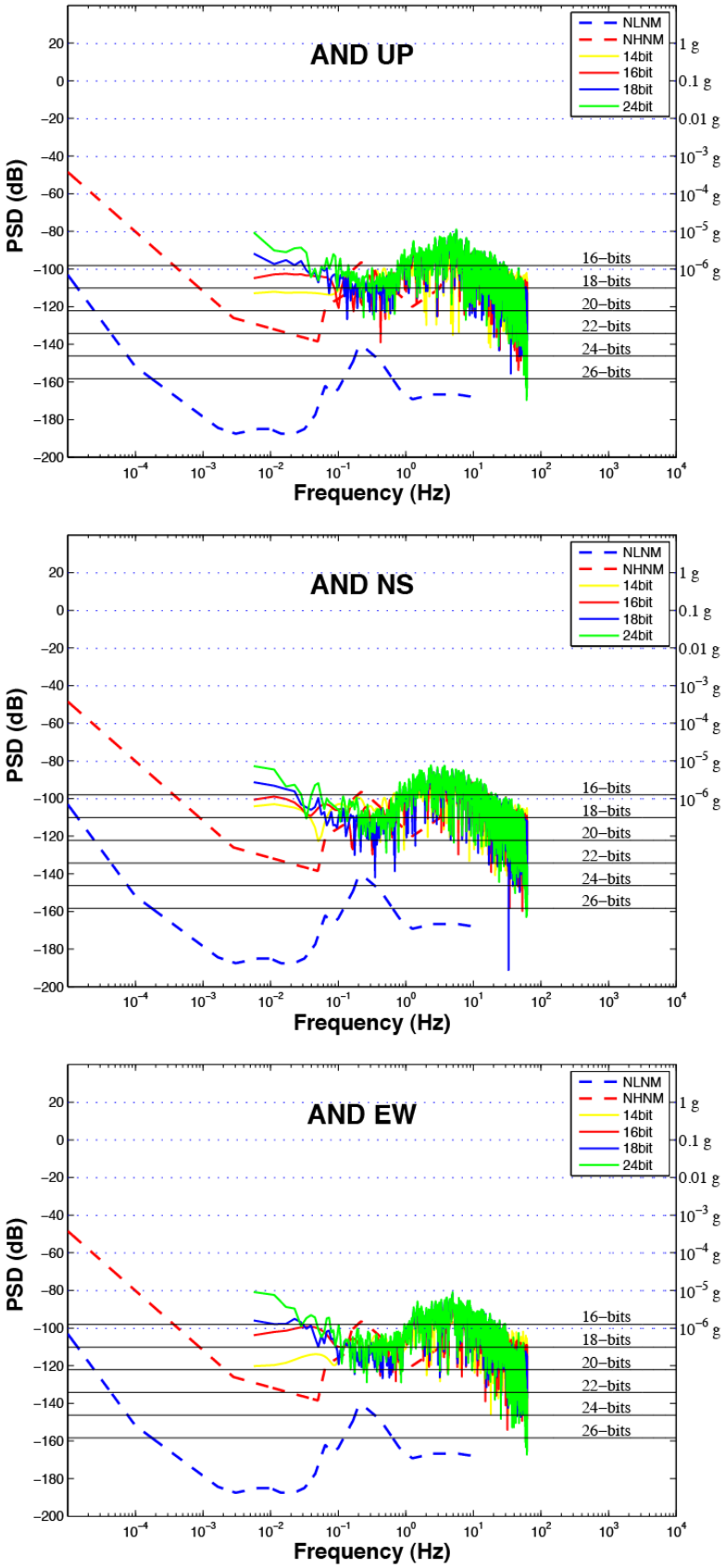

Figure 4.2.22. Same as Figure 4.2.16 but for station AND.

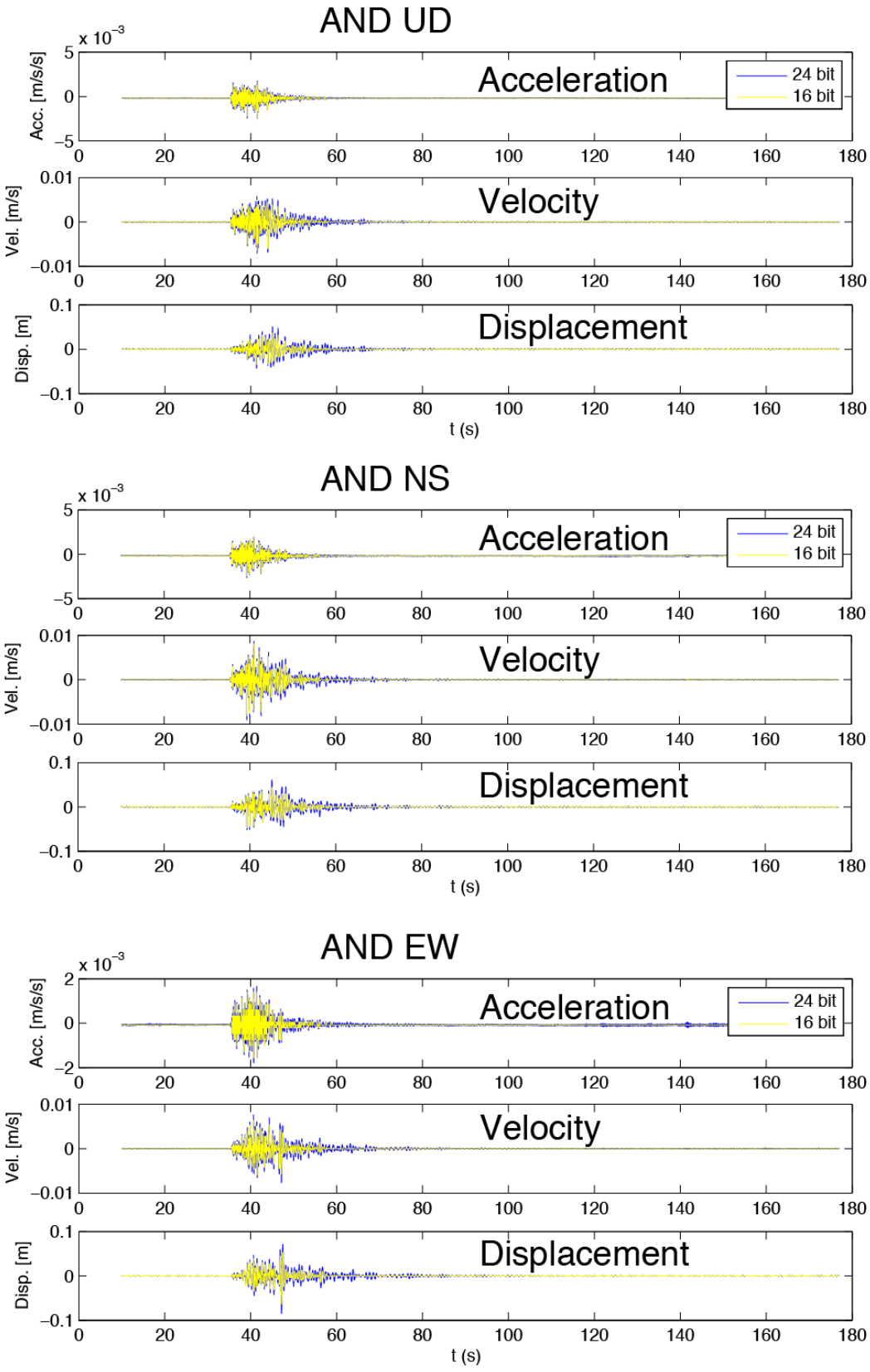

Figure 4.2.23. Same as Figure 4.2.17 but for station AND.

Iwate-Miyagi (Japan) 2008/06/14

The first application concerns the 14 June 2008 M_{jma} 7.2 Iwate-Miyagi (Japan) earthquake that was characterized by inverse fault mechanism. The station distribution and epicenter of the Iwate-Miyagi earthquake are shown in Figure 4.2.24. The data used were retrieved from the Kik-net database.

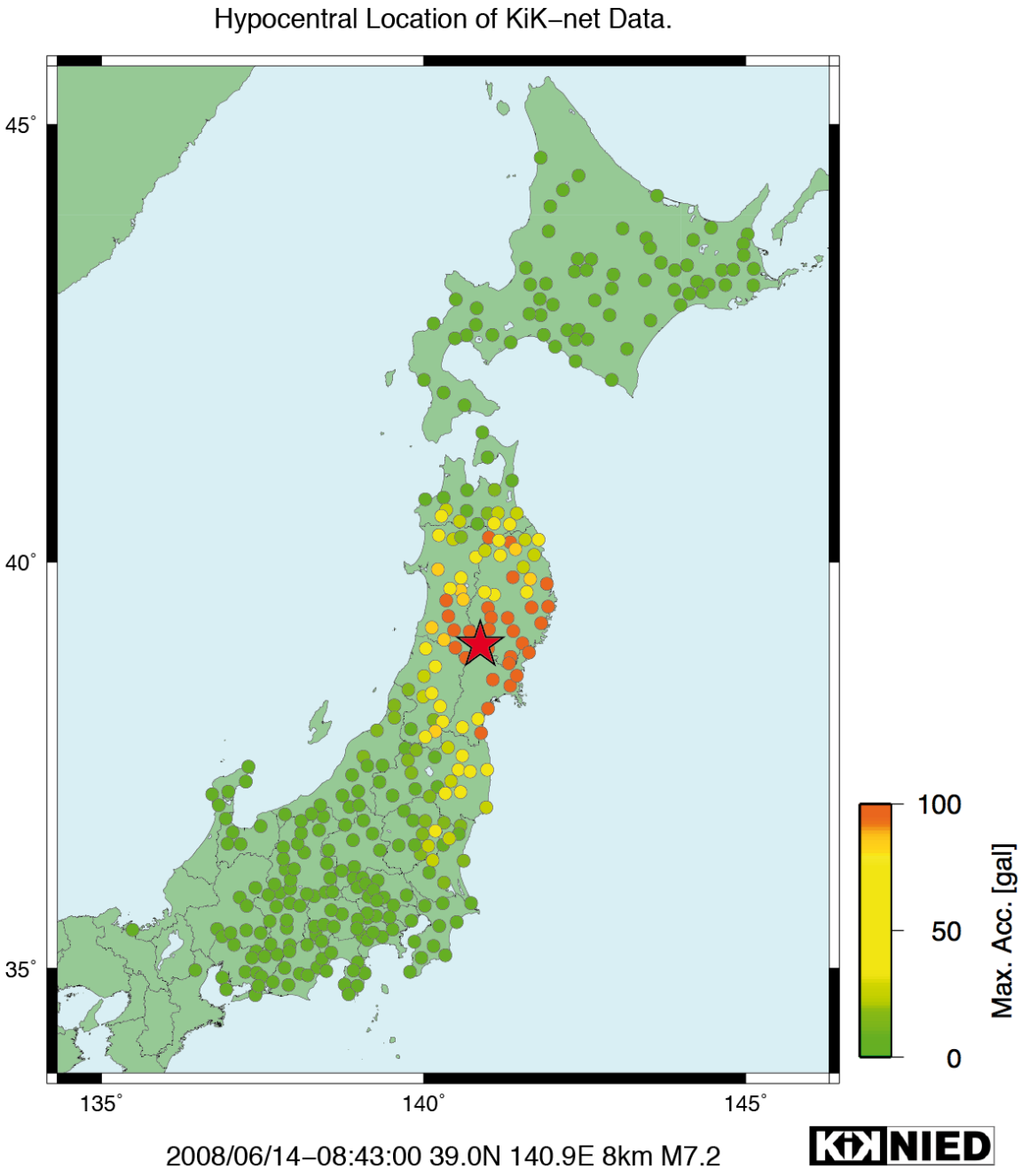

Figure 4.2.24. Hypocentral localization and acceleration map for Iwate-Miyagi (2008/06/14) earthquake retrieved from http://www.kik.bosai.go.jp.

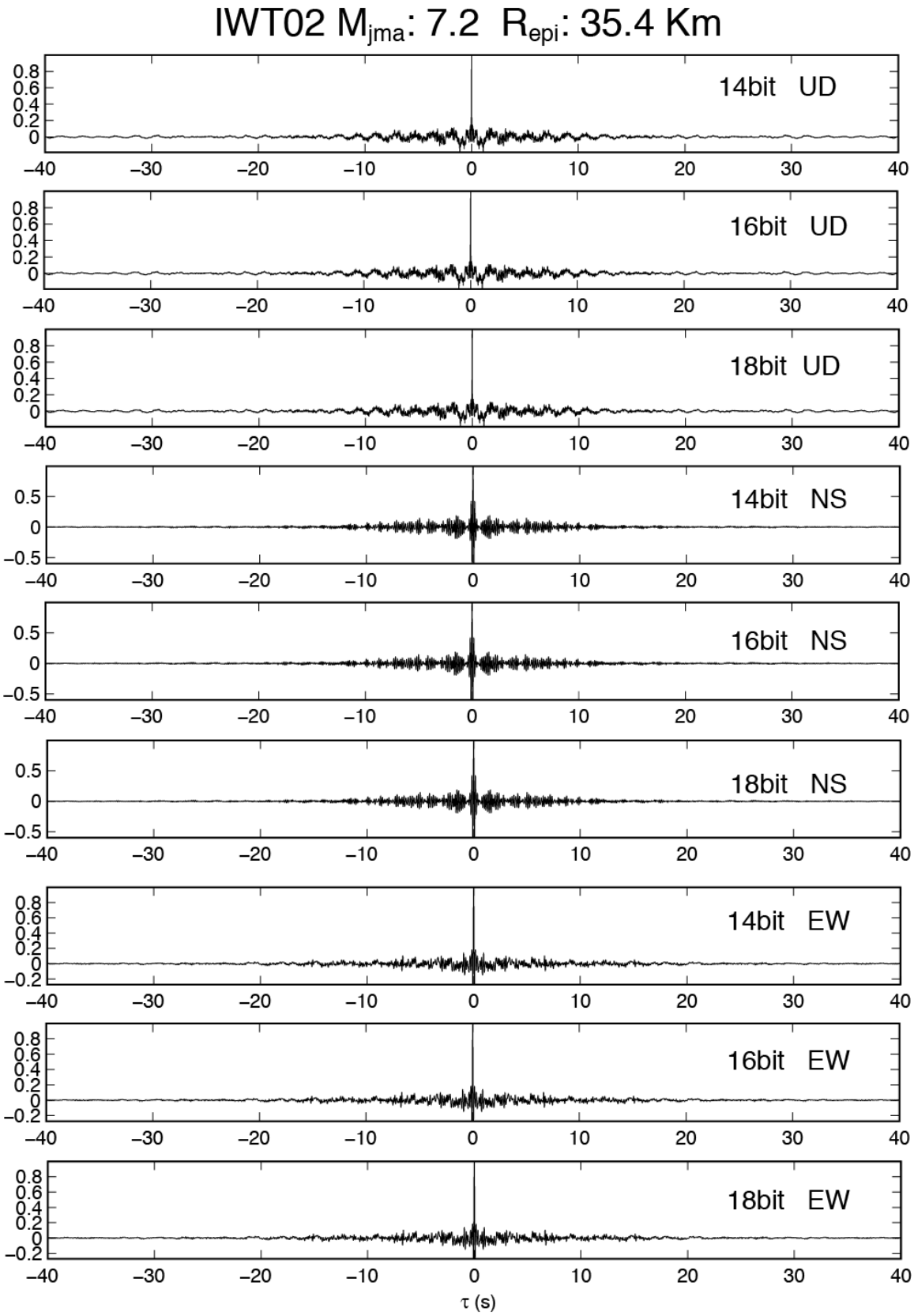

Figure 4.2.25. Cross-correlation plots at different number of bit (14, 16, 18) for the vertical (UD), North-South and East-West horizontal components for station IWT02.

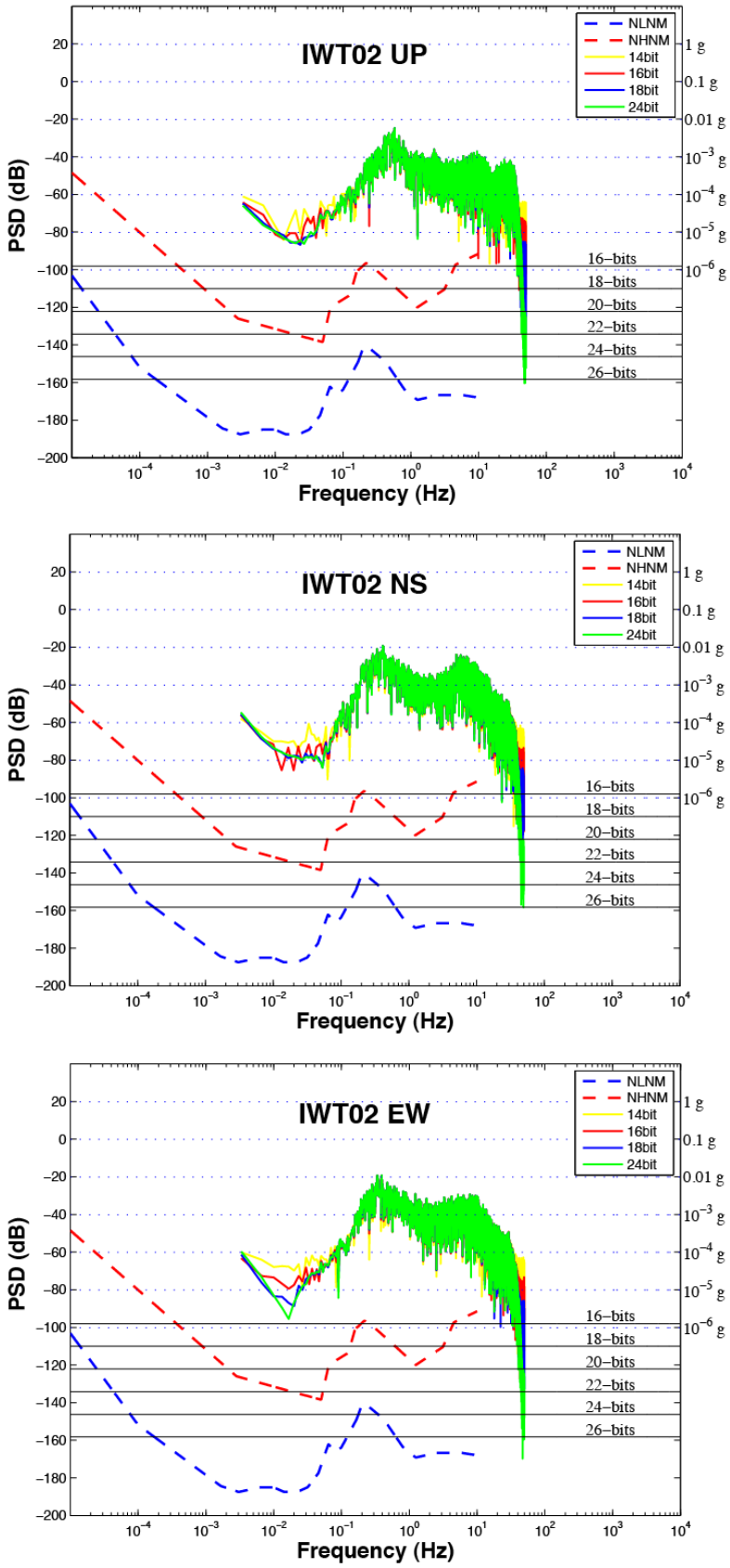

Figure 4.2.26. Power Spectral Density at different number of bit (14, 16,18,24) for the station IWT02. Top: vertical component (UD). Centre: North-South horizontal component (NS). Bottom: East-West horizontal component (EW). The red and blue dashed line represent the high and low global noise level respectively. The black horizontal lines represent the theoretical dynamic range of a data acquisition.

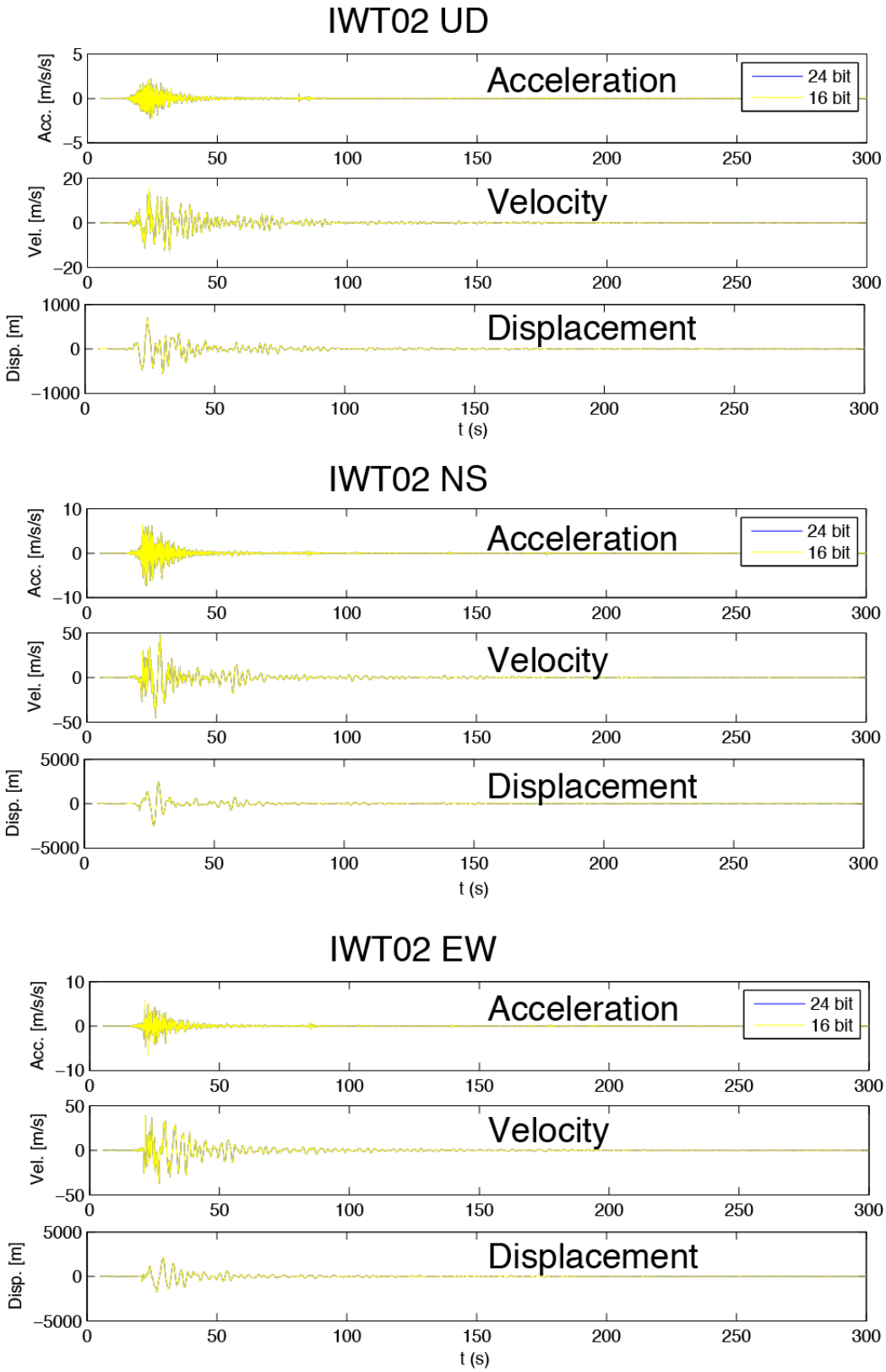

Figure 4.2.27. Seismograms at different number of bit (16 and 24) for the station MYG002. Top: vertical component (UD). Centre: North-South horizontal component (NS). Bottom: East-West horizontal component (EW). For each plot are reported the accelerogram (Top), the velocity (Centre) and the displacement (Bottom).

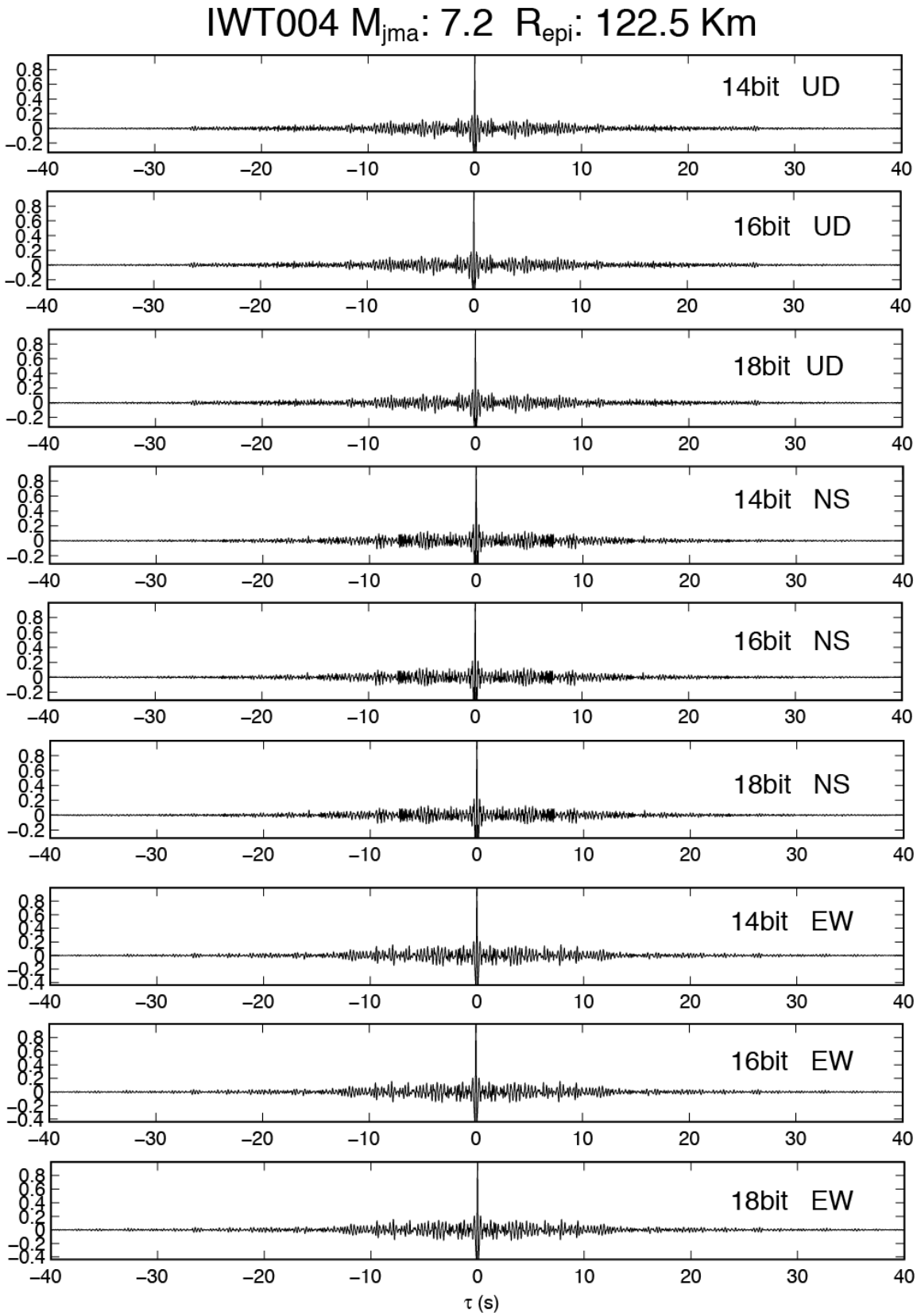

Figure 4.2.28. Same as Figure 4.2.25 but for station IWT004.

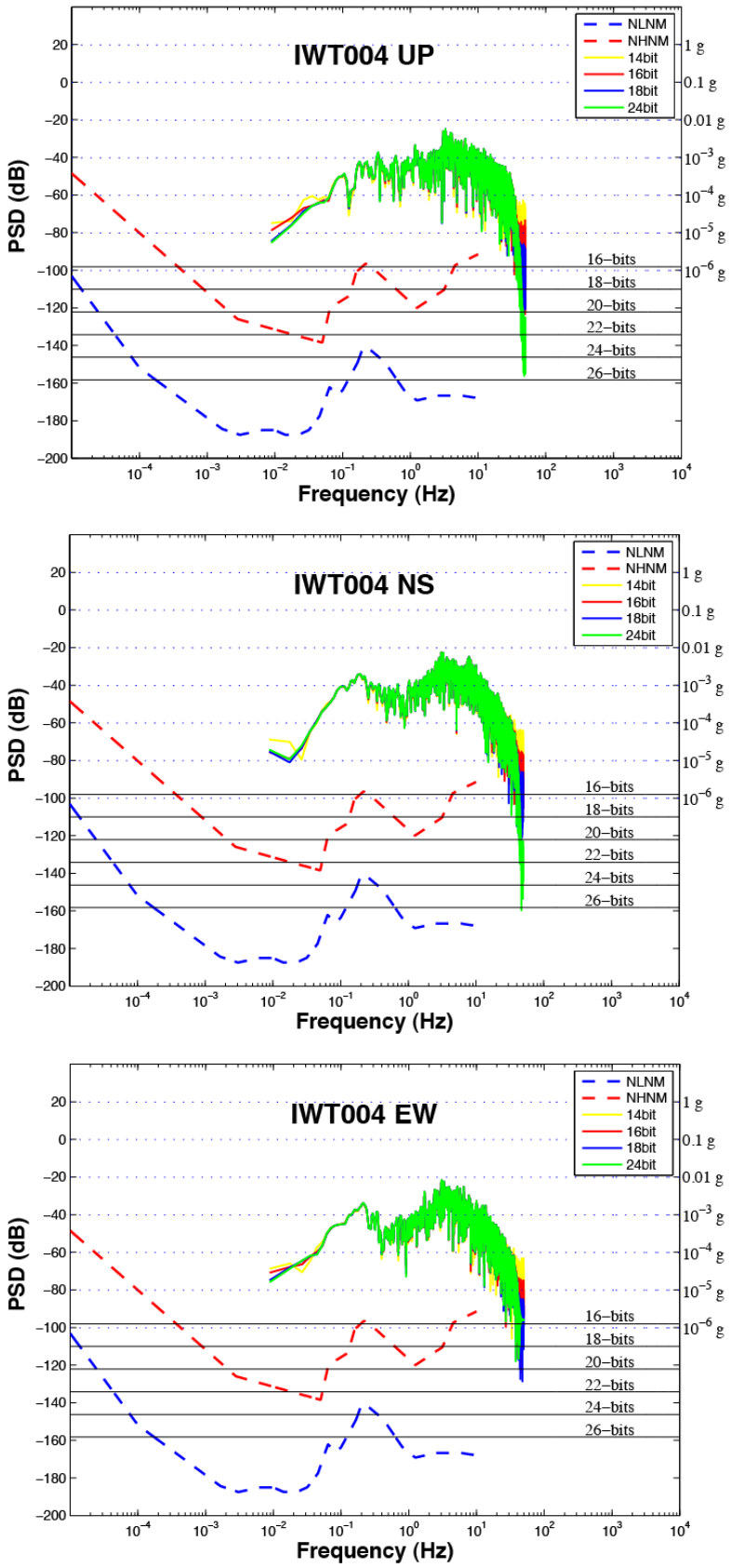

Figure 4.2.29. Same as Figure 4.2.26 but for station IWT004.

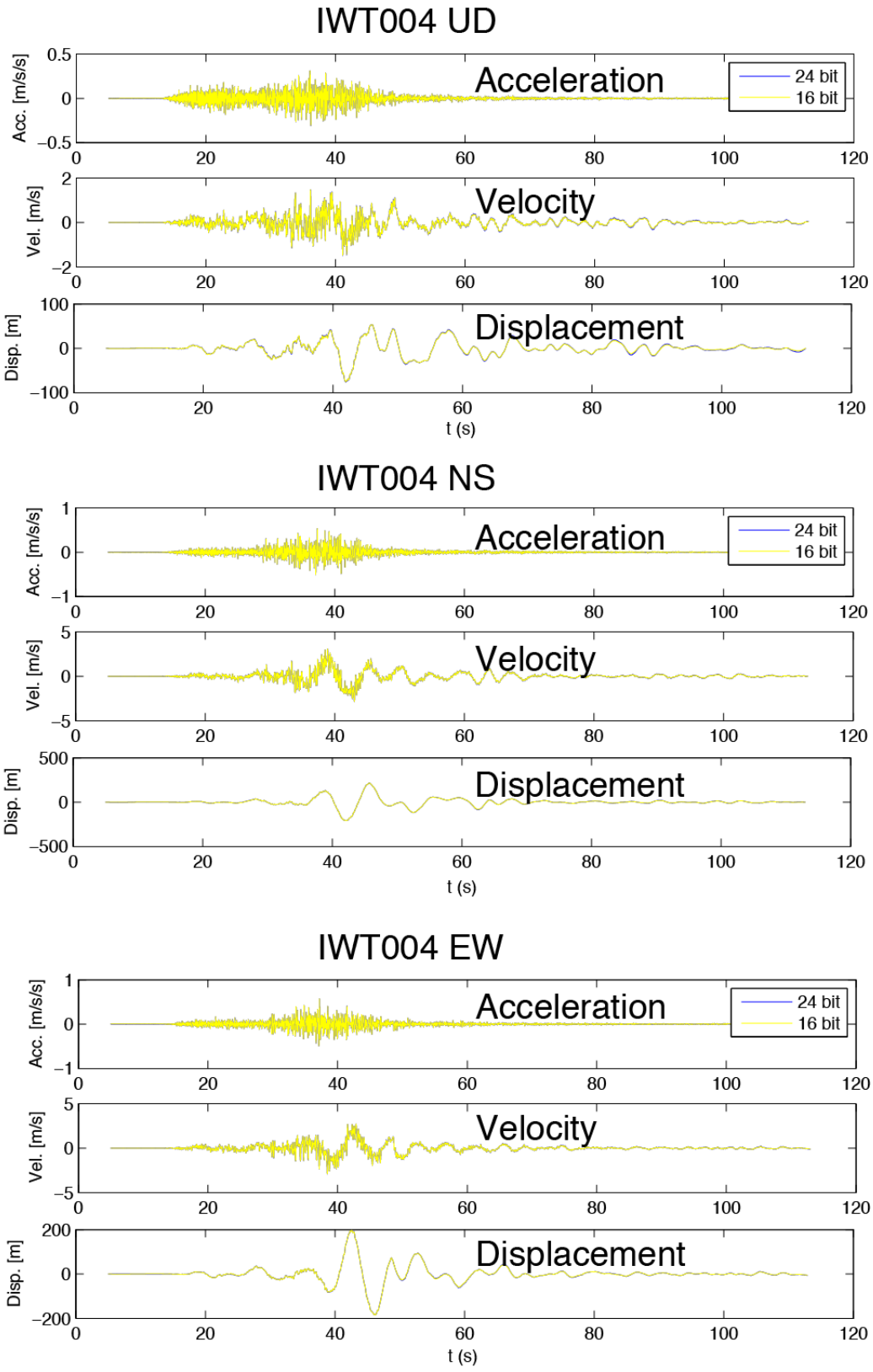

Figure 4.2.30. Same as Figure 4.2.27 but for station IWT004.

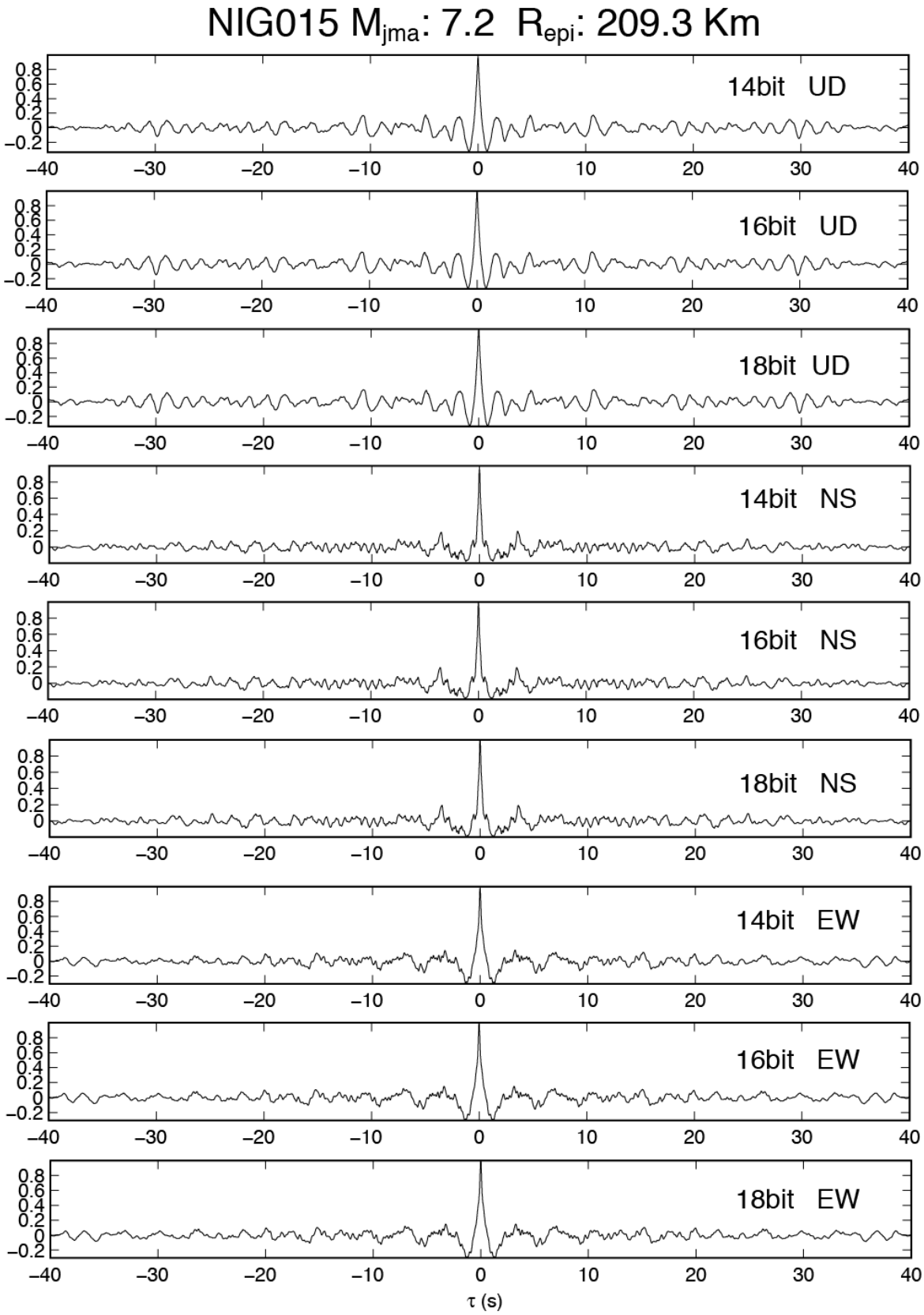

Figure 4.2.31. Same as Figure 4.2.25 but for station NIG015.

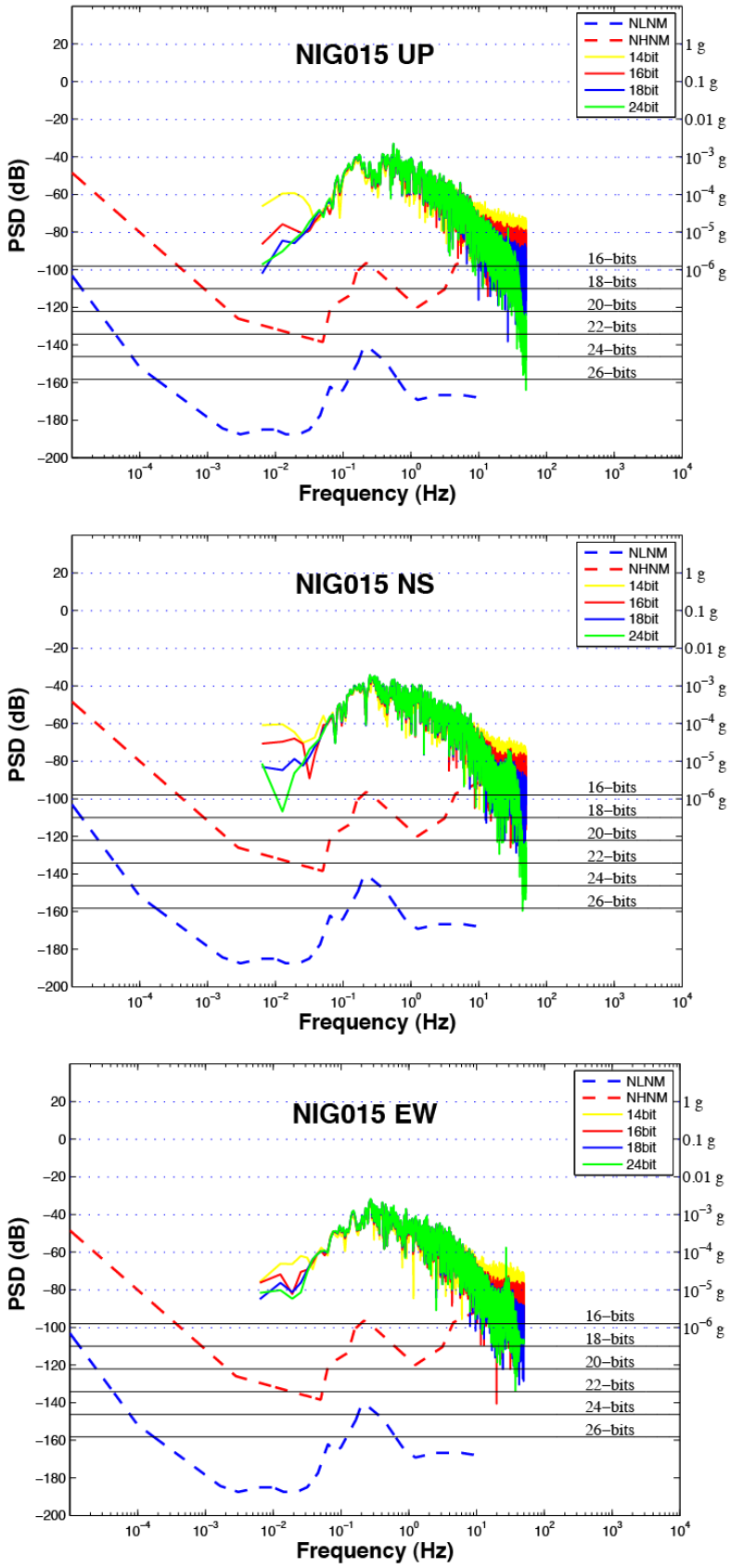

Figure 4.2.32. Same as Figure 4.2.26 but for station NIG015.

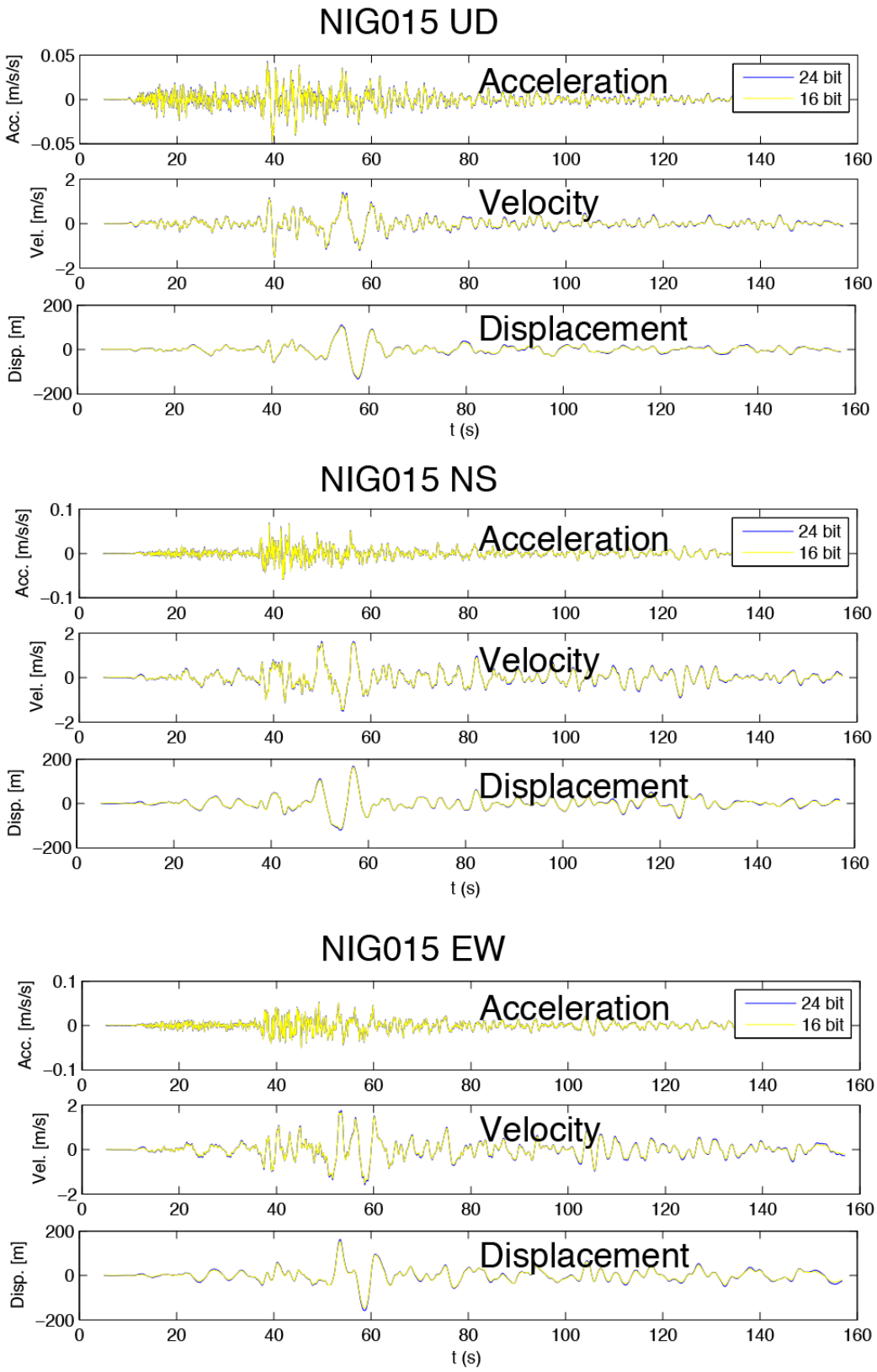

Figure 4.2.33. Same as Figure 4.2.27 but for station NIG015.

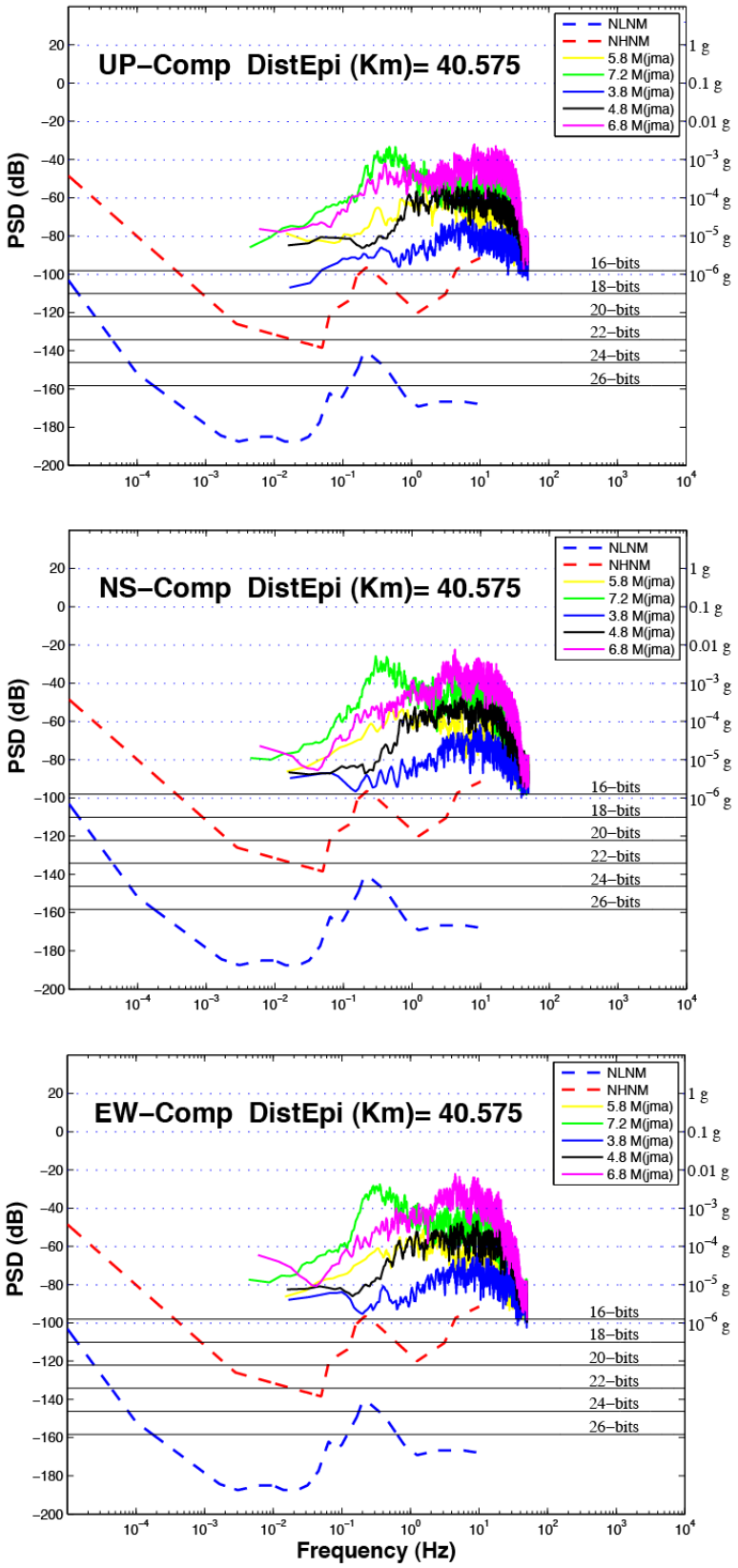

Figure 4.2.34. Power Spectral Density at 16 bit for different earthquakes (3.8-7.2 M_{jma}) recorded at the same station. Top: vertical component (UD). Centre: North-South horizontal component (NS). Bottom: East-West horizontal component (EW). The red and blue dashed line represent the high and low global noise level respectively. Data retrieved from Kik-net database. The black horizontal lines represent the theoretical dynamic range of a data acquisition.

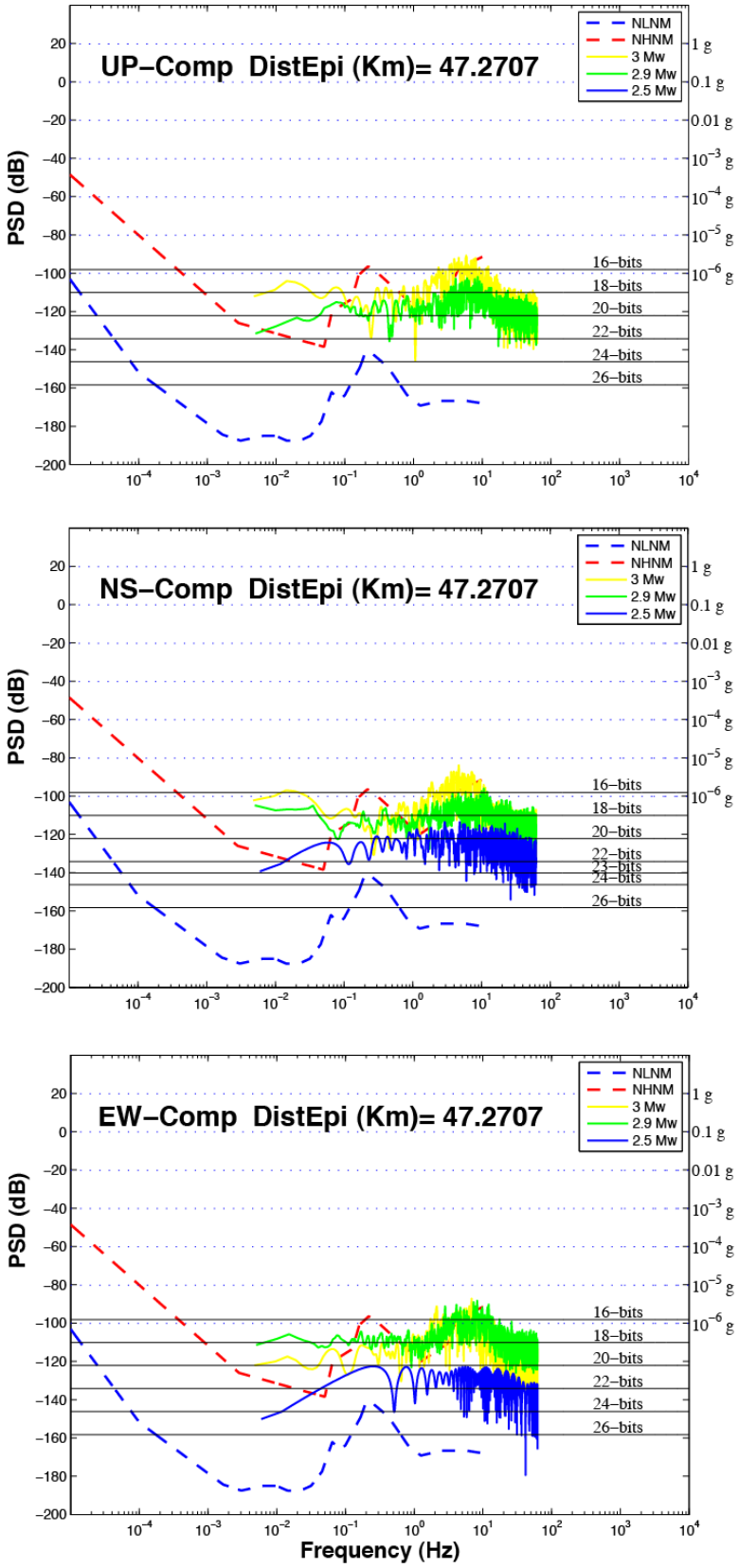

Figure 4.2.35. Power Spectral Density at 16 bit for different earthquakes (2.5-3.0 M_w) recorded at the same station. Top: vertical component (UD). Centre: North-South horizontal component (NS). Bottom: East-West horizontal component (EW). The red and blue dashed line represent the high and low global noise level respectively. Data retrieved from ISNet database. The black horizontal lines represent the theoretical dynamic range of a data acquisition.

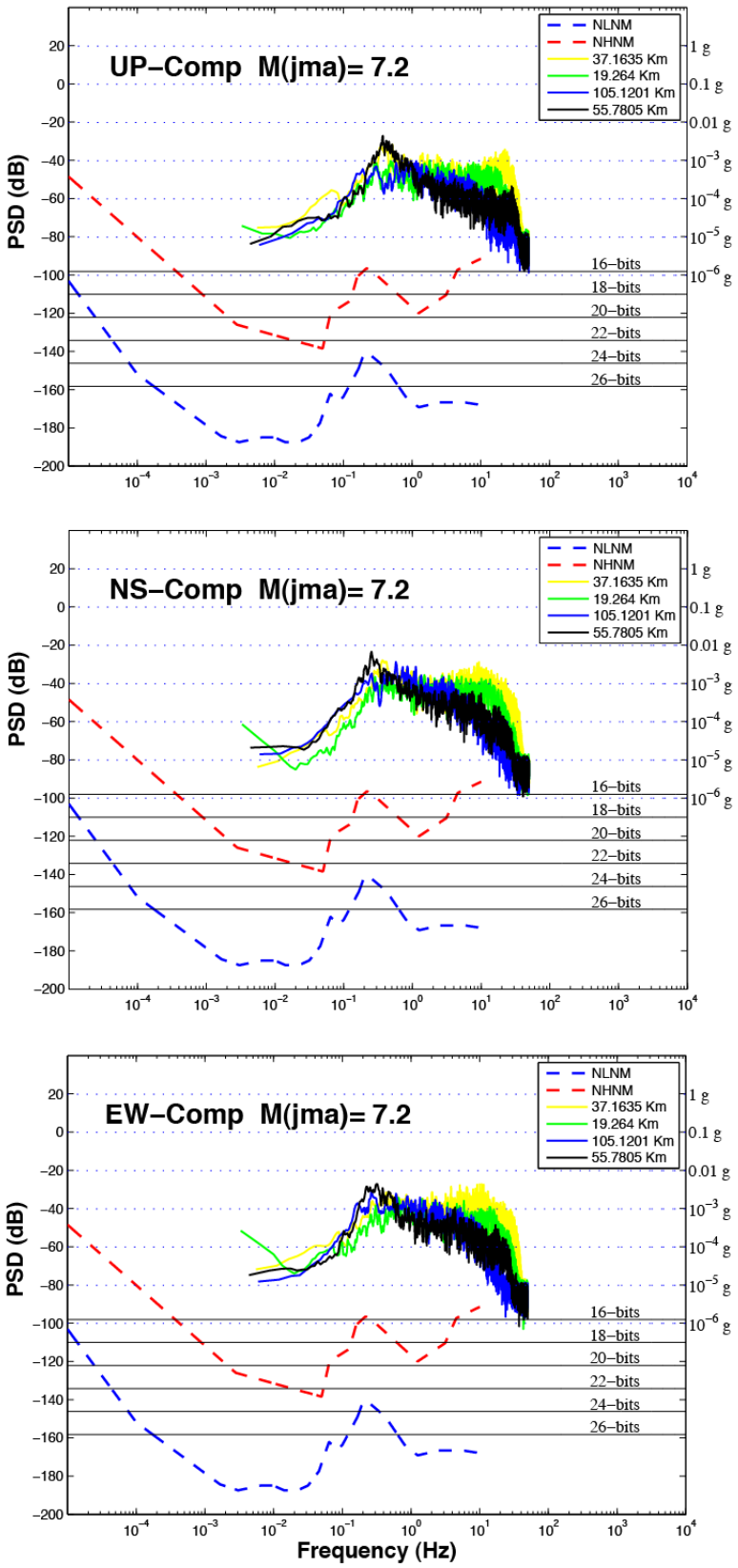

Figure 4.2.36. Power Spectral Density at 16 bit for an earthquakes of magnitude 7.2 M_{jma} recorded at different stations. Top: vertical component (UD). Centre: North-South horizontal component (NS). Bottom: East-West horizontal component (EW). The red and blue dashed line represent the high and low global noise level respectively. Data retrieved from Kik-net database. The black horizontal lines represent the theoretical dynamic range of a data acquisition.

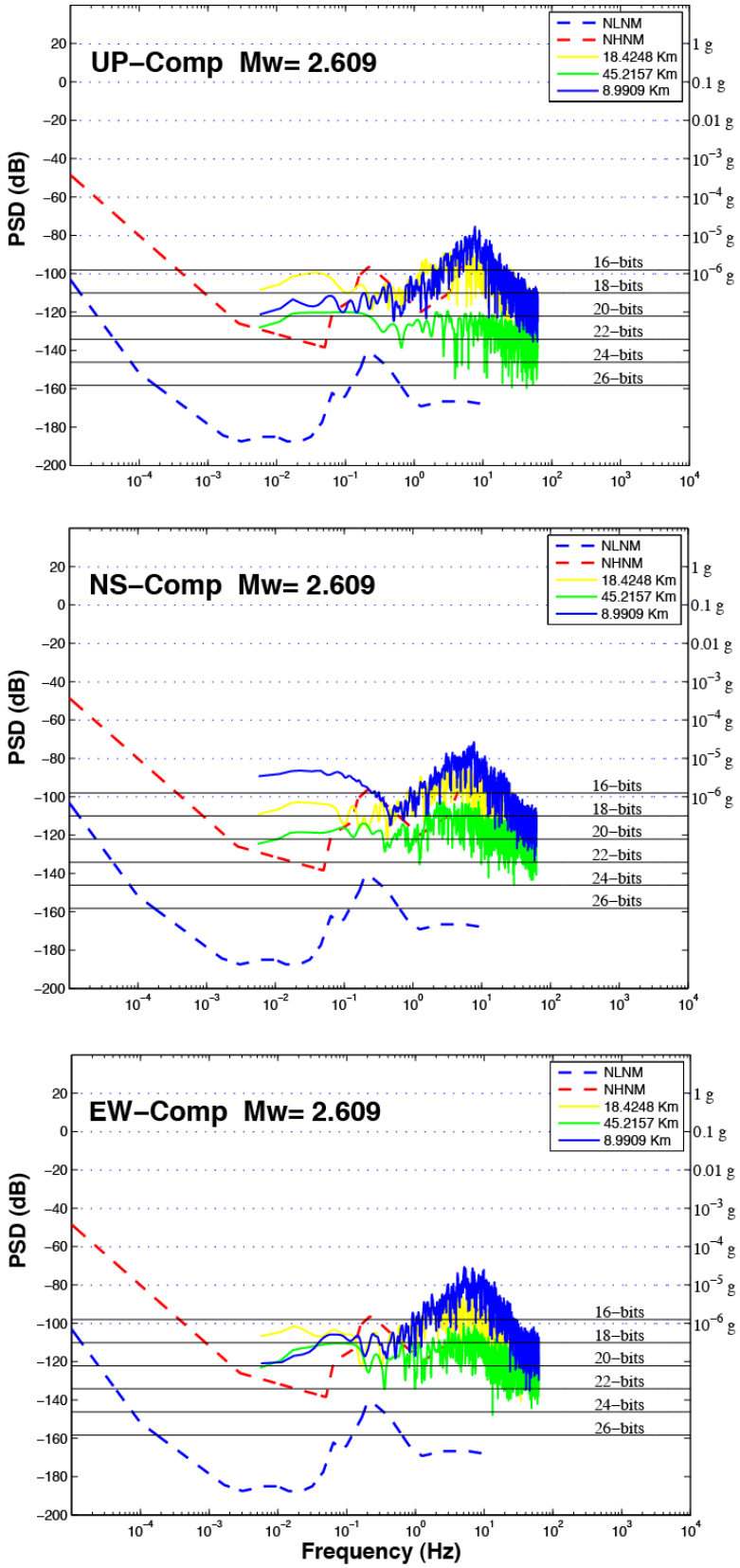

Figure 4.2.37. Power Spectral Density at 16 bit for an earthquakes of magnitude 2.6 M_w recorded at different stations. Top: vertical component (UD). Centre: North-South horizontal component (NS). Bottom: East-West horizontal component (EW). The red and blue dashed line represent the high and low global noise level respectively. Data retrieved from ISNet database. The black horizontal lines represent the theoretical dynamic range of a data acquisition.

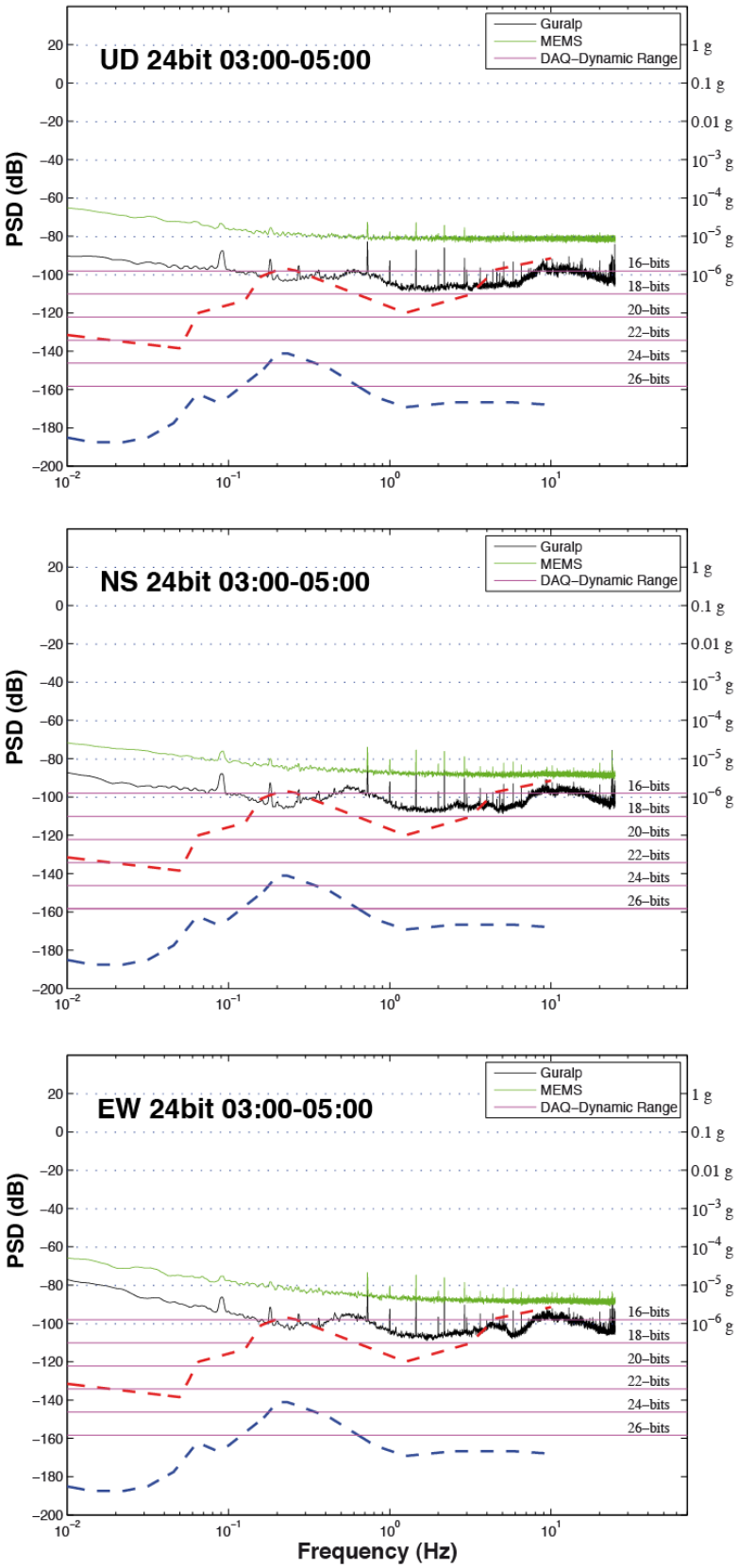

Figure 4.2.38. Power Spectral Density at 24 bit of seismic noise recorded by MEMS (green line) and Guralp (Black line) sensor at same site. Top: vertical component (UD). Centre: North-South horizontal component (NS). Bottom: East-West horizontal component (EW). The red and blue dashed line represents the high and low global noise level respectively. Data retrieved from ISNet database. The pink lines represent the theoretical dynamic range of a data acquisition. The date was recorded from 03:00-05:00 Am.

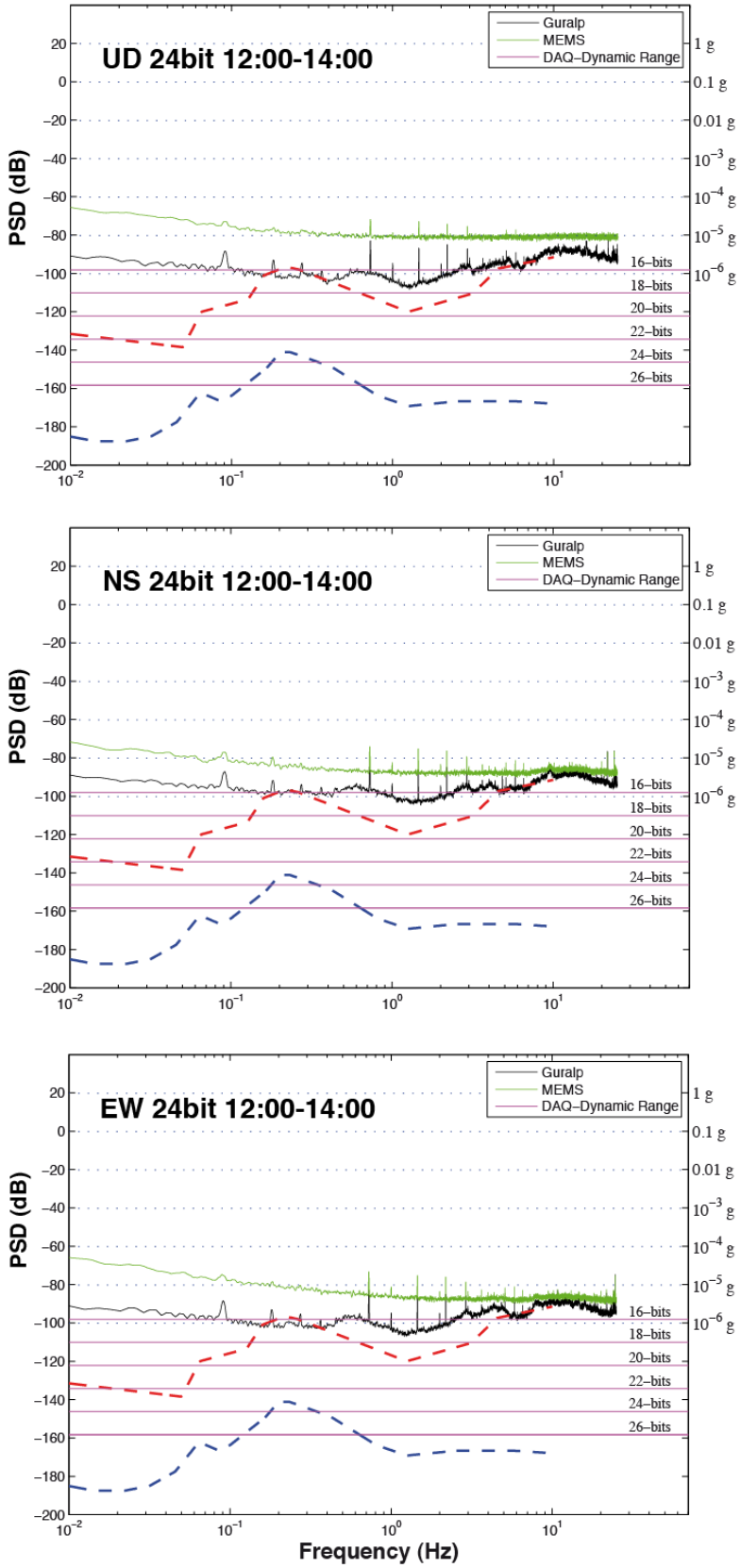

Figure 4.2.39. Power Spectral Density at 24 bit of seismic noise recorded by MEMS (green line) and Guralp (Black line) sensor at same site. Top: vertical component (UD). Centre: North-South horizontal component (NS). Bottom: East-West horizontal component (EW). The red and blue dashed line represents the high and low global noise level respectively. Data retrieved from ISNet database. The pink lines represent the theoretical dynamic range of a data acquisition. The date was recorded from 12:00-14:00 Am.

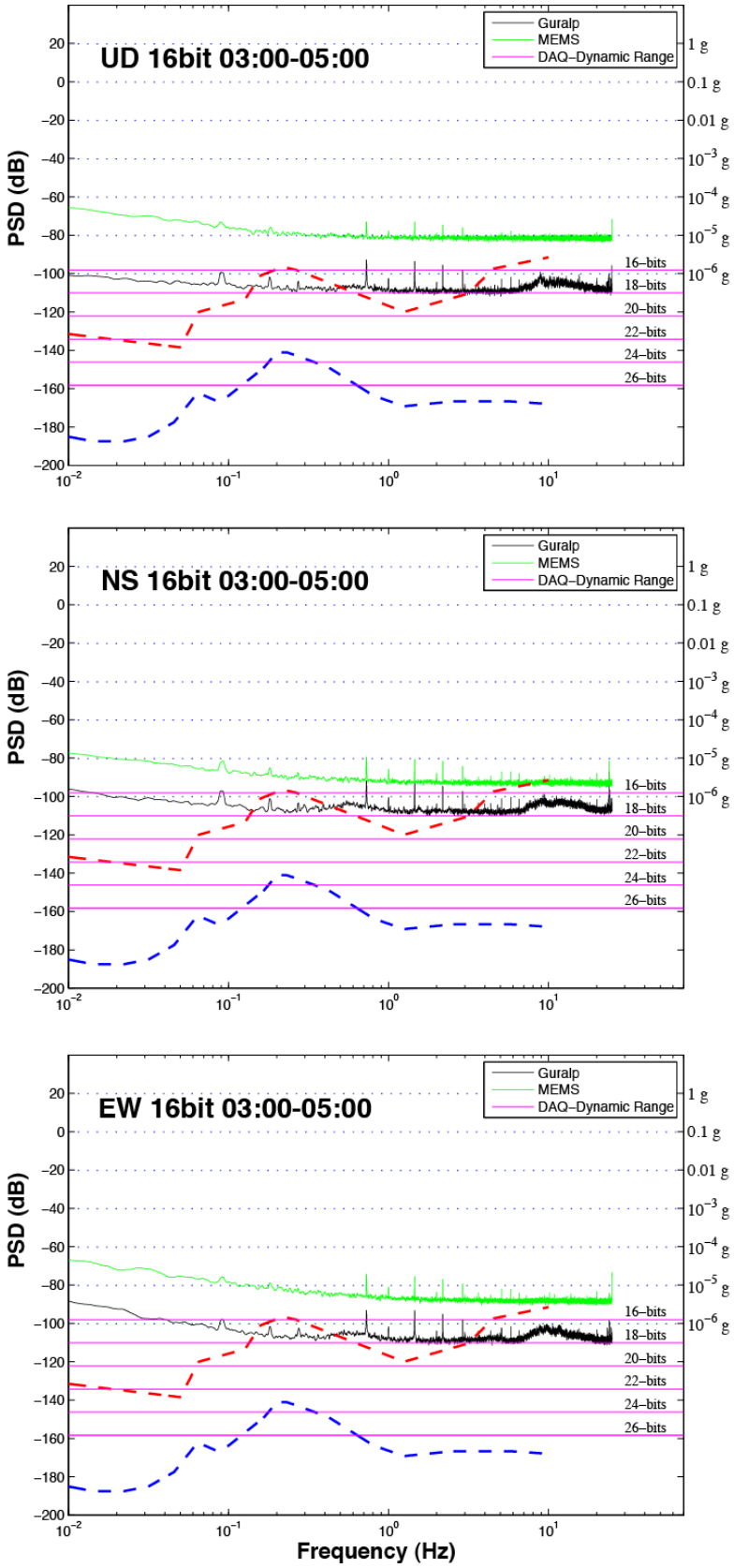

Figure 4.2.40. Power Spectral Density at 16 bit of seismic noise recorded by MEMS (green line) and Guralp (Black line) sensor at same site. Top: vertical component (UD). Centre: North-South horizontal component (NS). Bottom: East-West horizontal component (EW). The red and blue dashed line represents the high and low global noise level respectively. Data retrieved from ISNet database. The pink lines represent the theoretical dynamic range of a data acquisition. The date was recorded from 03:00-05:00 Am.

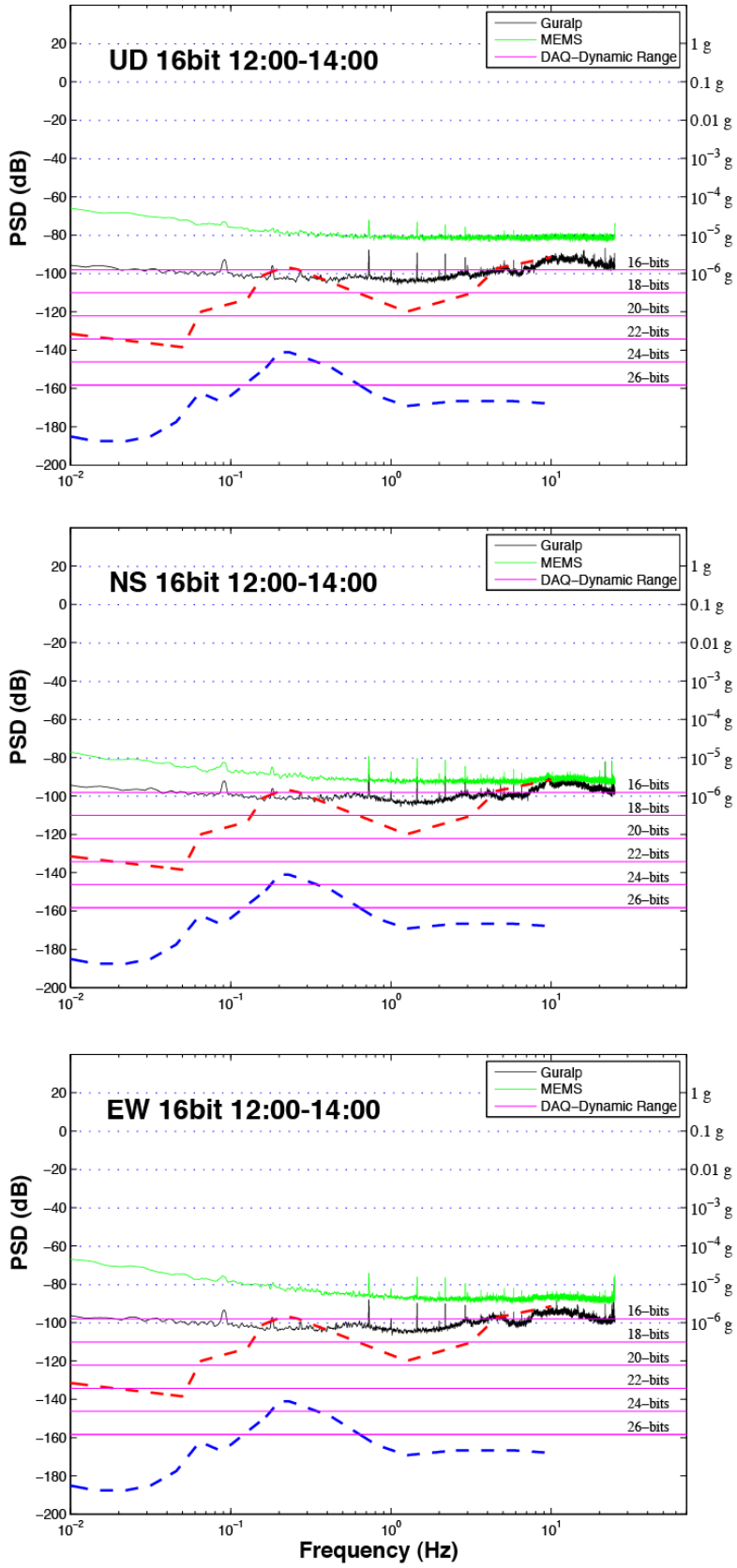

Figure 4.2.41. Power Spectral Density at 16 bit of seismic noise recorded by MEMS (green line) and Guralp (Black line) sensor at same site. Top: vertical component (UD). Centre: North-South horizontal component (NS). Bottom: East-West horizontal component (EW). The red and blue dashed line represents the high and low global noise level respectively. Data retrieved from ISNet database. The pink lines represent the theoretical dynamic range of a data acquisition. The date was recorded from 12:00-14:00 Am.

4.3 PRESTo on site

A methodology to analyse seismic signal in real time is mandatory in order to design a stand alone EEWS. A convenient approach could be a threshold-based algorithm (PRESTo) based on the simultaneous real-time measurements of the peak displacement (P_d) and the period parameter (τ_c) in 3 seconds time windows after first P wave arrival (Zollo et al., 2010). The combined use of these two parameters allows the identification of the damages caused by the incoming earthquake by using an alert level scheme (Figure 4.3.1).

Basically the threshold-based system proposed by Zollo et al. (2010) is based on three main empirical relationships between P_d, τ_c, namely peak ground velocity (PGV), magnitude and hypocentral distance. These relationships were retrieved by an off-line analysis of strong ground motion records from Japan, Taiwan and Italy areas.

A first empirical relationship has been retrieved correlating P_d and PGV (Eq.4.3.1) in order to obtain a prediction of the potential damaging effect of a moderate-to-large earthquake, through the instrumental parameter I_{MM} (Wald et al., 1999).

$$Log(PGV) = 0.73(\pm 0.01)\log(P_d) + 1.30(\pm 0.02) \qquad (4.3.1)$$

Where PGV is in cm/s^2 and P_d in cm.

The second equation (Eq.4.3.3) is based on the study of Nakamura (1988) and Wu & Kanamori (2005), that define the average period parameter (τ_c) :

$$\tau_c = 2\pi \sqrt{\frac{\int_0^{\tau_0} u^2(t)\, dt}{\int_0^{\tau_0} \dot{u}^2(t)\, dt}} \qquad (4.3.2)$$

Where the variable u represents the displacement and τ_0 is the time windows length (generally set to 3 sec.).

The average period is related to the earthquake magnitude by:

$$Log(\tau_c) = 0.21(\pm 0.01)M - 1.19(\pm 0.08) \quad (4.3.3)$$

Where M is expressed in moment magnitude and τ_c in second.

The last equation retrieved by Zollo et al. (2010) relates the initial peak ground displacement (P_d) with the average period parameter (τ_c) and the hypocentral distance R:

$$Log(P_d) = 0.6(\pm 0.1) + 1.93(\pm 0.03)\log(\tau_c) - 1.23(\pm 0.09)\log(R) \quad (4.3.4)$$

Where R is measured in Km, τ_c in seconds and P_d in cm/s^2.

The equation (4.3.4) looks like a Ground Motion Prediction Equation that allows estimating a ground motion parameter (P_d) as function of average period (τ_c) in a range of distance (R).

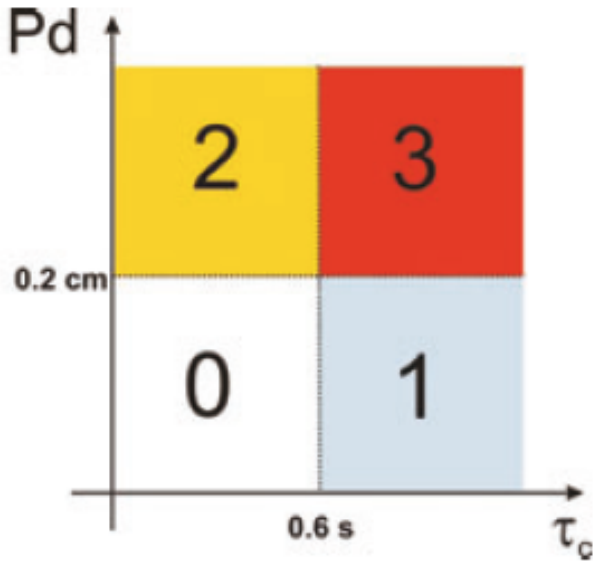

Figure 4.3.1. Alert levels and threshold values for observed early warning parameters. Four alert levels was defined: 3 = damages expected nearby and far-away from station; 2 = damages expected only nearby the station; 1 = damages expected only far way from the station and 0 = no expected damage. Pd versus τ_c diagram showing the chosen threshold values and the regions delimiting the different alert levels. Reported from Zollo et al. (2010).

For the two selected parameters (P_d and τ_c) a threshold values was chosen to define a set of alert levels. The maximum alert level (set to 3), associated to $P_d \geq 0.2$ cm and $\tau_c \geq 0.6$ cm/s^2, represents an event of large magnitude potentially dangerous nearby the recorded stations and far-away from it.

Level 2 represents a small magnitude earthquake potentially dangerous only in a limited area around the recorded station is associated ($P_d > 0.2$ cm and $\tau_c < 0.6$ cm/s^2).

Level 1 indicates a not dangerous event for the area around the station ($P_d < 0.2$ cm and $\tau_c > 0.6$ cm/s^2) and level 0 ($P_d < 0.2$ cm and $\tau_c < 0.6$ cm/s^2) means a small earthquake with no damage expected everywhere.

Using the equation (4.3.4) it is possible to calculate in real time a Potential Damage Zone (PDZ) defined as the area of radius R in which the ground motion is expected to overcome the threshold value of P_d (Fig.4.3.2). The PDZ can be rapidly assessed and notified without the estimation of the earthquake location and magnitude or predicting the ground shaking level through GMPE.

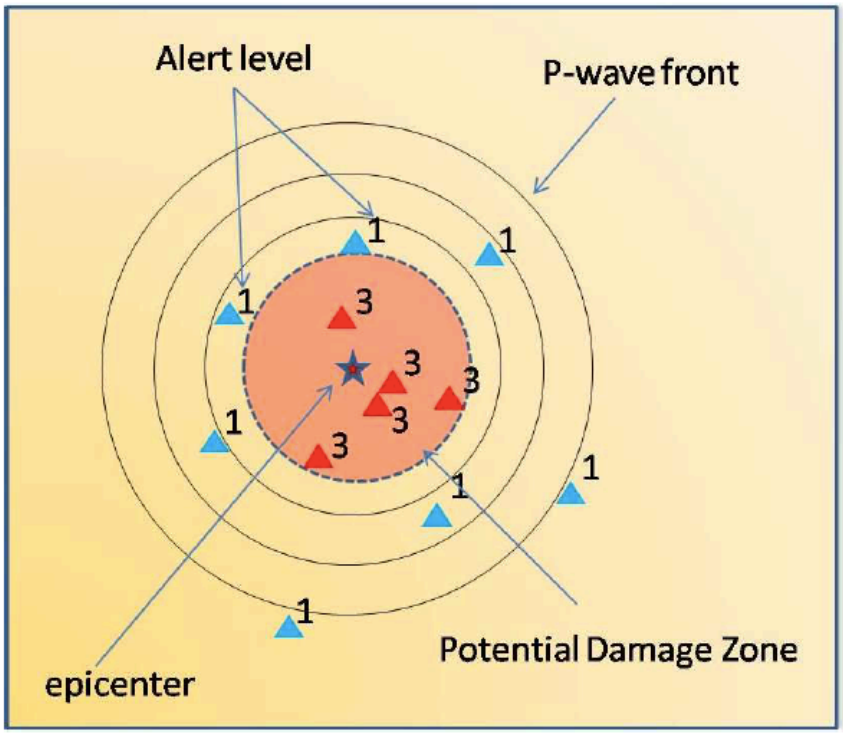

Figure 4.3.2. Potential damaged zone (PDZ). Reported from Zollo et al. (2010).

4.4 Results and perspectives

During the last months of this PhD thesis a preliminary study of a stand alone Earthquake Early Warning System (EEWS) was carried out and reported in this chapter. An EEWS could play a relevant role during the first instant of an earthquake giving an alert signal before the incoming of the most dangerous seismic wave. The technological and software development of an EEWS is not an easy task and requires the interplay of several interdisciplinary competences to combine seismological, programming and electronic know-how.

Different technical aspects were considered to define the main characteristics of an innovative, little, cheap and user-friendly system to minimize the immediate impact of an earthquake. A set of re-quantitation seismic registrations, at different number of bit, was considered as the first approximation of a seismic signal recorded by different ADC to acquire knowledge about the target range of the system in terms of magnitude-distance values.

The analysis performed pointed out that a 16 bit re-quantitation seismic signal is usually adequate up to 90Km (in case of moderate earthquake) and from 3.0/3.5 M_w. These values are not fixed and could vary as function of seismic signal attenuation for the area, focal mechanism and so on.

From tests performed on different sensor type it is clear that a 16 bit signal is enough to perform a seismic noise study. Moreover the PSD of MEMS sensor at 24 and 16 bit appears to be so similar to suggest the combination of MEMS with a 16 bit ADC as the most promising for a cheap EEWS able to work with moderate/large earthquake.

Future development of this preliminary study concern the installation of the EEWS-BOX (MEMS sensor, 16 bit ADC and “PRESTo on site” algorithm) in an active sismogenic area to record real seismic signal to perform a complete set of analysis. Moreover the MEMS sensor characterization in terms of transduction coefficient and sensor response at different frequencies is mandatory to correctly define the system performances.

4.5 References

Convertito et al. Rapid estimation of ground-shaking maps for seismic emergency management in the Campania Region of southern Italy. Nat Hazards (2010) vol. 52 (1) pp. 97-115

Kanamori, H.. Real-time seismology and earthquake damage mitigation. Annual Review of Earth and Planetary Science. 2004

Nakamura, Y., 1988. On the urgent earthquake detection and alarm system (UrEDAS), in Proceedings 9th World Conf. Earthquake Eng., Vol. 7, pp. 673–678.

Peterson, J. (1993). Observation and modeling of seismic background noise, U.S. Geol. Surv. Open-File Rept. 93-322.

Satriano, C., Elia, L., Martino, C., Lancieri, M., Zollo, A. & Iannaccone, G., 2010. PRESTo, the earthquake early warning system for southern Italy: concepts, capabilities and future perspectives, Soil Dyn. Earthq. Eng., doi:10.1016/j.soildyn.2010.06.008.

Wald,D.J., Quitoriano,V.,Heaton,T.H.&Kanamori, H., 1999. Relationships between peak ground acceleration, peak ground velocity and modified Mercalli intensity in California, Earthquake Spectra, 15, 557–564.

Wu, Y.M. & Kanamori, H., 2005. Rapid assessment of damage potential of earthquake in Taiwan from beginning of P waves, Bull. seism. Soc. Am., 95(3), 1181–1185, doi:10.1785/0120040193.

Zollo et al. A threshold‐based earthquake early warning using dense accelerometer networks. Geophysical Journal International (2010) vol. 183 (2) pp. 963-974

Zollo, A. et al., 2009a. Earthquake early warning system in southern Italy: methodologies and performance evaluation, Geophys. Res. Letters, 36, L00B07, doi:10.1029/2008GL036689.

Zollo, A. et al., 2009b. The earthquake early warning system in southern Italy, in Encyclopedia of Complexity and System Science, 5, 2395–2421, doi:10.1007/978-0-387-30440-3.